HAL
open science

Unsteady dynamics of corner separation in a linear compressor cascade

Gherardo Zambonini

To cite this version:

Gherardo Zambonini. Unsteady dynamics of corner separation in a linear compressor cascade. Other. Université de Lyon, 2016. English. NNT : 2016LYSEC049 . tel-01504626

HAL Id: tel-01504626

https://theses.hal.science/tel-01504626v1

Submitted on 10 Apr 2017

HAL is a multi-disciplinary open access archive for the deposit and dissemination of scientific research documents, whether they are published or not. The documents may come from teaching and research institutions in France or abroad, or from public or private research centers.

L'archive ouverte pluridisciplinaire **HAL**, est destinée au dépôt et à la diffusion de documents scientifiques de niveau recherche, publiés ou non, émanant des établissements d'enseignement et de recherche français ou étrangers, des laboratoires publics ou privés.

Numéro d'ordre : 2016LYSEC49

THÈSE de DOCTORAT DE L'UNIVERSITÉ DE LYON

Opérée au sein de

l'École Centrale de Lyon

École Doctorale 162: Mécanique, Énergétique, Génie Civil et Acoustique

Spécialité : Mécanique

Soutenue publiquement le 02/12/2016, par:

Gherardo Zambonini

Unsteady dynamics of corner separation in a linear compressor cascade

---

Devant le jury composé de :

Rob MILLER	Professeur, Cambridge University	*Rapporteur*
Dario PASTRONE	Professeur, Politecnico di Torino	*Rapporteur*
Ivana VINKOVIC	Professeure, Université Lyon I	*Examinatrice*
Pavlos ZACHOS	Professeur, Cranfield University	*Examinateur*
Xavier OTTAVY	Chargé de recherche, CNRS, LMFA	*Directeur de thèse*

“It is by logic that we prove,
but by intuition that we discover.”

HENRI POINCARÉ

Acknowledgements

I want to acknowledge the Université de Lyon and the CIRT (Consortium Industrie-Recherche en Turbomachines) for funding this work, and in particular Isabelle Trebinjac who promoted the visibility of the project.

I want to express my sincere acknowledgement to the Examiners, who accepted to review the manuscripts and participated at the viva in Lyon. I am sure that brilliant future projects will be developed between their universities and the LMFA.

I am deeply indebted with my PhD director Xavier Ottavy to have opened the door of the research to me, and guided into a world that was completely new and which I have loved. More of this, thank you for being always a reference for advises, support and definitely a good friend outside the laboratory.

This work would not have been possible without the presence of the colleagues and friends Sebastien Goguey, who helped me immensely with acquisition programs and supported me during several measurement campaigns, but also Pierre Laucher, Gilbert Halter and Benoit Paoletti, helpful for any other technical issue. You have been as a second family to me and I hope that you will keep the same good memories of me that I have of you. I want to thank all the other members of the Turbomachinery team for the discussions, the friendly atmosphere and the support that I have felt every day at the laboratory. I specially want to acknowledge Antoine Godard for the conversations on the uncertainty, the expert Nathalie Grosjean for the constant help with the PIV and Faouzi Laadhari for sharing his huge knowledge on the secrets of boundary layers.

Many thanks to Emmanuel Jondeau, Edouard Salze and Pascal Souchotte of the Acoustic team, for sharing the acoustic material and the patience to answer my many questions about these measurements.

Thanks to my office-PhD mates, the closest friends in this adventure: Quentin the botanic who loves good vibrations, Johannes the German expert of surge and stall, Zlatko for his home-made bubbles, Etienne and his passion for turbines, Emmanuel who shared with me his enthusiasm about diffusers and to Victor, the newest, I wish the best for his thesis and training on "baby-foot". Thanks to the ex-PhD guys but still friends Gao Feng, Nico and Marion, Guillaume, Pierre and Aurelian who initiated me to the french lifestyle and make me discover the best places in Lyon.

I want to thank my parents and my sister Samuela for the unconditional support and love, and I apologize for not being with them in delicate moments during these years spent abroad.

Finally, I dedicate this work to Alessandra, who has always been my beloved shield against madness and my thrust to overcome the defeats.

Abstract

The present work focuses on the study of the corner separation phenomenon in compressors carried out by experimental investigations on a subsonic linear cascade test rig ($Re = 3.8 \times 10^5$, $M = 0.12$, blade profile NACA 65-009).

Usually, this particular three-dimensional separation takes place in the corner between the blade and the endwall of compressor rows, mostly at hub, both in stators and rotors. Its main features are high total pressure losses and blockage of the flow, with consequent impacts on the efficiency. Whereas time averaged characteristics are well known from the past, only recent advanced experimental studies and improvements of numerical simulations, such as URANS and LES, have permitted to uncover the highly unsteady behavior of corner separation in compressors. Precedent studies on the same test rig have reported an intermittent unsteady behavior of corner separation, called *bimodal behavior*. In the present thesis it is shown that the bimodal behavior corresponds to two specific states of the flow: a closed separation, almost suppressed, and an open separation characterized by massive blockage and losses. Clearly hub-separation bimodal switches appearing in a real machine could have a first order detrimental effect on the stability of the flow in the compressor.

By using high speed PIV coupled with unsteady pressure measurements on the surface of the blade the flow in a single blade passage has been investigated for different incidences. The PIV measurements provide, for the first time, time-resolved flow visualizations of the size switch of the separation with an extended field of view covering the entire blade section. The interaction of random large structures of the incoming boundary layer with the blade is found to be a predominant element that destabilizes the separation boundary and enlarges the recirculation region. Such a massive separation persists until the blockage in the passage causes the breakdown of the largest structures in the aft part of the blade, reestablishing the closed separation state. Such dynamics coincide with the aperiodic intermittent flow regime of diffusers, called *transitory stall regime*, and the associated Fourier spectra show the largest energy amplitudes in the low frequency range. Conditional ensemble averages of pressure and proper orthogonal decomposition (POD) of velocity fields have been applied to show the feedback effect of the blockage of the separation on the flow angle around the blade leading edge. These results draw the picture of a self-sustained instability caused by the diffusion imposed by the interblade passage. To answer the question about the interaction between adjacent corner separations, time-resolved total pressure measurements have been carried out by using high frequency response sensors positioned in bimodal points of multiple passages. The coherent propagation velocity and the linearity of the phase angle found between the signals confirm that the unsteadiness of the separation can propagate in pitch-wise direction. It is interesting to underline that equivalent elements characterize rotating disturbances appearing in annular test rigs. This finally shows that, even in an isolated stator blade row, the intrinsic unsteadiness of corner separation can start the propagation of instabilities. It is the first time that such a propagation effect is observed in a linear compressor cascade.

Keywords: corner separation, compressors, turbulent intermittent flows, bimodal behavior, PIV, POD, time-resolved pressure measurements, microphones, disturbance propagation.

Résumé

Le présent travail concerne l'étude du décollement de coin de compresseurs par des investigations expérimentaux sur le banc d'essai subsonique grille d'aubes situé au LMFA ($Re = 3,8 \times 10^5$, $M = 0,12$, profil NACA 65-009) .

Habituellement, cette particulière séparation tridimensionnelle a lieu dans le coin entre l'aubage et la paroi du moyeu des rangées d'aubes, également dans les stators et les rotors. Les performances de l'étage sont ainsi dégradées à cause des pertes de charge et du blocage conséquent à la séparation de l'écoulement. Bien que les caractéristiques stationnaires sont bien connues par la littérature, uniquement des récentes études expérimentales avancées combinées aux améliorations de simulations numériques, telles que URANS et LES, ont permis de découvrir le comportement très instable du décollement de coin. Des études préalables sur le même banc d'essai ont rapporté un comportement intermittent du décollement, appelé *comportement bimodal*. Dans la présente thèse de doctorat, il est montré que le comportement bimodal correspond à deux états spécifiques du champ fluide: une séparation fermée, presque supprimée, et une séparation ouverte caractérisée par un blocage massif. Il est clair que cette commutation bimodale du décollement de coin apparaissant dans une machine réelle pourrait avoir un impact fortement déstabilisant.

En utilisant la méthode de mesure PIV haute vitesse couplée à des mesures de pression résolues en temps sur la surface de l'aubage, l'écoulement d'un canal inter-aube a été étudié pour deux différentes incidences. Les mesures PIV fournissent pour la première fois des visualisations résolues en temps et étendues à toute la section de l'aubage de la variation bimodale du décollement. L'interaction des grandes structures aléatoires de la couche limite à l'amont avec le bord d'attaque de l'aubage déstabilise le front du décollement et agrandit la région de recirculation. Une séparation ainsi massive persiste jusqu'à ce que le blocage dans le canal inter-aube provoque la rupture des plus grandes structures constituant la zone de recirculation. Successivement le débit recommence à accélérer et la séparation est presque supprimée. Cette dynamique coïncide avec le régime d'écoulement hautement instationnaire et apériodique des diffuseurs, appelé *large transitory stall*, caractérisé par des grandes amplitudes d'énergie dans la gamme des basses fréquences du spectre. Des moyennes conditionnelles de pression et la décomposition orthogonale modale (POD) des champs de vitesse ont été appliquées pour montrer l'effet rétroactif du blocage induit par la séparation ouverte sur l'angle local au bord d'attaque. Ces résultats supportent l'hypothèse d'une instabilité auto-entretenue causée par la diffusion imposée dans le stator. En fin, des mesures de pression totale résolues en temps ont été effectuées en utilisant des capteurs à haute réponse en fréquence, situés à la même position dans les différents canaux adjacents. La cohérence et la linéarité de l'angle de phase trouvée entre les capteurs confirment que l'instabilité du décollement peut se propager d'un canal a l'autre, en analogie avec les perturbations tournantes (*rotating instabilities*) apparaissant dans les bancs d'essai annulaires. Ceci montre pour la première fois que, même dans une grille d'aubes linéaire de compresseur, l'instabilité intrinsèque du décollement de coin peut déclencher la propagation d'instabilités.

Mots clés: décollement de coin, compresseurs, turbulence, écoulement instationnaire, caractère bimodal, PIV, POD, mesures de pression, propagation de perturbations.

Table of contents

List of figures xv

List of tables xxiii

Nomenclature xxix

Introduction 1

1 Context and physical mechanisms 5
1.1 Turbomachinery generalities . . . 5
1.2 Axial compressors . . . 7
1.3 Corner separation: fundamental mechanisms . . . 9
1.3.1 Junction flows . . . 9
1.3.2 Secondary flows . . . 10
1.3.3 Endwall boundary layer skew . . . 13
1.3.4 Spanwise boundary layer flow . . . 14
1.3.5 Topology of corner separation . . . 16
1.4 Impact of separations in compressors . . . 20
1.4.1 Loss generation . . . 20
1.4.2 Efficiency impact on high loaded stages . . . 24
1.4.3 Blockage . . . 25
1.4.4 Mismatching impact in multistage compressors . . . 26
1.5 Interaction with upstream rotor . . . 28
1.6 Instabilities in compressors . . . 30
1.6.1 Rotating stall . . . 30
1.6.2 Corner separation influence on spike-type stall inception and rotating instabilities . . . 30
1.7 Summary and Discussion . . . 36

2 Limitations and main goal of the study 39
2.1 Introduction . . . 39
2.2 Previous work on the LMFA cascade . . . 40
2.2.1 Bimodal distribution of velocity in literature . . . 40
2.2.2 Bimodal behavior in the LMFA cascade . . . 42

2.2.3 LES simulation of one half passage . . . 43
2.3 Prediction of separations . . . 44
2.3.1 De Haller number . . . 45
2.3.2 Liebelein diffusion factor . . . 45
2.3.3 Lei's criterion . . . 46
2.3.4 Corner shape factor . . . 47
2.3.5 Limits of RANS simulations . . . 48
2.4 Diffuser instability . . . 52
2.4.1 A focus on the transitory stall regime unsteadiness . . . 55
2.4.2 Interaction with inlet perturbations . . . 57
2.5 Summary and Discussion . . . 58

3 Experimental and analysis methods 61
3.1 Introduction . . . 62
3.2 The test rig . . . 63
3.2.1 Blades . . . 64
3.2.2 Cascade . . . 66
3.3 Inlet measurements . . . 68
3.3.1 Free flow characterization . . . 68
3.3.2 Inlet profile characterization . . . 69
3.4 Instrumented blade for pressure measurements . . . 71
3.5 Steady pressure measurements on the blade . . . 73
3.5.1 Experimental set up . . . 73
3.5.2 Steady pressure coefficient and uncertainty . . . 73
3.6 Time-resolved pressure measurements on the blade . . . 74
3.6.1 Microphones . . . 74
3.6.2 Calibration . . . 76
3.6.3 Data acquisition . . . 78
3.6.4 Data reduction . . . 78
3.6.5 Uncertainty . . . 79
3.7 Five hole pressure measurements . . . 84
3.7.1 Experimental set up . . . 85
3.7.2 Calibration and data reduction . . . 86
3.7.3 Uncertainty . . . 88
3.8 Time-resolved total pressure measurements . . . 89
3.8.1 Experimental set-up . . . 89
3.8.2 Uncertainty . . . 91
3.9 Time-resolved Particle Image Velocimetry (HS-PIV) . . . 92
3.9.1 Experimental set-up . . . 92
3.9.2 Calibration . . . 94
3.9.3 Convergence . . . 95
3.9.4 Uncertainty . . . 95
3.10 Stereo Particle Image Velocimetry (SPIV) . . . 99
3.10.1 Experimental set up . . . 99

3.10.2 Calibration 99
3.10.3 Uncertainty 100
3.11 Signal treatments and analysis methods 102
3.11.1 Average 102
3.11.2 Standard deviation and fluctuation Root Mean Square 103
3.11.3 Skewness 104
3.11.4 Kurtosis 104
3.11.5 Correlations 105
3.11.6 The Fourier transform 106
3.11.7 The power spectral density 106
3.11.8 Coherence function 107
3.11.9 Wavelet transform 107
3.12 Test rig adjustment 109
3.12.1 Parameters of sensitivity of the cascade 109
3.12.2 Symmetry and periodicity 110
3.13 Inlet boundary layer verification 114
3.14 Conclusions 119

4 Characterization of corner separation: Time-averaged VS Unsteady behavior 121
4.1 Introduction 121
4.2 Time averaged characterization 122
4.2.1 Inter-blade investigation 122
4.2.2 Downstream investigation 124
4.2.3 Comparison with previous work 130
4.3 The signature of the separation unsteadiness in pressure statistics 133
4.3.1 Main regions of unsteadiness in the suction surface pressure distribution 133
4.3.2 The separation detachment highlighted by skewness 133
4.3.3 Intermittency regions on the suction surface 136
4.4 The bimodal unsteadiness 137
4.4.1 Punctual time-resolved characterization 137
4.4.2 Decomposition of the unsteadiness 140
4.5 Summary and conclusions 142

5 Investigation of unsteady dynamics of corner separation 145
5.1 Introduction 145
5.2 Dynamics of the bimodal unsteadiness 146
5.2.1 Unsteady topology 146
5.2.2 Investigation of synchronized static pressures on the suction surface of the blade 149
5.3 The role of random incoming perturbations 156
5.3.1 Temporal evolution of flow angle of attack 156
5.3.2 Correlation between unsteady pressures on the blade 158
5.3.3 Effect of extreme incoming perturbations on the separation 159
5.4 The upstream effect of the separation blockage 163

5.4.1 Conditional ensemble average of pressure signals 163
5.4.2 Modal analysis 166
5.5 Comparison with diffuser regimes 174
5.6 Interactions between adjacent corner separations 176
5.6.1 Meaningful interactions 176
5.6.2 The pitchwise disturbance propagation 177
5.7 Summary and conclusions 183

6 Conclusions and perspectives 187
6.1 Conclusions 187
6.2 Perspectives 190

References 191

List of figures

1.1 Modern turbofan design and specifications 6
1.2 Axial compressor stage principles. 7
1.3 Performance characteristic map for an axial compressor. 8
1.4 Areas of interest of the smoothed-front rood wing junction flow and illustration of the wing-fuselage intersection of a technical configuration (Gand et al., 2010). 10
1.5 Sketch of the ensemble of secondary flow structures that can be encountered in a linear compressor cascade. Reproduced from Kang and Hirsch (1991) . 11
1.6 Secondary flow mechanisms of formation in cascades. 12
1.7 Effect of transverse pressure gradient on streamlines of the flow and formation of transverse velocity distribution (blue). 13
1.8 Competing effects of inlet boundary skew in a stator passage near hub wall: increasing incidence (red), reducing cross-flow (green). 13
1.9 Transverse surface pressure gradient magnitude (left) and related effect on development of corner separation increasing incidence (right). Case (a) shows the low lean blade affected by open corner separation; case (b) shows the high lean blade affected by trailing edge separation. Pictures are reproduced from the work of Taylor and Miller (2015). 15
1.10 Classification of critical points on the eigen-vector plane $[p-q]$. 18
1.11 Steady topologies identified for corner separations in compressor cascades. 18
1.12 Four basic type of flow for decomposition of complex 3D flow structures . . 19
1.13 Calculated parabolic increase of mixing losses for incompressible fully mixed out flow with wake of width w, reproduced from Cumpsty (1989). 21
1.14 Impacts of stage loading and corner separations on stage efficiency, reproduced from Dickens and Day (2011). 24
1.15 Blockage effect on mismatching in multi-stage axial compressor, adapted from Cumpsty (2010). 26
1.16 Comparison between corner separation in annular compressor cascade with and without upstream rotor, reproduced from Schulz et al. (1990a). 28
1.17 Unsteady investigation of corner separation in annular compressor cascade with upstream rotor, reproduced from Schulz et al. (1990b). 29
1.18 Rotating instabilities reported in annular compressor cascade of stator blades with and without hub clearance. 31

1.19 Spike formation in E3 rotor with zero clearance: (a) propagation of corner separation shown in section at 95% span; (b) three-dimensional radial structure. Reproduced from Pullan et al. (2015). 33
1.20 Investigation of the interaction between hub-corner separation and tip leakage flow in the inception of spike-type part stall, reproduced from Choi et al. (2008). 34
1.21 Inception of stall in stator hub of modern multistage high speed compressor by adjusting stator vanes to pass from an unloaded configuration Z to the experimental reference configuration A, reproduced form Dodds and Vahdati (2015). 36
1.22 Stall inception process found by Yamada et al. (2015) in multistage compressor by using DES. 37

2.1 Bimodal behavior in junction flows, reproduced from Devenport and Simpson (1990). 41
2.2 Bimodal behavior around a stalled airfoil, reproduced from Young Jr et al. (1978). 42
2.3 Illustration of bimodal behaviour 43
2.4 Time averaged topology resulted from the LES simulation and location of the bimodal point (a). Bimodal distribution captured by the simulation and fitting by Gaussian functions. 44
2.5 Lei's criterion: (a) explication of loading coefficient and stall parameter; (b) resulting correlation and overlap region at the critical value threshold. . . . 46
2.6 Definition of corner shape factor, from Taylor and Miller (2015) 47
2.7 Static pressure distributions at midspan (a), and in the separation region (b). Comparison between experiment and different turbulence models 48
2.8 Downstream total pressure losses at $0.363c_a$ axial distance from the TE. Comparison between experiments, LES and RANS simulations with different turbulence models. Reproduced from Gao (2014). 49
2.9 In-plane Reynolds stresses at the outlet section, $0.0c_a$ axial distance from TE. Comparison between LES, RANS Wilcox $k-\omega$ and Wilcox $k-\omega$ QCR, reproduced from Monier et al. (2016). 50
2.10 Figure (a): inlet profile generation in the range suggested by differences encountered between CFD and experimental inlet profile. Figure (b): consequent variation of predicted losses associated to the variation of the stator inlet incidence and comparison between low-lean and high-lean designs. Reproduced from Taylor and Miller (2015). 51
2.11 Geometry of two-dimensional, straight-wall diffuser and reference parameters (Reneau et al., 1967). 52
2.12 Flow regimes in subsonic, straight-wall, two-dimensional diffusers with steady inlet conditions (Reneau et al., 1967): (a) diverging angle influence and (b) aspect ratio influence. 53
2.13 Diffuser stall regimes. 54

2.14 Performances of subsonic two-dimensional diffuser at fixed N/W_1 (Reneau et al., 1967): (a) relationship between flow regimes and pressure recovery, (b) location of different optima of performance. 55
2.15 Histogram of stall periods for a water diffuser without forced inlet perturbations (Smith and Kline, 1974). 56

3.1 General view of the cascade at LMFA 63
3.2 Side view of the cascade and location of the reference point for inlet measurements. 63
3.3 Blade geometry 64
3.4 Figure (a): position of the trips at the LE of blade. Figure (b): influence of the presence of the trips on pressure distribution on the blade at midspan, $i = 0°$, reproduced from Ma (2012). 65
3.5 Cascade coordinates and parameters. Cascade reference system (x,y,z), blade reference system (x_b,y_b,z), curvilinear coordinates (s,n,z). 66
3.6 Instrumented Blade-II details. 71
3.7 Sketch of cavities geometry within the blade and plugged microphones. . . 73
3.8 Sketch of a condenser microphone and electric scheme 75
3.9 Microphone calibration instruments 76
3.10 Coherence (a), magnitude (b) and phase angle (c) between calibration A of reference and B for testing. Figures below are respective zooms on the low frequency range. 80
3.11 Signals reconstructed for different low-cut frequencies by exploiting calibration A (reference) and B (test). Figures on the right are respective zooms of cases on the left (y-axis adapted). 80
3.12 Figure (a): details of the five-hole probe used in the present study. Figure (b): associated angles in the probe coordinates $(x,y,z)_{5T}$ 85
3.13 Sketch of the downstream plane where total pressure measurements are performed. 85
3.14 Experimental calibration maps of the five-hole probe for the static pressure coefficient C_{Ps} (a), and the total pressure coefficient C_{Pt} (b). 86
3.15 Pressure gradient sensed on the probe head leading to angle misprediction. . 87
3.16 Kulite sensors used for time-resolved total pressure measurements. 89
3.17 Time-resolved coupled PIV-microphone measurements on the linear compressor cascade (a), laser head detail (b) and calibration plate installed in the passage (c). 93
3.18 Sketch of HS-PIV measurement configuration representing the planes and the position of PIV instrumentation. 94
3.19 Statistical significance of the PIV data at characteristic locations: sketch of sample locations and convergence diagram of relative standard deviations $\sigma_V/\overline{V_{tot}}$. Green line: single-set measurement, $N_1 = 2781$. 95
3.20 Stereo PIV experimental set up on the cascade test rig (a). Planes of measurement in the reference inter-blade passage (b). 100

3.21 Explaining illustration of kurtosis. Dotted lines show normal distributions, whereas the solid lines shows distributions with both positive kurtosis (left panel) and negative kurtosis (right panel), reproduced from DeCarlo (1997). 105
3.22 The Morlet wavelet: figure (a) shows the plot of the real part (solid) and imaginary part (dashed) for the wavelets in the time domain. Figure (b) gives the corresponding wavelet in the frequency domain. 108
3.23 Flap influence on the C_p of blade 5 at midspan: comparison between reference configuration and position 1, 2 and 3 of the bottom flap. 111
3.24 Experimental set-up for the boundary layer symmetry investigation. Removed blades are sketched in light gray color. 111
3.25 Original asymmetry between left and right endwall boundary layers 112
3.26 Final symmetry obtained between left and right endwall boundary layers. . 112
3.27 Total pressure losses comparison between original asymmetrical case (a) and final adjusted incoming boundary layers (b). 112
3.28 Downstream total pressure losses ω_t showing the final symmetry obtained between left and right corner separations in the reference passage between Blade 5 and Blade 6. 113
3.29 Final obtained periodicity of total pressure losses on left side of the test rig. 114
3.30 Sketch of inlet hot wire station of measurement. 114
3.31 Comparison between experimental results of the inlet boundary layer at the reference section $4.13c_a$ upstream of the blade obtained after setting the uniformity and previous measurements shown in Ma (2012). 116
3.32 Spectra of velocity for different points of the inlet boundary velocity profile measured at the reference section $4.13c_a$ upstream of the blade. 117
3.33 Time tracers of velocity in different locations of the inlet velocity profile acquired at the reference section L2 $4.13c_a$ upstream of the blade. Extraction of 1 sec from the signal, low-pass filter at $f = 1$ KHz 117
3.34 Top figure: skewness and kurtsosis of the measured velocity profile at $4.13c_a$ upstream of the reference blade. Bottom figure: Probability distributions of velocity fluctuations in the streamwise direction u' normalized by the inlet velocity at five chosen positions z/c, represented also on the top figure. . . . 118

4.1 Three dimensional visualization of 2D2C PIV velocity and streamlines . . . 122
4.2 Normalized Reynolds stresses achieved by SPIV measurements 123
4.3 Downstream plane of measurements for five hole measurements 124
4.4 Time average characterization of the corner separation at the section $x_c/c_a =$ 36.3% downstream of the TE for the configuration $i = 4°$. Total pressure losses (a), absolute velocity $\overline{V}/V_\infty$ (b), static pressure coefficient (c), secondary flow vectors (d), pitchwise angle (e) and spanwise angle of the flow (f). In secondary flow figure (d) the blue vectors give $SF_y > 0$ whereas red vectors are $SF_y < 0$. 125

4.5 Time average characterization of the corner separation at the section $x_c/c_a = 36.3\%$ downstream of the TE for the configuration $i = 7°$. Total pressure losses (a), absolute velocity $\overline{V}/V_\infty$ (b), static pressure coefficient (c), secondary flow vectors (d), pitchwise angle (e) and spanwise angle of the flow (f). In figure (d) the blue secondary flow vectors give $SF_y > 0$ whereas red vectors are $SF_y < 0$. 126

4.6 Figure (a) shows the pitchwise-mass-averaged total pressure loss coefficient from $z/c = 0.03$ (z= 5 mm) and $z/c = 0.53$ (z = 80 mm). Green: endwall boundary layer TBL. Red: wake. Blue: secondary flows losses SF. Bars represent the uncertainty associated to the measurements. Figure (b) resume the relative contribution of each term 127

4.7 Three-dimensional secondary vectors at $x_c/c_a = 36.3\%$ downstream of the TE for $i = 7°$. 129

4.8 Three dimensional visualization of static pressure coefficient C_p on the blade surface. Black cross indicated the reference data acquired in the previous work of Ma (2012). 131

4.9 Results of the previous campaign carried out by Ma (2012) at $i = 4°$. 132

4.10 Results of the previous campaign carried out by Ma (2012) at $i = 6°$. 132

4.11 Contour plot of $C_{p_{ss}}$ (a), $C_{p_{RMS}}$ (b), skewness (c) and kurtosis (d) on the suction surface of the blade, from end-wall ($z/c = 0.033$) to midspan ($z/c = 1.23$). 134

4.12 Schematic of near wall turbulent motion and associated wall pressure (a), reproduced from Astolfi and Forestier (1993). Separation process sketch for turbulent boundary layers (b) as proposed by Simpson et al. (1981): solid line denotes maximum shear locations; dashed line denotes $V = 0$ locations with V_{re}= mean re-entrainment velocity along $V = 0$. 135

4.13 Velocity RMS at section $z/c = 0.033$ for the configuration $i = 4°$ in Figure (a) and the configuration $i = 7°$ in Figure (b). Localization of positions $p1$, $p2$ and $p3$ utilized for the bimodal analysis in Section 4.4. 138

4.14 The bimodal behavior presented for the measurement case $i = 7°$, $z/c = 0.033$ at half of the blade profile $s^* = 0.5$. Comparison of velocity distributions and time tracers (middle plots, $n/c = 6\%$ from the surface of the blade) and not-bimodal points ($n/c = 1.7\%$ and $n/c = 13\%$). Green lines: instants from t1 to t6 selected for flow visualizations in Fig. 5.1. 139

4.15 Fourier transforms of velocity time tracers shown in Fig. 4.14 for the measurement case $i = 7°$, $z/c = 0.033$ at half of the blade profile $s^* = 0.5$. . . . 139

4.16 Mean velocity profiles and standard deviation of Mode 1 and Mode 2 composing the PDFs at section $z/c = 0.033$. The time-averaged velocity profile of the original distribution are represented by $\overline{u}_s$ and σ_s. Figure (a): configuration $i = 4°$, extraction line n at $s^* = 0.7$. Figure (b): configuration $i = 7°$, extraction line n at $s^* = 0.5$. 141

5.1 Visualization of main dynamics of the development of the separation, case $i = 7°$, $z/c = 0.033$. Closed separation at $t1$, propagation of perturbations from LE to separation at $t2$, separation-backflow collision at $t3$, large recirculation at $t4$, vortex sweep at $t5$ and reestablishing of closed separation at $t6$. 147
5.2 Pressure spectra at different sections from Channel 1 to 11 on the suction surface of the blade, case $i = 7°$. Steps between each zero level are characterized by $20dB$ variations. Dashed circles highlight the bump due to the tornado-like vortex in the aft part of the blade. 149
5.3 Coherence at different spanwise sections between the Channel 1 and consecutive Channels (2-11) in streamwise direction. 151
5.4 Time pressure signals for the selected Channels, green points in Fig. 5.1: (a) 3 Hz low-cut signals, (b) 50 Hz low-cut signals with indication of LDPI and HDPI region. Red vertical lines represent the time instants selected in Fig. 5.6 and 5.1. 152
5.5 Figure (a): displacement thickness calculated in the separation compared with integrated pressure distributions on the surface of the blade. Figure (b): unsteady pressure distributions captured for the selected instants $t1$, $t2$, $t4$ and $t6$ in relation to the flow visualization described in Section 5.2.1. 154
5.6 Unsteady flow angle map α_b of the extracted line in front of the LE, black line in Fig. 5.1. 156
5.7 Filtered displacement thicknesses calculated at LE and across the separation. The filtered lines are superposed to the unfiltered signals. Below: position of the extraction lines (on the left) and associated correlation (on the right). . . 157
5.8 Wavelet analysis of the pressure signal acquired by the Channel 4 synchronized with HS-PIV. 160
5.9 Wavelet conditional ensemble averaged of velocity u_b at section $z/c = 0.033$, $i = 7°$. Closed separation (a) and open separation (b) corresponding to two different wavelet power spectral thresholds as illustrated in Step 3 of Fig. 5.8a. Green point: trigger probe number 4. 161
5.10 Wavelet conditional ensemble RMS of v_b at section $z/c = 0.033$, $i = 7°$. Closed separation (a) and open separation (b), green point: trigger probe number 4. Dotted ellipse: “bridge" of high RMS associated to convected structures. 162
5.11 Ensemble average comparisons for negative thresholds between channel 1 at $s^* = 0.0$ and channels downstream, section at midspan ($z/c = 1.23$). 164
5.12 Ensemble average comparisons between channel 1 at $s^* = 0.0$ and channels downstream for positive and negative triggers in the separated region ($z/c = 0.133$). 164
5.13 Ensemble average comparisons for configuration $i = 7°$ between Channel 1 at $s^* = 0.0$ and channels downstream for negative (a) and positive (b) triggers in the separated region ($z/c = 0.133$). 165
5.14 Results of POD performed on the global field of data-set $i7°$ at $z/c = 0.033$, time data-set 1 sec ($N_1 = 2781$ samples). 168

5.15 Interpretation of Fig. 5.14a: sketch of the direction of the most extended vectors for the first four modes of POD applied to 2D velocity field, configuration $i = 7°$ at $z/c = 0.033$, 1 sec data-set measurement. 169
5.16 First 4 modes of POD on cut sections of the original field: Leading edge (LE) and Separation 170
5.17 Energy of the first 4 modes of local POD applied to cut sections of the original field: (a) Leading edge (LER), and (b) Separation (SR). Cumulated energy is sketched in the first left column of each diagram. 171
5.18 Red lines: highest correlations between different modes of the two selected regions, LE and Separation. Blue lines: auto-correlation of separation region modes; green lines: auto-correlation of LE region modes. Corresponding selected modes for correlations are sketched below each correlation graph. 173
5.19 Curved diffuser geometry (a) and location of first appreciable stall as a function of turning angle (b), reproduced from Fox and Kline (1962). The blue circle localizes the LMFA cascade operational point for $i = 4°$, the red circle for $i = 7°$. 175
5.20 Different configurations for the experimental investigation carried out with time-resolved total pressure probes. 177
5.21 Correlation between total pressure measurements carried out within three passages on both sides of the cascade (Configuration A). 178
5.22 Configuration B: time-resolved total pressure losses distributions (left column), associated time tracer for 1 second of acquisition (central column), and related Fourier spectra (right column). 179
5.23 Correlation between the reference passage, probe k2, and the four adjacent passages on the left side of the cascade (Configuration B). 180
5.24 Correlations between adjacent passages in configuration B. Figure (a): correlation peaks. Figure (b): related convection velocities. 180
5.25 Coherence analysis of the pitchwise disturbance between the first passage (probe k0) and following passages (k2-k4) in configuration B. Figure (a): coherence amplitudes. Figure (b): phase-lag angles. 181
5.26 Sketch of the equivalent parallel diffuser system setting the propagation of disturbances in pitchwise direction. 182
5.27 Proposed mechanism of mutual interaction between upstream perturbations and separation switch generating the pitchwise propagation. LE and separation regions derive from POD analysis. 183

List of tables

3.1 NACA 65-009 airfoil half thickness in blade coordinate. 65
3.2 Parameters of the cascade. 67
3.3 Coordinates of pressure taps on the Blade-II 72
3.4 Random error for the calculation of steady Cp on the suction surface of the blade for channels 1, 4 and 9. 74
3.5 Microphones calibration error variation at different low-cut frequencies . . 81
3.6 Relative error on pressure fluctuations for channels 1, 4 and 9 82
3.7 Microphones final relative error contributions 83
3.8 Random error in coherence calculation as a function of the coherence. . . . 84
3.9 Uncertainty of five hole pressure probe measurements 88
3.10 Relative systematic errors for Kulite time-resolved pressure sensors. 91
3.11 Time-resolved 2D2C PIV summarizing systematic uncertainties for three different measurement planes. 96
3.12 Statistical error of HS-PIV measurements 97
3.13 Statistical error of SPIV measurements 101
3.14 Quality parameters and errors for SPIV measurements 102
3.15 Parameters of the inflow boundary layer. 115

5.1 Static pressure correlations on the blade suction surface 158
5.2 Summary of POD correlations between LER and SR 172
5.3 Correlations of multi-passage pressure signals in configuration A 178

Nomenclature

Roman Symbols

A	Amplitude of a complex function
AR	Aspect ratio
c	Chord of the blade
c_a	Axial chord of the blade
C_p	Normalized static pressure coefficient
$CWT(f,t)$	Continuous wavelet transform
E	Measured tension
$e(X)$	Relative error on generic X, $e(X) = \varepsilon(X)/X\%$
e_{cal}	Calibration relative error %
e_p	Positioning relative error %
e_{st}	Statistical relative error %
e_{sys}	Systematic relative error %
f^*	Characteristic frequency $f^* = V_\infty/c$
f_r	Reduced frequency $f_r = f/f^*$
f_s, t_s	Sampling frequency and sampling time
$f_{low-cut}$	Low cut frequency for filtering signals
G	Gain of a sensor
H	Complex transfer function
h	Span of the blade
H_{12}	Boundary layer shape factor
i	Incidence angle
i^*	Optimum incidence
$I_{50}(CWT)$	Integrated wavelet transform from $f_{low-cut} = 50$ Hz

ICD_{x-y}	Integrated coherence deficit between signal x and y
K	Blade curvature
Ku	Kurtosis of a distribution (flatness)
M	Mach number
N	Length of a diffuser
N	Number of samples
N_1, N_{tot}	HS-PIV single-set samples, HS-PIV five-set samples
q_∞	Inlet dynamic pressure
R	Resistance of a sensor
$R_{12}(\tau)$	Cross correlation between data set 1 and 2
r_{mn}	Correlation coefficient between modes MmSR and MnLER
Re	Reynolds number
s,n,z	Curvilinear coordinate system of the cascade
s^*	Normalized curvilinear coordinate of the blade
s_p	Pitch-wise distance between blades
sc	CCD camera scale factor
Sk_3	Skewness of a distribution
St	Strouhal number
t	Time
t^*	Characteristic time of the flow $t^* = c/V_\infty$
Tu_∞	Inlet free stream turbulent level
U	Circumferential rotor velocity
u,v,w	Velocity components in the cartesian coordinate system of the cascade x,y,z
u_b,v_b,w	Velocity components in the coordinate system of the blade x_b,y_b,z
u_s,v_n,w	Velocity components in the curvilinear coordinate system of the cascade s,n,z
u_τ	Shear velocity $u_\tau = \sqrt{\tau_w/\rho}$
V	Absolute velocity
V_e	Mean velocity at the limit of the boundary layer
v_K	Tension of total pressure sensors
V_∞	Inlet free stream velocity
V_θ	Mean pitchwise velocity in the middle section $V_\theta = V_\infty \sin(\alpha_1)$

V_{ax}	Mean axial velocity in the middle section $V_{ax} = V_\infty \cos(\alpha_1)$
W	Relative velocity
W_1, W_2	Entry and exit surface of a planar diffuser
x, y, z	Cartesian coordinate system of the cascade
x_b, y_b, z	Cartesian coordinate system of the blade
x_{5T}, y_{5T}, z_{5T}	Cartesian coordinate system of the five hole probe
C_{p_s}	Static pressure coefficient at the outlet section of measurement
u^+	Dimensionless averaged velocity in inner variable u/u_τ
${u'_{rms}}^+$	Dimensionless velocity fluctuations in inner variable u'_{rms}/u_τ
h_t	Total enthalpy
p	Pressure
T	Temperature

Greek Symbols

2θ	Divergence angle of a planar diffuser
α	Pitchwise flow angle
α'	Blade metal angle
α_b	Angle of attack of the blade
α_{xy}	Pitchwise flow angle at the outlet section of measurement
$\Delta(\cdot)$	Variation of a generic quantity
δ^0	Deviation angle
δ_1	Boundary layer displacement thickness
δ_2	Boundary layer momentum thickness
δ_{99}	Thickness of the boundary layer
δ_{CS}	Displacement thickness across the separation
δ_{LE}	Displacement thickness in front of the LE
$\varepsilon(X)$	Absolute error on generic X such as $X \pm \varepsilon(X)$
ε_{cal}	Calibration error
ε_p	Positioning error
ε_{st}	Statistical error
ε_{sys}	Systematic error
γ^2	Coherence function

γ_b	Stagger angle of the blade
γ_{xy}	Spanwise flow angle at the outlet section of measurement
μ	Dynamic viscosity
ν	Kinematic viscosity
ω	Vorticity
ω_t	Total pressure losses coefficient
ϕ	Phase of a complex function
Φ_{xx}	Autospectrum of general variable $x(t)$
Φ_{xy}	Cross-spectrum between general variables $x(t)$ and $y(t)$
ρ	Flow density
σ	Standard deviation of a distribution
σ_b	Solidity of the cascade
σ_G	Gain error
σ_s	Sensitivity error
$\sigma_{v_{sensor}}$	Tension uncertainty of at zero flow
τ	Cross correlation time-lag
τ_w	Skin friction vector
θ_{12}	Deflexion or flow turning angle
φ	Camber angle of the blade
h_{LE}	Leading edge blade thickness
h_{TE}	Trailing edge blade thickness
k	Heat capacity ratio of air
$\omega_t{}^*$	Pitchwise-mass-averaged total pressure loss coefficient
β	Relative angle in rotor
Ω	Rotor angular velocity

Superscripts and Subscript

$5T$	Referring to five hole probe
∞	Inlet quantity
$\prime$	Fluctuation quantity
is	Isentropic
K	Referring to time-resolved total pressure sensor

s	Static quantity
t	Total quantity
$t-s$	Total-to-static quantity
CS	Referring to corner separation
IP	Referring to incoming perturbations

Acronyms / Abbreviations

D	Diffusion parameter
DF	Lieblein diffusion parameter
DH	De Haller number
(U)RANS	(Unsteady) Reynolds-averaged Navier-Stokes simulation
2D2C PIV	Two-dimensional two components PIV
CFD	Computational fluid dynamics
HDPI	High deviation pressure intervals
HS-PIV	High speed PIV
LC1	Locus of coherence 1
LC2	Locus of coherence 2
LDA	Laser doppler anemometry
LDPI	Low deviation pressure intervals
LE, TE	Leading edge, trailing edge
LES	Large eddy simulation
Ln	n-position of hot-wire measurement
MnLER	POD n-Mode of LE region
MnSR	POD n-Mode of separation region
PIV	Particle image velocimetry
POD	Proper orthogonal decomposition
PSD	Power spectral density
RMS	Root mean square
SF	Secondary flows vector
SPIV	Stereo PIV
TBL	Turbulent incoming boundary layer

Introduction

The research for the improvement of aircraft engines is a crucial challenge which has been pursuit from the beginning of the aircraft era in order to reduce the costs and to increase safety of flights. Beside this, the exponential evolution of the air traffic in the last two decades has added the urgent concern about the environmental sustainability.

The Airbus' Global Market Forecast for 2016-2035 and the IATA anticipate that air traffic will grow at 4.5% annually, i.e. more than doubling in next twenty years. The impact of this demand has dangerous environmental repercussions, concerning both the pollution and the economic sustainability due to the reduction of disposable fossil fuels associated to the increase of the price of kerosene.

In order to relief this world scenario, the ACARE (Advisory Council for Aeronautics Research in Europe) has proposed by 2020 strong objectives of reduction of the specific fuel consumption by 20% and CO_2 emissions by 50% .

In order to accomplish these tasks, the first key amelioration consists of increasing the efficiency of the gas turbine while reducing its size. Consequently, the compressor design has a major relevance in this process for two reasons. Since the compressor actually represents 40-50% of the engine weight, the reduction of the number of stages is directly associated to the decrease in weight and fuel consumption. However, the reduction of the number of stages leads to the increase of the single stage efficiency in order to assure the same pressure ratio, which in turn is related to the following second reason. Since an increase in the compressor efficiency of 1% directly favorites the decrease in the specific fuel consumption between 0.5% and 0.8% (Courtiade, 2012), the suppression of separations and other mechanism of entropy generation results to be the main goal of the design process.

Beside performance improvements, the engines must be safe, and also on this point the compressor has a major influence. The compression of a flow in fluid dynamics is an unnatural process which increases the possibility of the flow to separate. When rising the load on the blades of a single stage to increase its pressure ratio, the risk that the flow through the blade row becomes unstable is also increased. This explains the high sensitivity of compressors to inflow disturbances and abrupt operational changes, which can generate over-loading of the blades, especially during take-off phases, with the consequent sudden increase of separated flows and the inception of instabilities, such as rotating stall and surge. These unsteady flows not only lead to the break-down of the main flow but additionally induce mechanical efforts and vibrations of the blades.

The three-dimensional separation occurring at the junction between blades and walls, i.e. the corner separation, is one of these deleterious unsteady flows. Despite several

improvements in the comprehension and control of such phenomenon from the beginning of the research in turbomachinery, its unsteady nature has started to be clarified only during the last decade.

Numerical simulations and advanced experimental techniques have been exploited together to investigate the causes and the effect of the separation on performances of the compressor. However, flow visualizations of corner separation in complex high speed test rig are still unfeasible and current unsteady numerical simulations usually fail to accurately predict losses and the size of this separation. Furthermore, because of the high uncertainty surrounding the prediction of unsteady behavior of the separation, numerical simulations require always experimental validations in order to infer physical explanations. According to computational limitations, the state of the art at meaningful Reynolds numbers in compressors is represented by the Large Eddy Simulation (LES).

Even if this type of simulation could for the first time shed light on the physics of the unsteady flows in turbo machinery, its feasibility is nowadays limited to simplified cases of study and short physical times.

From this scenario arises the necessity of a specific dedicated experimental study of the unsteadiness of the separation, carried out in the present PhD work. The subsonic linear cascade situated at the LMFA was chosen to isolate the corner separation phenomenon from other co-existing flow unsteadiness in real compressors, in order to characterize the intrinsic unsteady behavior of the separation. A previous PhD work on the same test rig reported the existence of an unsteady variation between two statistical preferred states of the flow direction at the boundary of the separation, which was called *bimodal behavior*. The aim of the present work is to detail and understand the dynamics underpinning such bistable motion as well as the interaction between multiple separations.

The preliminary design and set up of the measurements, calibration and final measurements were carried out by the author during the present PhD thesis. Additionally, adapted post-processing methods were developed and exploited in order to analyze the results and to understand the physics of the unsteady separation.

Thesis outline

The present report describes major results achieved through such experimental data sets, as well as their physical interpretation.

The first Chapter reviews the state of the art of the comprehension of the time averaged mechanisms involved in the corner separation, as well as recent works focusing on the role of corner separations in the inception of instabilities in compressors.

The second Chapter presents previous results achieved on the present test rig as well as main questions from which the present work starts. The limitations related to the prediction of the unsteadiness of corner separation by means of the most recent numerical simulations are additionally discussed in this frame.

Experimental methods, the test rig and signal treatment tools are discussed in Chapter 3. Furthermore, the adjustment and the verification of the inlet boundary layer of the linear compressor cascade are explained and compared with the previous works.

The Chapter 4 presents the analysis of the investigated configurations at $i = 4^\circ$ and $i = 7^\circ$ through time average quantities, usually adopted when characterizing the corner separation. The bimodal behavior is then introduced in order to guide the reader through the comprehension of large differences between steady and unsteady topology of the corner separation.

Finally, Chapter 5 describes in detail the unsteady dynamics underpinning the bimodal behavior through the analysis of time-resolved flow visualizations achieved by particle image velocimetry and synchronized unsteady pressure measurements on the surface of the blade. This chapter additionally presents unsteady total pressure measurements carried out in multiple inter-blade passages in order to shed light on the unsteady interaction between adjacent separations.

The conclusion finally resumes the main achievements and the proposed final interpretation emerged from this work. But, as it commonly happens for challenging research subjects, results have lead to new questions and perspectives, which are described in the end of the thesis.

List of publications

1. Zambonini, G., Ottavy, X., and Kriegseis, J. (2017). Corner separation dynamics in a linear compressor cascade. *Journal of Fluids Engineering*

2. Zambonini, G. and Ottavy, X. (2015). Unsteady pressure investigations of corner separated flow in a linear compressor cascade. In *ASME Turbo Expo 2015*. American Society of Mechanical Engineers

3. Gao, F., Zambonini, G., Boudet, J., Ottavy, X., Lu, L., and Shao, L. (2015b). Unsteady behavior of corner separation in a compressor cascade: Large eddy simulation and experimental study. *Journal of Power and Energy*, 229(5):508–519

4. Gao, F., Ma, W., Zambonini, G., Boudet, J., Ottavy, X., Lu, L., and Shao, L. (2015a). Large-eddy simulation of 3D corner separation in a linear compressor cascade. *Physics of Fluids*, 27(8):085105

Chapter 1

Context and physical mechanisms

Contents

1.1 Turbomachinery generalities **5**
1.2 Axial compressors **7**
1.3 Corner separation: fundamental mechanisms **9**
1.3.1 Junction flows 9
1.3.2 Secondary flows 10
1.3.3 Endwall boundary layer skew 13
1.3.4 Spanwise boundary layer flow 14
1.3.5 Topology of corner separation 16
1.4 Impact of separations in compressors **20**
1.4.1 Loss generation 20
1.4.2 Efficiency impact on high loaded stages 24
1.4.3 Blockage 25
1.4.4 Mismatching impact in multistage compressors 26
1.5 Interaction with upstream rotor **28**
1.6 Instabilities in compressors **30**
1.6.1 Rotating stall 30
1.6.2 Corner separation influence on spike-type stall inception and rotating instabilities 30
1.7 Summary and Discussion **36**

1.1 Turbomachinery generalities

The aeronautic jet propulsion has jumped in a new era since the introduction of the air-breathing jet engine in the 30's with the parallel ideas of English and German pioneers

Frank Whittle and Hans von Ohain to build a reaction engine of very high ratio power/mass combining a gas turbine with a nozzle. Since then, enormous improvements have been made to arrive to modern aircraft engines, as the introduction of the double-flow turbofan concept, but a truly new technological breakdown is still future. The irreplaceable feature of jet engines is the capability to deliver for long periods of time enormous amounts of thrust compared to their mass, to be compact and reliable and to guarantee the aircraft propulsion in wide range of different missions.

In order to generate the propulsion, energy has to be provided to fluid at first, which is subsequently exploited to grant thrust and/or power at shaft for propellers. Such mechanism relies on the thermodynamic cycle of Brayton: the energy surplus is provided by the ignition at constant pressure of air-fuel mix in the combustion chamber. The pressure rise of the breathed air is needed to increase the efficiency of the cycle, so a compressor module is installed before the combustion chamber and a turbine is placed after the combustion chamber to extract from the exhaust gas the energy necessary to power the compressor. The remaining energy of the fluid is then converted in thrust by acceleration end ejection from a nozzle, or the energy is again transformed in shaft power by a second turbine to accelerate the fluid with a propeller or fan. The modern turbofan design integrate both concepts, the 20% of thrust is generated by the acceleration of the fluid in the core nozzle (hot gas) and the other 80% in the external duct, provided also of a nozzle, by the front fan (cold air).

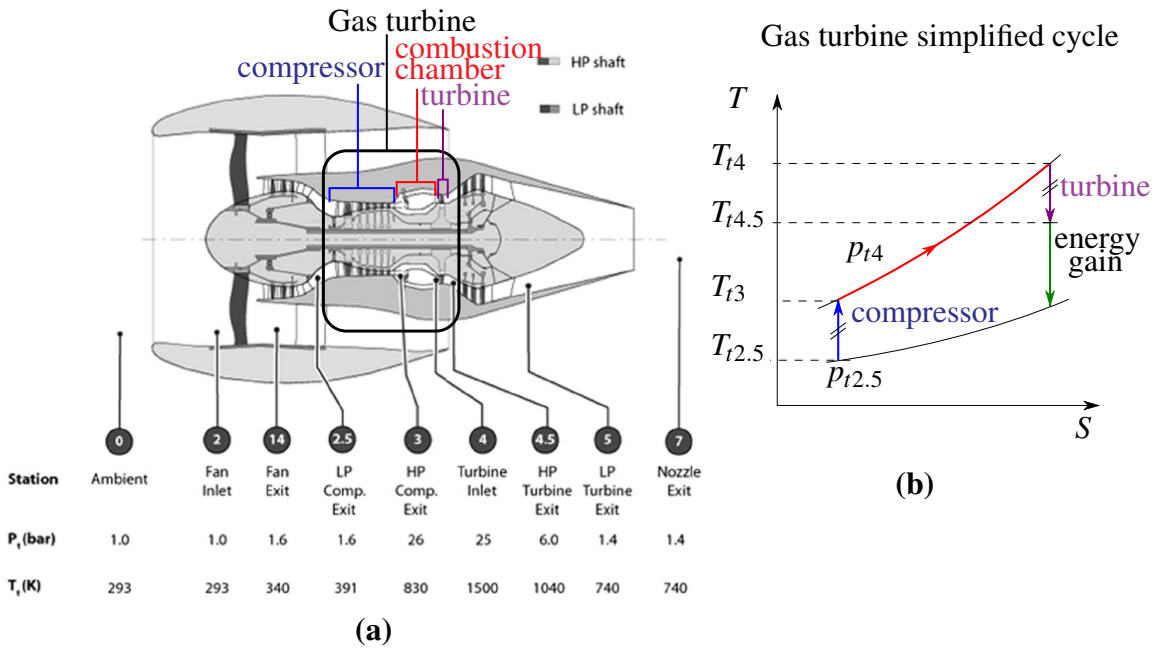

Fig. 1.1 Modern turbofan design and specifications (a). Gas turbine Brayton cycle (b).

A sketch of the gas turbine core is presented in Fig. 1.1a and the associated Brayton cycle in Fig. 1.1b. The surplus of energy is explained by the inherent divergence trend of the exponential isobar curbs when increasing the entropy of the flow. For this reason, the work spent for compression can be recovered by the expansion in the turbine module, saving energy in the fluid for propulsion.

1.2 Axial compressors

Axial compressor are constituted of sub-modules called *stages*, where a rotating blade row called *rotor* is placed upstream of a fixed blade row, i.e. the *stator*. The rotor is connected to the shaft, which is powered by the turbine, permitting to provide the fluid the total enthalpy gain in terms of kinetic energy (dynamic pressure) and static pressure increase. Anyway, the true compression of the flow is not possible without the fixed row: the stator is a diffuser that does not provide any work to the flow but is used to decelerate the flow and to recover the static pressure from the dynamic pressure provided by the rotor. Series of stages compose the compressor and permit to attain the required overall pressure ratio, p_{t3}/p_{t1} according to notation in Fig. 1.2b.

The basic principle of the stage is usually represented in a two-dimensional sketch at constant radial height, with the associated velocity vectors forming triangles, as shown in Fig. 1.2a. As common usage, U in this picture is the tangential velocity of the blade, V

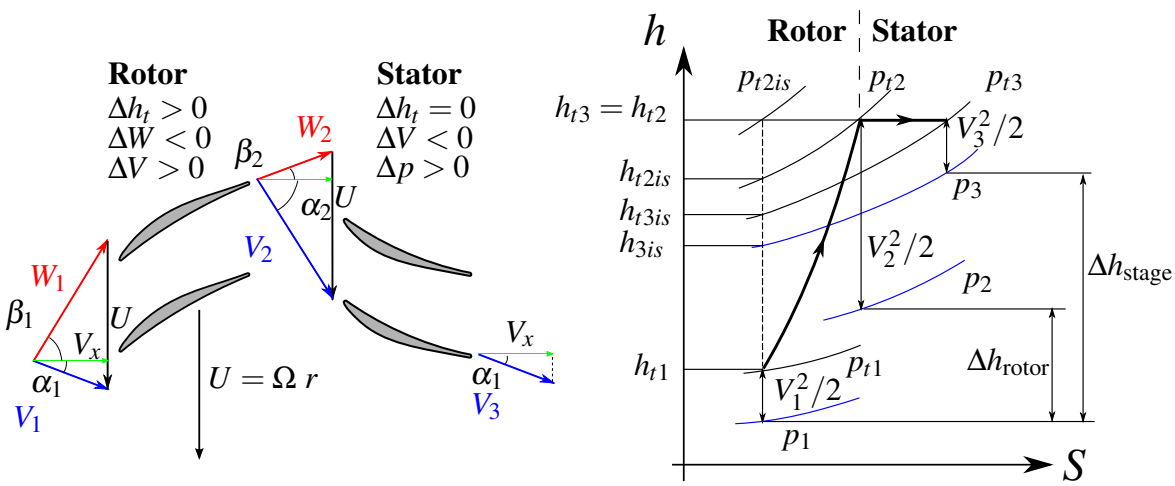

(a) Velocity triangles for axial compressor stage.

(b) Enthalpy diagram for a typical compressor stage with reaction degree $R = \Delta h_{rotor}/\Delta h_{stage} \approx 0.5$.

Fig. 1.2 Axial compressor stage principles.

the velocity vectors in the fixed frame and W the velocity vectors in the relative frame of reference (turning with the rotor). The total energy provided by the rotor to the flow ($\Delta h_t > 0$) can be expressed with the Euler equation, where U can be considered in first approximation equal and constant at the inlet and outlet of the rotor since calculated at the same radius, hence $U = U_1 = U_2 = \Omega r$.

$$\begin{aligned}\Delta h_0 &= U_2 V_{\theta 2} - U_1 V_{\theta 1} \\ &\approx U\left(V_{\theta 2} - V_{\theta 1}\right) \\ &= \Omega r\left(W_{\theta 1} - W_{\theta 2}\right) = \Omega r V_x\left(\tan\beta_1 - \tan\beta_2\right)\end{aligned} \tag{1.1}$$

Such relationship explains that the total energy provided to the fluid is linearly dependent to the difference of tangents of the relative angles of the flow in the rotor and the angular velocity of the shaft Ω.

The associated transformation on the enthalpy diagram is shown in Fig. 1.2b. The rotor accounts for the entire gain of total enthalpy but the compression is penalized by total pressure losses represented by the shifting from the p_{t2is} to p_{t2}. The stator has no transfer of energy with the flow but losses further decrease the stagnation pressure from p_{t2} to p_{t3}. The static pressure is shown in blue lines in order to present the reaction degree of the stage R defined as the ratio between the static enthalpy provided by the rotor and the entire static enthalpy gain across the stage.

The performance of a compressor is represented on maps of total-to-static pressure ratio π_{stage} and efficiency η_{stage} against mass-flow. Such quantities are respectively defined for a compressor stage as follows:

$$\pi_{stage}^{t-s} = \frac{p_{s3}}{p_{t1}} \tag{1.2}$$

$$\eta_{stage}^{t-s} = \frac{h_{3is} - h_{t1}}{h_{t3} - h_{t1}} = \frac{T_{t1}}{T_{t3} - T_{t1}} \left[\left(\pi_{stage}^{t-s} \right)^{\frac{k-1}{k}} - 1 \right] \tag{1.3}$$

Since the main scope of a compressor is to increase the pressure of the fluid passing through it, the major pressure gradient is opposed to the direction of the flow. The movement of the fluid particles is governed by the equilibrium between the inertial forces acting on the particles and such adverse pressure gradient which has to be contrasted.

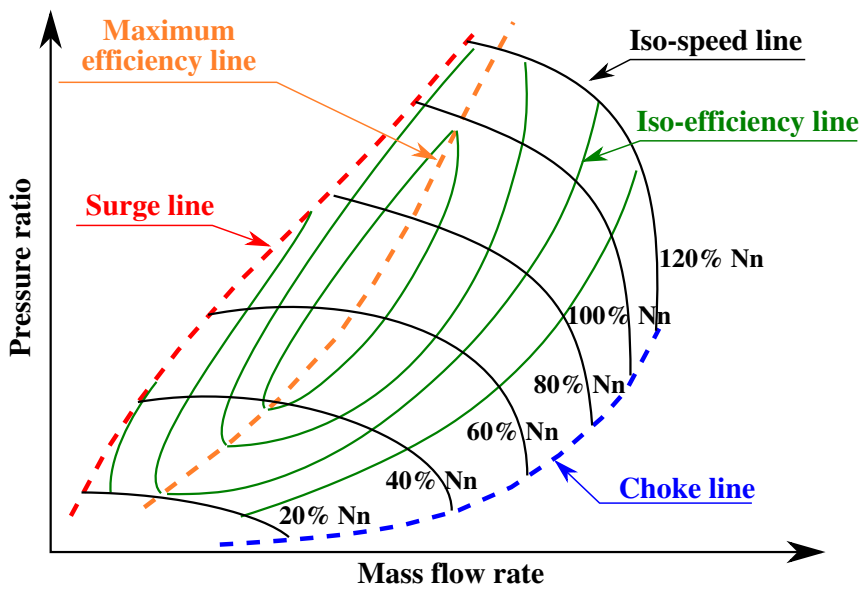

Fig. 1.3 Performance characteristic map for an axial compressor.

For a fixed and stable rotation velocity of the shaft, i.e. a fixed work provided to the fluid, the adverse pressure gradient acts as a throttle at the end of a duct representing the compressor. When the throttle is progressively closed, the pressure ratio and the adverse pressure gradient

increases so the flow rate decreases. Reversely, by opening the throttle, the flow is able to accelerate increasing the flow rate because of the decrease of the adverse pressure gradient. This characteristic behavior of the compressor is represented by the *characteristic curve*, or *performance characteristic* diagram, where the pressure ratio is traced against the flow rate for a fixed rotating speed of the shaft. Finally, multiple characteristic curves are obtained by varying the rotating speed and collectively form the characteristic map of the compressor. As seen before, the efficiency is a function of the pressure ratio, therefore contours of increasing efficiency levels can be drawn on the same map to obtain what is represented in Fig. 1.3.

The main goal of compressor designers is to attain the desired pressure ratio of the fluid before to enter the combustion chamber, while assuring to place the operational point of the machine in the maximum efficiency region of the characteristic map.

In order to achieve such goals, separations, secondary flow, wakes and clearance flow that dissipate the work provided to the fluid for compression must be reduced as much as possible. For this reason the understanding and suppression of corner separation has been one of the major targets of research in turbomachinery.

1.3 Corner separation: fundamental mechanisms

The corner separation phenomenon is presented in this section by reviewing the main flow mechanisms that characterize its existence.

The interaction between boundary layers occurring in corner of general junction flows is aggravated when considering blades which deflect the flow and the adverse pressure gradient, as in a linear compressor cascade. The passage vortex mechanism has to be considered when explaining the physics of the corner separation, as presented hereinafter. Furthermore, three-dimensional effects, such as the endwall boundary layer skew caused by upstream rotors and the spanwise boundary layer related to the geometry of the blade, have a significant impact on size and topology of the hub-corner separation in real compressors. The topology analysis is indeed one of the primary tools used to understand and visualize separations. Fundamentals of topology are therefore recalled in order to introduce time-averaged topologies commonly used to describe the corner separation in compressors.

1.3.1 Junction flows

The corner separation is a common feature of the flow around solid bodies that present a junction with a wall. The upstream boundary layer developed on the wall interacts with the boundary layer originating on the body, with a consequent increasing of the overall thickness of the boundary layer in the corner of the junction. The pressure gradients around the obstacle produce a three-dimensional separation that, except for very low Reynolds number associated to laminar flows, is characterized by high-intensity unsteady flow structures within the turbulent boundary layer, as described by Simpson (2001).

In case of a smoothed-front rood wing, as studied by Devenport and Simpson (1990) and Gand et al. (2010), the presence of the obstacle and the consequent blockage causes the incoming boundary layer to form the so-called horseshoe vortex. This vortex enrolls from

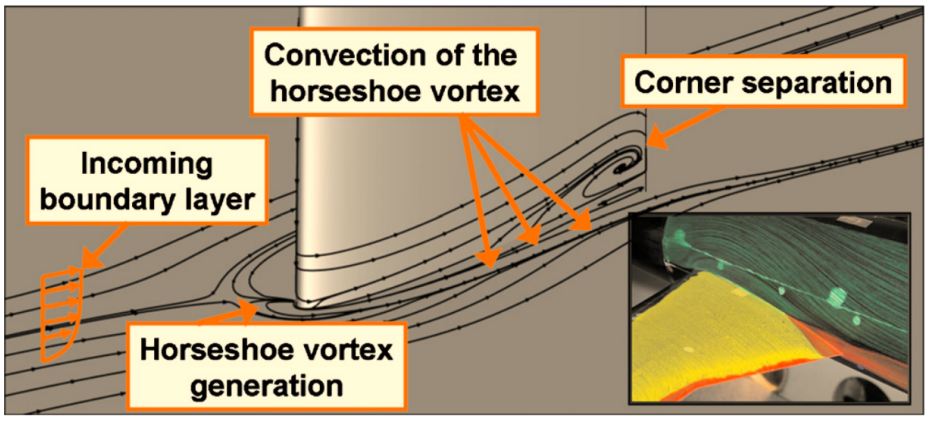

Fig. 1.4 Areas of interest of the smoothed-front rood wing junction flow and illustration of the wing-fuselage intersection of a technical configuration (Gand et al., 2010).

the leading edge into two legs which envelop the hub of the body and are convected further downstream. The acceleration between the LE and the maximum thickness location on the blade stretches the legs of the horseshoe vortex and then the adverse pressure gradient in the aft part of the blade favorites the separation, see Fig. 1.4.

The stagnation point located on the surface of the body at the leading edge represents the starting point for the separations lines that extend downstream on each side of the obstacle. As commonly referred for the study of such flow cases, the stagnation point on the body denotes the limit between the upstream and the downstream part of the flow.

Concerning compressors in turbomachinery, the leading edge horseshoe vortex is downsized because of the sharpness of the blades. The corner separation on the suction side of the blade near the trailing edge is instead exasperate by the adverse pressure gradient present in the inter-blade passage. Conversely in turbines, the thicker shape of the blades promotes the formation of the horseshoe vortex, while the suction side separation is more affected by the curvature of the blade. This because the beneficial pressure gradient and the acceleration of the flow in turbines support the attachment of the boundary layer on the blade surface.

1.3.2 Secondary flows

Secondary flows are defined as any flow that is in a direction different to the free stream. In turbomachinery, a wide range of different flows can be included in this general definition but in a compressor cascade with zero tip gap, the summary of the secondary flow that can be encountered is resumed in Fig. 1.5 and listed below, in agreement with the work of Kang and Hirsch (1991).

- Cross-flow or passage vortex
- Horseshoe vortex
- Corner vortex
- Trailing vortex
- Concentrated shed vortex

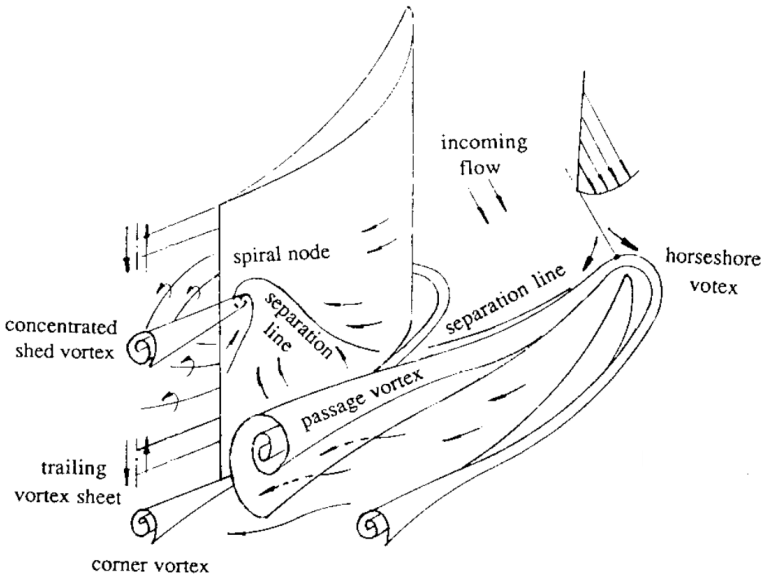

Fig. 1.5 Sketch of the ensemble of secondary flow structures that can be encountered in a linear compressor cascade. Reproduced from Kang and Hirsch (1991)

The major flow of this list is the cross-flow across the endwalls within the passage (Horlock, 1973; Lakshminarayana, 1996), also called *passage vortex*. This secondary flow represents the Prandtl's first kind of secondary flow, or skewed-induced vorticity, and it is explained by Fig. 1.6a. The inlet flow is considered completely axial with a velocity profile non-uniform as a result of friction between the fluid and the wall. The fluid in the boundary layer region of the end-wall (particle A) has lower velocity than the free stream outside the boundary layer (particle B). The pressure field within the passage faced by both particles is assumed to be the same, since isobars are almost straight in the spanwise direction. Entering the pressure field of the blade row, the particle A follows correctly the curvature of the blades and is kept balanced by the centrifugal force and the force induced by the traverse pressure gradient. Contrarily, the particle B, characterized by a lower momentum, is obliged to move to a smaller radius in order to attain such equilibrium. Consequently, the streamline radius of curvature near the end-wall is smaller than in the free-stream, leading to a cross-passage motion and the accumulation of lower total pressure fluid near the corner between the suction surface and the endwall. For a cylindrical frame of reference (r, θ, x), the equilibrium equation can be written in r direction normal to the blade surface as Eq. 1.4.

$$\frac{V^2}{r} = \frac{1}{\rho}\frac{\partial p}{\partial r} \tag{1.4}$$

Mathematically, this essentially inviscid or quasi-inviscid process (Bradshaw, 1987) can be estimated as reviewed by Dixon and Hall (2013). The incoming fluid particles must satisfy the no-slip condition at the wall. As consequence, the boundary velocity gradient dV_1/dz, perpendicular to the flow direction, establishes the vorticity vector ω_1. Entering the

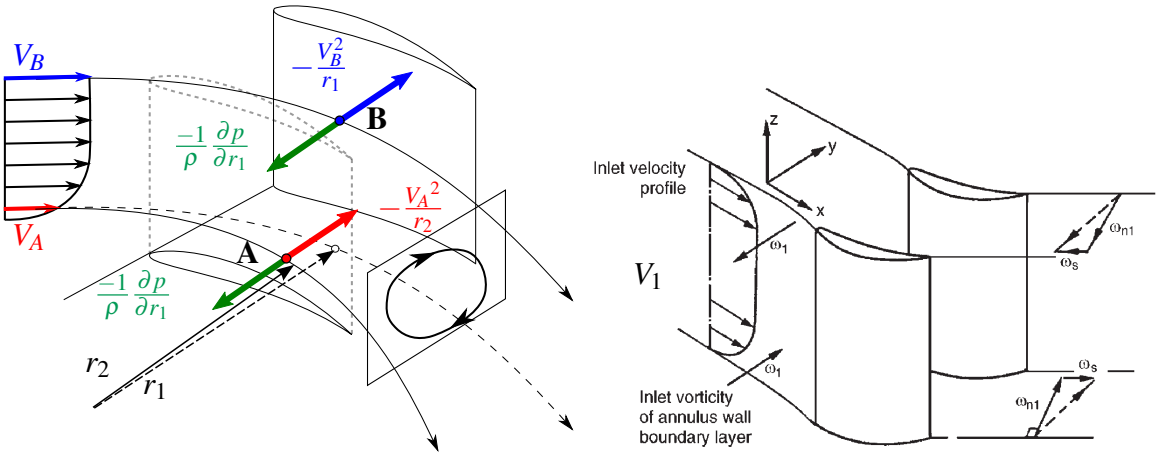

(a) Secondary flow physical mechanism in a blade row passage.

(b) Secondary flow vorticity model, reproduced from Dixon and Hall (2013) .

Fig. 1.6 Secondary flow mechanisms of formation in cascades.

cascade, such vector is deflected in a manner analogous to the motion of a gyroscope, i.e. in a direction perpendicular to the direction of turning. As result, a secondary vorticity vector ω_2 is generated at the outlet, parallel to the stream direction. Considering the deflection angle θ_{12} not large, the following estimation of secondary vorticity can be achieved as Eq. 1.5.

$$\begin{cases} \omega_1 = dV_1/dz \\ \omega_2 = -2\theta_{12}\omega_1 \end{cases} \rightarrow \omega_2 = -2\theta_{12}\frac{dV_1}{dz} \tag{1.5}$$

The horseshoe vortex is an inherent feature of junction flows and has already been described in the previous section. The size and the strength of this vortex is strongly dependent on the shape of the leading edge blade profile. In particular if the leading edge is sharp, the horseshoe vortex can be close enough to the surface to be rapidly diffused by viscous or Reynolds stresses (Bradshaw, 1987).

Turbulent boundary flows in a corner present the inherent characteristic to generate the so-called corner vortex. Its mechanism of formation is indeed attributed to the anisotropy of the stress tensor. As proved in the experimental investigation of Gessner (1973), transverse gradients of Reynolds shear stress components influence the streamwise shear of the primary flow and are directly responsible for the generation of secondary streamwise vorticity in the corner.

The presence of corner vortex does not imply directly the flow detachment (Bradshaw, 1987) and it should not be confused with the corner separation. The topology of the corner vortex will be discussed later in the topology review, Section 1.3.5, beside more complex topologies describing separations.

Another type of secondary flow can be distinguished inside the blade wake, where two discrete vortices and a vortex sheet form, rotating in same sense but opposite to the passage vortex.

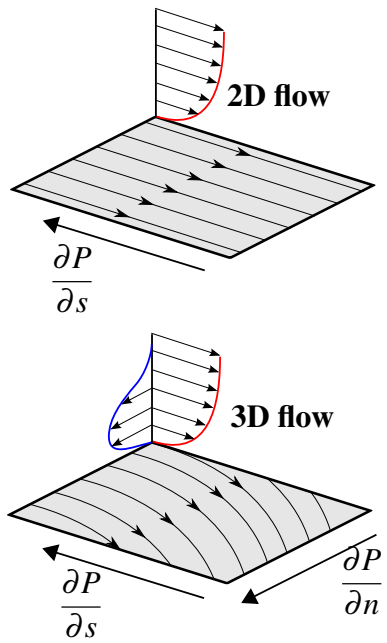

Fig. 1.7 Effect of transverse pressure gradient on streamlines of the flow and formation of transverse velocity distribution (blue).

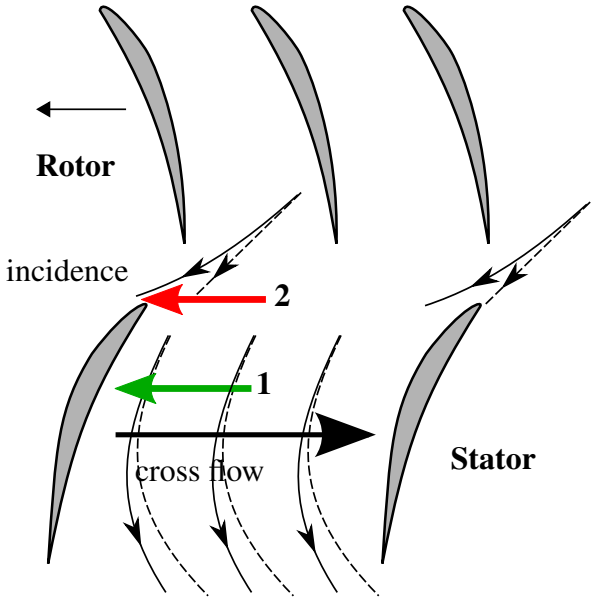

Fig. 1.8 Competing effects of inlet boundary skew in a stator passage near hub wall: increasing incidence (red), reducing cross-flow (green).

Finally, Kang and Hirsch (1991) highlighted the presence of other concentrated vortices, which shed from the spiral node on the suction surface near trailing edge, as depicted in Fig. 1.5. The existence of these concentrated vortices and their interaction with the corner vortices interferes with the cross-flow, producing a reduction of the amount of overturning caused by the passage vortex.

1.3.3 Endwall boundary layer skew

As explained in previous sections, secondary flow and viscous effects occurring in a blade row cause overturning of the flow near the endwall and consequently produce a skew, or swirl, in the endwall boundary layer at the outlet.

Concerning stator vanes, the effect of the upstream rotor has to be considered. The hub of a rotor row turns and transmits energy and momentum in circumferential direction to the hub boundary layer within the rotor. Consequently, the inlet boundary layer at the endwall upstream of the stator presents high skew due to these three effects.

The effects of the endwall boundary layer skew are not present in a linear cascade, which instead presents a uniform two-dimensional direction of the flow inside the inlet boundary layer. Considering a single row, two main implications of inlet boundary layer skew can be highlighted:

1. to oppose to the cross-flow with a consequent reduction of corner flow.
2. to increase the local incidence of the flow upstream of the blade at the endwall.

The first effect, shown in green in Fig. 1.8 was taken into account in the work of Lei et al. (2008) as important effect to include in the non-dimensional diffusion parameter D, further discussed in Section 2.3, but neglected in the two-dimensional Lieblein diffusion parameter DF. They remarked indeed that sometimes compressor geometries with $DF = 0.7$, larger than the critical value of 0.6, surprisingly do not present hub corner separation.

The second effect is supported by experimental results obtained in the work of Wadia and Beacher (1990), which showed that high incidence near the endwall exist and has a negative effect on the three-dimensional flow. However, such a phenomenon is not severe as expected by two-dimensional analyses because it results to be attenuated when considering the third dimension of the flow and the continuity of the pressure field in the passage, as later discussed by Cumpsty (1990).

1.3.4 Spanwise boundary layer flow

The spanwise, or transverse, boundary layer flow is the component of the flow that migrates locally on the blade surface in spanwise direction.

Such flow is driven by the magnitude of the transverse pressure gradient. In the past, little importance was given to such effect, whereas spanwise flow usually occurs in rotor blades. In the hub region, the static pressure field from the hub to the casing is able to centrifuge out toward the casing the low momentum fluid near the blade surface more than the higher momentum fluid in the free stream.

Both in rotor and stator, the blockage due to hub corner separation has a larger influence both on spanwise flows and the extent of the backflow region, if the separation is further aggravated by secondary flow (Horlock et al., 1966). The shift of streamlines from the endwall to the midspan due to endwall separation has been reported by Goodhand and Miller (2012) in a low-speed single-stage compressor. The contraction of the boundary layer on stator blades is very close to the surface. The work of Dong et al. (1987) experimentally demonstrated by injecting tracer gas upstream of the LE and measuring its concentration downstream of the trailing edge, that only layers of the boundary layer with the lowest momentum are affected by spanwise direction of the flow.

The recent work of Taylor and Miller (2015) empathizes the importance of the spanwise pressure gradient and the related flow in blade design for suppression of corner separation. They manipulated the transverse pressure gradient on the stator blade by changing lean and sweep angles of the blade but holding the spanwise loading and angle distribution downstream of the blade. The first blade design, showed on the left in the comparison in Fig. 1.9a, has a low lean and consequently a lower transverse pressure gradient than the blade designed with higher lean. Such difference in the pressure gradient induces a strong transverse flow on the suction surface of the blade with higher lean, showed in Fig. 1.9b, which induces the stream tube contraction of the boundary layer fluid. Conversely, the stream line curvature in the hub corner region is less severe for the high lean design than for the low lean design. This feature has a major importance in the development of the corner separation topology when the upstream incidence is increased. This because the high streamline curvature of the low

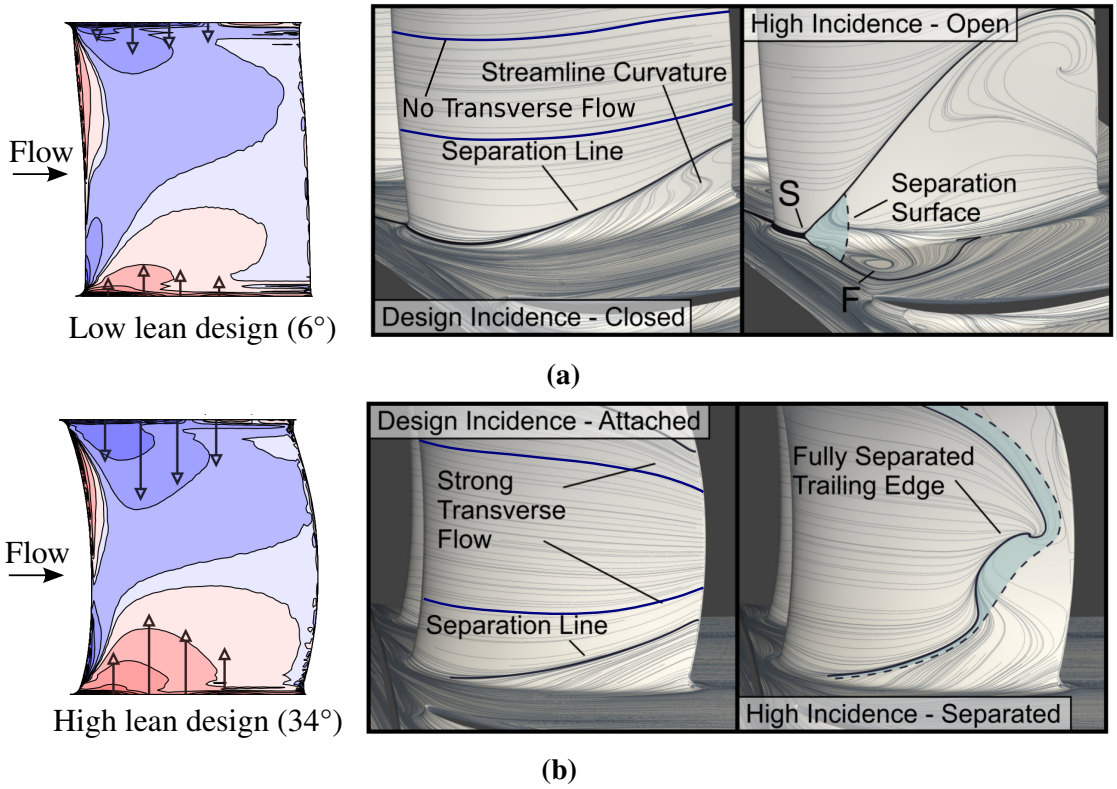

Fig. 1.9 Transverse surface pressure gradient magnitude (left) and related effect on development of corner separation increasing incidence (right). Case (a) shows the low lean blade affected by open corner separation; case (b) shows the high lean blade affected by trailing edge separation. Pictures are reproduced from the work of Taylor and Miller (2015).

lean configuration suddenly evolves in the so-called open corner separation, when a critical level of incidence is reached, see right of Fig. 1.9a.

For the low lean configuration losses increase dramatically in comparison with the high lean blade, for which hub corner separation remains close. However, high lean blades present higher losses associated to trailing edge separation on the suction surface away from the endwall.

The explanation given by Taylor and Miller (2015) relies on the unsteady RANS numerical investigation of the topology associated to the corner separation. The innate severe streamline curvature close to the hub in the low lean blade is further increased with the incidence. When the critical incidence is reached and the curvature of streamlines becomes infinitely sharp near the hub, a saddle point and a focus originate. These points migrate in opposite directions, the saddle point toward the leading edge and the focus on the hub endwall farther from the blade surface, respectively.

The high transverse pressure gradient existing in the high lean design prevents such a mechanism and the separation remains closed without back-flow near the hub. A further discussion concerning the work of Taylor and its relation with the present work is provided

in Sections 2.3.4 and 2.3.5, whereas a review of the topological rules and classical topologies associated with corner separation are examined in the next section.

1.3.5 Topology of corner separation

Thanks to the improving of numerical simulations, topology analyses were widely reported in literature as advantageous tool to understand the evolution of the flow in compressor. Oil visualization are usually performed to validate qualitatively the numeric topology, but both the experimental visualization and usually numerical results are limited to steady topology geometries provided by steady RANS.

The topology of a three-dimensional flow can be understood analyzing the skin friction lines. These are curves instantaneously tangent to the local shear stress vector on the surface τ_w (or skin friction), thus its components $\tau_{wx}(x,y)$ and $\tau_{wy}(x,y)$.

Differently, the streamlines are considered in fluid dynamics as curves instantaneously tangent to the velocity vector field that describe the direction of the flow particle at fixed time. Streamlines are defined as:

$$\frac{dx}{u} = \frac{dy}{v} = \frac{dz}{w} \tag{1.6}$$

where u, v and w are the components of the velocity field and x, y and z are the spatial representation of a single streamline. In the same manner, skin friction lines are per definition the solution of the differential system:

$$\frac{dy}{dx} = \frac{\tau_{wy}}{\tau_{wx}} \tag{1.7}$$

By approaching the body surface, streamlines tend to skin friction lines and the term surface (or wall) streamlines defines the curves tangent to the velocity vector of the flow infinitesimally close to the surface, hence as h tends to zero. Mathematically the relation between surface stream lines and skin friction lines is demonstrated by the Eq. 1.8 (Gbadebo et al., 2005).

$$\frac{dy}{dx} = \lim_{h\to 0} \frac{v}{u} = \left.\frac{\partial v/\partial z}{\partial u/\partial z}\right|_{h=0} = \left.\frac{\tau_{wy}}{\tau_{wx}}\right|_{h=0} \tag{1.8}$$

As stated by Délery (2001), this concept is fictitious since the velocity is zero on the surface but it permits to study the flow direction very near the surface of the body easily by using the propriety of skin friction field. Indeed, the positions where skin friction components are simultaneously identically zero,i.e. $\tau_{wx}(x,y) = \tau_{wy}(x,y) = 0$, denote critical points which are signatures of detachment or reattachment of the flow on the surface.

Furthermore, these critical points can be classified in relation to the behavior of skin friction lines in their proximity, also referred as limiting streamlines, by solving the associated eigenvalue problem. As presented by Délery (2001), by introducing the Jacobian matrix in

Eq. 1.9 and letting p = -(trace of J) and q = (determinant of J), the eigenvalues are given by Eq. 1.10.

$$\tau_w = \begin{cases} \tau_{wx}(x,y) \\ \tau_{wy}(x,y) \end{cases} \qquad J = \begin{bmatrix} \frac{\partial \tau_{wx}}{\partial x} & \frac{\partial \tau_{wx}}{\partial y} \\ \frac{\partial \tau_{wy}}{\partial x} & \frac{\partial \tau_{wy}}{\partial y} \end{bmatrix} \tag{1.9}$$

$$S_{1,2} = \frac{-p \pm \sqrt{p^2 - 4q}}{2} \tag{1.10}$$

The classification of critical points can be represented on the eigenvector plane $[p-q]$ of Fig. 1.10, where each sketch represents the skin friction lines in the vicinity of the critical point.

Basic critical points are summarized as follows:

- Saddle point S: a point through which two particular (critical) lines pass, each acting as a barrier in the field of limiting streamlines or skin friction lines. The saddle point causes a set of streamlines to be inaccessible to the adjacent set, which represent as consequence the separation and the attachment lines, respectively.

- Regular node N: a point common to an infinite number of limiting streamlines. A regular node can be viewed as a separation point if all the limiting streamline converge to it or a point of attachment if the limiting streamline issues from it.

- Focus F: a point around which an infinite number of limiting streamlines spiral. Focuses can show the presence of a vortex lifting off the surface. A further division describes focuses of separations, where adjacent streamlines spiral into it, and focuses of attachment, if the limiting streamlines spiral outward.

Flegg (1974) provided an *index rule* that regulates the number of each type of critical point that can occur on surfaces of a given type. Basically index 1 is assigned to all the critical points in the region $q > 0$, i.e. foci and nodes, which are hence counted as nodes. In contrast, the index -1 is assigned to saddle points in the region $q < 0$. The sum of the number of foci and nodes, N, and saddle points, S, must sum to a constant value at all instants in time, i.e. χ.

$$\sum N - \sum S = \chi \tag{1.11}$$

Gbadebo et al. (2005) showed that in turbomachinery the number χ depend on the geometry of the blade passage, in particular $\chi = 2$ for blades with hub or tip clearance and $\chi = 0$ for zero clearance blades, as for stator blades.

$$\sum N - \sum S = 0 \ \text{ no tip gap} \tag{1.12}$$

$$\sum N - \sum S = 2 \ \text{ with tip gap} \tag{1.13}$$

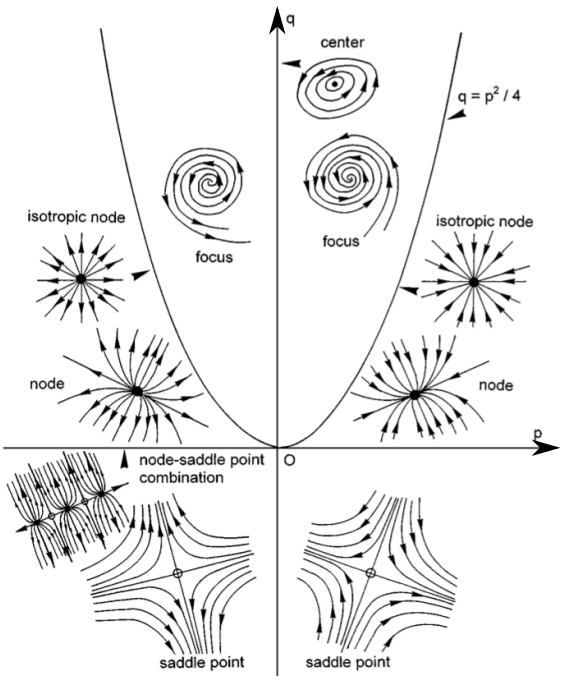

Fig. 1.10 Classification of critical points on the eigen-vector plane $[p-q]$.

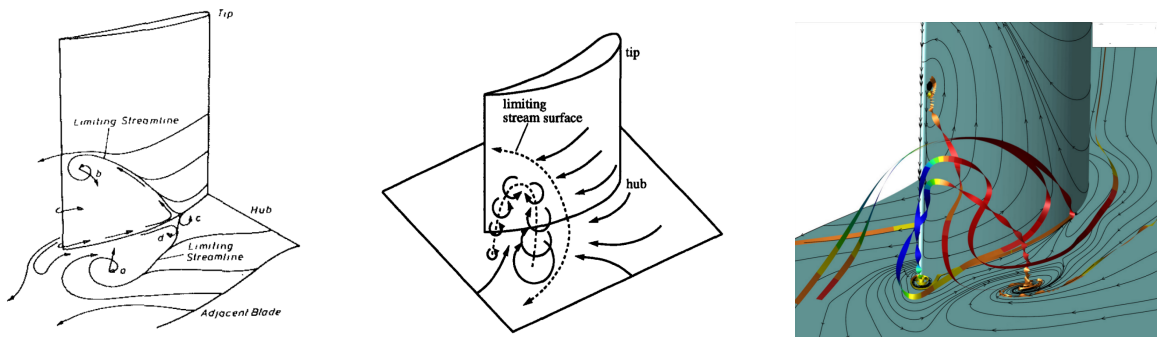

(a) Schulz et al. (1990a) **(b)** Hah and Loellbach (1999) **(c)** Lewin et al. (2010)

Fig. 1.11 Steady topologies identified for corner separations in compressor cascades.

Gbadebo et al. (2005) demonstrated such topological rules studying numerically and experimentally the evolution of the topology against the increase of incidence in two type of linear compressor cascades equipped with NACA 65 profile blades without clearance. As the incidence was increased, the number of singularities increased as well as the complexity of the separated region and the related losses.

Several authors have studied the topology of the corner separation in compressor cascades and proposed steady topological interpretations, among other Schulz et al. (1990a) and Schulz et al. (1990b), Hah and Loellbach (1999) and Lewin et al. (2010). The respective sketches are reproduced in Fig. 1.11.

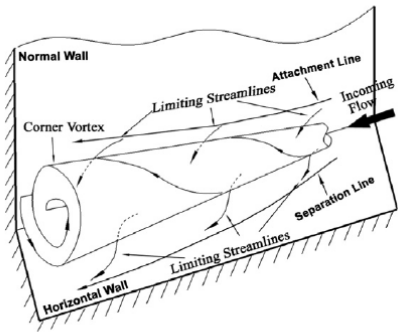

Flow topology of corner vortex (type A).

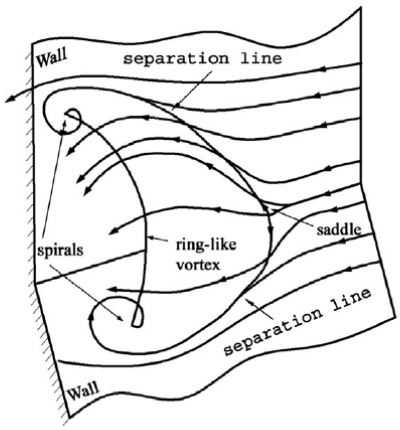

Flow topology of corner separation with ring-like vortex (type B).

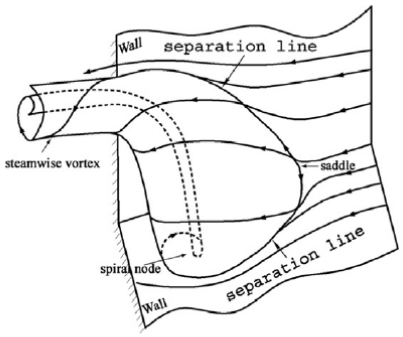

Flow topology of corner separation without ring-like vortex (type C).

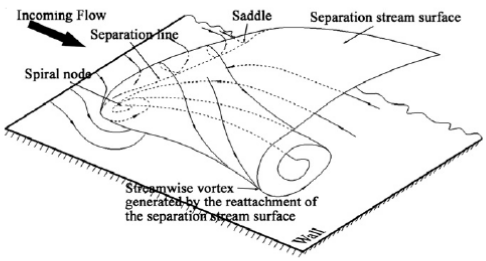

Flow topology of blade surface flow separation (type D).

Fig. 1.12 Four basic type of flow for decomposition of complex 3D flow structures in stator passage of an axial compressor stage (Yu et al., 2013).

Yu et al. (2013) studied 3D separated flows in the stator of a low-speed compressor test facility. Oil flow visualizations and stereoscopic particle image velocimetry were conducted at four compressor operating conditions from the design to near-stall conditions. It was confirmed that, as the mass flow rate decreased, the flow topologies of 3D separations became much more complex and the evolution processes of the 3D flows were significantly affected by both the secondary flow interactions inside the stator passage and the rotor-stator interactions between blade rows. However, the complex three-dimensional flow structures in the stator passage always consisted with four basic types of flows shown in Fig. 1.12 and resumed as follows.

The corner vortex flow (Type A)

The corner vortex is a streamwise vortex. This type of flow structures can usually be seen in turbomachinery as the results of both strees-induced or skewed-induced vorticity generation processes, as explained before for junction flows and secondary flows in Section 1.3.1 and 1.3.2.

The flow of the corner separation with the ring-like vortex (Type B)
The separation lines on the two surfaces of a corner start from the same saddle point and end with spiral nodes (focuses). For this type of corner flow separation, the separation stream surface curls up as a ring vortex, which impinges on the two surfaces at the spiral nodes.

The flow of the corner separation without the ring-like vortex (Type C)
This type of flow is the evolution flow type of the ring-like vortex. Only one of the two separation lines ends with a spiral node, the other one directly flows downstream. The corner separation of flow of this type may occur when the back pressure decreases below a certain value.

The blade surface separation flow (Type D)
The topologies of the limiting streamlines for the 3D separations on blade surface (or near the mid-span region) always appear as the flow type D. This type of flow separation is usually called closed separation and has very stable flow topology and 3D flow structure.

1.4 Impact of separations in compressors

The deleterious impacts of corner separation on the overall performance of the machine are well known: total pressure losses and blockage. How these effects concur to decrease the efficiency and also the stability limit of the entire machine is the subject of the present section. Beside classical awareness of the impact of corner separation on steady performance, the importance of this phenomenon on off-design and transitory states has arisen and its implications as concurring effect for inception of compressor instabilities is nowadays coming back into play.

1.4.1 Loss generation

Losses in a compressor stage quantify the dissipation of the work transmitted from the rotor to the flow in terms of entropy increase and total pressure drop. The main losses sources in turbomachinery are related to viscous effects in boundary layers, viscous effects in mixing processes, shock waves and heat transfers across temperature differences. For subsonic incompressible flows without heat exchanges, losses can be categorized according to Denton (1993) as follows:

- profile loss;
- secondary or endwall loss,
- leakage loss

Correlations obtained from experimental data are the main tool used by compressor designers to evaluate these sources of losses, but such empirical relations rely on steady studies that do not take properly into account the unsteady interaction between different

sources of losses. All of them are strongly dependent from the type of machine, blade aspect ratio, tip clearance and three-dimensional blade design.

The loss coefficient used in the present work to evaluate losses through the blade row is given by the difference between the total pressure at the inlet and the outlet of the blade row normalized by the dynamic head, as in Eq 1.14.

$$\omega_{t\,out} = \frac{p_{t_\infty} - p_{t_{out}}}{p_{t_\infty} - p_{s_\infty}} = \frac{p_{t_\infty} - p_{t_{out}}}{\frac{1}{2}\rho V^2{}_\infty} \tag{1.14}$$

Profile losses

The term profile losses is referred to the losses generated on the surface of the blade away from the endwall, at spanwise sections where the flow could be considered two-dimensional. Such simplification permits to evaluate the losses by cascade studies and through two-dimensional boundary layer calculations. Profile losses are related to the boundary layer and to the viscous effects in the viscous sublayer of the blade surface. The viscous shear stress is defined as a linear function of the velocity gradient at the wall in the perpendicular direction imposed by the no-slip condition at the wall.

$$\tau_w = \mu \frac{\partial u}{\partial y}\bigg|_{y=0} \tag{1.15}$$

where μ is the dynamic viscosity of the flow.

These viscous, frictional stresses cause energy dissipation in the fluid, which appears as heat. Since it takes an enormous amount of energy to heat a gas or liquid to an appreciable temperature, this heat generation is not usually important at subsonic speeds.

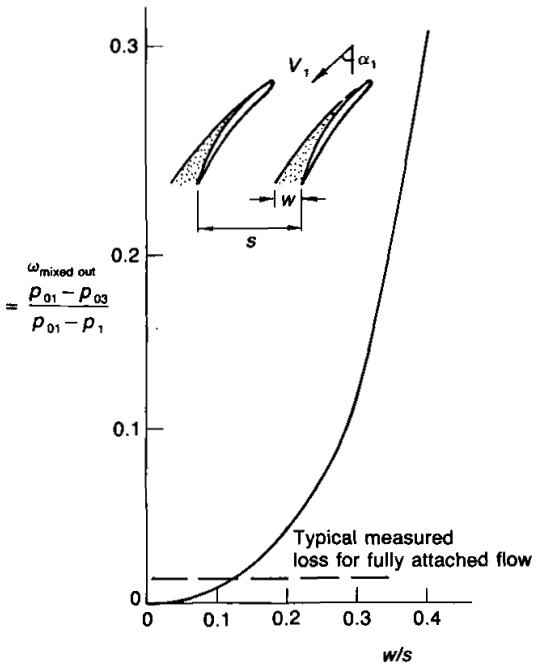

Fig. 1.13 Calculated parabolic increase of mixing losses for incompressible fully mixed out flow with wake of width w, reproduced from Cumpsty (1989).

When considering the flow attached, laminar and turbulent boundary layers have different velocity gradients, in particular higher the Reynolds number of the flow, larger the velocity gradient and hence the shear stress. Beside this, the shear stress and the losses of detached flows are different because the slope of the detached velocity profile is negative.

The flow separates when it can not sustain the adverse streamwise pressure gradient, which can be produced both from the main adverse pressure gradient of the duct (diffuser) or the local adverse pressure gradient due to the curvature of the blade. This curvature causes

the flow to accelerate on the convex surface (suction surface) near the LE and the decelerate in the aft part of the profile.

Considering the case of a compressor blade profile, it is not excluded the existence of a laminar boundary layer very near the leading edge or just downstream of the region of maximum velocity (Cumpsty, 1989). In that region the boundary layer separates, forming a laminar bubble in which the flow recirculates. Usually, laminar-turbulent transition occurs in the bubble and the flow reattaches because the turbulent boundary layer is able to sustain larger adverse pressure gradients than in laminar regime. Anyway, downstream of the bubble the boundary layer thickness increases and when the turbulent separation occurs, it produces larger wake losses compared to a fully turbulent detached boundary layer without separation. Furthermore, the laminar bubble increases the instability risk of the flow on the blade to the sudden increase of angle of attack, since at high incidences the bubble can suddenly burst and prevent the turbulent reattachment causing a larger separation from the LE of the blade.

As stated by Cumpsty (1989), if the flow separates and produces a wide wake it is also important to quantify the losses generated by downstream mixing of the separated flow wake. The mixing process is the mechanism that returns the wake/separated flow to uniform conditions and hence produces high losses. The loss coefficient that completely takes into account the mixing losses should be calculated at the downstream section where the flow mixes out to uniform conditions, marked as 3 in Eq. 1.16. For incompressible flows this can be reduced to geometrical parameters of the wake.

$$\omega_{t\,mixed\ out} = \frac{p_{t1} - p_{t3}}{\frac{1}{2}\rho V^2} = \cos^2\alpha_1 \left(\frac{w}{s-w}\right)^2 \tag{1.16}$$

As shown in Fig. 1.13, the wake needs to reach one-eight of the passage pitch distance ($w/s = 0.125$) before the mixing losses generated from it are comparable to losses of cascades with attached flows and affected only by profile losses.

As discussed in Section 1.3.4, profile losses and endwall losses usually play opposite roles when designing compressor blades.

Endwall losses

Endwall losses include the losses generated by the interaction between the annulus boundary layer, both at the hub and casing, with the blade row. Such an interaction causes secondary flows that are complex and highly three-dimensional. Losses are directly due to the annulus boundary layer, but also to the interaction between the secondary flows and the boundary layers of the blade and the endwall. The mechanisms of formation of secondary flows is inviscid *per se*, as shown in Section 1.3.2, but in reality the wall velocity gradient caused by viscous effects of the boundary layer is always present and gives the basic vorticity component. Secondary flows interact with existing boundary layers and cause low momentum fluid displacement that promotes separation and thickening of boundary layers, as for corner separations and horseshoe vortex.

The work of Horlock et al. (1966) is one of the first detailed works on corner separation in compressor cascades that quantifies separately the effects of secondary flows and wall stall. They reported that losses associated uniquely to secondary flow were of the order of magnitude of the profile loss, hence low, but were the major parameter affecting the displacement of the point of minimum under-turning measured at the outlet section. Conversely, corner separations were proved to generate high losses, around 190% of the profile losses, but without a strong effect on under-turning.

Three-dimensional separations at the endwall also generate high mixing losses downstream and the correct prediction of their magnitude is still problematic for modern RANS models.

Leakage losses

Leakage losses are present at the tip gap for unshrouded rotor and at the hub for stator with hub clearance, also called cantilevered stators. The tip leakage in rotor rows is one of the most studied source of losses and instabilities since the flow spilling into the gap from the pressure side to the suction side of the blade produces the tip gap vortex. Such structure enrolls into the blade passage downstream, causing high losses and blockage as for separations. The increment of the gap results in the decrease of both the efficiency and the maximum pressure ratio peak of the entire stage, beside the rise of instabilities risk and rotating stall.

In stator rows, hub leakage can be a solution for suppression of corner separation because high momentum fluid moves through the gap from the pressure to the suction side, re-energizing the low momentum fluid in the suction side corner (Dong et al., 1987).

The first work reporting this benefit was conducted by Lakshminarayana and Horlock (1967) in a linear compressor cascade. The results showed that an *optimum value* of clearance exists in order to prevent the corner separation formation without increasing the losses generated by larger leakage flow associated to larger gap. However, since the leakage flow magnitude depends on the pressure difference between pressure and suction side, higher losses are expected in case of incidence variations. These occur in off-design conditions, as a consequence of the reestablishment of corner separation or the rising of intensity of the clearance flow. As inference, the hub clearance gap should be adapted to the operational point, as clearly stated in the experimental study on a NASA low speed compressor by Barankiewicz and Hathaway (1998). Their results demonstrate that at peak efficiency, where separations were small, the partial hub sealing, i.e. from LE to 50% of the blade chord, was the best configuration to prevent the high losses generated by LE leakage. Conversely at peak pressure, both the configuration completely sealed and the configuration partially sealed permitted large reduction of losses. Solely at near stall point, i.e. when corner separations were massive, the unsealed full chord configuration gave the best performance among the other partial sealed configurations. These, in turn, appeared useless since affected by the same amount of corner separation losses than the sealed configuration. It was further highlighted that the reduction of losses in the full gap configuration was paid with a high spanwise non-uniformity due to larger gradients, causing deleterious effects on the downstream rotor.

In conclusion, it is important to stress the attention that has to be put when considering hub gap to avoid corner separation, without thinking exclusively about its presumed benefits.

1.4.2 Efficiency impact on high loaded stages

Since the compressor accounts for a half of the entire engine weight, one of the major goal for a designer is to minimize the number of stages needed to achieve the target overall pressure ratio. The increase of loading of the stage is hence necessary but this process has to deal with the unavoidable growth of separations and decrease of efficiency.

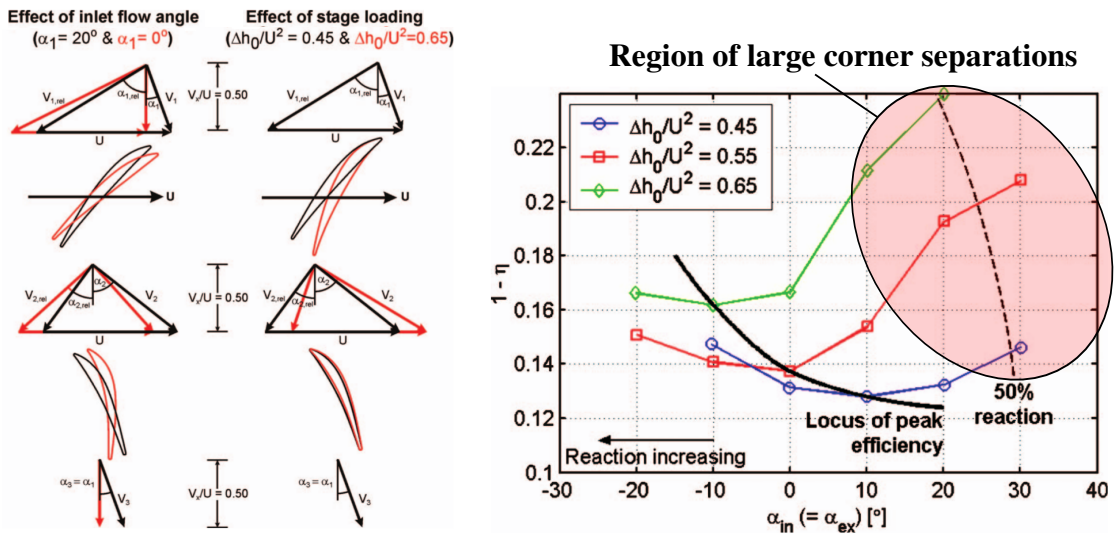

(a) Velocity triangles for loaded axial compressor stage.

(b) Effect of stage loading and inlet flow angle on predicted stage efficiency.

Fig. 1.14 Impacts of stage loading and corner separations on stage efficiency, reproduced from Dickens and Day (2011).

The stage load can be increased by designing rotor blades that increase the deviation of the flow and can support higher angles of attack, hence raising the work transmitted to the flow according to Euler equation. Consequently, the angle of attack of the downstream stator row is increased. As result, the flow in the stator passage brakes down at first because of the large corner separation development.

Dong et al. (1987) observed an extreme non-linear response of corner separation in stator row to high load in a single-stage, low-speed, high-reaction axial compressor.

In order to relief the stator, the work of Dickens and Day (2011) claims that the stage reaction has to be increased by increasing the stage inlet flow angle (increase of the relative angle of attack on the rotor), as shown in Fig. 1.14a, thus shifting the load to the rotor, which is more tolerant of high loading than the stator. Values of reaction usually around 50%, higher better, are less dangerous for the formation of large corner separations. The reaction limit relies in the high velocities that can be achieved in the rotor tips, which can in turn induce shocks and separations of the boundary layer.

Consequently, the increasing of the stage inlet flow angle has the opposite effect in rotor and stator. Dickens pointed out that an optimum efficiency can be achieved by a wise choice of reaction levels and inlet flow angles, but the maximum value of the stage efficiency is

inevitably reduced of 3% for load factor shift from 0.45 to 0.65, as shown by experiments and CFD results reproduced in Fig. 1.14b.

1.4.3 Blockage

The blockage generated by the bulk of separation deviates the flow causing spanwise boundary flows and the contraction of the streamlines towards midspan with the consequent acceleration of the main flow at midspan section of the blade passage. Blockage is defined as in Eq. 1.17 and can be rewritten as a integral of the displacement thickness across the passage:

$$B = 1 - \frac{\text{effective flow area}}{\text{geometric flow area}} = 1 - \frac{(A - \sum \delta^*)}{A} \tag{1.17}$$

$$\delta^* = \int \left(1 - \frac{\rho u}{\rho_\infty V_\infty}\right) \mathrm{d}y \tag{1.18}$$

Here the ρ_∞ and V_∞ are the free-stream density and velocity upstream of the blade passage. However, complex non-uniform flows across the passage are usually present in turbomachinery, leading to a difficulty to define the free stream condition (Cumpsty, 1989).

Corner separation induces blockage in the blade passage with a consequent radial migration of the fluid toward midspan, reported by many authors such as Dong et al. (1987) and Li and Cumpsty (1991).

Following the approach of Khalid et al. (1999) an overall exit blockage related to the one-dimensional static pressure rise was given by Gbadebo et al. (2008).

The ideal static pressure rise coefficient across the blade row can be written as

$$C_{p2} = \frac{P_2 - P_1}{\frac{1}{2}\rho V_1^2} = 1 - \left(\frac{V_2}{V_1}\right)^2 \tag{1.19}$$

Taking the overall averaged exit velocity both in pitchwise and spanwise direction, denoted as $\overline{\overline{V_2}}$, the overall velocity ratio can be expressed as

$$\left(\frac{\overline{\overline{V_2}}}{V_1}\right) = \sqrt{1 - C_{p2}} = \left(\frac{A_1}{A_{2e}}\right) \tag{1.20}$$

where A_1 and A_{2e} are the inlet and the effective exit flow areas, respectively. Blockage can be written as a function of the ratio between the effective exit flow area and the geometric

exit area A_2 and then related to the static pressure rise coefficient.

$$B = 1 - \frac{A_{2e}}{A_2} \tag{1.21}$$

$$B = 1 - \frac{A_1}{A_2}\sqrt{1 - C_{p2}} \tag{1.22}$$

$$B = 1 - \frac{\cos\alpha_1}{\cos\alpha_2}\sqrt{1 - C_{p2}} \tag{1.23}$$

where α_1 and α_2 are the inlet and exit flow angles of the blade passage at the midspan. Such a relation highlights that the blockage factor increases when the diffusion of the inter-blade channel (the pressure coefficient C_{p2}) rises, keeping the flow angles constant at nominal values.

1.4.4 Mismatching impact in multistage compressors

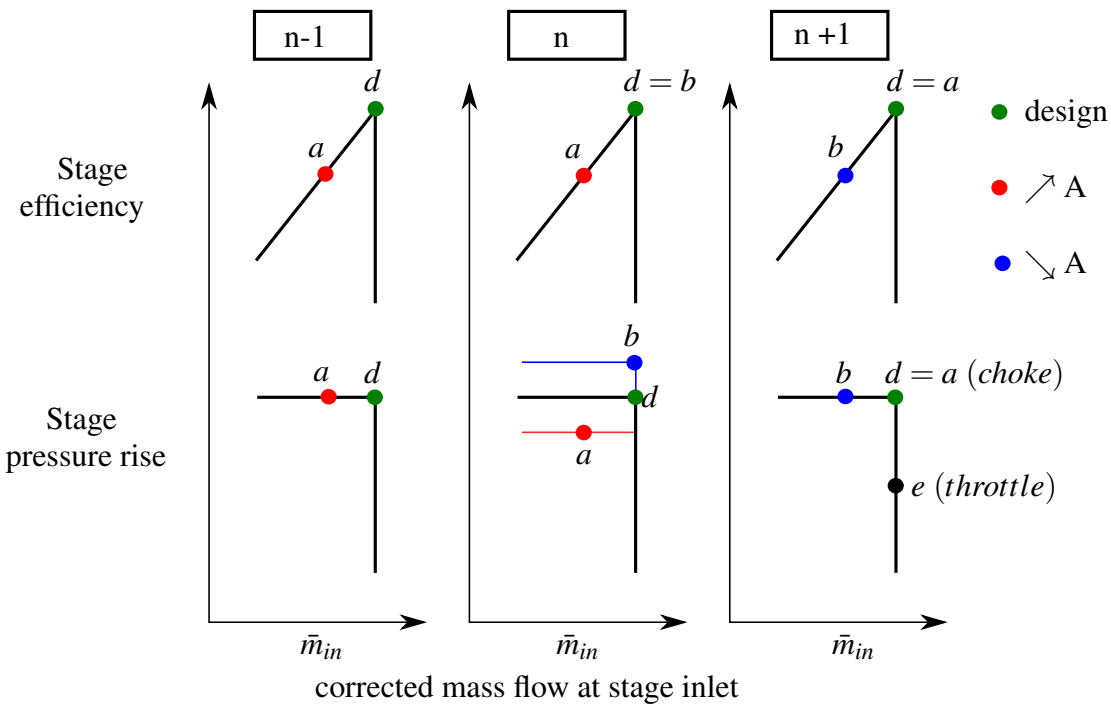

Fig. 1.15 Blockage effect on mismatching in multi-stage axial compressor, adapted from Cumpsty (2010).

The blockage generated by separations affects the one-dimensional matching of multi-stage compressors, i.e. the capability of all stages to work at the design point. The simplified concept can be explained following the approach of Cumpsty (2010), by introducing the inlet

corrected mass flow normalized as:

$$\overline{m} = \frac{\dot{m}\sqrt{c_p T_0}}{A P_0} \tag{1.24}$$

In this definition $\dot{m}$ is the mass flow rate, T_0 and P_0 are the stagnation temperature and the stagnation pressure, respectively; the flow effective area parameter A is the area after allowing for blockage by the boundary layers resulting from the leakage flow, tip clearance and hub corner separation. Errors in evaluation of A translates into errors in $\overline{m}$, which then cause alterations of the stage pressure ratio and hence into mismatching of the whole machine. The simplified sketch of Fig. 1.15 illustrates three consecutive stages of a high speed machine.

The general design intent is to operate at the same performance point, marked d, in each stage, hence in the *well-matched* condition. In the figure, the corrected mass flow at the inlet of the respective stage, marked $\overline{m}_{in}$, is the outlet of the previous stage.

Case *a*. Supposing that the stage n has a blockage larger than the value assumed in the design, then the pressure rise produced by this stage will be low, shifting on the level denoted by the red line. This outlet condition for the stage n is the inlet condition for the stage $n+1$, implying that stage $n+1$ also produces a lower pressure rise than intended in the design. The corrected mass flow at stage $n+1$ will be also higher than the design because of the pressure ratio decrease in the stage.

In extreme cases such mass flow increment can lead to chocking of the stage $n+1$. Consequently, the corrected mass flow outgoing the stage n will be limited by the downstream chocked condition of the stage $n+1$ and, since the pressure out of stage n is below the design intent, the mass flow through stage n will be reduced as well, leading to the operational point a. Since stage n is accepting less mass flow than the design intent, stage $n-1$ also has a reduced mass flow. As a final result, the efficiency of stages $n-1$ and n is reduced.

Case *b*. Conversely, if the pressure rise in the stages up to stage n is higher than the design, then the corrected mass flow into stage $n+1$ will be lower than the design because the mass flow in the $\dot{m}$ through the stage n decreases moving on the characteristic curve to higher pressure ratios (before stall occurs). Consequently, the operating point of stage $n+1$ will be shifted at the left of the efficiency peak on a lower level and the stage $n+1$ may stall. Even if the last stage, in the case considered the stage $n+1$, is generally regulated by downstream components, as could be the throttle representing by point e, such outlet throttle will have no effect on the first and second stages. If these stages are not operating correctly they could not be corrected by opening or closing this downstream throttle.

In conclusion, it is evident how the variation of blockage from nominal values due to separations plays a crucial role in multistage compressors. In particular, not only higher values of blockage, but also lower values than the nominal expected by designers, can decrease the overall efficiency.

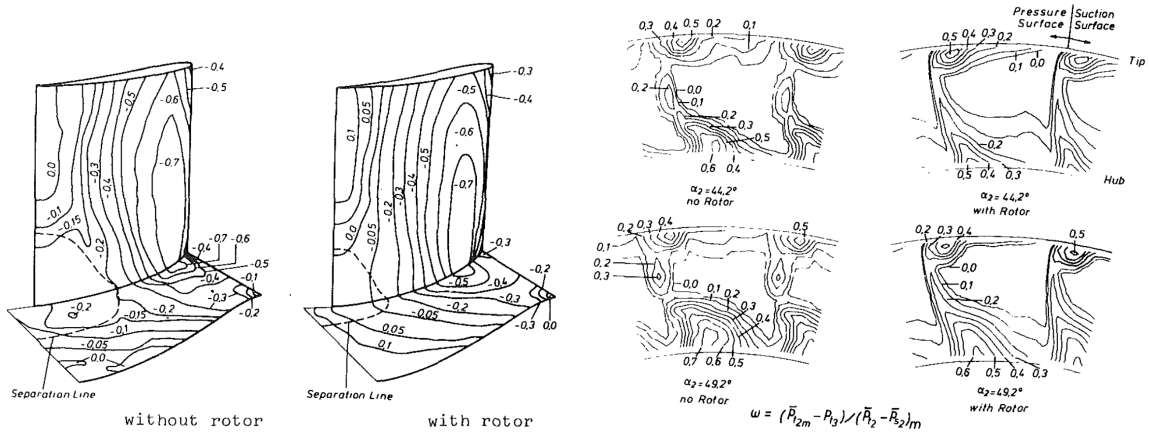

(a) Static pressure coefficient C_p. **(b)** Cascade exit total pressure losses contour.

Fig. 1.16 Comparison between corner separation in annular compressor cascade with and without upstream rotor, reproduced from Schulz et al. (1990a).

1.5 Interaction with upstream rotor

Shulz and Gallus produced three important works about the three-dimensional separations in subsonic annular compressor cascades with and without upstream rotor. The first one (Schulz and Gallus, 1988) reports a study of the influence of the blade loading on the three-dimensional flow, in particular the hub end-wall separation, with undisturbed, steady incoming flow at increasing incidence angles. The angle variation is achieved by changing the stagger angle of the upstream IGV. This work is a very unique example of the utilization of the sliding blade technique in order to achieve velocity by hot films on the suction surface of the blade. Unsteady static pressure fluctuations are also achieved, detailing for the first time the crucial relationship between the separation boundary and the presence of local maxima of p_{RMS} in such region (random fluctuations). The separation is massive covering almost the 75% of the entire blade span but this case of study present laminar-turbulent transition on the suction surface of the blade, upstream of the turbulent transition characterizing the corner separation. The question arisen from the work is if the introduction of an upstream rotor would produce significant changes in the flow dynamics.

The following work (Schulz et al., 1990a) was hence focused on the comparison of the previous results in case of isolated stator with a configuration where an upstream rotor is introduced in the facility. The rotor is not constituted by classical blades but indeed of cylindrical bars rotating at constant speed (3000 rpm), permitting to achieve nearly identical inlet conditions as those of the configuration without rotor at constant rotational speed of the rotor but by changing inlet angles. The results achieved in the work of 1990 part 1 (already cited for the proposed topology in Section 1.3.5) carefully answer the previous question: the rotor wake completely changes the flow characteristics because the increasing of the flow turbulence causes the disappearance of the laminar bubble on the stator suction side. Profile losses measured at the outlet by 5 hole probe increase but as shown in Fig. 1.16a, the size of corner separation diminishes and so the related endwall losses. Collectively, the losses

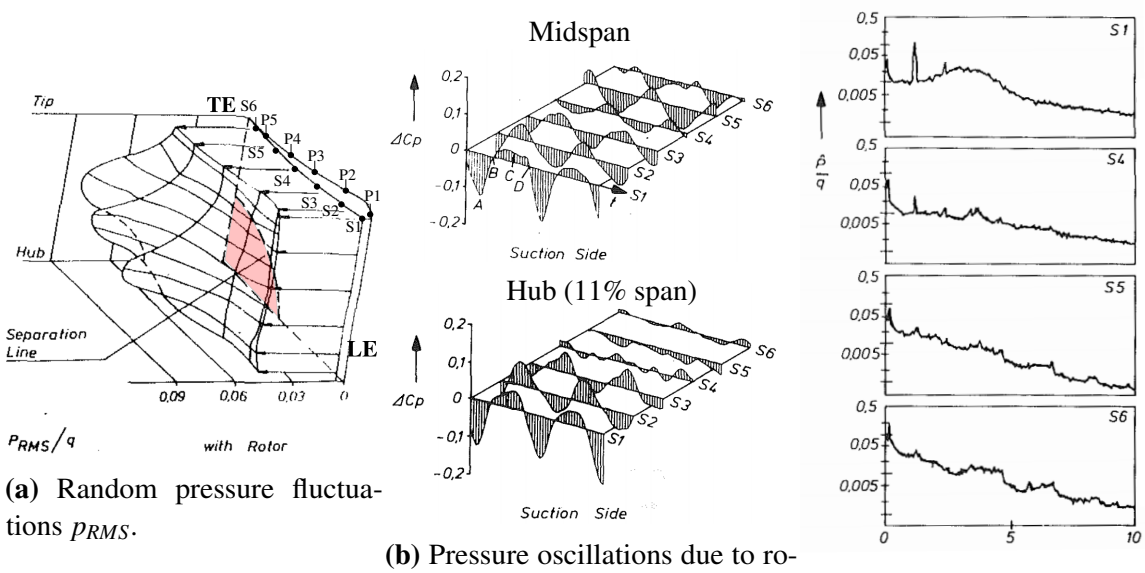

(a) Random pressure fluctuations p_{RMS}.

(b) Pressure oscillations due to rotor wake ΔC_p.

(c) FFT spectra of pressure signals at 11% span.

Fig. 1.17 Unsteady investigation of corner separation in annular compressor cascade with upstream rotor, reproduced from Schulz et al. (1990b).

decreased of the 40%. The comparison between the shape of the total pressure losses is reproduced in Fig. 1.16b. It can be noted that the wake of the blade is thicker, but the shape of outlet losses is sharper and characterized by a triangular shape.

The Part 2 of the paper (Schulz et al., 1990b) presents detailed unsteady pressure investigations, carried out by installing fast response Kulite sensors on the surface of the sliding blade, and hot wire measurements at 0.15 mm above the surface of the blade both at midspan and at 11% of the chord. The random pressure fluctuations p_{RMS} are increased by the presence of the rotor and the maximum peak is situated at the front of the hub corner separation, see Fig. 1.17a. The fluctuations are significantly increased at the LE due to the deceleration of the flow, then reduced by the diffusion and dissipation of the turbulent flow in the blade passage until the boundary of the separation. Conversely, the periodic fluctuations associated to the passage of the rotor wakes decay on the suction side at the hub, as is shown in Fig. 1.17b, implying that the wake can not penetrate into the already separated region on the suction side of the blade. This is also confirmed by Fourier spectra of the pressure signals in the separation presented in Fig 1.17c: the amplitude of the blade passing frequency (BPF) is smaller than the noise level due to the turbulence generated in the separation. Such a major result implies that the flow with the end-wall corner separation is shielded from the rotor wakes by the separation boundary. Conversely, the higher turbulence level of the incoming flow changes the global shape of the separation increasing profile losses and decreasing hub losses. This reported independence of hub separation from the rotor wake has driven the choice to investigate the LMFA compressor cascade without upstream rotor. The main goal of the present work is indeed to isolate the unsteadiness of the flow due uniquely to the corner separation.

1.6 Instabilities in compressors

1.6.1 Rotating stall

The interest to investigate and to suppress corner separations do not rely only in the effort to decrease the losses and increase the efficiency of the compressor. The unsteady behavior of the separation starts to play a crucial role in the inception and evolution of instabilities when the mass flow of the compressor is decreased.

In axial compressors indeed, the peak of the fixed-speed performance characteristic coincide with the point of occurrence of instabilities of the flow, as the increasing in pressure and velocity fluctuations. The further decreasing of the flow rate causes sudden loss of the pressure rise due to the massive separation of the flow from the internal surfaces of the machine. Such separations are local, three-dimensional and highly topologically complex and are called "stall".

Stall can be fixed to the blades surfaces, as in the case of *corner stall* or trailing edge stall, or rotate at a fraction of the velocity of the rotor in circumferential direction. The latter type, called *rotating stall*, is an unsteady apparent circumferential perturbation occurring in the rotor row that describe the existence of an azimuthal part of the annulus where the flow is separated from the blades, called *cell*. Therefore, as firstly presented by Day and Cumpsty (1978), within the cell the averaged axial velocity is near zero and the static wall pressure at casing increase as well as the total pressure losses. The cell moves at fraction of the velocity of the rotor in the absolute frame of reference, hence in the opposite direction of the rotation, by taking the relative frame of the rotor blades as reference. Multiple cells formed on different circumferential position at the casing merge together when their boundaries collide. Outside the cell the flow is unstalled but presents anomalies due to the presence of the blockage created by the stall cells, therefore the averaged axial velocity within the unstalled flow is above the design value.

The question arises as to which are the phenomena that initiate the rotating stall and if such an instability can be predicted. Most of the times the observable stall begins in the vicinity of the rotor tips and can be initiated by long length-scale disturbance (modes), involving entire portions of the circumferential length, or short length-scale disturbance (spikes), measured in terms of blade pitches, but very often the flow breakdown occurs in a range of patterns between these two.

As presented below, in the last ten years new cases have been reported where the rotating stall inception was generated not only by the rotor, but also by stator hub separations.

1.6.2 Corner separation influence on spike-type stall inception and rotating instabilities

As stated by Day (2016), an increasing uncertainty surrounds the stall behavior when investigations further explore which is the first phenomenon triggering the stall inception. So far, it is unknown the exact way a newly designed compressor will behave when pushed to stall for the first time. Only by running a first experimental test it can be precisely stated what to expect from the machine during stall. This section review some recent works that focus on

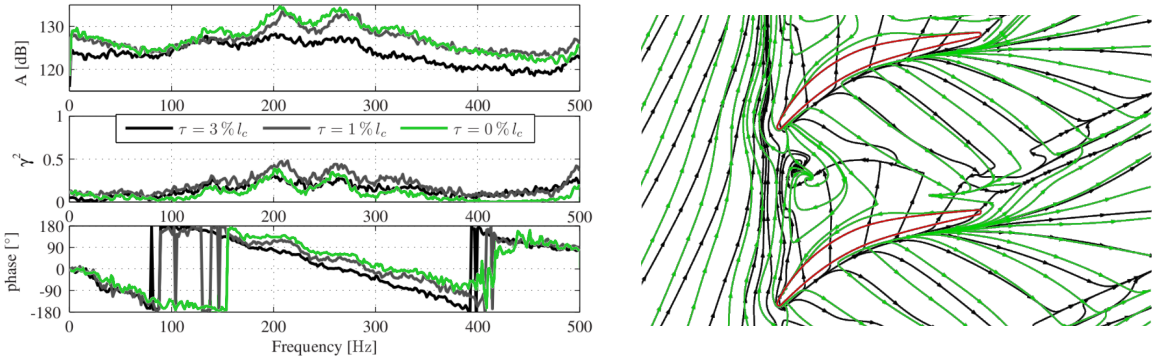

(a) Spectral analysis of the wall pressure fluctuations on the hub in the vicinity of the blades LE for three different hub clearances, (Beselt et al., 2013a).

(b) Numerical endwall streamlines between case with (black) and without clearance (green) (Beselt et al., 2013b).

Fig. 1.18 Rotating instabilities reported in annular compressor cascade of stator blades with and without hub clearance.

the the role played by corner separations on the inception of instabilities, demonstrating that several different mechanisms can intervene depending on the compressors design.

Rotating instabilities

A very disputed subject concerns pre-stall disturbances which are unsteady patterns that exist at mass flow rates higher than the stall point, unrelated to modes or spikes. The term *rotating instabilities* refers to prestall disturbances that occur near the tips of rotor blades, long before the stability limit is reached. Such perturbations are usually characterized by small extension (one or two blade pitches) but high circumferential count, rotate at approximately 50 % of the rotor speed and are highly unsteady in frequency, length-scale and intensity. For this reason the typical footprint of rotating instability is the presence of a bump in the static pressure frequency spectrum around 30% of the BPF, both on casing wall and rotor blade surface, and the presence of a coherent time of propagation in circumferential direction.

What is the physical structure hidden behind the rotating instabilities is so far an unanswered question. Several works pointed to coherent structures generated by the presence of large clearance and interactions of tip clearance flows. Recent studies carried out by Beselt et al. (2013a) on annular compressor cascade have reported the existence of rotating instabilities varying with the variation of tip clearance, but one of the most surprising result is that rotating instabilities were reported also when the tip clearance was zero. In this configuration, the blockage due to corner stall, which deviates the flow from one passage to the adjacent, was the major cause of hub separation upstream of the leading edge and the propagation of disturbance in circumferential direction detected by the linearity of the phase response, see Fig. 1.18b.

These results are in contrast with the past belief that rotating instabilities should appear only in rotor with large clearance gap, so a new hypothesis explaining rotating disturbances was formulated by Porowitz and Beselt: shear layer instability waves of different wavelengths

could be generated at *stochastically distributed moments in time* by interaction of secondary flow at the end-wall and then starting the propagation in circumferential direction.

As support of this theory, rotating instabilities have been recently reported in the experimental work of Pardowitz et al. (2015) for a shrouded rotor where the tip clearance vortex and the leakage flow were suppressed.

Spike-type stall generation mechanisms

In the last ten years a new mechanism has been found to be involved in the generation of rotating instabilities: a radial tornado-type vortex forming near the leading edge of the rotor blades and impinging both on the suction surface of the blade and the casing.

Such structure was introduced at first by Inoue et al. (2000) in a work on a low pressure compressor, not dealing with the RI but with multiple small stall cells, which remained stable for an operational point on the left of the peak of compressor characteristic. Inter-blade radial vortex structures were subsequently found in the works of März et al. (2002), Young et al. (2011) and Inoue et al. (2004).

One of the footprint of the radial vortex is the associated low pressure region in front of the leading edge of the rotor at tip. Investigations on spike-type rotating stall also reported such behavior of the wall static pressure, suggesting that the propagation of tornado-like vortex at the casing between adjacent blade passages could be the main cause of stall inception (Inoue et al., 2001).

The recent numerical work of Pullan et al. (2015) on the origin of spike-type rotating stall confirms such hypothesis. Validating the simulation with experimental data of several different test cases (axial and centrifugal compressors and cascades), the work of Pullan focus on the NASA E3 rotor, by increasing the geometrical complexity of the domain, with and without the tip clearance. A linear cascade of E3 rotor tip profiles without tip clearance was simulated at first, followed by the three-dimensional E3 rotor without tip clearance and finally the configuration with tip clearance.

The work shows that spikes are caused by a separation at the leading edge due to high incidence in each configuration. The vorticity generated by this process forms a radial vortex that, in the same manner than the vortex proposed by Inoue, spans between the suction surface of the rotor blade and the casing, see Fig. 1.19b. Furthermore, the vortex head impinging on the casing wall moves toward the pressure side of the adjacent blade triggering the separation of the flow on the suction surface of such blade and hence starting the propagation of the disturbance.

The case with real tip clearance does not present any corner separation because of the main clearance flow. In this case, it is the unsteadiness of the tip clearance vortex that generates multiple LE separations and related perturbations that finally lead to the major leading edge structure and start the spike propagation.

However the surprising result arises when the clearance is reduced to zero value, so a corner separation exists, but the same vortex shedding is observed as in configurations with clearance. In Fig. 1.19a it is clearly visible the difference between corner separation sizes of blade 1, 2 and 3 highlighted by large vorticity values. The blockage created by the increased corner separation of the blade 1 and 2 perturbs the incidence of the blade 3 causing

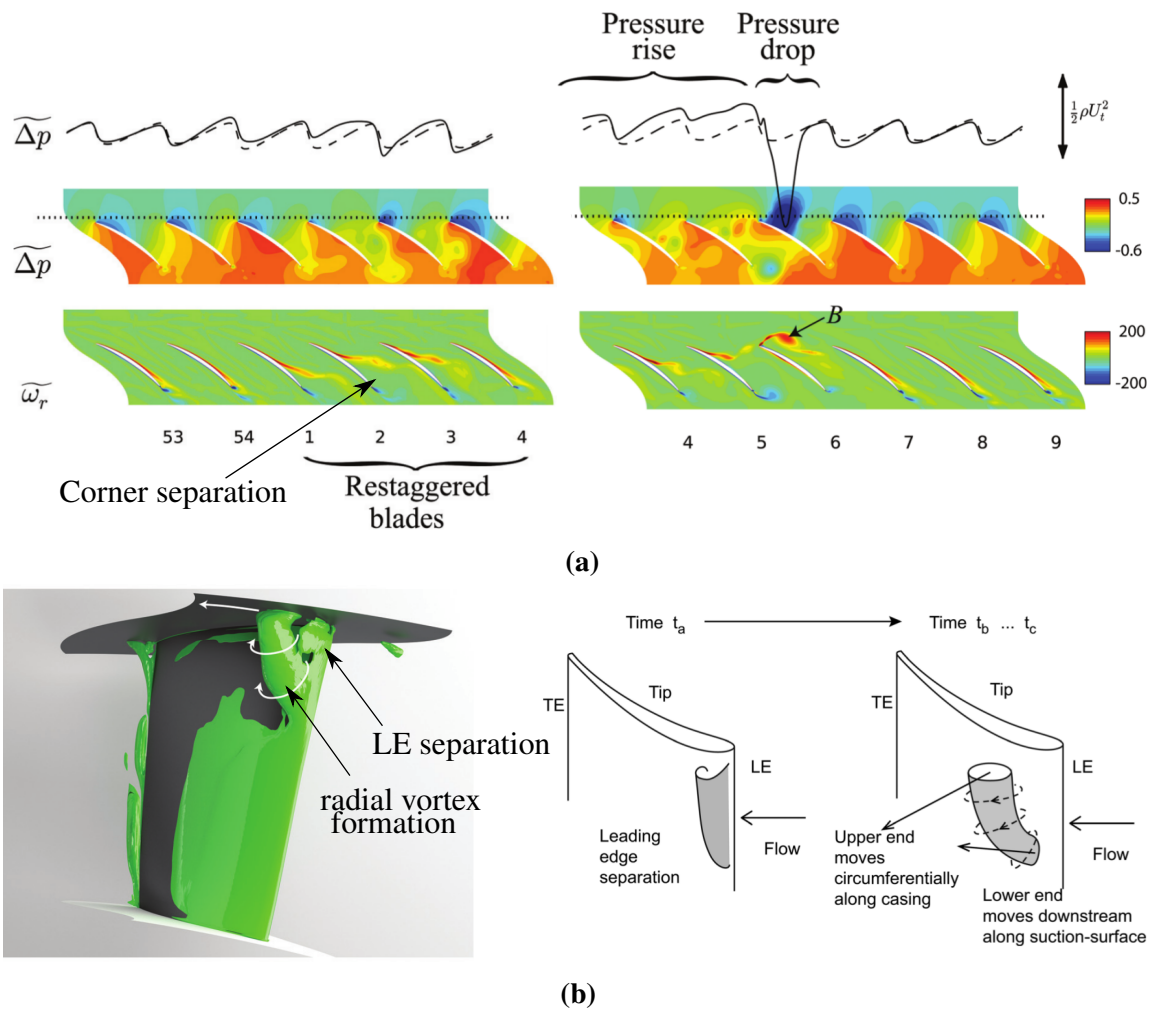

Fig. 1.19 Spike formation in E3 rotor with zero clearance: (a) propagation of corner separation shown in section at 95% span; (b) three-dimensional radial structure. Reproduced from Pullan et al. (2015).

a pressure drop in front of the LE and larger separation in such passage also. The perturbation propagates from blade to blade moving away from the restaggered blades where at first was generated, until the separation front boundary moves very close to the LE of the adjacent blade. In Fig. 1.19a the blade passage between blade 5 and 6 is completely blocked pushing the boundary of the separation of blade 5 toward the LE of the blade 6 and inducing the critical leading edge separation with the inception of the radial tornado-like vortex. Such a structure is highlighted by the high vorticity spot marked *B* and generates the large spike-type pressure drop at the same position. Vortex *B* triggers a new leading edge separation once it arrives at blade 7, causing a new shedding of vorticity.

The implication is that such coherent radial structures are not related to the tip clearance vortex but are due to the flow stall in the blade passage caused by large values of incidence at the leading edge. The results of the simulation of the full E3 rotor with zero tip clearance

show exactly the same process than the linear cascade constituted by E3 tip rotor profile without clearance, i.e. the corner separation induces the key blockage which trigger the LE separation vortex and its propagation in circumferential direction.

The conclusion of such work is that the high incidence, which causes the LE separation, the radial vortical structure and hence the spike stall inception, occurs in every circumstance, depending to the design of the compressor, even for very small tip gap that would probably retain corner separation at casing because of very weak clearance flows.

Rotor stall triggered by hub separation

An interesting work showing a direct effect of hub corner separation on the rotating stall is due to Choi et al. (2008). The three-dimensional unsteady RANS numerical study is carried out on a low speed axial compressor rotor used in the study of Wagner et al. (1985) and Dring et al. (1982) for studies on the effect of the thickness of the incoming boundary layer on the hub corner separation.

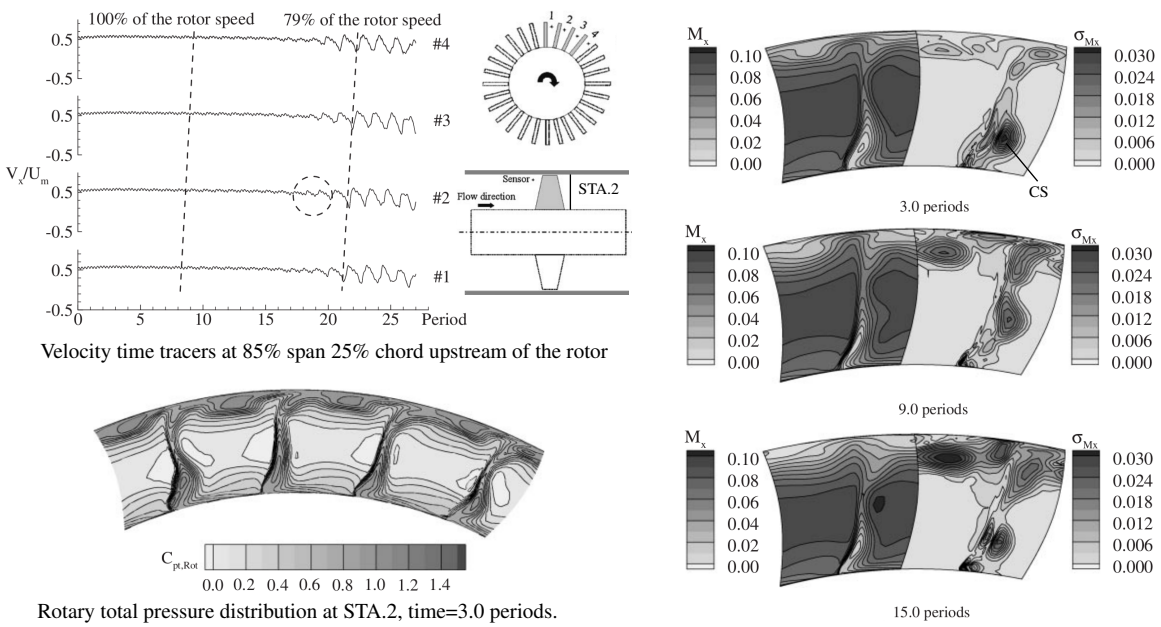

(a) Stall inception sensed at the casing and asymmetry of hub corner separation in outlet losses.

(b) Evolution of the axial Mach number and its standard deviation.

Fig. 1.20 Investigation of the interaction between hub-corner separation and tip leakage flow in the inception of spike-type part stall, reproduced from Choi et al. (2008).

The spike-type rotating stall was abruptly found as part span stall generated at the rotor tip by detecting time-history of axial velocity by numerical probes at casing, shown in Fig. 1.20a.

But analyzing the unsteady flow in the entire rotor domain, this work highlights that is the hub corner separation that resulted to be the very first disturbance triggering the movement of the tip leakage flow.

At period 3.0 no disturbance existed in casing probes, as proved in Fig. 1.20a, whereas the hub-corner-separation already showed an asymmetric behavior, which can be recognized at 3.0 periods in Fig. 1.20b by larger values of standard deviation of axial Mach number in the region of hub-corner-separation boundary (marked CS) than in the tip region.

When the CS region moves radially toward the casing at 9.0 periods, it increases the standard deviation in the tip region and the disturbance starts to be detected also by the axial velocity probes placed in the tip region.

At this point the classical dynamic of the stall develops: between 3.0 and 19.0 periods the front line moves upstream till the attached stall cell reaches a critical size. The tip leakage flow locally moves around the leading edge of the next blade spilling into the adjacent flow passage due to blockage of the attached stall cell. Consequently, the spike-type rotating stall starts at 20 periods whereas the hub corner separation was reduced, see Fig1.20b at 15.0 periods, as a consequence of the increased blockage of the tip flow.

These results led to the conclusion that the first asymmetric disturbance was transferred to the tip leakage flow from the hub-corner-separation, which was the trigger for the instability inception of spike-type rotating stall at the casing.

Hub stall inception in stators

Another recent work showing the inception of instability was carried out by Dodds and Vahdati (2015) on a Rolls Royce compressor representative of a modern high speed machine equipped with variable stator vanes (VSVs). The VSV were adjusted to deliberately mismatch the front stages of the compressor and induce stall. Comparing experimental and numerical 3D URANS results they showed how starting from a configuration Z unloaded and unstalled, and moving to the reference configuration A, the stall was initiated at the first stator hub. In ten revolutions, the axisymmetric flow was disturbed by the growth of stator hub corner separation until the related blockage regions coalesced into multiple short length-scale disturbances, rotating in the same sense as the shaft. By analyzing the static pressure spectra upstream of the leading edge of rotor and stator rows, at 10% span, they proved that the rotating stall was exactly originated within the stator vane and not by any rotor.

The radial redistribution caused by blockage of the hub stall cells, locally rises the velocity toward the casing and lowers the casing pressure of the stalled stator. For this reason the static pressure peak at casing appears farther downstream, i.e. on the following stator. This case shows that even if the rotating stall formation in stator hub region is not commonly reported, the relative change in the shape of the velocity triangles at the hub and tip causes the loading at the hub to rise more rapidly than that at the tip, as the compressor is throttled.

The same result has been found in the last work of Yamada et al. (2015), where a 14 stages compressor developed for a 30MW-class high-efficiency industrial gas turbine was simulated by using DES. The growth of the hub corner separation in the 6th stage was found to lead to the generation of the leading-edge separation mechanism presented by Pullan, as explained by the Fig 1.22. Then such a separation evolved into the rotating stall and propagated in the neighbor blades. Yamada concludes that the rotating stall propagates to the upstream and downstream of blade-rows due to its large blockage effect spreading throughout the compressor.

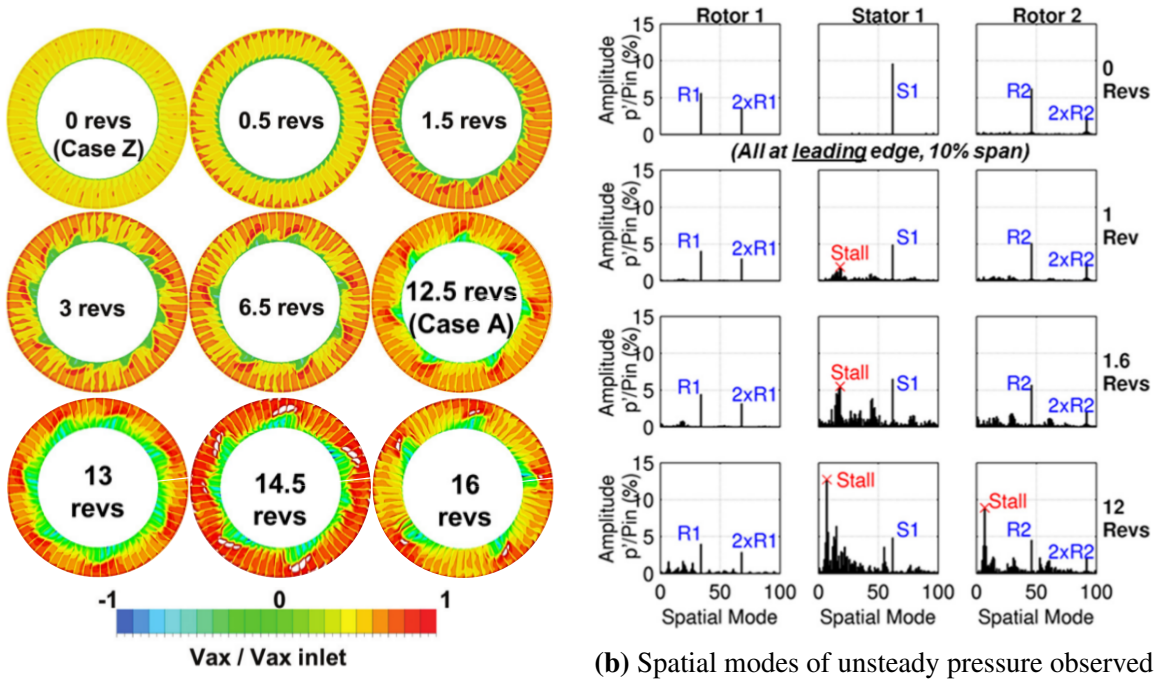

(a) Transient solution at Stator 1 trailing edge, when vanes are moved from unloaded case Z to reference case A.

(b) Spatial modes of unsteady pressure observed as stall forms from at the 10% span, immediately upstream of the Rotor 1, Stator 1 and Rotor 2 from case Z to case A.

Fig. 1.21 Inception of stall in stator hub of modern multistage high speed compressor by adjusting stator vanes to pass from an unloaded configuration Z to the experimental reference configuration A, reproduced form Dodds and Vahdati (2015).

1.7 Summary and Discussion

This chapter presents the context and the subject of the present study: the corner separation in axial compressors. So far, several mechanism have been found to be involved in the development of this particular junction flow. The blade load, the blade geometry, the incoming endwall boundary layer and the spanwise boundary layer on the suction surface of the blade have a primary influence on secondary flows and the time-averaged topology of the corner separation. The main impacts related to the corner separation are the loss of efficiency of the entire stage due to total pressure losses and the blockage of the flow. Even if the corner separation in compressor was one of the first phenomena investigated in the past in order to avoid its deleterious impacts, a final method of control has not been yet achieved. The corner separation still remains a first order problematic for multistage compressor designers, especially when dealing with high efficiency machines at off-design conditions close to the surge limit.

The blockage generated by the corner separation has indeed deleterious consequences on the stability of the compressor. When pushed to the stability limit, compressors that suffers of hub corner separation experience the rotating stall due to the separation growth and unsteadiness. The most recent simulations show that the related blockage deviates the

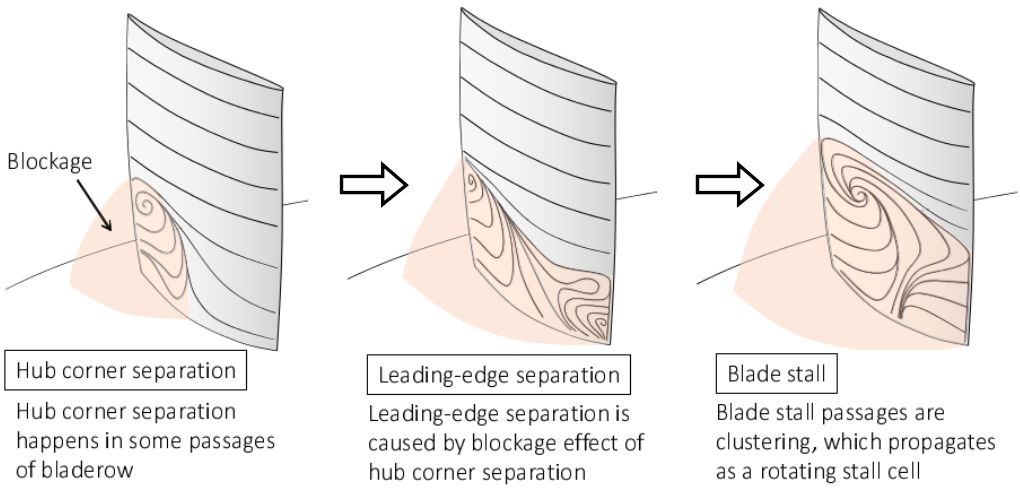

Fig. 1.22 Stall inception process found by Yamada et al. (2015) in multistage compressor by using DES.

incoming flow until a separation of the flow on the leading edge of the blades is produced. This in turn can lead to a radial vortex that moves in circumferential direction and propagates in neighbor blade passages, starting the rotating stall. Furthermore, the blockage of the hub corner separation has been found to be related also with the generation of rotating disturbances, disputed pre-stall phenomena which in the past were explained only by the existence of large tip clearances and related flows in the rotor.

Thanks to the progress of experimental methods and numerical simulations, the importance of hub corner separation in instabilities inception has come back in the limelight in the last decade. But the unsteadiness and the sensitivity of this phenomenon to several variables of the surrounding flow are still a challenge for the prediction task. The next chapter will focus on the actual questions and problematics limiting the understanding of the dynamics of the corner separation.

Chapter 2

Limitations and main goal of the study

Contents

2.1 Introduction **39**

2.2 Previous work on the LMFA cascade **40**

2.2.1 Bimodal distribution of velocity in literature 40

2.2.2 Bimodal behavior in the LMFA cascade 42

2.2.3 LES simulation of one half passage 43

2.3 Prediction of separations **44**

2.3.1 De Haller number 45

2.3.2 Liebelein diffusion factor 45

2.3.3 Lei's criterion 46

2.3.4 Corner shape factor 47

2.3.5 Limits of RANS simulations 48

2.4 Diffuser instability **52**

2.4.1 A focus on the transitory stall regime unsteadiness 55

2.4.2 Interaction with inlet perturbations 57

2.5 Summary and Discussion **58**

2.1 Introduction

As presented in Chapter 1, the corner separation unsteady behavior has been reported to take on primary importance in the understanding of the instability in compressors. The Chapter 2 presents main limitations to overcome when investigating such unsteady dynamics: above all, the sensitivity to the inflow conditions, the narrow predictability offered by criteria and the uncertainty withheld by RANS simulations. The background and starting point of this work are presented: past studies on the LMFA compressor cascade, the bimodal behavior of the

corner separation and a review of diffuser flow regimes, fundamental tool to understand the results of Chapter 5. Finally, all the questions targeted by the present work are here clarified.

2.2 Previous work on the LMFA cascade

The corner separation has been already subject of study in two works on the LMFA compressor cascade: the experimental work of Ma (2012) and the numerical study of Gao (2014). At first, the experimental study carried out in the PhD work of Ma (2012) characterized the cascade at different operational incidences and investigated the unsteady features of this separation. Even if some results of that work present incorrect measurements, as will be further discussed in Chapter 4, the phenomenon observed through LDA measurements concerning the unsteady behavior of the separation has been confirmed in the present thesis. Such an unsteadiness is the so-called *bimodal behavior* of the corner separation and it is discussed in the following section.

The second PhD study of Gao (2014) presents several RANS and LES simulations carried out on the half of the NACA 65009 profile of the LMFA compressor cascade. Whereas RANS always mispredicts the separation, LES results agree with current experiments and confirm the unsteadiness of the corner separation. These results are here reproduced in order to have an overall view of the case of study and the unsolved questions inherited by these previous works, which motivated the current study.

2.2.1 Bimodal distribution of velocity in literature

The bimodal distribution for a probability density function appears like two distinct peaks in the shape of the histograms. For a generic quantity, the presence of these two bumps represents the higher probability that the quantity studied assumes two distinct preferred values.

Bimodal velocity distributions were reported in the literature especially in junction flows and are distinguished by a peak for values close to zero, or negative, and a peak for positive values. The presence of these two preferred states reflects the intermittent switches between two preferred values of velocity without a precise periodicity. Such statistical distributions have been reported in the LMFA compressor cascade by Ma (2012), but the mechanisms behind bimodality were not understood in that study.

Devenport and Simpson (1990) were the first to report the bimodal velocity probability phenomenon performing three-components LDA measurements on a rood wing. Typical bimodal histogram for streamwise velocity component are shown in the Fig. 2.1a, and the locus of bimodal points is highlighted by the solid line in the Fig. 2.1b. This work also showed the peculiarity of the flow in this region to switch aperiodically between two basic modes: the “back-flow mode” and the “zero-flow mode”.

- In the back-flow mode, the return flow is able to penetrate far upstream and forms a strong wall reverse jet.

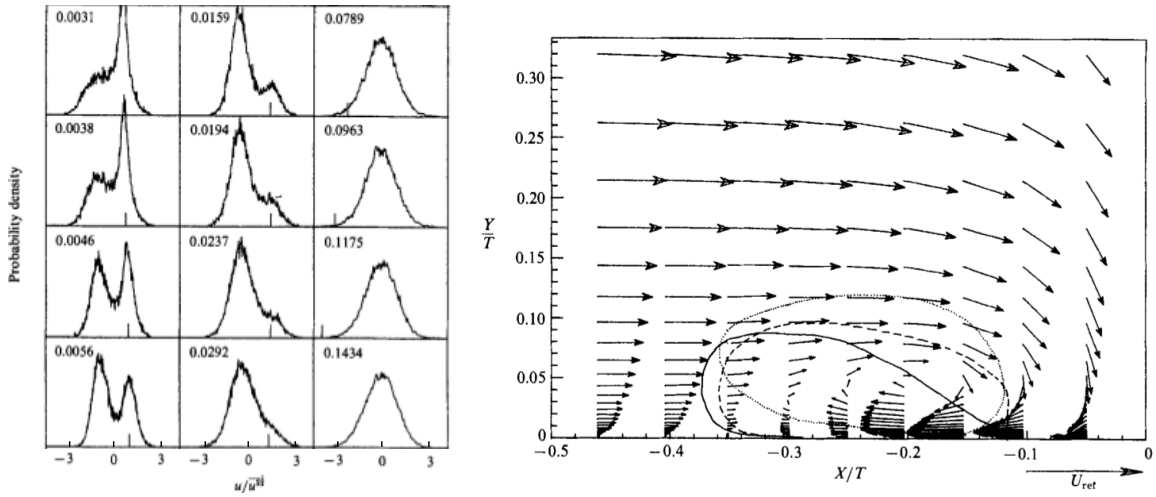

(a) (b)

Fig. 2.1 Bimodal behavior in junction flows, reproduced from Devenport and Simpson (1990).

- In the zero-flow mode, the return flow is unable to penetrate upstream and is ejected vertically upward away from the wall.

The same case of study was the object of the LES simulation carried out by Gand et al. (2010), which captured the bimodal behaviour of the horseshoe vortex in front of the nose of the rood wing. Analyzing the power spectral density of the streamwise velocity at positions affected by bimodal distributions, it was remarked that 20% the entire fluctuations was contained at low frequencies, in a range of Stroual number based on the incoming boundary layer thickness between 0.05 and 0.1. The double peak distributions were anyway less pronounced that the case reported by Devenport and Simpson (1990). This difference was explained by the authors as a consequence of different bluntness factors of the body. From such a remark it can be inferred that for blades with low bluntness factor, as in case of compressors blades, the horseshoe vortex is reduced and the related unsteadiness associated to the appearance of the bimodal behaviour near the LE is consequently suppressed.

Zierke and Deutsch (1989) studied the boundary layers and wakes across a highly loaded, double-circular arc compressor blade in cascade. Transition trips were not used because it was claimed that the artificially induced development of the boundary layer is rather misleading, in contrast with the argumentation of Evans (1971). Bimodal velocity distributions were found when the time-average velocity away from the surface was near zero.

Young Jr et al. (1978) investigated the flow-field above a stalled wing with an NACA 0012 section and $AR = 8$. The angle of attack was 19.5°, the Mach number was 0.49, and the Reynolds number was 1.4×10^6. The flow field was characterized by the periodic shedding of discrete vortices from the region near the crest of the airfoil. Bimodal histograms were found near the LE.

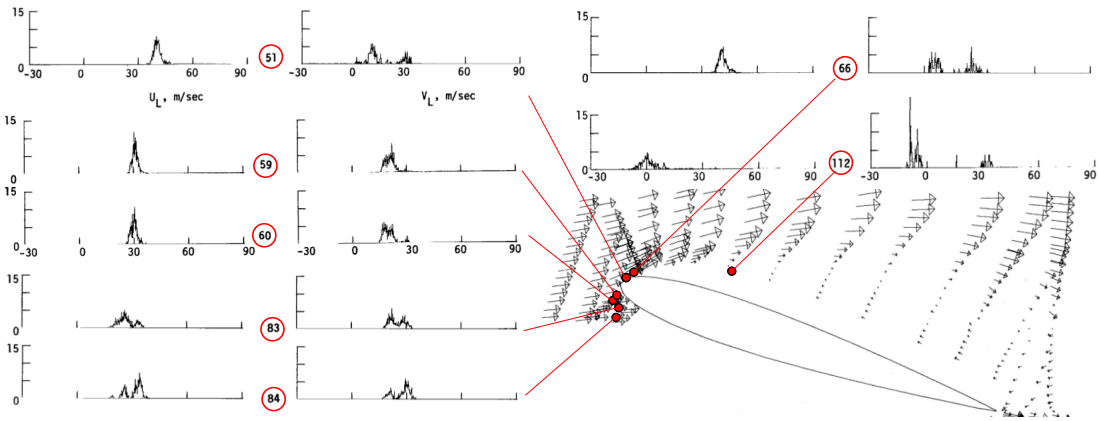

Fig. 2.2 Bimodal behavior around a stalled airfoil, reproduced from Young Jr et al. (1978).

2.2.2 Bimodal behavior in the LMFA cascade

As previously introduced, Ma (2012) reported bimodal points in the tangential velocity on the suction surface of the blade in the same cascade utilized for the current work. LDA measurements were carried out at $i = 4°$ starting from points on the wall of the blade and then moving in normal direction from the surface toward the center f the inter-blade passage. The bimodal points mainly appear in the region around the time average interface between separated flow and non-separated flow on the suction surface of the blade. In cascade coordinate u_x and u_y resulted both affected by bimodal distributions, but after the transformation in coordinates relative to the blade, only the tangential velocity u_s was found to be characterized by the bimodal behavior, while the normal velocity u_n showed in any case Gaussian distributions.

Analyzing the decomposition of the two modes in terms of tangential and normal velocity it was found that the velocity components u_n and u_s in a bimodal point are non-independent. The spectra of the velocity components measured by LDA were also calculated and no obvious peak was reported, leading to the conclusion that the two modes are continuous and aperiodic. The bimodal dynamics was hence described as the aperiodic interplay of two basic modes: large-scale mode and small-scale mode. Large-scale mode means that the velocity is affected by an instantaneous large-scale vortex and $u_s < 0$. Small-scale mode represents the velocity influenced by an instantaneous small-scale vortex and $u_s > 0$. Furthermore, the physical mechanism of bimodal histogram in such experiments was considered not associated with the horseshoe vortex.

Because this description lacks of details, the first scope of the present study was to establish which flow structures were associated to these modes. In light of results presented in Chapter 5, the classification provided by Ma can be considered exact locally in the region of the separation if the large scale mode is associated to the open separation and its characteristic recirculation region. Conversely, the small scale mode can be associated to the closed separation and the smaller coherent structures surviving in such an almost attached boundary layer.

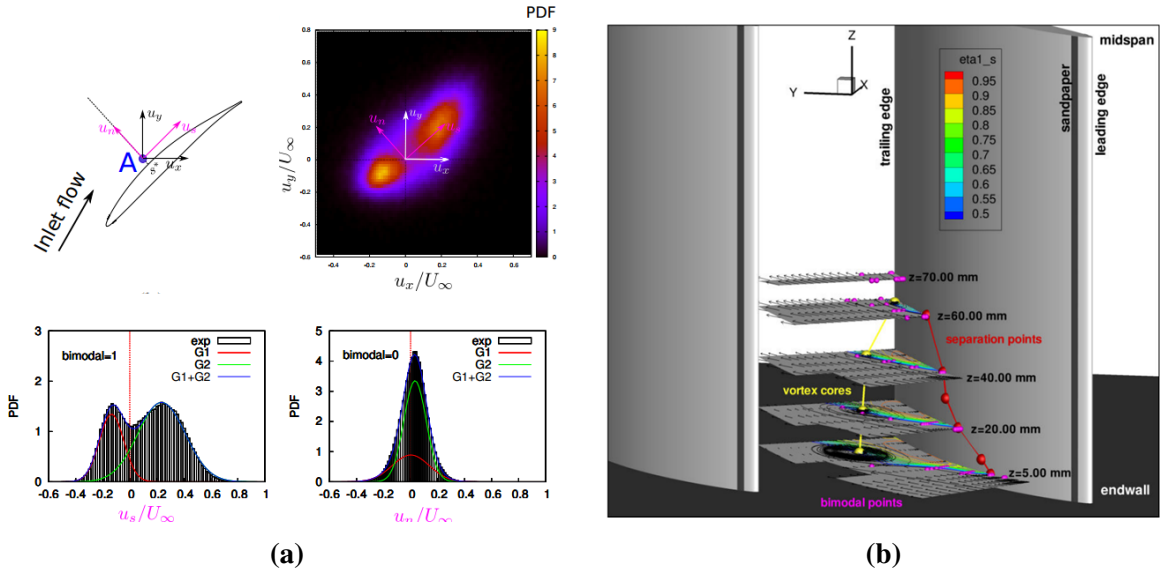

(a) **(b)**

Fig. 2.3 Illustration of bimodal behaviour found on the LMFA linear compressor cascade by Ma (2012): LDA measurements (a) with red points=separation points, yellow points=cores of the vortex, pink points= points with bimodal histograms. Example of bimodal point found on the suction surface at the measurement point $z = 5.00mm$, $s = 0.41$ and $n = 6.50mm$ (b), two-dimensional PDF in the point showing correlation between PDF of u_s and u_n (c), bimodal behavior of tangential velocity u_s (d), normal behavior of normal velocity u_n (e) in the bimodal point.

2.2.3 LES simulation of one half passage

On the numerical side, the unsteadiness of the corner separation was the case of study of the LES simulation carried out by Gao (2014), implemented using the in-house finite-volume compressible N-S equation solver *Turb'Flow* (Boudet et al., 2007) developed at the LMFA (*Laboratoire de Mécanique des Fluides et d'Acoustique*). The detailed comparison of LES results and measurements campaigns carried out during the present PhD work is resumed in the Gao et al. (2015b).

The shear-improved Smagorinsky model (SISM) by Lévêque et al. (2007) was chosen to model the subgrid-scale (SGS) eddy viscosity because capable to correctly solve complex non-homogeneous engineering flows, as demonstrated by Cahuzac et al. (2011). The simulation employed the 4-point Jameson centered spatial scheme and three-step Runge-Kutta scheme for temporal discretization. The numerical domain was limited to one passage and one half of the blade: symmetric conditions were imposed at the mid-span of the blade, whereas the boundary condition was periodic in pitchwise direction.

The inlet plane of the simulation domain was located at $4.13c_a$, position chosen in the experimental work of Ma (2012) for the hot wire characterization of the inlet flow, further compared with the present measurements in Section 3.13. A three-dimensional boundary layer simulation of a flat plate was performed in parallel with the blade passage simulation in order to provide inflow turbulent information on the inlet plane.

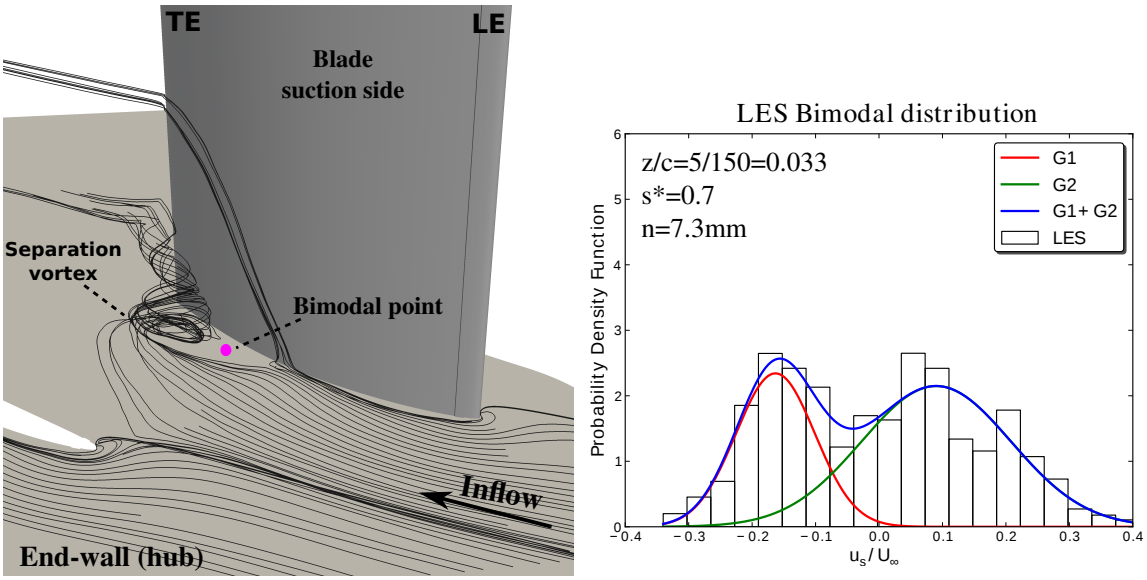

(a) (b)

Fig. 2.4 Time averaged topology resulted from the LES simulation and location of the bimodal point (a). Bimodal distribution captured by the simulation and fitting by Gaussian functions.

The time average of the three dimensional flow gave the time average topology reproduced in Fig. 2.4a. The main separation vortex impinges on the endwall, where a focus exists, but its rotation axis is then twisted in streamwise direction over the aft part of the blade near the trailing edge. This topology is different from common RANS predictions, which in case of open separations show topologies characterized by a focus on the endwall and a focus on the suction surface of the blade.

Furthermore, the LES simulation was able to capture the unsteadiness of the corner separation. Bimodal distributions were indeed found in the separated region, as shown in Fig. 2.4b, after a simulated physical time of ten periods, which was reached in order to ensure a reasonable statistical convergence. Probably because of this limitation, the bimodal distribution was less smooth than in the experimental results. However, two distinct Gaussian fits highlight the existence of two preferred modes of the flow in the selected location.

2.3 Prediction of separations

The common methods to evaluate the performance of a blade row in compressors is to relate the diffusion factor of the blade passage to the velocity at inlet and outlet of the passage. Since in turbomachinery velocities are functions of flow angles, which in turns are related to the geometry of the blade, it is possible to evaluate the diffusion factor during the design of the blade. The interest to known the diffusion factor of the designed blade row is to compare it with critical values of diffusion obtained from previous experimental data correlations. In this way the designer can be warned about the occurrence of stall and sudden drops of

performance of the blade as load increase. Three criteria are the most common in order to accomplish this task and are shown below in ascending order of complexity.

2.3.1 De Haller number

The basic criterion to evaluate the critical conditions of a compressor blade row is to evaluate the deceleration between inlet velocity V_1 and outlet velocity V_2 of the row. De Haller established by experimental investigations in cascades that the outlet velocity should not be less than 0.72 times the inlet velocity to prevent stall, i.e. $DH > 0.72$.

$$DH = \frac{V_2}{V_1} \tag{2.1}$$

Obviously, a one-dimensional criterion can be used for mid-span evaluations but it is not reliable considering wall stall. Furthermore this parameter does not take into account the diffusion from V_{max} to V_2, which is more penalizing than V_1.

2.3.2 Liebelein diffusion factor

Lieblein et al. (1953) factor empirically relates the peak velocity on the suction surface of the blade to the velocity at the trailing edge. The equation accounts for the one-dimensional deceleration of the fluid as for De Haller number but taking into account also the effect due to flow turning, ΔV_θ, and solidity σ. The general expression is given by Eq. 2.2, but for incompressible flows with unique axial velocity upstream and downstream of the cascade, DF could also be expressed as in Eq. 2.3.

$$DF = 1 - \frac{V_2}{V_1} + \frac{\Delta V_\theta}{2\sigma V_1} \tag{2.2}$$

$$= 1 - \frac{\cos\alpha_1}{\cos\alpha_2} + \frac{\cos\alpha_1}{2\sigma}\left(\tan\alpha_1 - \tan\alpha_2\right) \tag{2.3}$$

Values of DF larger than 0.6 are commonly avoided since blade stall could occur, and a typical design choice is usually 0.45. Since this formulation is valid only near the design point, because it is based on the design value of suction-surface diffusion ratio, the *equivalent diffusion factor* was introduced in the work of Lieblein (1959) as an empirical adaptation for off-design operational conditions of the blade.

$$D_{eq} = \frac{\cos\alpha_2}{\alpha_1}\left[1.12 + a\left(i - i^*\right)^{1.43} + 0.61\frac{\cos^2\alpha_1}{\sigma}\left(\tan\alpha_1 - \tan\alpha_2\right)\right] \tag{2.4}$$

where i^* is the optimum incidence which gives the diffusion factor corresponding to the minimum loss conditions and $a = 0.0117$ is a constant coefficient for NACA 65(A_{10}) blades. The critical value to not exceed for this formulations is $DF_{eq} = 2$. This criterion remains two-dimensional, so it is inaccurate in order to predict three-dimensional mechanisms discussed in Chapter 1 occurring in separations.

2.3.3 Lei's criterion

The three-dimensional effects of inlet skew and cross flow, as well as the adverse pressure gradient in the blade passage are taken into account in the work of Lei et al. (2008), which addresses specifically to hub corner separation problem. They provided a stall indicator a posteriori based on the reduction of the local blade loading relative to flow conditions outside the separated region, as shown in Fig. 2.5a, referred to as Zweifel blade loading coefficient Ψ in Eq. 2.5. Conversely, the diffusion parameter accounts a priori for the ideal static pressure rise coefficient as a function of the blade geometry, the turning, which results from the cross-passage pressure gradient acting on the skewed incoming boundary layer, and the solidity of the blade row. The final equations obtained for stall and diffusion factor are Eq. 2.6 and Eq. 2.7, respectively.

$$S = \Psi\Big|_{z/c=0.5AR} - \Psi\Big|_{z/c=0.1AR} \tag{2.5}$$

$$= \left[\int_0^1 \frac{p_{ps}(x) - p_{ss}(x)}{p_{t_1} - p_{s_1}} \left(\frac{\mathrm{d}x}{c_a}\right)\right]_{z/c=0.5AR} - \left[\int_0^1 \frac{p_{ps}(x) - p_{ss}(x)}{p_{t_1} - p_{s_1}} \left(\frac{\mathrm{d}x}{c_a}\right)\right]_{z/c=0.1AR} \tag{2.6}$$

$$D = \frac{s}{c}\left\{1 - \left[\frac{\cos(i+\gamma+\varphi/2)}{\cos(\gamma-\varphi/2)}\right]^2\right\}(i+\varphi+\Delta\eta) \tag{2.7}$$

where c_a is the blade axial chord length, p_{ps} and p_{ps} are the static pressures on the pressure side and suction side, respectively. p_{t_1} denotes the upstream total pressure, p_{s_1} is the upstream static pressure and AR is the blade aspect ratio.

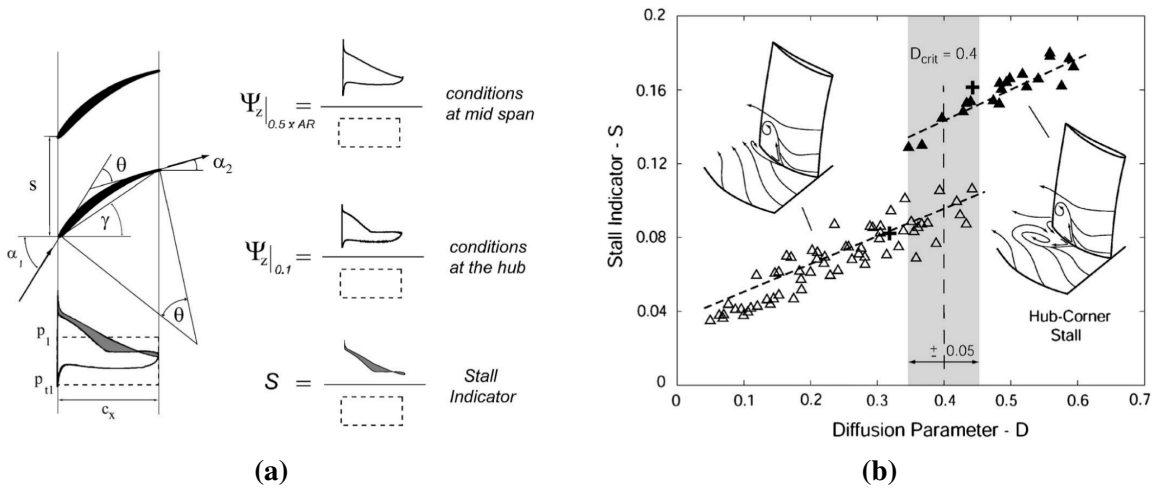

Fig. 2.5 Lei's criterion: (a) explication of loading coefficient and stall parameter; (b) resulting correlation and overlap region at the critical value threshold.

The application of these two parameters to a wide range of different three-dimensional steady RANS simulations gave the map presented in Fig. 2.5b. The geometry of the blade profile, i.e. the angles, as well as the solidity, the Reynolds number, the aspect-ratio, the inlet boundary layer thickness and the inlet swirl angle were varied in the simulations. The stall

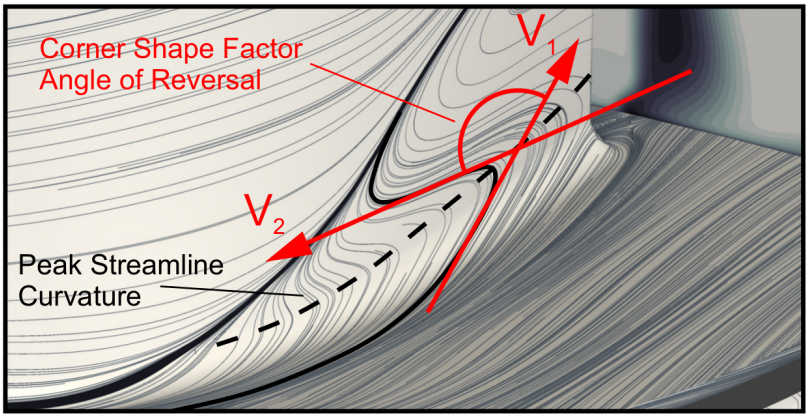

Fig. 2.6 Definition of corner shape factor, reproduced from Taylor and Miller (2015).

indicator was found to have little or no appreciable sensitivity to the Reynolds number, the Mach number, the inlet boundary layer thickness and the blade aspect ratio.

The result for stall indicator against the diffusion parameter of Fig. 2.5b shows two distinct branches, which represent the case of closed corner separation, on the left, and open corner separation on the right. Lei preferred to name the open and closed configurations of the separation with the terms *corner stall* for large corner separation and merely corner separation referring to the closed separation. The branches shift around a critical value $D = 0.4$ and overlap over a range of diffusion factor values that envelops the critical one, hence $D_{cr} = 0.4 \pm 0.05$ was taken as final parameter for the criterion. The causes of this double-value behavior were not identified in the work of Lei.

The question arises as to whether this particularity implies the intrinsic instability of the corner separation associated to the bimodal behavior.

2.3.4 Corner shape factor

Taylor and Miller (2015) deduced a topological criteria named *corner shape factor* from the investigation on the impact of three-dimensional blade design on the spanwise pressure gradient.

The corner shape factor is defined as the angle between the co-flow vector, here identified as V_1, and the reversed flow vector V_2, varying between 0 and π. As the angle tends towards π the local streamline surface curvature tends towards infinity and the topology collapse to a singularity forming a saddle and a focus pair in the corner. As seen in Section 1.3.4 such topological configuration correspond to larger separations, increasing progressively as the focus migrate on the hub wall farther from the suction surface.

In their work, Taylor and Miller (2015) show how the correct design of blades, for example increasing the blade lean, permits to prevent the reversing of streamlines and the increase of corner shape till π.

The corner shape factor criterion rests on RANS simulations, so even if skin friction lines can be adequately predicted by such simulations (Gbadebo et al., 2005), the overall topology of the separation remains very sensitive to limitations of the RANS model. Such

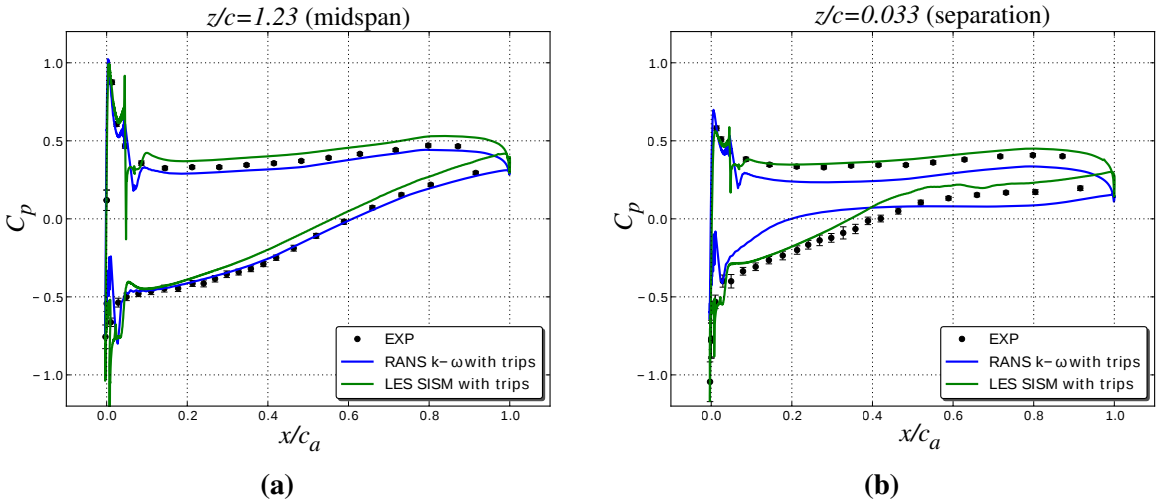

Fig. 2.7 Static pressure distributions at midspan (a), and in the separation region (b). Comparison between experiment and different turbulence models (Gao, 2014).

limitations and the related uncertainty that must be taken into account when relying on RANS predictions are further discussed in the next section.

2.3.5 Limits of RANS simulations

The importance of understanding the physics of corner separation lays in the necessity to improve the numerical simulations capability to predict the losses and the operational range of a blade row.

It is commonly know that Reynolds-averaged Navier-Stokes simulations (RANS) mispredict the corner separation in terms of the extension of losses and blockage. Gbadebo et al. (2005) showed in their work on topology that farther from the surface of the blade and the endwall, the losses were overestimated. Conversely, the variation of the size of the corner separation as a function of inlet incidence of the flow was captured by RANS.

Detailed numerical studies on corner separation in the LMFA compressor cascade were achieved in the last years. In the work of Gao (2014), Wilcox $k-\omega$ and Kok $k-\omega$ turbulent models were investigated and the extension of the separated region on the blade surface, described by the plateau in the static pressure distributions, and the downstream losses resulted to be overvalued, see Fig. 2.7 and Fig. 2.8. The results achieved by LES correctly match the total pressure losses downstream of the cascade obtained in the experiment. A comparison between the experimental measurements, RANS and LES downstream losses is presented in Fig. 2.8.

The shape of the core of losses is different between the well predicted separation of LES and the RANS, in particular focusing on the curvature of the boundary region, where the gradient is high and Reynolds stresses reach the maximum magnitude.

Furthermore, the study presented by Monier et al. (2016) investigates the difference between LES and RANS using the $k-\omega$ model of Wilcox 1988 with and without quadratic

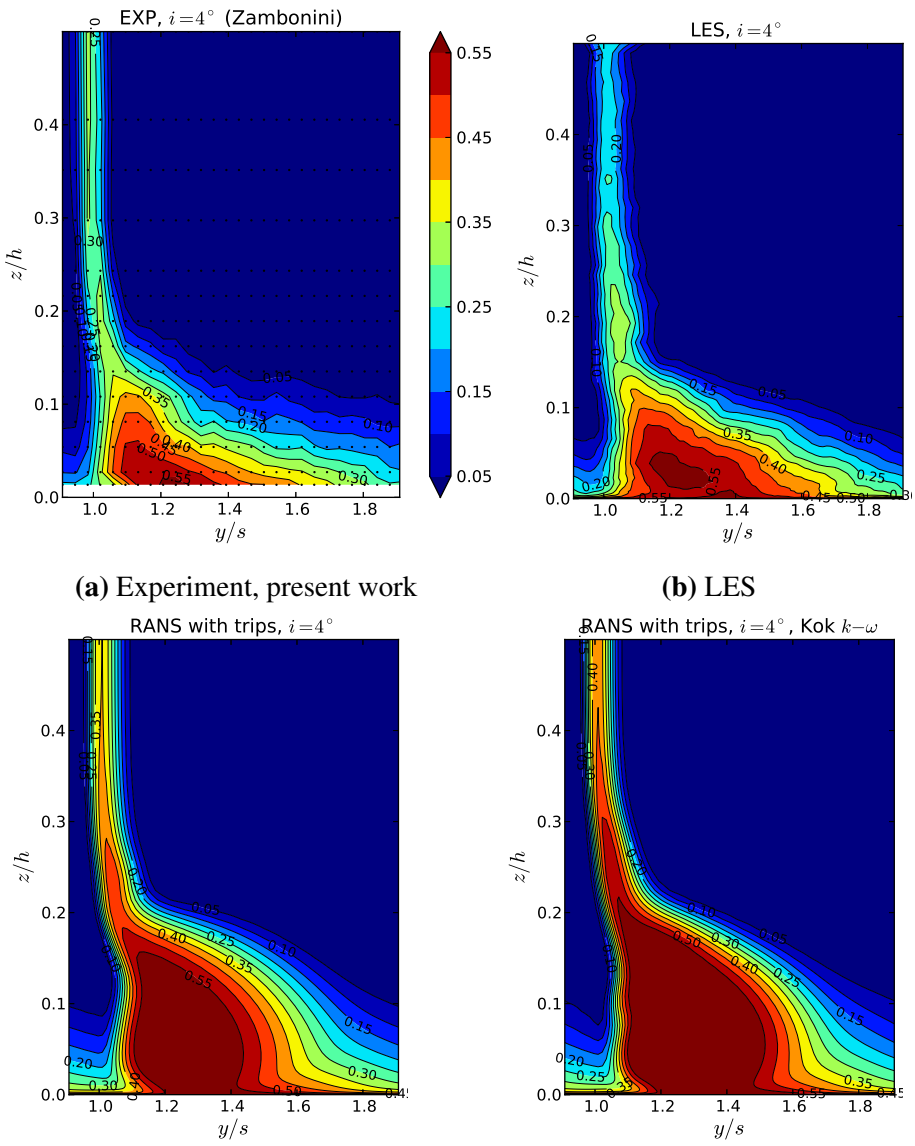

(a) Experiment, present work

(b) LES

(c) RANS Wilcox $k-\omega$

(d) RANS Kok $k-\omega$

Fig. 2.8 Downstream total pressure losses at $0.363c_a$ axial distance from the TE. Comparison between experiments, LES and RANS simulations with different turbulence models. Reproduced from Gao (2014).

consitutive relation (QCR) (Spalart, 2000). The RANS was found to fail to correctly represent the Reynolds shear, see Fig 2.9, normal stresses and the transport of turbulent kinetic energy (TKE), which was underlined to be the main cause in the accumulation of production and dissipation of TKE in the same critical region at the boundary of the separation. As conclusion, the modifications given by the QCR model were not significant enough to improve the Wilcox model and to approach the LES results.

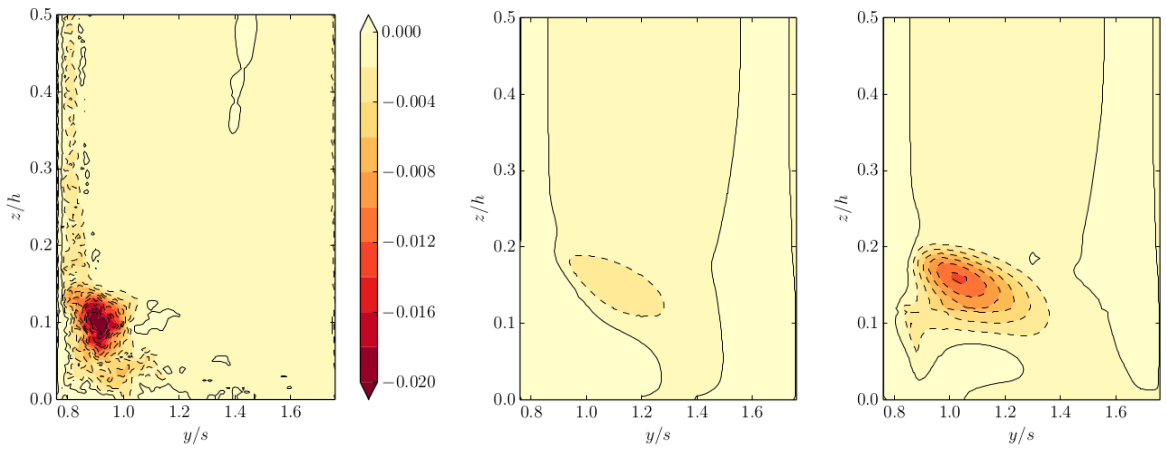

(a) LES **(b)** RANS Wilcox $k-\omega$ **(c)** RANS Wilcox $k-\omega$ QCR

Fig. 2.9 In-plane Reynolds stresses at the outlet section, $0.0c_a$ axial distance from TE. Comparison between LES, RANS Wilcox $k-\omega$ and Wilcox $k-\omega$ QCR, reproduced from Monier et al. (2016).

Beside such limitations, RANS remains the most suitable computational method in turbomachinery because it is fast and anyway conservative in design process, due to the overestimation of losses. The computational costs of LES remain nowadays too expensive to consider such type of simulation for compressor design, without speculating on the difficulties related to its implementation.

Steady and unsteady RANS simulations can be exploited to design and optimize the machine but attention has to be put on the effect of unsteady non linear phenomena associated to separations in order to avoid catastrophic aerodynamic failures. This subject is analyzed in the work of Taylor and Miller (2015) comparing the way to failure of blades with low and high degrees of lean angle. As reviewed in Section 1.3.4, low lean blades fail by abrupt inception of open corner separation, while high lean blades avoid the closed-to-open switch but are affected by trailing edge stall, which occurs gradually as the incidence is increased.

The "risk" or uncertainty in CFD prediction for a given design is not taken into account if the ability of the CFD to predict results is not evaluated against the variation of critical parameters at the failure point, for instance the inlet incidence.

The uncertainty of RANS predictions was found by Taylor and Miller (2015) to be high even with small changes of the inlet condition in the region of the design space where the open separation controlled the failure of the flow, i.e. for blades with low lean at high incidence operational conditions. In the design space region controlled by trailing edge failure, the uncertainty of CFD was found to be low and the results of simulations were in better agreement with the experiments.

The authors reported that the first clue of the existence of high uncertainty appeared in the discrepancy of the losses evaluation between experiments and CFD for low lean blades above the critical incidence. In the numerical simulation, an error of 2° in the inlet profile of the stator resulted in a misprediction of the side wall on which the separation occurred.

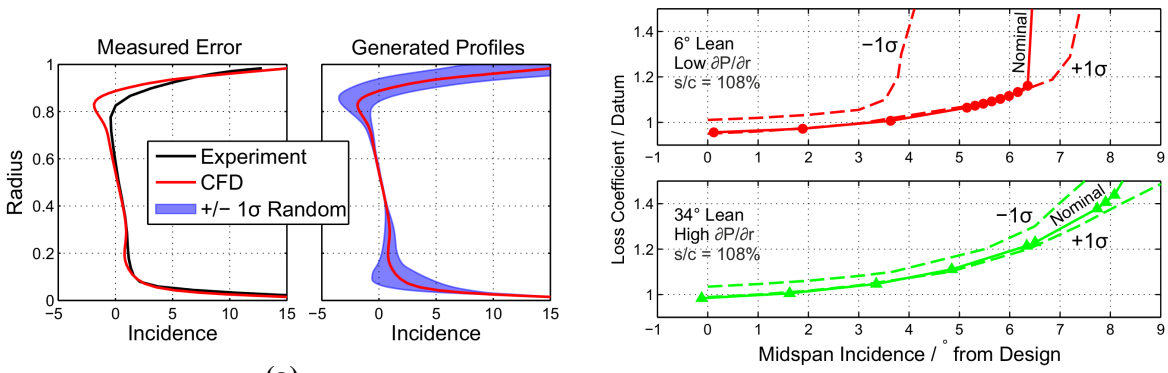

Fig. 2.10 Figure (a): inlet profile generation in the range suggested by differences encountered between CFD and experimental inlet profile. Figure (b): consequent variation of predicted losses associated to the variation of the stator inlet incidence and comparison between low-lean and high-lean designs. Reproduced from Taylor and Miller (2015).

To investigate the causes of such error, different inlet profiles were generated as shown in Fig. 2.10a, in order to reproduce the possible random variations in the inlet flow angle, especially in sensible regions close to the endwalls. The losses predicted by CFD set up with these manipulated profiles are presented in Fig. 2.10b. It can be seen that the 6° lean case shows a larger uncertainty than the 34° lean case. If it is assumed that the "nominal" curve rapresents the real evolution of the corner separation against the inlet incidence, when a small increment is introduced in the inlet condition of the stator ($+1\sigma$), the predicted losses suddenly increase at the incidence of 3.5° in a non-linear fashion. On the other hand, if the inlet condition of the stator is under estimated by the simulation of the upstream rotor row (-1σ), the resulting prediction of the corner separation will give a delayed critical point at the incidence of 7°. Both such cases lead to a crucial misprediction of the performance of the stator row. For this reason, the low-lean case is denoted as an high-risk design whereas the high-lean design is a low-risk design.

For low-risk design the reported uncertainty was lower than 10%, whereas for high risk design, was 40%. As conclusion, the choice of the blade design based on RANS simulations has to take into account the main goal of the machine: if the operational range is expected to be wide and sudden failure want to be avoided, the low-risk design has to be preferred. Conversely, if the required operational incidence range of the blade is narrow, the high-risk design is able to achieve high performance, but extensive experimental validations of CFD prediction would be advised.

The present work's aim is to experimentally investigate the flow unsteadiness for the high-risk design blades. The gain of awareness of physical mechanisms and related cause-effect relationships behind such an unpredictability is the first step to improve simulation techniques and analytic modeling.

2.4 Diffuser instability

In compressors, the stator blade passage is usually designed as a diffuser, which permits to convert a fraction of the dynamic pressure of the flow, gained after the rotor passage, into static pressure. Furthermore, the unsteadiness uncovered in the present work has many common features with dynamics of planar diffusers. For this reason a survey on two-dimensional, low speed diffuser is presented below and will be later recalled in Chapter 5 in order to analyze the unsteadiness of the flow. Reneau et al. (1967) presented the flow characteristics of a subsonic, two-dimensional, straight center line diffuser for different geometries and boundary layer thickness. Keeping the inlet flow steady and homogeneous, the angle of the diffuser 2θ and the geometrical factor N/W_1 were varied, see Fig. 2.11. Four major regimes of the flow in the diffuser are presented in the recommended correlations, reproduced from Reneau et al. (1967) in Fig. 2.12, which were achieved in experimental configurations with uniform turbulent boundary layer at the inlet, Reynolds number larger that 5×10^4 and Mach number lower than 0.2.

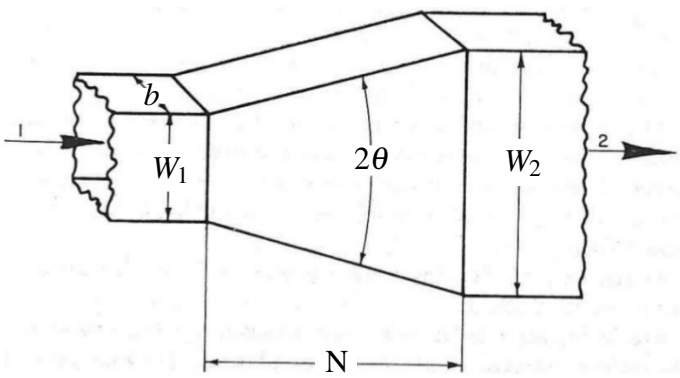

AR = aspect ratio = b/W_1

AS = area ratio = W_2/W_1

$$\text{AS} = 1 + 2\frac{L}{W_1}\tan\theta$$

Fig. 2.11 Geometry of two-dimensional, straight-wall diffuser and reference parameters (Reneau et al., 1967).

Four different regimes describe the state of the flow as it is summarized below, and the corresponding flow paths are sketched in Fig. 2.13.

- **A - No appreciable stall regime**: for the first range of divergence angles, i.e. reduced diffusion, the normal operational condition is the stable flow pattern with absence of stall, or very small separations. The increasing of the angle leads to a thickening of the boundary layer, but the flow remains symmetric on both walls.

- **B - Large transitory stall regime**: Increasing the diffusion of the channel, the unsteadiness of the flow arises and bigger oscillations of the flow characterize this highly pulsating flow. Separations of the boundary layer on the wall increase randomly, starting intermittent cycles of build-up and wash-out on both the walls alternatively. The term wash-out describes the rapid entertainment and expulsion of stalled fluid that is sufficient to cause a major change in the exit plane velocity profile. The position of the separations is not fix, moving upstream and downstream on the wall, and the

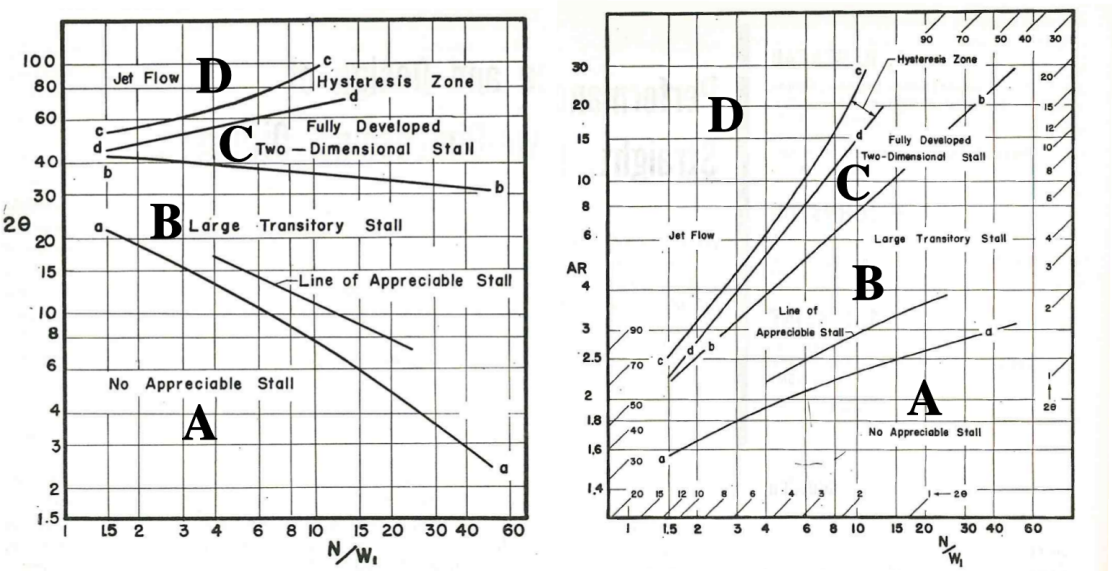

(a) (b)

Fig. 2.12 Flow regimes in subsonic, straight-wall, two-dimensional diffusers with steady inlet conditions (Reneau et al., 1967): (a) diverging angle influence and (b) aspect ratio influence.

size also varies on a wide range. Another interesting feature of this regime implies the alternate presence of the separation on the walls: when the stall exists on one wall the flow remains attached on the other and vice-versa. The elapsed time between the formation of the separation, its growth and the final break-down of the structure is $100t$, where t is the time necessary to a particle to pass through the diffuser. This value is larger compared to characteristic times of the other regimes where variations are of the order of $10t$. Furthermore, the time necessary for the stall build-up phase is usually considerably longer than that necessary for stall wash-out.

- **C - Two-dimensional stall regime**: This regime present a fully developed stall with a massive stable separation persisting only on a single wall of the diffuser. The boundary of the separation moves upstream and the separation front is positioned at the throat of the divergent. High intensity turbulence characterize the shear region between the separation boundary and the main flow but the global dynamic of the flow remains stable. Anyway, such stability can be changed by a sufficient large perturbation occurring both at the inlet and at the outlet of the diffuser. Consequently, the separation moves on the second wall and the flow reattaches on the wall previously stalled.

- **D - Jet flow regime**: In this final range the geometrical aspect ratio of the diffuser is exasperate and the flow is completely detached from both diverging walls very near the throat. This regime corresponds to the jet flow, in which velocity and pressure profiles remain relatively steady and stable except for the shear layer at the edges of the jet.

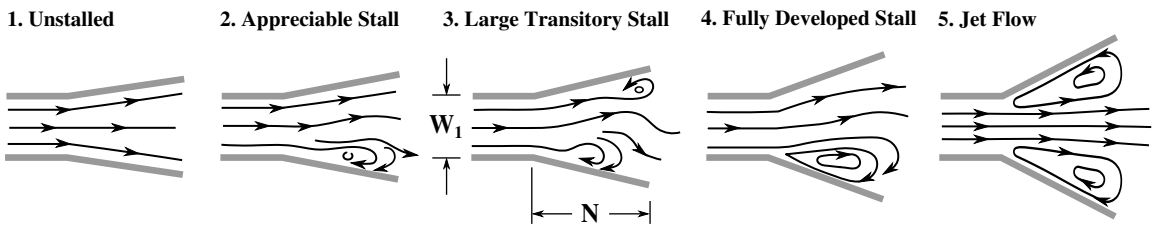

Fig. 2.13 Diffuser stall regimes.

The performance of the diffuser are commonly quantified by the static pressure recovery coefficient between inlet p_1 and outlet p_2 of the diffuser in the Eq. 2.8. The efficiency η associated to the flow regime, hence varying the geometry, is calculated as the ratio between the real C_p and the ideal static pressure recovery for incompressible one-dimensional flow given in the Eq. 2.9, valid in the assumption of reduced angles of divergence of the duct.

$$C_p = \frac{p_2 - p_1}{1/2\rho V_1^2} \tag{2.8}$$

$$C_{p_{is}} = 1 - 1/AS^2 \tag{2.9}$$

The pressure recovery against the geometry variation, which can be the aspect ratio or the divergence angle, is reproduced in Fig. 2.14a at fixed N/W_1.

In the region A, where no stall is present, the increasing of the angle leads to an increase of the diffusion, till a maximum is reached barely after the flow transition to regime B. Beyond the maximum, the C_p decreases moving toward region C, where a new stable state is reached. For larger values of divergence angle, when the jet flow of regime D is established, two stable states are possible and are associated to two shifted levels of constant pressure recovery. As result, the flow condition can oscillate between these two states describing hysteresis cycles.

The best performance is reached at the stability limit between regions A and B but the maximum efficiency peak is located in the unstalled region A on the left of transition $a-a$. Conversely, the maximum pressure recovery is reached in transitory stall region B, on the right side of the line $a-a$ in Fig. 2.14b.

Furthermore, Reneau et al. (1967) underlined the importance of inlet conditions, as the inlet velocity profile and turbulence level, and studied the variation of C_p and efficiency against the thickness of the inlet boundary layer. Regions A, C and D maintained almost the same performance, whereas the region B showed a higher degradation of performance. As inference, inlet conditions mainly affects the unstable region B rather than the others stable regimes.

It is interesting to note that the work of Moore Jr and Kline (1958), which was the first to establish the dividing lines between different regimes by studying water diffusers, reported that, at the onset of transition between region A and B, the separations firstly appeared at the corner between diverging walls and endwalls and subsequently developed into complex transitory stall in the whole duct.

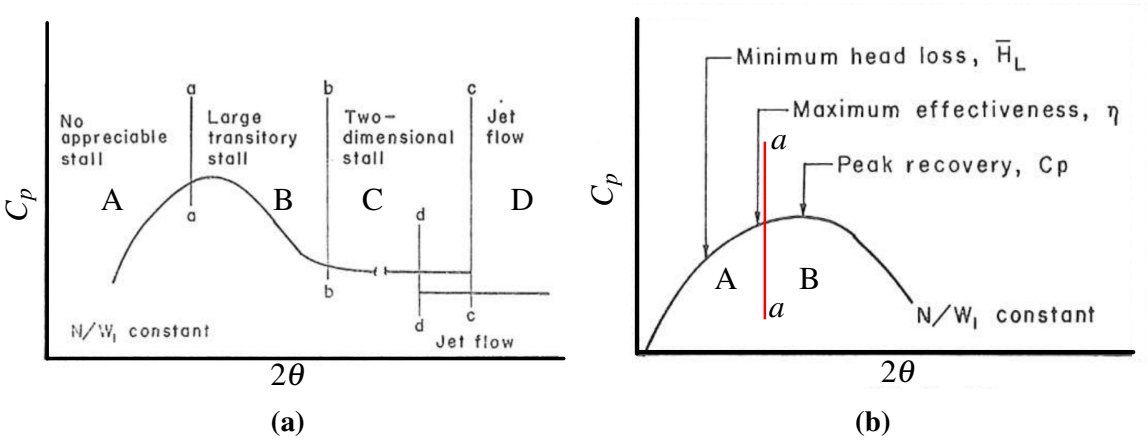

Fig. 2.14 Performances of subsonic two-dimensional diffuser at fixed N/W_1 (Reneau et al., 1967): (a) relationship between flow regimes and pressure recovery, (b) location of different optima of performance.

2.4.1 A focus on the transitory stall regime unsteadiness

After the measurements of Kline, new measurements of unsteady pressure on the diffuser walls were carried-out by Ashjaee and Johnston (1980), always for two-dimensional symmetric diffusers, with inlet trips on the four walls to assure the development of identical turbulent boundary layer at inlet, $V_\infty = 46.6$ m/s, $Re = 2.2 \times 10^5$.

The value of $2\theta = 8°$ was individuated as a limit beyond which asymmetry at the outlet section related to regime B started to develop, and the pressure recovery bump was confirmed to be located in the transitory stall region. In particular, the maximum value appeared when both sidewalls showed some degrees of unsteady reverse flow, hence at the inception of regime B. Degradation of the performance followed when asymmetry appeared and the stall on one side became larger than the other. It is necessary to stress that flow asymmetries developed even if the geometrical symmetry of the test rig was perfect, with differences of the angle between the walls of 0.01, hence within the uncertainty of the measurements. Consequently, the unpredictability of the position of the separation in a perfect symmetrical configuration is very high because the stall occurs randomly on one wall or the other one.

The investigation of Ashjaee showed that in regime B it was possible to switch manually the stall from one wall to the other but occasionally the flow switched by itself without apparent reason. Such a phenomenon was identified with the name *stall switch* and was associated to a characteristic time of stall transition that was very long, i.e. several minutes. The term stall switch will be used also in the analysis of the flow visualization in Section 5.2.1, in that case referring to the switch of the corner separation between open and closed states on the same wall of the curved duct formed by two neighbor blades, i.e. the suction surface.

Another new physical insight of such work was the introduction of an *intermittency parameter* γ_p to describe the flow regime B. Such intermittency was defined by the fraction of the time that the flow in the boundary layers was equal to the main flow in the free stream, i.e. forward downstream direction, averaging on large time intervals. Three regimes were

individuated: 99% as incipient detachment (ID), 80% as intermittent transitory detachment (ITD) and 50% as transitory detachment (TD). The separation front line was found to be located very close to the TD point.

The intermittency parameter was used to study the symmetry of the separations on the two wall and the asymmetry degree. At the inception of region B ($2\theta = 9°$), the two walls were subjected to some degree of reverse flow not in a symmetric manner. Furthermore, they reported a spanwise increase of the intermittency near the endwalls at first, underling the attention that should be put on the role of corner flow effects and blockage.

This is a critical clue for the present work and the question arises as whether an open corner separation could behave as two-dimensional flow in a blade row, working at the edge between unstalled and transitory stall regime of the passage. Smith and Kline (1974) further studied the intermittency concept in water diffuser focusing on the behavior of transitory stall periods in presence of inlet disturbances as a wake followed by a jet superimposed on the inlet velocity profile.

The intensity of fluctuations was measured to increase sharply from a minimum near the line $a - a$ to a maximum near the center of the transitory stall regime, for an angle 2θ included between 20° and 24°, then to gradually decrease approaching the line $b - b$. The diffuser length, angle and average velocity of the core flow had a major impact on the performance of the diffuser, causing degradation of C_p up to 25%.

For the first time, the stall period was defined as the time required for completion of a stall wash-out cycle. The statistical distribution of the separation periods, reproduced in Fig. 2.15, shows the quasi-periodic nature of the wash-outs. This behavior establishes a key analogy with results achieved in the present work, and it will be further discussed in Section 5.2.1.

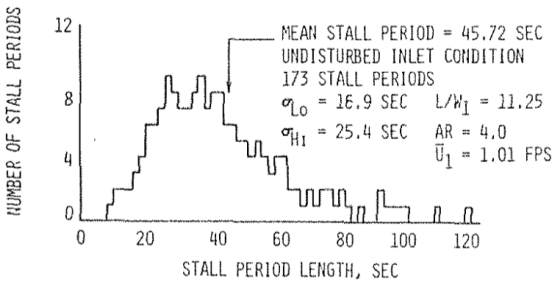

Fig. 2.15 Histogram of stall periods for a water diffuser without forced inlet perturbations (Smith and Kline, 1974).

Two distinct phenomena were found to describe the stall period cycle:

1. the phase of separation and/or build up of the stalled fluid to the point where it becomes unstable,
2. the phase of triggering of wash-out of the stall by an upstream disturbance.

The time for one natural cycle of these events varies around a value called *typical mean stall period* T_N. The averaged stall period was reported to be 100 or more stall-washout events, but individual periods ranged from $0.3T_N$ and $2T_N$ or more. Artificially induced disturbances obviously triggered the transition, but no triggering disturbance was recognized

in case of natural wash-out, even if it was hypothesized to be either a large turbulent eddy or a fluctuation in flow-rate. Visual investigations substantiated that relatively small disturbances were sufficient to cause the wash-out, but data were insufficient to predict the necessary size of such perturbations.

The unsteady flow in diffuser was finally modeled in the work of Kwong and Dowling (1994). Carrying out measurements on conical and rectangular diffusers, very low frequencies were found, with typical values from 2 to 4 Hz. Such a work reported a duplex behavior: local streamwise oscillations of the front of the separation at several Hertz, superposed to shifts in the position of the stall, corresponding to stall wash-out cycles characterized by periods of seconds. The former dynamic was detected as the main unsteadiness affecting the pressure oscillations in the diffuser. Furthermore, stall cells were found mostly in corners, switching from one corner to another over an interval of seconds in an apparently random way.

2.4.2 Interaction with inlet perturbations

The investigations presented so far considered a Mach number lower than 0.3 and uniform inlet conditions. Wolf and Johnston (1969) tested different velocity profiles at the inlet: wake, jet and step. All of them degraded the reference homogeneous inlet conditions. The perturbation effect caused the inception of the regime B to appear at lower diffusion angles. In case of asymmetric inflow conditions, the separated flow became a stable two-dimensional stall downstream of the flow deficit. Conversely, the symmetric inflow conditions with symmetric deficits, as jets, gave a bi-stable two-dimensional stall affected by the stall-switch phenomenon.

The impact of inlet wake on the transition between flow regimes A and B was further investigated by Kaiser and McDonald (1980). Two competing mechanisms were individuated: the inviscid amplification due to diffusion of the wake in the diffuser section, and the redistribution of the wake energy due to the viscosity. In a small wake, the second effect had a beneficial impact on the apparition of the separated state B, which was hence postponed. Conversely, the inviscid diffusion of the wake was larger in case of larger disturbances, overcoming the viscous dissipation and leading to a stall inception for geometries less divergent than the datum.

Other studies carried out in the work of Smith and Kline (1974) showed that one of the most important parameters in the interaction between periodic inlet disturbances and transitory stall periods is the characteristic frequency of the inlet disturbance.

If the forcing frequency is higher than the natural frequency of the instability, then the flow in the diffuser is not sensitive to the period of the disturbance per se, but only to the higher degree of turbulence of the flow. Such a deduction reminds the results of Schulz et al. (1990b) concerning the rotor wake effect on corner separation in annular compressor cascade. If the forcing frequency is comparable to the characteristic frequency of the separation, i.e. from 0.5 to 1 times the natural period of the separation, the switch of the separation starts to be forced by the disturbance, and the wash-out is triggered and synchronized by the imposed

perturbation. By further lowering the frequency of the perturbation, the separation comes back to its natural period and the wash-out returns to be naturally triggered.

The intermittent behavior of the flow was confirmed also by Adenubi (1976) in a study dealing with an axial annular diffuser, placed downstream of an axial compressor stage composed by rotor and stator. Statistical correlations quantifying the time of the separated state of the flow were in good agreement with the results of Smith, even if data resulted to be not sufficient in order to firmly confirm the results.

Unsteadiness in subsonic plane wall diffuser generated by transitory stall was investigated further by Smith and Layne (1979), by focusing on air and high Reynolds numbers with undisturbed inlet conditions and 1% turbulent intensity at the inlet, as extension of the work of Smith and Kline (1974).

Transitory stall was described as a coexistence of two time-scales: the longer of the two time scales was the result of a total stall wash-out, whereas the shorter was 20% of the longer time scale, describing the oscillating transient behavior of the upstream edge of the separation.

By carrying out experimental tuft visualizations and correlations with inlet pressure and velocity, it was remarked for the first time that transitory stall in a diffuser directly induces inlet flow unsteadiness. As inference, it was hypothesized in their report that the inlet flow unsteadiness results from changes in effective exit flow area due to transitory stall build up and wash-out. The inlet pressure spectral distribution for frequencies lower than 50 Hz up to 400 Hz was reported to be directly affected by the presence of the unsteady flow regime B, and such low frequencies were function of the time-varying exit blockage induced by transitory stall in the diffuser, generating also flow noise.

Disturbances at the inlet were related to the length of the diffuser, and maximum fluctuations of 35% of C_p and 12% of the inlet velocity from the mean value were reported near $2\theta = 20^\circ$ as the length of the diffuser was decreased. For short diffuser, less than $N/W_1 = 6$, the distortion at the diffuser exit due to flow blockage was claimed to be the primary cause of the inlet unsteadiness, whereas for longer diffusers such an influence was reduced by the increased viscous effect in the duct.

2.5 Summary and Discussion

The study of the unsteadiness of separations is clearly not a simple task. This Chapter shows how the RANS simulations usually mispredict losses and the size of the corner separation at off-design conditions. The incoming flow has a primary importance in the development of the separation and simulations become uncertain especially when dealing with multistage compressor, where errors accumulate and propagate as incoming conditions for downstream stages. Different turbulence models must be compared and verified against experimental data and advanced simulation, such as LES. Unfortunately, both are expensive and often not available, so RANS simulations must be conducted considering the related uncertainty as the separation gets worst. Several works have underlined that the separation is unstable, suddenly growing in a nonlinear fashion when crossing a critical incidence value. This phenomenon appears as a switch between one state where the separation is closed, limiting blockage and

losses, and another state where the separation is open, abruptly increasing its size. Lei's empirical criterion gives a good baseline to evaluate whether a stator blade presents closed or open hub corner separation, but it is unable to explain the jump and the overlap region between these two different states.

Previous works on the LMFA compressor cascade have reported the existence of the bimodal flow in the region close to the time-averaged separation surface. In such points, statistical distributions of velocity show two distinct bumps: one for values near zero velocity, or negative, and another bump for positive larger values. Such feature reveals that the flow intermittently switches between two preferred states, i.e. attached and detached flow.

In conclusion, the questions undergoing the present work are the following:

- Is the bimodal behavior the local manifestation of a larger-scale global separation switch?
- What is the overall unsteady pattern and topology of the flow when approaching the critical limit?
- What are the dynamics and the cause-effect mechanisms involved in the separation switch? Are these dynamics completely aperiodic or can be associated to a specific range of frequencies?
- Why such an instability seems to be intrinsic to the corner separation?
- Finally, the study of subsonic planar diffuser presents the existence of different flow regimes, among the others the intermittent transitory stall regime. The question arises as to whether and which characteristics the transitory regime and the corner separation instability have in common.

Chapter 3

Experimental and analysis methods

Contents

3.1 Introduction 62

3.2 The test rig 63

3.2.1 Blades 64

3.2.2 Cascade 66

3.3 Inlet measurements 68

3.3.1 Free flow characterization 68

3.3.2 Inlet profile characterization 69

3.4 Instrumented blade for pressure measurements 71

3.5 Steady pressure measurements on the blade 73

3.5.1 Experimental set up 73

3.5.2 Steady pressure coefficient and uncertainty 73

3.6 Time-resolved pressure measurements on the blade 74

3.6.1 Microphones 74

3.6.2 Calibration 76

3.6.3 Data acquisition 78

3.6.4 Data reduction 78

3.6.5 Uncertainty 79

3.7 Five hole pressure measurements 84

3.7.1 Experimental set up 85

3.7.2 Calibration and data reduction 86

3.7.3 Uncertainty 88

3.8 Time-resolved total pressure measurements 89

3.8.1 Experimental set-up 89

3.8.2 Uncertainty 91
3.9 Time-resolved Particle Image Velocimetry (HS-PIV) 92
3.9.1 Experimental set-up 92
3.9.2 Calibration 94
3.9.3 Convergence 95
3.9.4 Uncertainty 95
3.10 Stereo Particle Image Velocimetry (SPIV) 99
3.10.1 Experimental set up 99
3.10.2 Calibration 99
3.10.3 Uncertainty 100
3.11 Signal treatments and analysis methods 102
3.11.1 Average 102
3.11.2 Standard deviation and fluctuation Root Mean Square 103
3.11.3 Skewness 104
3.11.4 Kurtosis 104
3.11.5 Correlations 105
3.11.6 The Fourier transform 106
3.11.7 The power spectral density 106
3.11.8 Coherence function 107
3.11.9 Wavelet transform 107
3.12 Test rig adjustment 109
3.12.1 Parameters of sensitivity of the cascade 109
3.12.2 Symmetry and periodicity 110
3.13 Inlet boundary layer verification 114
3.14 Conclusions 119

3.1 Introduction

At first, this chapter presents the geometry of the linear cascade, blades and details of the new blade developed for time-resolved pressure measurements. Then, the experimental set up, data acquisition process and uncertainty are discussed for steady pressure measurements, inlet flow characterization, time-resolved pressure measurements, stereo-PIV and time-resolved 2D2C PIV measurements. Signal treatment methods exploited in the data analysis are successively presented in Section 3.11. The final two sections of the chapter discuss the adjustment of the test rig and the inlet boundary layer related to the sensitivity of the set up of the cascade to periodicity, symmetry and repeatability of the measurements. Such results are additionally compared with previous results obtained in the work of Ma (2012).

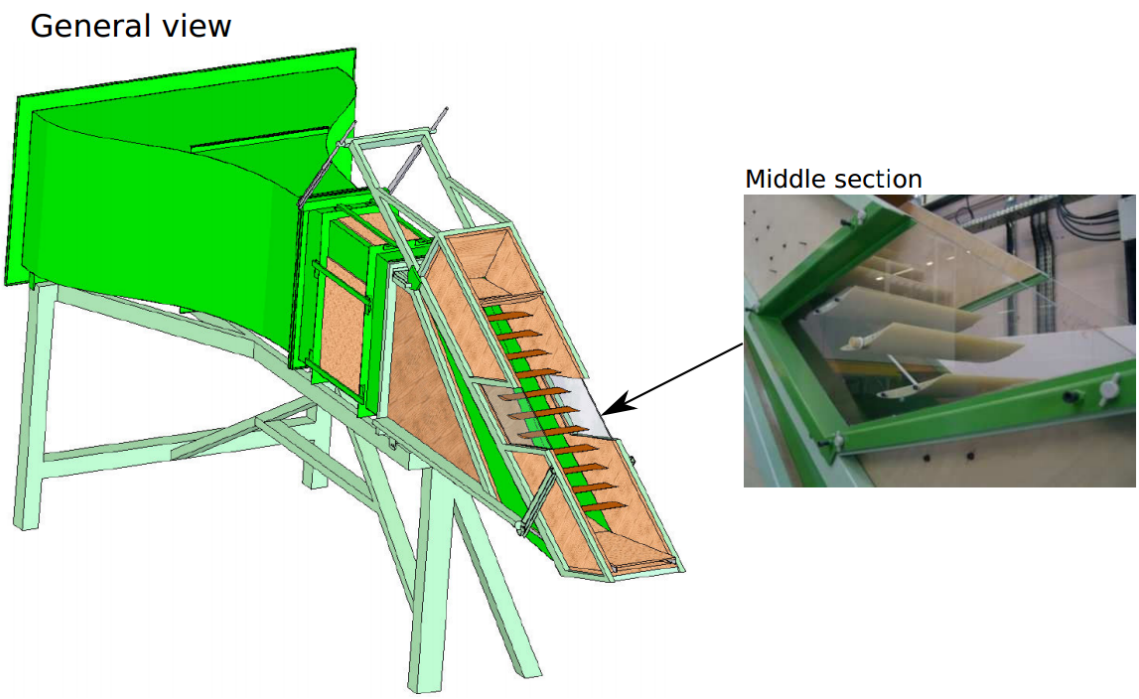

Fig. 3.1 General view of the cascade at LMFA

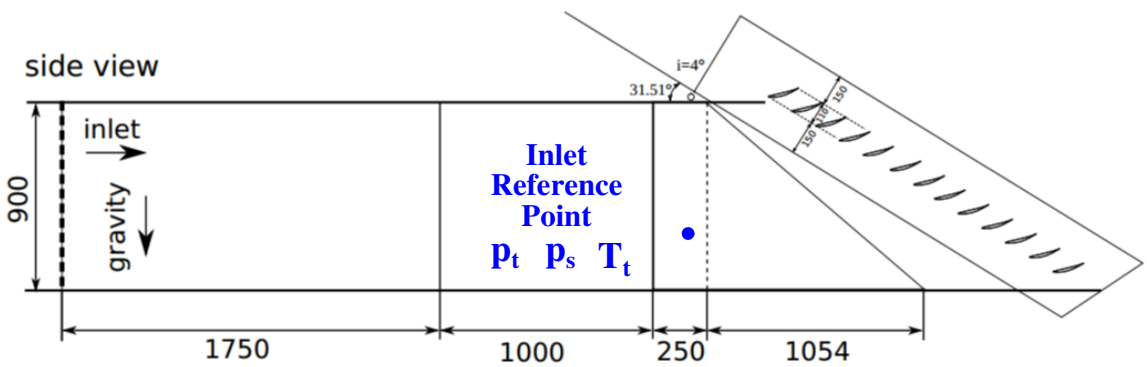

Fig. 3.2 Side view of the cascade and location of the reference point for inlet measurements.

3.2 The test rig

The present investigation is carried out on a low speed cascade wind tunnel. The facility is powered by a 60 KW centrifugal blower and the test section is a rectangular duct with a cross-section of 900 mm high by 370 mm wide. Figures 3.1 and 3.2 show the cascade and the test section, respectively.

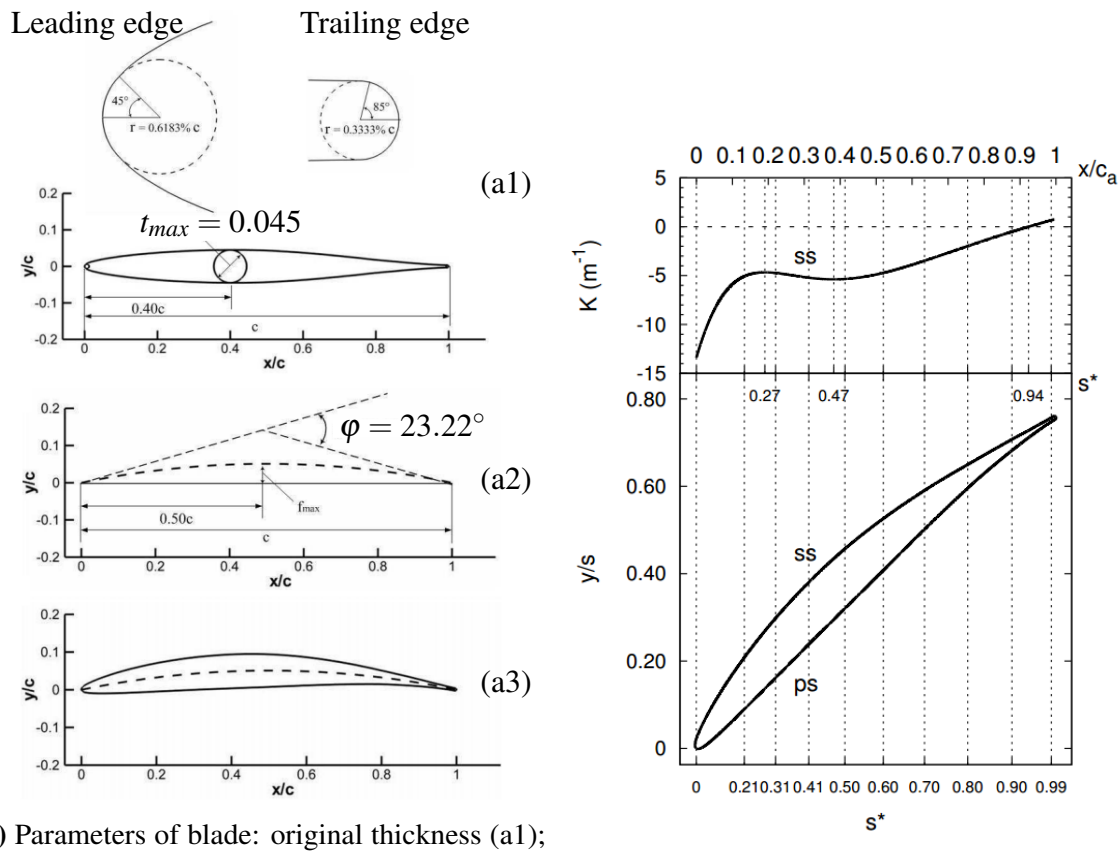

(a) Parameters of blade: original thickness (a1); mean chamber line (a2); cross-section (a3)

(b) Curvature of the blade suction side

Fig. 3.3 Blade geometry

3.2.1 Blades

The cascade consists of 13 blades. The original thickness distribution of the blade profile is NACA 65-009, airfoil coordinates reference in NACA Report Abbott et al. (1945).

Airfoil parameters

According to the convention for NACA airfoils, the digits give the following information.

- The first digit “6” simply represents the series name.
- The second digit “5” indicates, in the basic symmetrical airfoil version at the zero-lift position, that the location of the airfoil minimum pressure is at 50% of the chord from the leading edge. The maximum airfoil thickness is located at 40% chord.
- The final two digits “09” indicate that the maximum airfoil thickness is 9% of the chord.

The blade has circular leading and trailing edges. The radii are 0.6183% and 0.3333% of the chord, respectively. The original thickness distribution of the blade is given in Table 3.1

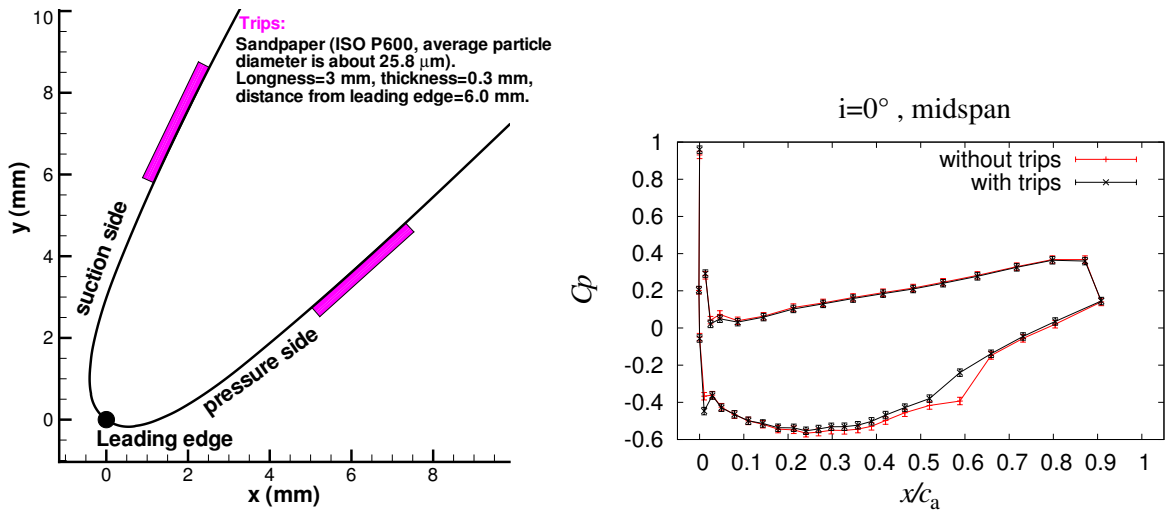

(a) (b)

Fig. 3.4 Figure (a): position of the trips at the LE of blade. Figure (b): influence of the presence of the trips on pressure distribution on the blade at midspan, $i = 0°$, reproduced from Ma (2012).

Table 3.1 NACA 65-009 airfoil half thickness in blade coordinate.

$x(\%c)$	$y(\%c)$	$x(\%c)$	$y(\%c)$	$x(\%c)$	$y(\%c)$	$x(\%c)$	$y(\%c)$
0	0	10	2.7360	45	4.4667	80	1.7883
0.5	0.6948	15	3.2994	50	4.3308	85	1.2465
0.75	0.8388	20	3.7287	55	4.0770	90	0.7290
1.25	1.0521	25	4.0527	60	3.7314	95	0.2754
2.5	1.4166	30	4.2840	65	3.3138	100	0
5.0	1.9593	35	4.4316	70	2.8404	L.E.R.	0.6183
7.5	2.3823	40	4.4964	75	2.3256	T.E.R.	0.3333

and plotted in Figure 3.3a1. The mean camber line is a circular arc, as depicted in Fig. 3.3a2, and the camber angle φ is 23.22°. Coordinates for the blade cross section are plotted in Fig. 3.3a3.

Blade curvature

The curvature of the blade suction side $K = 1/R$, with R as the curvature radius referring to the degree of bending, is one of the most important parameters. The curvature of the suction side is shown in Fig. 3.3b as a function of $s^* = s/L$, where s is the length of arc from the leading edge to the measurement location and L is the length of arc from the leading edge to the trailing edge. From the leading edge, K initially increases for values $0 < s^* < 0.27$, then slightly decreases in the range $0.27 < s^* < 0.47$ and finally increases monotonically

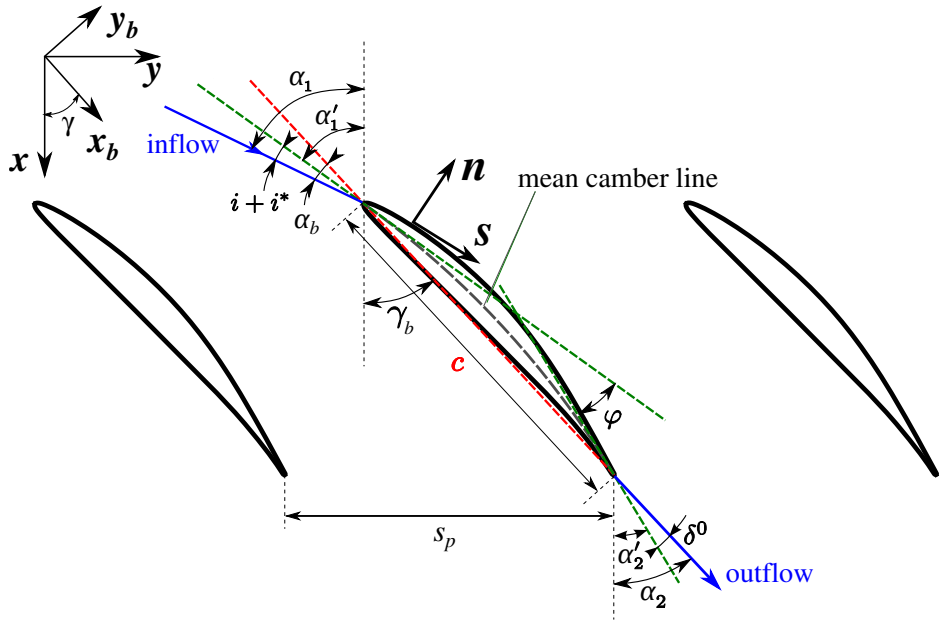

Fig. 3.5 Cascade coordinates and parameters. Cascade reference system (x,y,z), blade reference system (x_b,y_b,z), curvilinear coordinates (s,n,z).

until the trailing edge, i.e. for values $0.47 < s^* < 1.00$. Since K is equal to zero at $s^* = 0.94$, smaller than zero in the range $0 < s^* < 0.94$ and larger than zero for $0.94 < s^* < 1.00$, the blade suction side is *convex* where $0 < s^* < 0.94$, and is *concave* where $0.94 < s^* < 1.00$. Furthermore, the curvature values are larger in the former part, $0 < s^* < 0.70$, then in the latter part, $0.70 < s^* < 1.00$.

3.2.2 Cascade

Parameters of the cascade

The notation used to describe the LMFA subsonic compressor cascade is shown in Fig. 3.5. The stagger angle of the cascade $\gamma_b = 42.7°$. From the relations between the angles, the designed inlet angle of the flow α_1' is 54.31°. The designed outlet angle of the flow α_2' is 31.09°. The chord length c, the span h and the spacing (or pitch) s_p of the blade are 150 mm, 370 mm and 134 mm, respectively. This implies that the aspect ratio is $AR = 2.47$ and solidity is $\sigma_b = 1.12$. The parameters of the cascade are summarized in Table 3.2.

Transition trips

In order to ensure and fix the location of the boundary layers transition, which leads to large consequences on the corner separation as discussed in Section 1.5, both suction and pressure side of each blade were equipped with sandpaper transition trips at a distance of 6.0 mm from the apex of the leading edge. The width in streamwise direction and thickness of the

Table 3.2 Parameters of the cascade.

Symbol	Name	Magnitude	Relation
c	Chord	150.0mm	
L	Length of arc from LE to TE	153.7mm	
φ	Camber angle	23.22°	
γ_b	Stagger angle	42.7°	
s	Pitch	134.0mm	
h	Blade span	370.0mm	
σ_b	Solidity	1.12	$\sigma = c/s$
AR	Aspect ratio	2.47	$AR = h/c$
i	Incidence angle	4° and 7°	
γ_c	Cascade adjustment angle	31.5° and 28.5°	
i^*	Optimum incidence (Lei et al., 2008)	0.18°	
α_1'	design upstream blade angle	54.31°	$\alpha_1' = \gamma_b + \varphi/2$
α_1	upstream flow angle		$\alpha_1 = \alpha_1' + i + i^*$
α_2'	design downstream blade angle	31.09°	$\alpha_2' = \gamma_b - \varphi/2$
α_2	downstream flow angle		$\alpha_2 = \alpha_2' + \delta^0$
δ^0	flow deviation angle		
θ_{12}	flow turning angle		$\theta_{12} = \alpha_1 - \alpha_2 = \varphi + i + i^* - \delta^0$
V_∞	Free stream velocity	40.0m/s	
Ma_∞	Free stream mach number	0.12	
Tu_∞	Free stream turbulent level	0.8%	
Re_c	Chord-based Reynolds number	3.82×10^5	
h_{LE}	LE blade thickness % c	1.236	
h_{TE}	TE blade thickness % c	0.666	

sandpaper are 3.0 mm and 0.3 mm, respectively. The grid size of the sandpapers is ISO P600 (average particle diameter is about 25.8 μm). The sketch of trips is shown in Fig. 3.4a.

Imposing the transition at the leading edge of the blade permits to achieve a fully turbulent boundary layer on the blade and to avoid the laminar separation bubble, which would be present without trips. A fully turbulent flow is necessary to be consistent with the majority of flows encounter in real compressors, as stated by Evans (1971). Except for fan and first stages of booster, rear stages experience a fully turbulent incoming flow due to the high turbulence level in the free stream induced by front stages wakes and separations. A comparison between the case fully turbulent and the case affected by laminar-turbulent transition on the present cascade can be gathered by drawing the pressure distribution on the blade at midspan for $i = 0°$ as in Fig. 3.4b, reproduced from the work of Ma (2012). The C_p discontinuity at in the region $0.5 < x/c_a < 0.7$ highlights the transition region where the laminar bubble accelerates the flow above and consequently diminishes the pressure recovery.

3.3 Inlet measurements

The inlet flow was characterized by four types of measurements, described in this section. Concerning the time average characterization, total pressure $p_{t\infty}$, static pressure $p_{s\infty}$ and total temperature $T_{t\infty}$ were acquired at the reference position, as shown in Fig. 3.2, during every measurement. Additionally, hot-wire measurements were carried out in order to characterize the turbulence level and the unsteady state of the inlet boundary layer upstream of the reference blade.

3.3.1 Free flow characterization

Total and static pressures

A Pitot probe was used to measure the inlet total pressure $p_{t\infty}$ and inlet static pressure $p_{s\infty}$. Successively, this device was replaced by a total pressure probe placed at the same position, whereas the static pressure was acquired by a tap on the right end-wall of the test rig placed in front of the blade row. The exact position of such tap was carefully chosen in order to have the same magnitude of the static pressure as the previous Pitot measurements. Using vinyl tubes, both inlet pressures were connected to VALIDYNE Model DP45-×× electronic differential pressure transducer (the number after the dash "××" indicates the correct range according to the DP45 data sheet). Then the pressures were monitored using Carrier Demodulators, which have an output voltage range of ± 10 V. The transducer output voltage was recorded by a NIcDAQ-9172 data acquisition system through a NI 9205. All the data were acquired and controlled by LabVIEW software. The measured pressures are differential quantities, so the read values are differences between the total and static absolute pressure and the atmospheric pressure.

Total temperature

A thermocouple was used to measure the total temperature of the flow $T_{t\infty}$. The probe is connected with the National Instruments thermocouple input module NI 9211, then the output voltage is recorded by the National Instruments data acquisition card NI cDAQ-9172. The uncertainty in the temperature measurement is about 1°.

Data reduction

The inlet total, static pressure and total temperature were simultaneously acquired during every measurements. This permits to calculate the dynamic pressure q_∞, the density of the flow, the Reynolds number and the Mach number as resumed in the following equations.

1. Static temperature

$$T_{s\infty} = T_{t\infty} \left(\frac{p_{t\infty}}{p_{s\infty}} \right)^{-\frac{k-1}{k}} \qquad k = 1.4 \tag{3.1}$$

2. Mach number

$$M_\infty = \sqrt{\frac{2}{k-1}\left[\left(\frac{p_{t\infty}}{p_{s\infty}}\right)^{\frac{k-1}{k}} - 1\right]} \tag{3.2}$$

3. Velocity of sound

$$c_\infty = \sqrt{k\,R\,T_{s\infty}} \qquad R = 287.06\ \mathrm{J/(kgK)} \tag{3.3}$$

4. Velocity

$$V_\infty = M_\infty\, c_\infty \tag{3.4}$$

5. Density

$$\rho_\infty = \frac{p_{s\infty}}{R\,T_{s\infty}} \tag{3.5}$$

6. Viscosity (Sutherland formula)

$$\mu_\infty = 1.7161 \times 10^{-5}\left(\frac{T_{s\infty}}{273.16}\right)^{1.5}\left(\frac{273.16+124.0}{T_{s\infty}+124.0}\right) \tag{3.6}$$

7. Reynolds number

$$\mathrm{Re}_\infty = \frac{\rho_\infty\, V_\infty\, L}{\mu_\infty} \tag{3.7}$$

3.3.2 Inlet profile characterization

The inlet profile was characterized by constant temperature anemometer hot-wire measurements upstream of the reference blade. The Dantec 55P05 probe was chosen since the head of the sensor is specifically designed for boundary layers investigations. The shape of the prongs permitted measurements close to the wall without disturbing the flow with the blockage induced by the steam of the probe. This was indeed installed with an angle of 20° in spanwise direction on a support moved by a computer controlled traverse system. The active length and diameter of the wire are $l = 1$ mm ($l^+ = lu_\tau/\nu = 100$) and $d = 4\ \mu$m, respectively. These characteristics verify $l/d > 200$, which is the condition to respect in order to avoid conduction errors.

The transverse system permitted the spanwise translation as well as the rotation of the probe in order to adjust the angle of the probe to place the wire perpendicular to the incoming flow. When investigating regions very close to the wall, a control of the probe position was set by the same methodology used in the previous work by Ma (2012). An electric circuit was created by placing a conduction tape on the endwall in the location of the approach of the probe. This tape was connected to a battery which provided the tension to the circuit. On the other hand the probe also was a part of the circuit, since the hot wire is alimented by a tension at its ends, and it was used as a switch device. The measurement of the inlet profile were started at midspan moving toward the endwall step by step. The voltage measured in this case was constant and it was the half of the battery voltage. When approaching the

endwall at distances that tend to zero, the wire of the probe interacted with the tape placed on the endwall and the voltage measured by the voltmeter reached zero, implying that the hot-wire probe was touching the endwall.

Calibration

The probe was calibrated in a separated calibration facility by placing the sensor and its support within the potential cone of a jet flow. The first step was the adjustment of the Wheatstone bridge of the anemometer to the specific characteristics of the sensor, determining its resistance. Successively, the calibration of the output tension E against the variation of the jet velocity V_{jet} was performed in order to obtain the calibration constants C of the polynomial fit, see Eq. 3.8.

$$V_{jet} = C_0 + C_1 E + C_2 E^2 + C_3 E^3 + C_4 E^4 \tag{3.8}$$

Data reduction

The acquired signal E_a on the compressor cascade was at first re-scaled by gain G and offset E_{offset} of the anemometer, see Eq. 3.9. Then the temperature correction was applied in order to take into account the difference between the temperature of the flow in the test rig T_a and during the calibration procedure T_w.

$$E(t) = \frac{E_a(t)}{G} - E_{offset} \tag{3.9}$$

$$E_{corr}(t) = E(t)\sqrt{\frac{T_w - T_{ref}}{T_w - T_a}} \tag{3.10}$$

$$T_w = T_{ref} + \frac{a}{\alpha_0} \qquad a = \frac{R_w - R_{ref}}{R_{ref}} \tag{3.11}$$

In the previous equations a is the overheat ratio ($a = 0.8$ in our experiment), R_w is the sensor resistance at operating temperature T_w during the calibration, R_{ref} is the resistance at the ambient (reference) temperature T_{ref} during the calibration. The coefficient $\alpha_0 = \alpha_{20^\circ} = 0.36\%$ is the sensor temperature constant of the probe 55P05 due to the resistance at the ambient (reference) temperature T_{ref}.

Finally the corrected voltages were used in the calibration transfer function in order to obtain the instantaneous velocity signal, as in Eq.3.12.

$$V(t) = C_0 + C_1 E_{corr}(t) + C_2 {E_{corr}}^2(t) + C_3 {E_{corr}}^3(t) + C_4 {E_{corr}}^4(t) \tag{3.12}$$

Uncertainty

The uncertainty of the hot wire measurements is detailed in the work of Ma (2012). Outside the boundary layer, the typical input data are: $T_w - T_0 = 225^\circ$ C, $V = 40$ m/s, $\partial V/\partial E = 40.0$

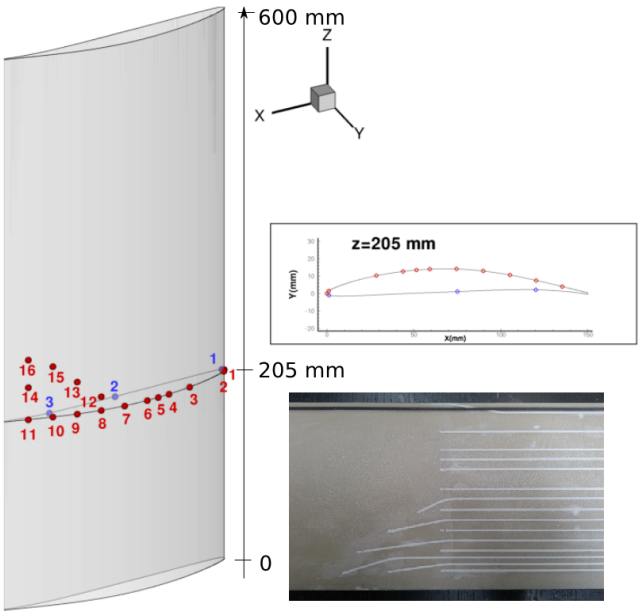

(a) Position of pressure taps

(b) Blade-II instrumented with microphones

Fig. 3.6 Instrumented Blade-II details.

m/(s Volt). By accounting for the relative errors e_{sys_i} of calibration, linearization, A/D resolution, probe positioning (negligible), temperature variations, ambient pressure and humidity (negligible), a sum of the final relative error can be estimated as in Eq. 3.13.

$$e_{sys}(V) = 1.96 \cdot \sqrt{\sum (e_{sys_i})^2} \approx 0.02 = 2\%. \tag{3.13}$$

The final absolute uncertainty on mean velocity both in the free stream and boundary layer is hence $\varepsilon(V) = 1$ m/s. Finally, the relative uncertainty in velocity fluctuations outside the boundary layer is about $e(u') = 4$ % whereas in the boundary layer, it increases gradually by approaching the endwall because the velocity tends to zero.

3.4 Instrumented blade for pressure measurements

In the previous work of Ma (2012), a blade equipped with forty pressure taps was used in order to characterize the pressure distribution C_p on the surface of the blade and to investigate its variation as a function of nominal incidence imposed to the blade row. This blade is referred in the present work as Blade-I. Then a new blade with the same external geometry was developed in order to allow the investigation of unsteady pressure fluctuations on the surface at the same time that steady pressure levels. This blade is named in the present work as Blade-II.

The Blade-II was specially designed in collaboration with the LMFA acoustic team based on the remote microphone technique for disk antenna described by Salze et al. (2014). The

Table 3.3 Coordinates of pressure taps on the Blade-II in blade coordinates.

Suction side				
N.	$s^* = s/L$	x [mm]	y [mm]	z [mm]
1	0	0.00	0.00	205
2	0.01	1.00	1.56	205
3	0.2	28.47	10.28	205
4	0.3	43.71	12.73	205
5	0.35	51.39	13.52	205
6	0.4	59.1	14.03	205
7	0.5	74.54	14.14	205
8	0.6	89.93	12.95	205
9	0.7	105.2	10.69	205
10	0.8	120.33	7.56	205
11	0.9	135.37	4.05	205
12	0.6	89.93	12.95	220
13	0.7	105.2	10.69	240
14	0.9	135.37	4.05	240
15	0.8	120.33	7.56	260
16	0.9	135.37	4.05	270
Pressure side				
N.	$s^* = s/L$	x [mm]	y [mm]	z [mm]
1	0.01	1.10	-0.93	205
2	0.5	74.93	1.13	205
3	0.8	120.17	2.22	205

length of the entire blade is 605 mm and nineteen miniaturized tubes are incorporated within its body. Pressure signals are carried from the surface of the blade to an external side part of the blade, as illustrated in Fig. 3.6, where nineteen perpendicular cavities are fitted for microphone plugging. The ensemble of each miniaturized tube, plus the plugged microphone, plus the connecting wire from the microphone to the acquisition system is called *Channel* in the present work. Three taps on the pressure surface and sixteen on the suction surface are shown in Fig. 3.6a. These taps are not equally spaced neither in stremwise nor in spanwise direction, but are placed strategically at the LE, at positions where bimodal velocities are expected, and in the separated region. Their coordinates are summarized in the Table 3.3. The miniaturized tubes continue straight outside the blade and are connected to nineteen 2.5 m vinyl tubes. The internal geometry of the tubes is sketched in Fig. 3.7. Particular step-like modifications of the size of channel were manufactured to avoid resonances of proper modes of the ducts but calibration was anyhow necessary to correct the acquired signal by plugged microphones.

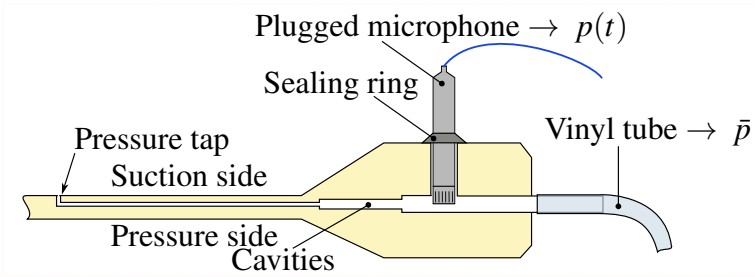

Fig. 3.7 Sketch of cavities geometry within the blade and plugged microphones.

3.5 Steady pressure measurements on the blade

3.5.1 Experimental set up

The pressure taps on instrumented blades were connected to a Scanivalve through the nineteen vinyl tubes. The output of the Scanivalve's exit channel was connected to a Validyne pressure transducer. Finally, the acquisition was done in the same fashion that for total and static pressure at the inlet. The demodulators were calibrated by imposing a reference pressure in order to adjust gain and offset. Therefore, the bias error in the steady measurements due to the acquisition chain can be considered negligible compared to the random error.

3.5.2 Steady pressure coefficient and uncertainty

The static pressure coefficient distribution on the blade surface is defined as follows.

$$C_p = \frac{p_s - p_{s_\infty}}{p_{t_\infty} - p_{s_\infty}} \tag{3.14}$$

The uncertainty in the calculation of the steady pressure coefficient on the blade are determined according to the propagation law of uncertainties. Only the statistical error is taken into account in the Eq. 3.15, since the bias error due to the acquisition system, the demodulators and the pressure traducers is negligible.

$$\varepsilon_{Cp}^2 = \left(1.96\frac{\partial Cp}{\partial p_s}\sigma_{p_s}\right)^2 + \left(1.96\frac{\partial Cp}{\partial p_{t_\infty}}\sigma_{p_{t_\infty}}\right)^2 + \left(1.96\frac{\partial Cp}{\partial p_{s_\infty}}\sigma_{p_{s_\infty}}\right)^2 \tag{3.15}$$

where:

$$\frac{\partial Cp}{\partial p_s} = \frac{1}{p_{t_\infty} - p_{s_\infty}} \qquad \frac{\partial Cp}{\partial p_{s_\infty}} = \frac{p_s - p_{t_\infty}}{(p_{t_\infty} - p_{s_\infty})^2} \qquad \frac{\partial Cp}{\partial p_{t_\infty}} = \frac{p_s - p_{s_\infty}}{(p_{t_\infty} - p_{s_\infty})^2} \tag{3.16}$$

Three channels are chosen in order to give representing value of uncertainty: Channel 1 at the LE, Channel 4 at the boundary of the separation and Channel 9 in the aft part part of the blade within the separation. Absolute and relative values are summarized in Table 3.4. The absolute uncertainty is higher near the LE due to the high level of pressure fluctuations

Table 3.4 Random error for the calculation of steady Cp on the suction surface of the blade for channels 1, 4 and 9.

	Endwall $z/c = 0.033$		Midspan $z/c = 1.23$	
Channel	Absolute error	Relative error	Absolute error	Relative error
Ch 1	0.073	7.8%	0.048	31.5%
Ch 4	0.035	26.9%	0.025	6.0%
Ch 9	0.016	12.9%	0.018	26.7%

induced by the unsteady movement of the stagnation point. The absolute values are larger at the LE and then progressively decrease moving toward the TE of the blade, both near the endwall and at midspan. Conversely, the relative values are influenced by the C_p value of the normalization, which can cross the zero leading to high relative errors.

3.6 Time-resolved pressure measurements on the blade

The unsteady static pressure on blades is usually one of the most challenging quantities to measure because it requires time-resolved sensor which can reach the investigated regions of the field without perturbing the flow. In the present work the microphones were plugged at the end of the Blade-II, as shown in Fig. 3.7, to sense the unsteady pressure fluctuations, which are carried from the surface to the sensor through miniaturized tubes.

In the present section the characteristics of such a measurement technique and the associated issues are clarified. Among others, the calibration of the system tube-probe is necessary in order to obtain the correct transfer function to apply to the raw data. The uncertainty related to these manipulations is also estimated by a specifically developed method.

3.6.1 Microphones

The microphones utilized for the unsteady pressure measurements on the surface of the blade are Bruel&Kjaer $\frac{1}{4}''$ polarized condenser microphones type 4935. These sensors are free-field microphones, so they have a uniform frequency response for the measurement of the free-field pressure. Even if microphones are best suited to sense a front signal, they can be used in flush mounted configuration as in the work of Marsden et al. (2012).

Peculiarities of the condenser microphones are high stability, plate frequency response in a wide frequency range, low distortion, low internal noise and high sensitivity in a wide dynamic range.The dynamic range of a microphone is the interval between the minimum and the maximum of the measurable sound pressure level. The lower limit is determined by the noise of electrical nature within the preamplifier and the thermal noise is due to thermal agitation of the diaphragm. The upper limit is given instead by the limit of distortion of the entire system. Beyond this limit nonlinear phenomena cause unacceptable accuracy.

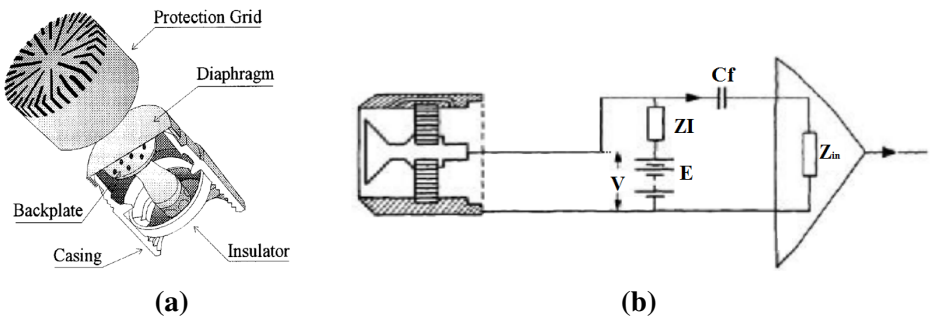

Fig. 3.8 Sketch of a condenser microphone (a) and electric scheme of an external polarized microphone (b)

Working mechanism

The sensitive element of the microphone is the diaphragm which vibrates if subjected to pressure fluctuations as an acoustic field. A metallic plate, called back-plate, is parallel to the diaphragm forming a capacitor in air. Most of the microphones have a small hole of high acoustic impedance that permits to expose and equalize the inner cavity to the ambient pressure in order to prevent damage due to high pressure variations. When the diaphragm vibrates, the capacitance varies, reproducing the pressure variations by output tension variations. The B&K microphones used in present measurements are equipped with a front-face equalizing hole instead of a bottom venting hole. This choice was especially preferred in order to prevent pressure leakages through back venting hole necessarily located outside the sealing ring.

The B&K 4935 are externally polarized , i.e. alimented by a generator of continue current provided by the chassis. The system diaphragm-backplate is hence charged by the generator E with a high impedance ZI in order to have a combination capacity-dynamic response faster than the period of the acoustic waves. In this way the value of the current in the circuit can be considered negligible whereas the charge Q of the capacitor can be considered constant. The output tension from the capacitor is therefore a linear relationship of the displacement Δd as in Eq. 3.17.

$$V = \frac{Q}{C} = \frac{Q}{\varepsilon A} d \quad \Longrightarrow \quad \Delta V = \frac{Q}{\varepsilon A} \Delta d = k \Delta d \tag{3.17}$$

$C =$ capacity [Farad]
$\varepsilon =$ air dielectric constant [-]
$A =$ area of overlap of the two plates $[m^2]$
$d =$ separation between the plates $[m]$
$k =$ constant value

The continuous component of the signal is filtered by the capacitor C_f and the fluctuating component, amplified by the preamplifier, is sent to the acquisition system.

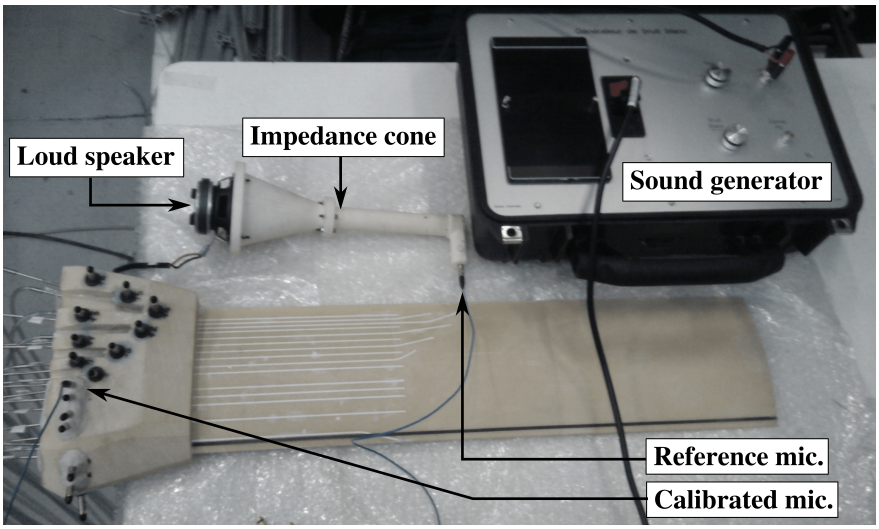

Fig. 3.9 Microphone calibration instruments: sound generator and impedance cone utilized in the calibration of each channel of the blade.

Frequency range

Microphones with high sensitivity have narrow ranges of frequency because these two characteristics are in competition and are function of the size of the microphone. In general bigger probes have high sensitivity but narrowed frequency range. For the B&K $1/4$, nominal values of low and high cut frequency are respectively 10 Hz and 50 KHz with a sensitivity of about 3 mV/Pa. These nominal values usually differ from the real values, which depend on the specific experimental set up and which can be known solely by performing the calibration of each sensor mounted on the blade. In particular, the low cut frequency depends on the size of the venting hole because a part of the acoustic waves can penetrate into it and can hamper the movement of the diaphragm. Concerning the present instrumentation equipped of front-face equalizing hole, the specific calibration showed that a continuous smooth transfer function can be obtained starting from low-cut frequency of 3 Hz. Additionally, even if the nominal high-cut frequency of the B&K 4935 is $f = 50$ KHz, the calibration showed that the limit of acceptable higher frequency is reduced to 12 KHz because of the resonances within the cavities of the blade. In conclusion, the widest frequency range considered in this work is comprised between 3 Hz and 12 KHz, but high uncertainty is associated to the low frequencies, as discussed in further Section 3.6.5.

3.6.2 Calibration

The calibration of each microphone was necessary because of the geometry of the blade and the presence of cavities between the pressure taps and the microphones. Each channel was carefully calibrated before measurements without removing or changing the position of any microphone. The utilized procedure is standard and examples of studies involving the same methodology can be found in literature, as Dickens et al. (2007) and Lee and Sung (1999).

The basic principle of microphones calibration for aeroacoustic measurements is to send a white noise signal to two sensors at the same time. One of the two sensors is the plugged microphone of the channel which has to be calibrated, the second sensor is called reference microphone and is placed on the tap of the channel. When the same signal is sensed by the two sensors ensuring a coherence between them, i.e. without leakages or distortions which are not due to the effective geometry of the channel, it is possible to establish a relationship between the modified output of the channel and the correct output of the reference sensor. This relationship is called transfer function and it permits to reconstruct the correct signal as the pressure wave would be sensed directly on the surface of the blade if there were not cavities and protecting grids of the sensors plugged into the blade.

Calibration set up

The impedance matching cone utilized in the calibration was instrumented with a reference condenser microphone perpendicularly plugged to the lower cylindrical part of the cone and without protective grid. A loudspeaker powered by a sound generator was placed at the top of the cone, generating the white noise pressure wave which sweeps the entire frequency range. The cone was placed on each tap on the blade surface paying attention to avoid leakages. The sensitivity of the reference microphone was sensed by a pistonphone, which uses a closed coupling volume to generate a precise sound pressure wave for the calibration of microphones. Both output signals from the channel and from the reference sensor were acquired at $f_s = 102.4$ KHz for $t_s = 20$ sec in order to average the transfer functions. Several acquisition were carried out for each channel of the blade in different configurations and surrounded conditions, in order to avoid all the spurious effects due to random environmental noises.

The transfer function

The transfer function between the output of the reference microphone $x(t)$ and the output of the sensor microphone $y(t)$ in a linear time invariant system can be estimated as proposed by Mueller (2002):

$$H(f) = E\left[\frac{\tilde{\Phi}_{yy}(f)}{\tilde{\Phi}_{xy}(f)}\right] \tag{3.18}$$

where:

$x(t)$ = output of reference microphone =input of $H(f)$
$y(t)$ = output of microphone to calibrate =output of $H(f)$
$E[.]$ = expected value = mean converged value
Φ_{yy} = autospecrtum of $y(t)$
Φ_{xy} = cross-spectrum between $x(t)$ and $y(t)$
$\tilde{\Phi}$ =estimation based on the discrete time series with finite record length of spectrum

The complex transfer function is then divided in the rate of amplitude $A(f)$ and the phase retard $\phi(f)$ between the two signals. During the calibration, the coherence function between the sensor of the channel and the reference sensor was simultaneously performed and

visualized by the acquisition program. Coherence values of 1 were obtained in the frequency range exploited for measurements assuring the accuracy of transfer function, according to Mueller (2002).

3.6.3 Data acquisition

Static pressure measurements and instantaneous fluctuating pressure measurements were performed at different spanwise sections by sliding the blade into the cascade. Instantaneous signals were acquired for eleven channels on the suction side of the blade at the same spanwise position both on the suction and pressure side of the blade. The acquisition system adopted for such measurements was composed by a 4-slot NI PXI-1031DC chassis supporting three NI PXI 4472 8-channel signal acquisition devices of 24-bit resolution, input signal rage of $\pm$10V and maximum $f_s = 102.4$ KHz. Concerning pressure measurements synchronized with time-resolved PIV, the sampling frequency was set to $f_s = 102.4$ KHz for sampling time $t_s = 1$ sec. This limited sampling time was imposed by the PIV setting as further discussed in Section 3.9. Separate acquisitions for the statistical analysis, spectra and coherence were performed at $f_s = 51.2$ KHz for $t_s = 30$ sec, in order to have meaningful details on the lowest frequencies.

3.6.4 Data reduction

The transfer function has to be applied in frequency domain so the pressure signals were post-processed by Fourier transform, corrected in amplitude and phase and transformed back to signals as time functions (Lee and Sung, 1999). This process called reconstruction is presented as follows.

1. The first step consists to perform the discrete Fourier transform (DFT) of the entire output signal:
$$Y(f_k) = \sum_{n=0}^{N-1} y_n exp\left(-i\frac{2\pi kn}{N}\right) \tag{3.19}$$
where $k = N$ when the FFT algorithm is used.

2. The decomposed transfer function $H(f)$ yields discrete amplitude function $A(f)$ and phase lag function $\phi(f)$ which need to be reflected and interpolated in order to match the k raw coefficients of the DFT. Furthermore, $A(f)$ and $\phi(f)$ were cut within the range of frequencies where the coherence was acceptably equal to unity:
$$A_k(f_{cut}) = I\left[A(f_{cut}), k\right] \tag{3.20}$$
$$\phi_k(f_{cut}) = I\left[\phi(f_{cut}), k\right] \tag{3.21}$$
where $f_{low-cut} < f_{cut} < f_{high-cut}$ with $f_{high-cut} = 12$ KHz and $f_{lowcut} = 3$ Hz, i.e. the characteristic low-cut frequency of the channels.

3. In order to correct the DFT of the raw signal the transformation in polar coordinate was performed, hence:
$$Y(f) = a - ib = r \cdot e^{i\theta} \tag{3.22}$$

4. The transfer function correction was then applied to the raw signal by multiplying the inverted, cut and interpolated amplitude function and adding the cut and interpolated phase-lag function:
$$\begin{cases} B(f_k) = r(f_k) \cdot A_k^{-1}(f_{cut}) \\ \beta(f_k) = \theta(f_k) - \phi_k(f_{cut}) \end{cases} \rightarrow X(f_k) = B(f_k)e^{i\beta(f_k)} \tag{3.23}$$

5. Finally the processed data were returned to Cartesian coordinates and the inverse-discrete Fourier transform was performed, yielding the dynamically corrected time series :
$$x_n = \frac{1}{N}\sum_{n=0}^{N-1} X(f_k) exp\left(i\frac{2\pi kn}{N}\right) \tag{3.24}$$

The power spectral density (PSD) of such reconstructed signals was verified to yield exactly the same values of the PSD achieved directly from raw data and subsequently corrected by applying the amplitude of the transfer function.

3.6.5 Uncertainty

The combined uncertainty for time-resolved measurements can be divided into the statistical, or random, error $\varepsilon_{st}(p)$ and the systematic error $\varepsilon_{sys}(p)$, which is also called bias error. The systematic error is the bias which affects the mean of the measured signal. It is hence necessary to take it into account when evaluating the mean results of a measurement.

The random error not only affects the mean, but also RMS and other higher order statistical moments. However, the random error can be minimized by increasing the number of the acquired samples used to perform the average. Furthermore, when computing the Fourier transform of a time-resolved signal the systematic error is limited to the first amplitude, which corresponds to the mean value. Usually, the Fourier transform is directly calculated on the fluctuating part of the signal, so the bias error is avoided, but the random error still affects the amplitudes of the final spectrum.

The systematic error is due to the spatial positioning error of the probes, the digitizing error and the calibration error .

Systematic error

The major source of bias error for static pressure measurements carried out with the technique of plugging microphone in the blade is due to the calibration error. No direct general relations exist in literature to quantify this error because of the variability in calibration procedures. Furthermore there are random components of error that intervene when performing the calibration. The cone generator is placed manually on the taps of the blade and, for LE taps,

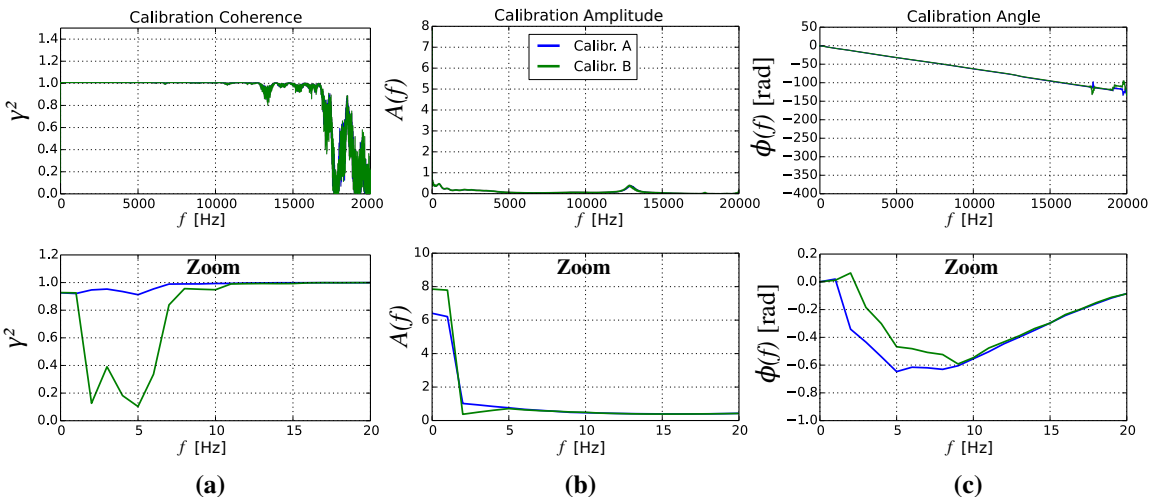

Fig. 3.10 Coherence (a), magnitude (b) and phase angle (c) between calibration A of reference and B for testing. Figures below are respective zooms on the low frequency range.

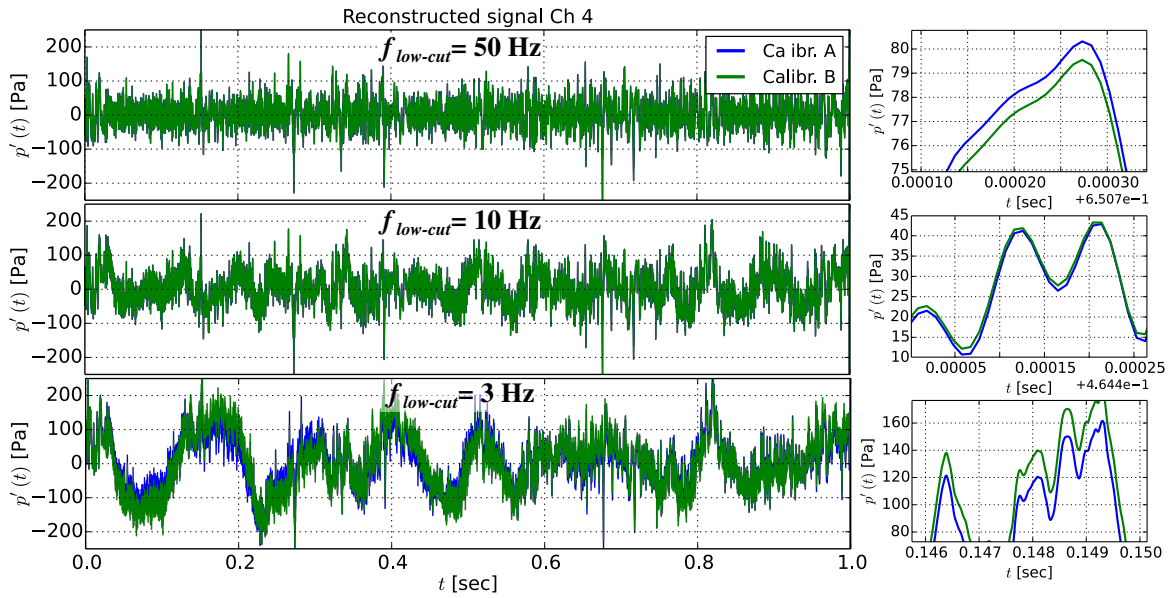

Fig. 3.11 Signals reconstructed for different low-cut frequencies by exploiting calibration A (reference) and B (test). Figures on the right are respective zooms of cases on the left (y-axis adapted).

sealing must be assured in the junction between the cone and the tap. The main parameter used to evaluate the accuracy of the calibration is to verify that the coherence between the sensing and reference microphones tends to 1 across the entire range of interesting frequencies. This is usually verified for these microphones in range of frequencies from 50 Hz to 10 KHz, when sensors are correctly installed. Anyway, the phenomenon investigated in this work is characterized by frequencies lower than 50 Hz, for this reason it is necessary to estimate the error induced by the calibration at these frequencies. Several calibrations were

Table 3.5 Microphones calibration error variation at different low-cut frequencies.

	$f_{low-cut}$ [Hz]	Coherence deficit ICD_{A-B}	Error on fluctuations
Channel 1	50	0.0023	0.3 %
	10	0.1325	1.3 %
	6	0.667	6.8 %
	3	1.291	13.9 %
Channel 4	50	0.0032	0.9 %
	10	0.0784	1.8 %
	6	0.919	10.6 %
	3	3.046	25.0 %
Channel 9	50	0.0025	0.4 %
	10	0.023	0.7 %
	6	0.102	1.26 %
	3	0.684	11.5 %

carried out for each tap before to reach the best one. Here the chosen reference measurement "Calib. A" is compared with a discarded test "Calib. B", which is affected by coherence deficit in the low frequency range.

The magnitude, the phase angle and the coherence against frequency are shown in Fig. 3.10a, Fig. 3.10b and Fig. 3.10c, respectively. The coherence drops between 1 Hz and 11 Hz and clear differences can be seen in the same frequency range for the magnitude and the phase angle. How these differences impact the final signal reconstructed by the process described above in Section 3.6.4 is assessed by using the test calibration to post-process the raw data. Then the obtained result is compared with the pressure signal derived by the reference calibration A. Different low-cut frequencies are tested, so the error originated from coherence deficits can be estimated against different levels of such a lack of coherence.

The Fig. 3.11 shows a comparison between the signals reconstructed with calibration A and B over one second, when the low-cut frequency is varied between 3, 10 and 50 Hz. The discrepancy visible in this figure is quantified and summarized in Table. 3.5, where it is additionally listed the accumulated coherence deficit, which is calculated for each test case by starting from the minimum allowed frequency, i.e. the low-cut frequency. This value can be formulated as the discrete integral in the Eq. 3.25. The error associated to the final pressure fluctuations results to be proportional to the integral coherence deficit.

$$ICD_{A-B} = \sum_{i=f_{low-cut}}^{F} |\gamma_{A_i}^2 - \gamma_{B_i}^2|\Delta f \qquad F = f \; t.c. \; \gamma(f)^2 \rightarrow 1 \tag{3.25}$$

This study permits to estimate the uncertainty associated to the reference calibration for this special case. The integrated coherence deficit penalizing the reference calibration at low frequency of 3 Hz is $ICD_{A-1} = 0.3323$, i.e. if the coherence level is compared to an ideal calibration which would give a coherence value equals to 1 on the entire spectra.

Table 3.6 Relative error on pressure fluctuations for channels 1, 4 and 9 by variation of the low-cut frequency for the reference calibration A.

$f_{low-cut}$ [Hz]	$e_{cal}(p)$ Channel 1	$e_{cal}(p)$ Channel 4	$e_{cal}(p)$ Channel 9
3	6.8%	4.2%	14.5%
10	0.6%	1.5%	0.5%
50	0.32%	1.0%	0.5%

The proportionality between the integrated coherence deficit and the error is applied to the reference calibration permitting to calculate for the Channel 4 the final value $e_{cal}(p) = 4.2\%$.

The resuming Table 3.6 shows the results of the such a process applied to Channel 4 for low cut signals at 3, 10 and 50 Hz, along with same calculations for Channel 1 and Channel 9. The calibration error decreases with the increase of the low cut frequency applied to the signals, because the coherence level tends to 1. Limiting the lower frequency to 50 Hz, the maximum error produced is 1%. Conversely, the error rises when admitting lower frequencies in the signal. The time tracers of signals low cut at 3 Hz will be presented in results of Chapter 5 but a very high uncertainty on the physical meaning of such frequencies exists and can not be quantified. Even if the error on the calibration function can be estimated as shown before, the process of calibration itself for frequencies in the range 3-10 Hz is affected by the inherent uncertainty due to the generator device.

The generator used for the calibration generates acceptable power solely in a range of frequencies comprised between 10 Hz and 20 KHz. Below 10 Hz, the generator power is so attenuated that collateral sources as vibrations or low frequency noise of the environment can generate misleading values of high coherence between the reference sensor and the target sensor. Attention was put to avoid such collateral factors during the calibration process, but the uncertainty due to the lack of power at low frequency of the noise generator is sill high. Furthermore, additional uncertainty is associated to the dynamic response of the condenser due to the filter effect provided by the equalizer hole of the microphone at low frequencies.

Finally, in order to estimate the error on the value of $C_{p_{RMS}}$, defined as $C_{p_{RMS}} = \sigma_p/q_\infty$ (see Section 3.11.2), the absolute calibration error $\varepsilon_{cal}(C_{p_{RMS}})$ can be written as the propagation of the error on fluctuations due to the calibration $\varepsilon_{cal}(\sigma_p)$. This error is calculated as in Eq. 3.26 by applying the relative uncertainty of the calibration estimated for the fluctuations, i.e. $e_{cal}(p)$, to the standard deviation of the pressure fluctuations σ_p.

$$\varepsilon_{cal}(C_{p_{RMS}}) = \frac{\partial C_{p_{RMS}}}{\partial \sigma_p}\varepsilon_{cal}(\sigma_p) = \frac{1}{q_\infty}e_{cal}(p)\sigma_p = e_{cal}(p)\, C_{p_{RMS}} \tag{3.26}$$

The associated relative calibration errors are resumed in Table 3.7, along with the final relative statistical and combined errors discussed below.

Table 3.7 Microphones final relative error contributions $e(C_{p_{RMS}}) = \varepsilon(C_{p_{RMS}})/C_{p_{RMS}}$ for channels 1, 4 and 9, signal $f_{low-cut} = 3$ Hz

	Calibration error	Statistical error	Combined error
Channel 1	6.81%	4.83%	8.35%
Channel 4	4.23%	4.82%	6.41%
Channel 9	14.52%	4.82%	15.30%

Statistical error

The statistical errors associated to the quantities used in the pressure analysis are here provided. Skewness, kurtosis, power spectral density and coherence are defined in Section 3.11. The random error for the pressure coefficient RMS due to the random fluctuations of the pressure is estimated at 95% of confidence as in Eq. 3.27 (Ventsel, 1973). The quantity q_∞ is the dynamic pressure at the inlet, σ_p is the standard deviation of the pressure fluctuations and N is the number of samples.

$$\varepsilon_{st1}(C_{p_{RMS}}) = \sqrt{\sqrt{\frac{2}{N-1}}1.96\frac{\sigma_p}{q_\infty}} \tag{3.27}$$

$$= E(N, q_\infty)\sigma_p \tag{3.28}$$

$$= E(N)C_{p_{RMS}} \tag{3.29}$$

It can be seen that this error is proportional to the level of $C_{p_{RMS}}$ multiplied by the factor $E(N)$, which depends only on the number of samples of the data set.

The global random error $\varepsilon_{st}(C_{p_{RMS}})$ is given by the square sum of the error on the standard deviation of the static pressure fluctuations, as well as the propagation of the variance of static and total pressure at the inlet. The Eq. 3.30 can be written for the calculation of the error, where the derivatives are given in Eq. 3.31. Statistical errors are resumed in Table 3.7, along with the combined errors.

$$\varepsilon_{st}^2(C_{p_{RMS}}) = \varepsilon_{st1}^2(C_{p_{RMS}}) + \left(1.96\frac{\partial C_{p_{RMS}}}{\partial p_{t\infty}}\sigma_{p_{t\infty}}\right)^2 + \left(1.96\frac{\partial C_{p_{RMS}}}{\partial p_{s\infty}}\sigma_{p_{s\infty}}\right)^2 \tag{3.30}$$

$$\frac{\partial C_{p_{RMS}}}{\partial p_{t\infty}} = \frac{\partial C_{p_{RMS}}}{\partial p_{s\infty}} = \frac{\sigma_p}{(p_{t\infty} - p_{s\infty})^2} \tag{3.31}$$

Concerning skewness and kurtosis it is possible to define the standard error of skewness *ses* and the standard error of kurtosis *sek*. These quantities reveal if the distribution is significantly skewed or the kurtosis value is significant, respectively. The *ses* and the *sek* can

Table 3.8 Random error in coherence calculation as a function of the coherence.

$\gamma_{12}{}^2$	0.2	0.4	0.6	0.8
$e_{st}(\gamma_{12}{}^2)$	32.7%	17.3%	9.4%	4.1%

be roughly estimated using the Eq. 3.32, according to Tabachnick and Fidell (1996):

$$ses = \sqrt{\frac{6}{N}} = 0.0019 \quad sek = \sqrt{\frac{24}{N}} = 0.0039 \tag{3.32}$$

If absolute values of skewness and kurtosis are higher than 2 *ses* and 2 *sek*, the distributions can be considered meaningfully affected.

Power spectral densities and coherence are performed utilizing 120 and 60 ensemble sets (N_d) containing 12800 and 25600 data points respectively and the random error estimation can be hence expressed as (Bendat, 1978):

$$e_{st}(PSD) = \frac{1}{\sqrt{N_d}} \qquad e_{st}(\gamma_{12}{}^2) \approx \frac{\sqrt{2}\left(1-\gamma_{12}{}^2\right)}{\gamma_{12}\sqrt{N_d}} \tag{3.33}$$

which gives $e_{st}(PSD) = 9\%$ for power spectral densities and coherence error values estimated in Table 3.8 as function of the coherence itself.

Combined error

The final error on the computed $C_{p_{RMS}}$ is the sum of the statistical error and the calibration error affecting the pressure fluctuations as in Eq. 3.34.

$$\varepsilon^2(C_{p_{RMS}}) = \varepsilon_{st}^2(C_{p_{RMS}}) + \varepsilon_{cal}^2(C_{p_{RMS}})^2 \tag{3.34}$$

The statistical error is calculated as in Eq. 3.30, whereas the calibration error is estimated by Eq. 3.26. Table 3.7 resumes the results for channels 1, 4 and 9.

Whereas the relative statistical error is almost constant on the whole measurement domain, so $e_{st}(C_{p_{RMS}}) = 4.85\% \pm 0.2\%$, the largest error is due to the calibration and the low-cut frequency. When very low frequencies are admitted, the combined error $e(C_{p_{RMS}})$ rises and ranges between 6% and 15%.

3.7 Five hole pressure measurements

The five hole pressure probe was commonly used at the beginning of each campaign of measurements in order to check the correct adjustment of the cascade. The probe and the calibration map are presented below, as well as definitions of the calibrations coefficients. Further details on the methodology, set-up and uncertainty associated to the five hole pressure measurements are exposed in the work of Ma (2012).

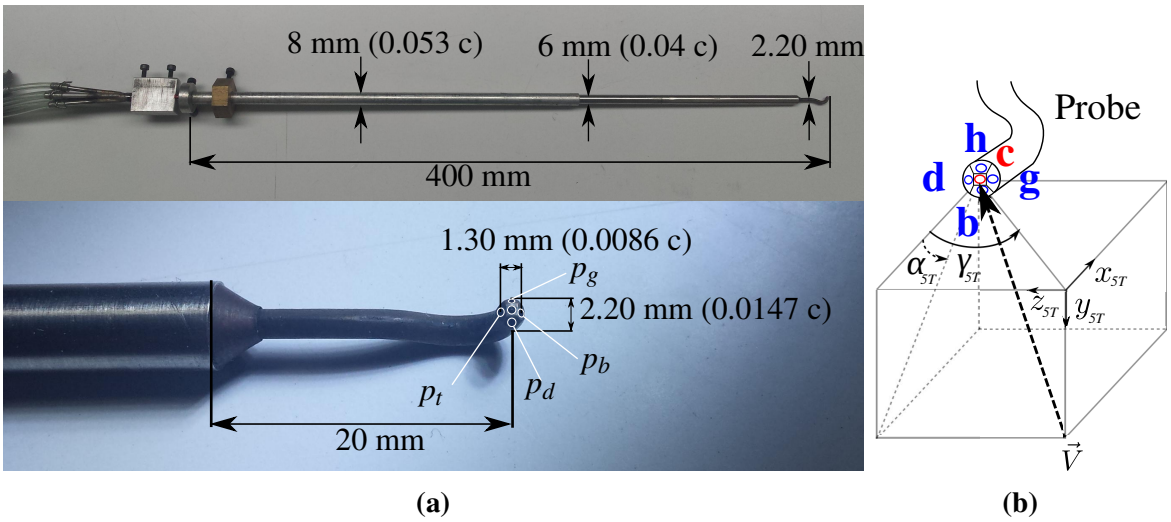

(a) **(b)**

Fig. 3.12 Figure (a): details of the five-hole probe used in the present study. Figure (b): associated angles in the probe coordinates $(x,y,z)_{5T}$.

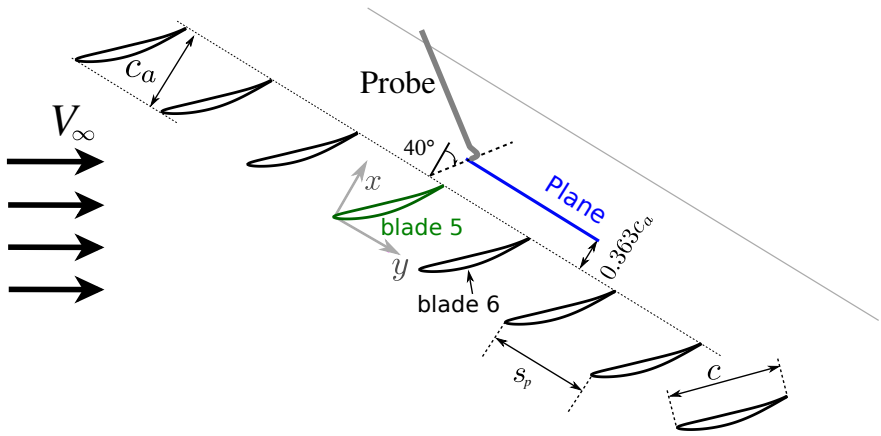

Fig. 3.13 Sketch of the downstream plane where total pressure measurements are performed.

3.7.1 Experimental set up

The five hole probe used in the present study is presented in Fig. 3.12. The diameter of the head of the probe is 2.20 mm or $0.0147c$, the distance between two opposite holes is 1.30 mm and the steam diameter is 8 mm or $0.053c$. The half of the diameter of the steam was the imposed limit of minimum distance achievable near the endwall during the measurements.

The five-hole pressure probe was connected with pressure traducers by 3 m plastic tubes. Consequently, the acquisition time reserved for each point of measurement was 5 sec to let the pressure set properly in the tubes. The plane of measurements sketched in Fig. 3.13 spans from $z = 5$ mm, i.e. $z/c = 0.033$, to midspan. The chosen step in pitchwise direction is 5 mm, i.e. $0.037s_p$, small enough to describe gradients across the wake profile at midspan.

A plane at the same axial distance from the TE is considered in the investigation of the uniformity and symmetry of endwall boundary layers, further presented in Section 3.12.2.

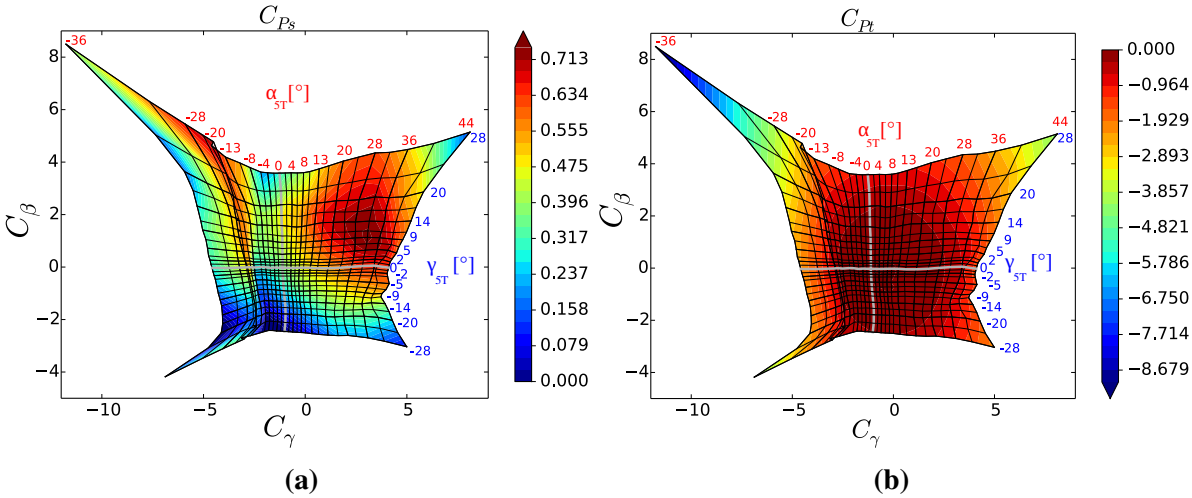

Fig. 3.14 Experimental calibration maps of the five-hole probe for the static pressure coefficient C_{Ps} (a), and the total pressure coefficient C_{Pt} (b).

3.7.2 Calibration and data reduction

At first the calibration was performed in a separated wind tunnel, which is a convergent duct, positioning the probe in the potential cone of the jet. In the process of calibration, the flow was kept at constant mach number $M = 0.121$, whereas the probe was yawed and pitched in the range $-28° < \gamma_{5T} < 28°$ and $-36° < \alpha_{5T} < 44°$ respectively, with angle increments varying between 1° and 3°. The pressures acquired permitted to build the calibration maps shown in Fig. 3.14 by calculating the parameters in Eq. 3.37 at constant velocity.

$$p_{gd} = \frac{p_g + p_d}{2} \tag{3.35}$$

$$C_{\gamma_{5T}} = \frac{p_g - p_d}{p_c - p_{gd}} \qquad C_{\alpha_{5T}} = \frac{p_b - p_h}{p_c - p_{gd}} \tag{3.36}$$

$$C_{p_t} = \frac{p_c - p_{t_{ref}}}{p_c - p_{gd}} \qquad C_{p_s} = \frac{p_{gd} - p_{s_{ref}}}{p_c - p_{gd}} \tag{3.37}$$

During the measurements on the test rig, the probe was aligned with the mean exit flow angle at midspan, i.e. 40° in the cascade reference system. These measured pressures were used again to calculate the coefficients given in Eq. 3.37, which in turns were re-interpolated on the known calibration map obtaining the resulting static pressure, total pressure, pitch and yaw angle for each measurement point.

When performing five hole measurements in a separated region, it is necessary to applied the gradient correction to the acquired raw signals. This necessity arises from the existence of the non-negligible pressure gradient between two opposite holes of the probe, especially across the boundary of separated regions and wakes. The pressure gradient yields to a difference in the pressure sensed between two opposite holes of the five-hole probe even if

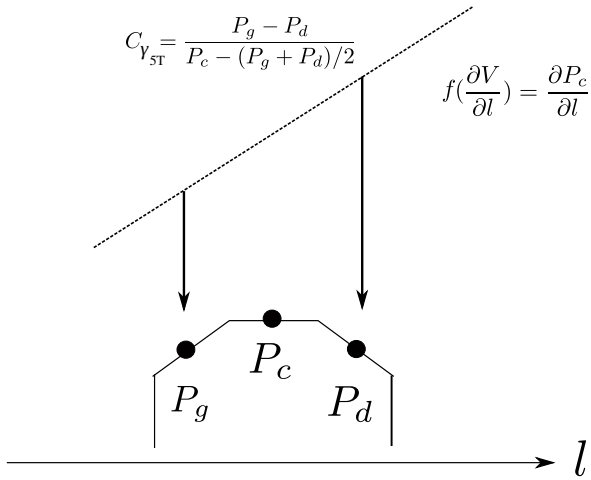

Fig. 3.15 Pressure gradient sensed on the probe head leading to angle misprediction.

the angle of the flow is zero, as sketched in Fig. 3.15. If not corrected, this error leads to the misprediction of all the coefficients which are interpolated on the calibration map, as well as angles, static pressure and total pressure.

The coefficients of Eq. 3.37 can be re-written as in Eq. 3.40 by using the gradient calculated for the pressure signal p_c on the discrete grid of the experimental plane. The superscript $(\prime)$ denotes corrected parameters and the superscript (i) denotes interpolated parameters. The quantities ${p^i}_{c\to g}$, ${p^i}_{c\to d}$, ${p^i}_{c\to h}$ and ${p^i}_{c\to b}$ are the interpolated values of p_c to the left, right, top, and bottom hole, respectively. The values ${p^i}_{g\to c}$ and ${p^i}_{d\to c}$ are the interpolated values of p_g and p_d to the center hole.

$$p'_{gd} = \frac{{p^i}_{g\to c} + {p^i}_{d\to c}}{2} \tag{3.38}$$

$$C'_{\gamma_{5T}} = \frac{p_g - p_d}{p_c - p'_{gd}} - \frac{{p^i}_{c\to g} - {p^i}_{c\to d}}{p_c - p'_{gd}} \tag{3.39}$$

$$C'_{\alpha_{5T}} = \frac{p_b - p_h}{p_c - p'_{gd}} - \frac{{p^i}_{c\to b} - {p^i}_{c\to h}}{p_c - p'_{gd}} \tag{3.40}$$

$$C'_{p_t} = \frac{p_c - p_{t_{ref}}}{p_c - p'_{gd}} \tag{3.41}$$

$$C'_{p_s} = \frac{p_{gd} - p_{s_{ref}}}{p_c - p'_{gd}} \tag{3.42}$$

This procedure finally yields to the corrected quantities resumed in Eq. 3.43 and Eq. 3.44.

$$p'_t = p_c - C'_{p_t}\left(p_c - p'_{gd}\right) \tag{3.43}$$

$$p'_s = p'_{gd} - C'_{p_s}\left(p_c - p'_{gd}\right) \tag{3.44}$$

The three components of the velocity can be calculated as in Eq. 3.47 from pressures and angles of the flow in the probe reference frame. Subscripts $(x,y,z)_{5T}$ indeed denote the

Table 3.9 Uncertainty of time averaged quantities deduced for five hole pressure probe measurements.

	Separation		Free stream	
	Absolute error	Relative error	Absolute error	Relative error
Velocity	2 [m/s]	8%	1.2 [m/s]	5%
Pressure losses	0.04	12%	0.05	-
Pitch angle	4°	6%	2.5°	3%
Yaw angle	3°	30%	1°	-
Static pressure	40 Pa	< 0.1 %	60 Pa	0.1%

velocities that are obtained in the frame of reference of the probe. Finally, the orientation angle of the probe in pitchwise direction is considered in order to transform the components into the cascade frame of reference.

$$u_{x_{5T}} = V\sqrt{\frac{1}{1+(\tan\gamma_{5T})^2+(\tan\alpha_{5T})^2}} \tag{3.45}$$

$$u_{y_{5T}} = -V\tan\alpha_{5T}\sqrt{\frac{1}{1+(\tan\gamma_{5T})^2+(\tan\alpha_{5T})^2}} \tag{3.46}$$

$$u_{z_{5T}} = V\tan\gamma_{5T}\sqrt{\frac{1}{1+(\tan\gamma_{5T})^2+(\tan\alpha_{5T})^2}} \tag{3.47}$$

3.7.3 Uncertainty

The uncertainty of five hole probe can be calculated with the same procedure used by Ma (2012) for the calculated quantities. Values of uncertainty in total pressure, velocity, angles and static pressure are resumed in Table 3.9. Such errors are averaged in space on selected homogeneous regions of measurement, both within the separation wake and within the free-stream flow. This because local peaks of error can be induced by out-of-range angles of the flow across the boundaries between deficit regions and free-stream and very near the endwall. Such angles are indeed beyond acceptable limits of the five hole probe given by the calibration map.

Velocity, pitch angle and static pressure relative uncertainties are small in the free stream. Reversely, values of pressure losses and yaw angle that ideally tend to zero in this region, yield to relative uncertainty values which are not meaningful and therefore are marked in the table as "-" values. The error committed in the separated region is larger, because the flow arrives to the head of the probe with angles close to the admitted boundaries of the calibration map.

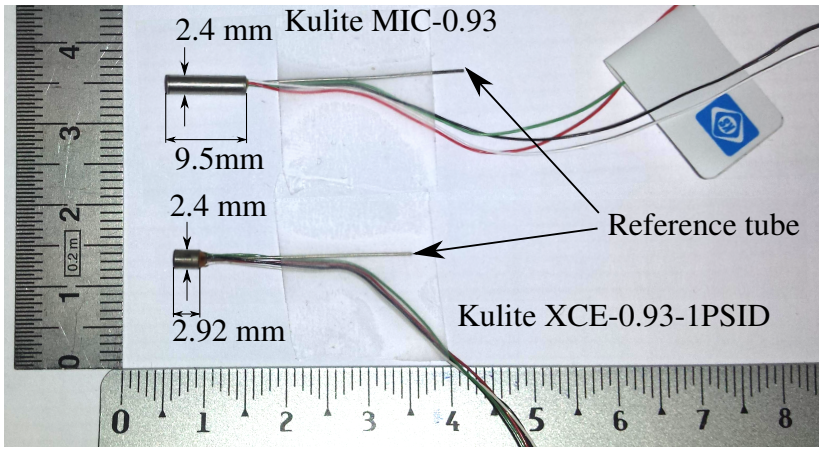

Fig. 3.16 Kulite sensors used for time-resolved total pressure measurements.

3.8 Time-resolved total pressure measurements

The choice of the time-resolved pressure sensors was made to target minimum aerodynamic perturbation of the flow and high sensitivity. Both characteristics have a primary importance. The small encumbrance is necessary because the probes were installed in the inter-blade passage within the separation to acquire the time-resolved total pressure at positions affected by bimodal flow. On the other hand, high sensitivity is necessary to capture such low energy pressure fluctuations that characterize a subsonic test rig in comparison with high speed test rigs.

The Kulite MIC-093 and XCE-093-1PSID were consequently chosen and are shown in Fig. 3.16. These differential sensors are provided of a back annealed reference tube which was settled to reference pressure in order to measure the correct quantity on the head of the probe. Furthermore, the sensitivity of each sensor was experimentally calculated by acquiring a calibrated signal of amplitude 1 Pa and frequency 1 KHz provided by a reference pistonphone instrument.

3.8.1 Experimental set-up

Data acquisition chain

The pressure signals acquired by the pressure transducers were analogically amplified, low-pass filtered by in house conditioners, digitized and finally stored.

The acquisition board PXI-6123 was used for digitization. This board can reach sampling frequencies of 500 KHz with a resolution of 16 bit. The conditioners permit amplification and filter processes. The amplification is necessary in order to adapt the signal to electronic components of the filter, in this case a gain of 10 was applied. The filtering process is necessary to cut high frequencies of the signal in order to avoid aliasing problems due to parasite currents and other environment noises. The filter was a 4-th order Bessel filter providing an attenuation of 3 dB at 150 KHz. Different acquisition frequencies were used in the present work, in order to verify the absence of aliasing due to unresolved frequencies in

the bandwidth of measured signals. The acquisition of 30 KHz for total sampling times of 20 seconds showed slight aliasing at 10 KHz, which is outside the meaningful range for the investigation of the bimodal phenomenon. Additionally, different times of acquisition and sampling rates were tested in order to ensure the proper capture of bimodal histograms for the longer time possible, without exceed storage limitations. This was necessary in order to study the low frequencies characterizing this phenomena. The best compromise to correctly sample such low frequencies, without introducing aliasing amplitudes and limiting stored data, was found by settings the sampling rate at 1 KHz for a total sampling time of 600 seconds.

Positioning

With a total of six probes available, two configurations were investigated in the present work. The first configuration has two probes for passage, which means a single probe for each corner separation on both side of three blade passages. The second configuration has five probes on the left side, which correspond to five corner separations, and only one probe on the right side in the reference blade passage. These configurations are further sketched in Fig. 5.20a and Fig. 5.20b in Section 5.6, in order to help the reader in the understanding of results of Chapter 5.

The exact point in the space where the head of each sensor was positioned corresponded to a bimodal point. Such configuration was chosen in order to investigate the correlation between the unsteady behavior of these six corner separations. The chosen bimodal point corresponds to the blade coordinates $s^* = 0.7$, $n/c = 9.3\%$ ($n = 14$mm) and $z/c = 0.13$ ($z = 20$ mm) from the endwall on both sides of the test rig.

Data reduction

The data treatment is done in three steps for the raw data of each sensor, obtaining the final Eq. 3.48. During the measurement the voltage offset $v_{Koffset}$ was recorded without flow and it is used to correct the raw signal acquired during real measurements $v_K(t)$. The amplification of the signal by the conditioner is taken into account by applying the transfer function in the frequency range corresponding to the sampling rate. In the range of resolved frequencies, i.e. up to 30 KHz, the gain and the phase lag can be considered constant since the Bessel filter was set to cut 3dB at the higher frequency of 150 KHz.

The final value of the gain was therefore $G = 10$ and the phase shift was zero. The corrected signal in Volt is then transformed to Pascal through the application of the measured sensitivity s_K. Finally, the reference pressure applied to the annealed reference tube was the atmospheric pressure. The Eq. 3.48 is hence obtained for the signal treatment of Kulites' output raw tensions.

$$p_{tK}(t) = \frac{1}{G\, s_K}\left[v_K(t) - v_{Koffset}\right] + p_{atm} \tag{3.48}$$

Table 3.10 Relative systematic errors for Kulite time-resolved pressure sensors.

Sensors	Calibration error		
	$\varepsilon_{cal}(\overline{p_{tK}})/\overline{p_{tK}}$	$\varepsilon_{cal}(p'_{tK})/\overline{p_{tK}}$	$\varepsilon_{cal}(\overline{\omega_t})/\overline{\omega_t}$
k0	0.012%	0.05%	2.62%
k1	0.007%	0.03%	1.61%
k2	0.007%	0.15%	2.23%
k3	0.007%	0.16%	2.15%
k4	0.007%	0.08%	1.90%
k5	0.013%	0.085%	3.42%

The obtained unsteady pressure signal for each sensor p_{tK} is further normalized accordingly to the definition of total pressure coefficient ω_t in order to permit the comparison between different measurements.

$$\omega_t(t) = \frac{p_{t\infty} - p_{tK}(t)}{p_{t\infty} - p_{s\infty}} \tag{3.49}$$

3.8.2 Uncertainty

The uncertainty associated to time-resolved total pressure measurements is related only to the systematic part of the error $\varepsilon_{sys}(p_{tK})$. Indeed, the statistical error due to the oscillation of the measured quantity is not meaningful because such oscillations already are the object of the time-resolved investigation.

The main systematic error is associated to the spatial positioning error of the probes, the digitizing error and the calibration error.

The positioning of the probes is the major source of error for such measurements, because the walls were pierced yielding to fixed positions of the steam of the probes. Anyways, the significant reference for these measurements was the bimodality of the total pressure distribution measured by Kulite probes. Bimodal points are related to the size of the separation rather than to a geometrical coordinate, consequently, once installed, the probes were slightly adjusted in order to find the position were the distributions showed the maximum bimodality. Consequently, this error has been corrected *a posteriori* and for this reason it is more meaningful to report the measured deviation of the final position from the theoretical reference coordinate. The measured final position deviation is $\pm$5mm in n direction.

The digitizing error is due to the encoding of the pressure signal by the acquisition board. Since the encoding is 16 bits, 65536 values are used to describe the full scale of sensors. The maximum scale for Kulite XCE-093 and MIC-093 is 2 PSI and 5 PSI, respectively. The maximum sampling error is therefore $\pm$0.5 Pa, which can be neglected.

The calibration error can be estimated as the systematic error associated to the acquisition chain and the sensor during the measurements. From the Eq. 3.48 it can be calculated the calibration error associated to the sensitivity σ_s, to the gain σ_G, to the fluctuation of the signal acquired by the sensor without flow $\sigma_{v_{sensor}}$ and to the reference pressure $\sigma_{p_{atm}}$. One equation

for the pressure mean, i.e. Eq. 3.50, and another equation for the pressure fluctuations, i.e. Eq. 3.51, can be hence written accordingly to what done by Courtiade (2012).

$$\varepsilon_{cal}(\overline{p_t}_K)^2 = \frac{1}{G^2\ s^2}\left[\left(\overline{v}_K - v_{Koffset}\right)^2\left(\frac{\sigma_s^2}{s^2}+\frac{\sigma_G^2}{G^2}\right)+\sigma_{v_{sensor}}^2\right]+\sigma_{p_{atm}}^2 \tag{3.50}$$

$$\varepsilon_{cal}(p'_{tK})^2 = \frac{1}{G^2\ s^2}\left[\left(\max\left(v'_K\right)\right)^2\left(\frac{\sigma_s^2}{s^2}+\frac{\sigma_G^2}{G^2}\right)+2\sigma_{v_{sensor}}^2\right] \tag{3.51}$$

The meaningful error on the total pressure coefficient is consequently induced only by the calibration error of the pressure. It is calculated by applying the propagation law as shown in the Eq. 3.52.

$$\varepsilon_{cal}(\overline{\omega_t}) = \frac{\partial\omega_t}{\partial\overline{p_t}_K}1.96\varepsilon_{cal}(p_{tK}) = 1.96\frac{\varepsilon_{cal}(\overline{p_t}_K)}{p_{t_\infty}-p_{s_\infty}} \tag{3.52}$$

The results of the calibration relative error for each sensor are resumed in Table 3.10.

3.9 Time-resolved Particle Image Velocimetry (HS-PIV)

In order to investigate time-resolved velocity field in the separated region, the time-resolved two-dimensional two-components (2D2C) PIV, also called High Speed PIV, was adopted in this work. Such technique is an improvement of the classical two-components two-dimensional PIV because it reaches higher frequency sampling rates, permitting to resolve the flow path in time. The basic principles of PIV technique can be found in the detailed guide of Raffel et al. (2013) and will not be review in the present work. Such PIV measurements were synchronized with the time-resolved static pressure measurements on the blade surface carried out with microphones.

3.9.1 Experimental set-up

The PIV experimental set up is shown in Fig. 3.17a. Two Phantom v12 CCD cameras with resolution 1280×800 pixels were used to acquire instantaneous measurements of the flow field from the front of the LE to the TE of the blade at fixed spans, as sketched in Fig. 3.18. In order assure the adequate optical access, the cameras were positioned on the opposite side of the test rig (right) than the side where was located the head of the Blade-II (left), which was instrumented with microphones. The laser head was positioned underneath the test rig as shown in Fig. 3.17b.

The acquisition frequency is imposed by the memory stocking capacity of the camera. Consequently, for such field of view, the maximum sampling rate of PIV measurements was set to $f_s = 2781$Hz and $t_s = 1$sec for each measurement, which yields $N_1 = 2781$ for a single data set. Such a sampling frequency gives a time-step $\Delta t_f = 3.6 \times 10^{-4}$ sec, which is 10% of the convective time $t^* = c/V_\infty$. Furthermore, five runs of 1 sec were carried out consecutively in order to obtain a complete data set of 5 sec for each plane.

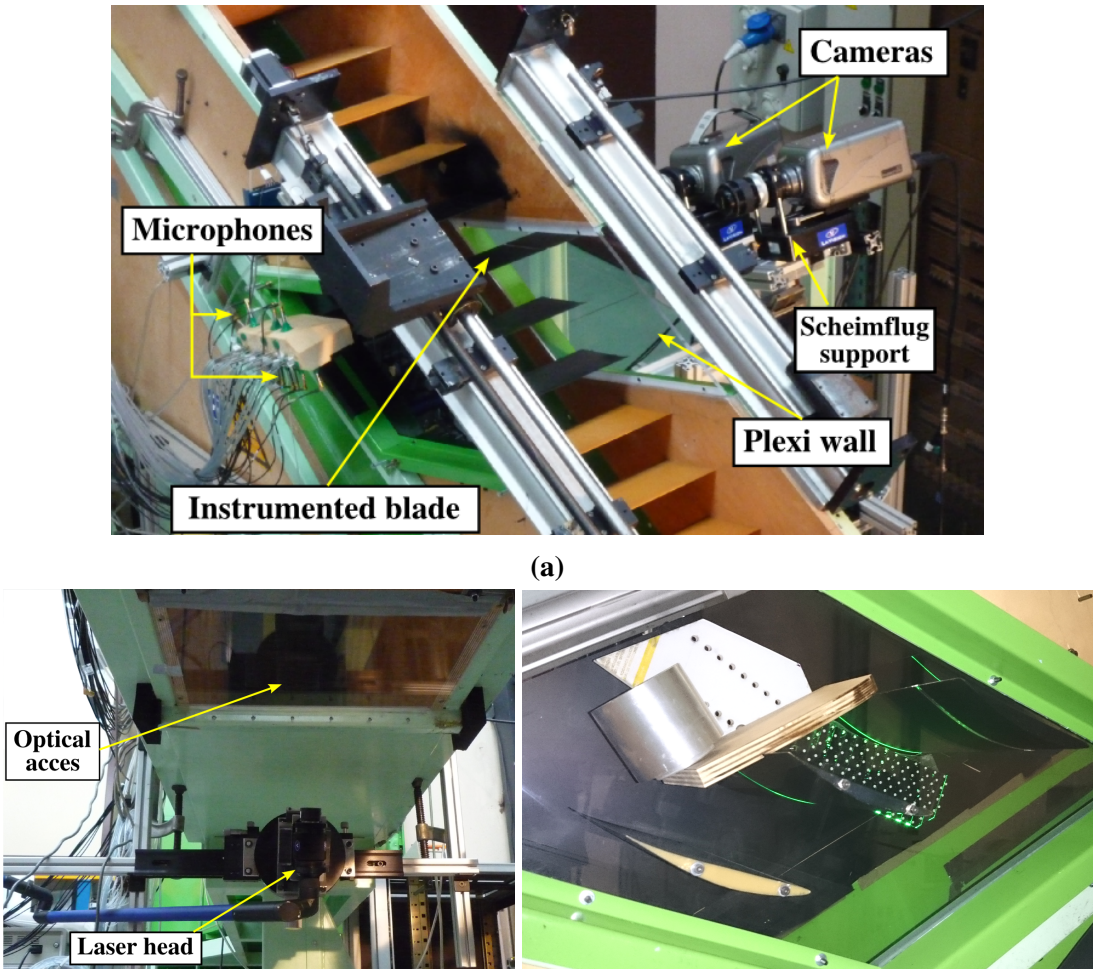

Fig. 3.17 Time-resolved coupled PIV-microphone measurements on the linear compressor cascade (a), laser head detail (b) and calibration plate installed in the passage (c).

Therefore, the number of obtained instantaneous fields for each measurement plane was $N_{tot} = N_1 \cdot 5\text{sec} = 13.905 \times 10^3$ samples. By using this complete set it is possible to check the significance of the single-set measurement as discussed in Section 3.9.3.

The laser is a double cavity pulsed Nd:YLF, capable to reach 10 KHz with a maximum energy of 18 mJ at 1 KHz. The laser light sheet thickness was set to 1 mm, i.e. 0.27% of span-height h. The acquisition was performed by DaVis® commercial software. The multi-pass calculation implemented in this software was set up to use investigating windows of 16×16 pixels improved by elliptical and circular Gaussian windows with an overlap of 50%. The investigating window at the chosen size of the field of view was therefore 1 mm^2, i.e. $0.66c\%$. This scale is 100 times the Kolmogorov length in the viscous sublayer $\eta^+ = 1$ and 20 times the Kolmogorov length in the log region.

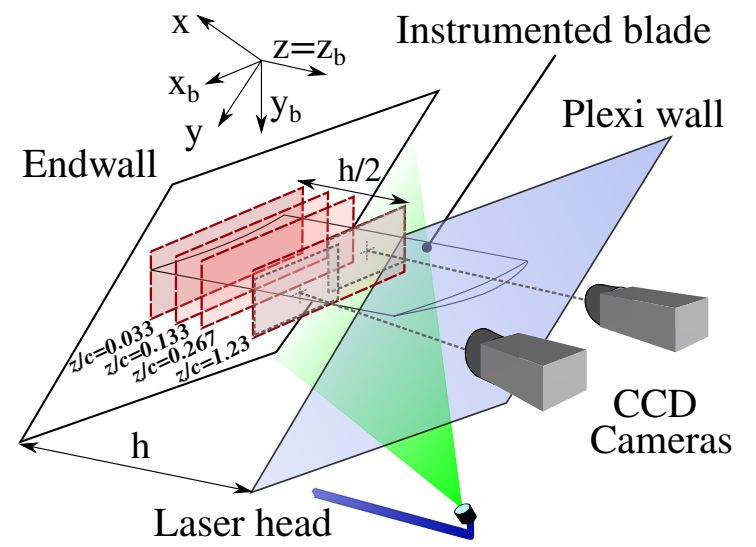

Fig. 3.18 Sketch of HS-PIV measurement configuration representing the planes and the position of PIV instrumentation.

3.9.2 Calibration

The process of calibration was done for each plane of measurement and it consists of several steps with iterative adjustment in order to have the best calibration level. Whereas some steps are common and automatically handled by the acquisition software, the calibration plate represented in Fig. 3.17c is a fundamental tool, which has to be be adapted for every different test rig and plane of measurement.

The main goal of HS-PIV measurement was to cover the whole chord-wise section of the blade in the field of view. The limiting elements for this requirement were neighbor blades, which bounded the field reachable by the laser sheet. For this reason the angle and the width of the laser was carefully regulated in order to cover the entire target region with equal illumination power. The best compromise was found for each measurement section by iterations of tests of acquisitions and adjustments of laser's lens. Finally, the sustain and the accurate positioning of the calibration plate at the measurement section was solved by manufacturing a support for the calibration plate that was shaped as the suction surface of the blade and carved to wedge two trailing edges of the blades, which bounded the reference measurement passage, see Fig. 3.17c.

The main steps of the calibration process are resumed below.

1. Positioning of the calibration plate flushing the desired plane of measurement
2. Positioning of the laser sheet to align with the reference surface of the calibration plate
3. Positioning of the cameras, adjustment of objective focus and regulation of angle of Scheimpflug supports, see Fig. 3.17a, to obtain an homogeneous view of the plate.
4. Acquisition of images with proper illumination for the calibration numerical procedure.
5. Calibration process and setting of the plane's zero reference on the calibration map.
6. Measurement test with laser to check reflection and adjustment of the seeding mass-flow.

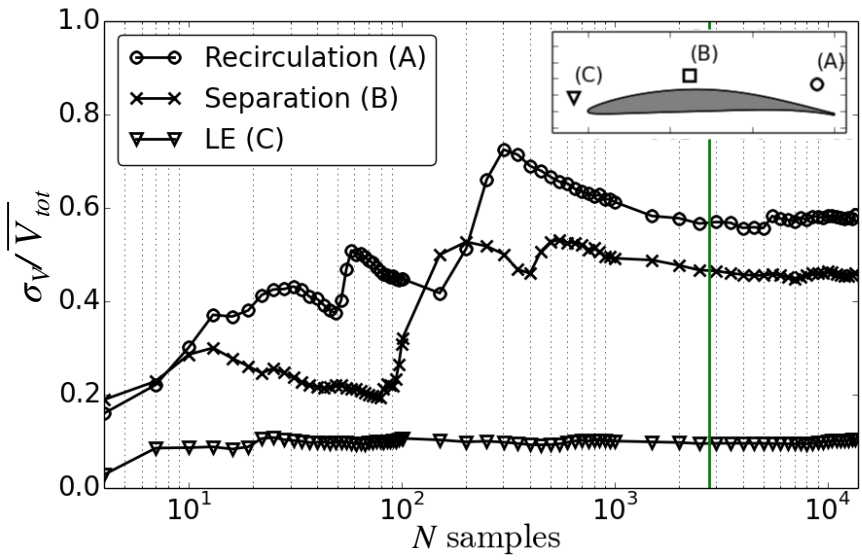

Fig. 3.19 Statistical significance of the PIV data at characteristic locations: sketch of sample locations and convergence diagram of relative standard deviations $\sigma_V/\overline{V_{tot}}$. Green line: single-set measurement, $N_1 = 2781$.

3.9.3 Convergence

In order to check the statistical significance of the measurements acquired for 1 sec against 5 sec, the relative standard deviation of the velocity $V(t) = \sqrt{u^2(t) + v^2(t)}$ is calculated as a function of N samples ranging in the interval $[1 : N_{tot}]$, hence

$$\frac{\sigma_V}{\overline{V_{tot}}} = \frac{\sqrt{\frac{1}{N-1}\sum_{i=1}^{N}\left[V_i - \frac{1}{N}\sum_{i=1}^{N}(V_i)\right]^2}}{\frac{1}{N_{tot}}\sum_{i=1}^{N_{tot}} V_i} \tag{3.53}$$

Three crucial positions are chosen for the evaluation of $\sigma_V/\overline{V_{tot}} = f(N)$ and the convergence of such function is shown in Fig 3.19. The green line stands for the single-set measurement of 1 sec, $N_1 = 2781$ samples, and its relative standard deviation for cases A, B and C differs from the final value obtained at N_{tot} of 2.7% (A), 1.4% (B) and 8.9% (C). Such difference is fairly acceptable, meaning that one single set measurement can be considered already significant to the second statistical moment. Consequently, investigations further presented in Section 4 are performed exploiting only single measurements data-set of 1 sec, i.e. $N_1 = 2781$ samples.

3.9.4 Uncertainty

Systematic error

The systematic error in the PIV measurements is basically due to the effect of calibration errors, peak-locking phenomena, low illumination within the investigated field of view and

Table 3.11 Time-resolved 2D2C PIV summarizing systematic uncertainties for three different measurement planes.

	z/c = 0.033	z/c = 0.13	z/c=1.23
Scale sc [mm/pixel]	65.88×10^{-3}	66.09×10^{-3}	67.41×10^{-3}
Calibration error σ_{cal} [pixel]	0.0486	0.0437	0.0520
Max velocity error $\varepsilon_{sys}(V)$ [m/s]	0.488	0.481	0.507
Peak-locking	0.015	0.03	0.02
Max rejected vectors	2%	1.6%	1.2%
Plane position uncertainty ε_p [mm]	2.7	1.9	3.9

lack or excess of seed particles during the measurement. When a commercial code is utilized, as in the present study, the uncertainty can not be calculated by the propagation law as for the case of total pressure measurements. This because inter-correlation adaptive algorithms used in the software are not open source and the exact derivatives can not be estimated.

In reverse, commercial software dispose of ad-hoc parameters that give an estimation of the quality of PIV measurement. The calibration algorithm provide the error as deviation of the fit of the camera field on the real image in term of RMS of pixel. Additionally, the peak-locking coefficient is an empiric parameter of the quality of PIV measurements, since it gives the bias error related to the fact of privileging particle displacements corresponding to entire pixels. The threshold maximum value suggested by commercial software provider LaVision to have measurements of quality is 0.1, as explained by Godard (2010).

Whereas calibration and peak-locking can be described by a single value, the other sources of error can be estimated solely by running iterative measurements tests and by post-processing the results. After a first calculation of the velocity field, other post-process steps are usually carried out in order to discard localized irregularities of groups of vectors that do not satisfy imposed thresholds on quality parameters, such as the correlation peak ratio and the continuity with neighbor vectors. The quantification of these errors permits to ensure the immediate major correction of the set up by adjusting the laser lens and the seed mass-flow.

Even if the precision on the value of displacement calculated by inter-correlation is dependent on the algorithm, an estimation of the maximum uncertainty can be done as follows. The study of Stanislas et al. (2008) stated that this error is generally comprised in the range 0.004 to 0.1 pixel. By adopting the maximum value and including also the effect of the calibration error, the systematic error on the velocity can be calculated as in Eq. 3.54. In this equation, sc is the value of the image scale, which is adopted to convert pixels in millimeters and is provided by the calibration.

$$\varepsilon^2{}_{sys}(V) = \left(\frac{sc\ 0.1}{\Delta t}\right)^2 + \left(\frac{sc\ \sigma_{cal}}{\Delta t}\right)^2 \tag{3.54}$$

Results of the max absolute velocity error due to the bias error are summarized in Table. 3.11 for three different measurement planes $z/c = 0.033$, $z/c = 0.13$ and $z/c = 1.23$.

Table 3.12 Statistical error of HS-PIV measurements at $z/c = 0.033$, configuration $i = 7°$.

	Recirculation (A)	Separation (B)	LE (C)
$\varepsilon_{st}(\overline{V})$ [m/s]	0.16	0.36	0.12
$e_{st}(\overline{V})$	2.1%	1.8%	0.4%
$\varepsilon_{st}(V_{RMS_{xy}})$ [m/s]	0.18	0.24	0.08
$e_{st}(V_{RMS_{xy}})$	2.2%	2%	1.9%

Additionally, to give an order of magnitude, the max velocity error at the section $z/c = 0.033$ can be compared with mean velocities values in three region of the flow at the same section. In the recirculation, separation and LE region, the relative error is 8%, 3.3% and 1.5%, respectively.

During the process of calibration, an error is also committed on the location of the origin of the plane of measurement. Indeed, a clearance exists between the calibration support and the suction surface of the blade, as well as at the LE, in order to permit the installation of the calibration plate. Such a clearance can not be measured during the installation and hence it is source of error for the exact location of the blade within the plane of measurement. Even if a correction of the position of the zero value can be provided *a posteriori* by assuming the LE of the blade in the acquired image as reference, a non negligible uncertainty still exist about its exact position. Estimation of this uncertainty can be done by assuming the error equal to the correction on the offset. This correction is the results of a translation of the zero and a rotation of the acquired image. The final positioning error ε_p is calculated in Eq. 3.57 as the sum of the maximum error committed by shifting the plane both in x and y direction, defined as ε_{0p}, and the uncertainty on the pitchwise alignment between the calibration plate and the blade chord, defined as $\Delta\theta_0$.

$$\varepsilon_{0p}{}^2 = \Delta x_{0p}{}^2 + \Delta y_{0p}{}^2 \tag{3.55}$$

$$\varepsilon_{\theta_0} = \Delta\theta_0\, c \tag{3.56}$$

$$\varepsilon_p{}^2 = \varepsilon_{0p}{}^2 + \varepsilon_{\theta_0}{}^2 \tag{3.57}$$

However, this error is fixed for each specific measurement plane and it does not affect the calculation of error of the velocity. The resulting values found for the HS-PIV measurements at $z/c = 0.033$ (z=5mm), $z/c = 0.13$ (z=20mm) and $z/c = 1.23$ (midspan) are summarized in Table.3.11.

Statistical error

The statistical error for HS-PIV is calculated in the most fluctuating measurement configuration $z/c = 0.033$, $i = 7°$. The absolute statistical error at 95% of confidence for the mean of

velocity value, i.e. $\overline{V} \pm \varepsilon_{st}(\overline{V})$, is calculated as in Eq. 3.58.

$$\varepsilon_{st}(\overline{V}) = \frac{1.96\sigma_V}{\sqrt{N_1}} \qquad e_{st}(\overline{V}) = \frac{\varepsilon_{st}(V)}{\overline{V}} \tag{3.58}$$

where N_1 is the number of acquired vector fields considered.

The values for the three chosen positions are given in Table 3.12. The absolute statistical error, such as $V_{RMS_{xy}} \pm \varepsilon_{st}(V_{RMS_{xy}})$ and the relative statistical error for the RMS of the velocity, defined as in Eq. 3.69, can be calculated as follow:

$$\varepsilon_{st}(V_{RMS_{xy}}) = \frac{1.96\sigma_{V_{RMS_{xy}}}}{\sqrt{N_1}} \qquad e_{st}(V_{RMS_{xy}}) = \frac{\varepsilon_{st}(V_{RMS_{xy}})}{V_{RMS_{xy}}} \tag{3.59}$$

In this equation, the standard deviation $\sigma_{V_{RMS_{xy}}}$ is calculated as

$$\begin{aligned} \sigma_{V_{RMS_{xy}}} &= \sqrt{\left(\frac{\partial V_{RMS_{xy}}}{\partial u'^2}\sigma_{u'^2}\right)^2 + \left(\frac{\partial V_{RMS_{xy}}}{\partial v'^2}\sigma_{v'^2}\right)^2} \\ &= \frac{1}{2\,V_{RMS_{xy}}}\sqrt{\left(\sigma_{u'^2}\right)^2 + \left(\sigma_{v'^2}\right)^2} \end{aligned} \tag{3.60}$$

where

$$\sigma_{u'^2} = \sqrt{\frac{1}{N_1 - 1}\sum_{i=1}^{N_1}\left(u_i'^2 - \overline{u'^2}\right)^2} \qquad \sigma_{v'^2} = \sqrt{\frac{1}{N_1 - 1}\sum_{i=1}^{N_1}\left(v_i'^2 - \overline{v'^2}\right)^2} \tag{3.61}$$

The values are listed in Table 3.12 for the wake region (A), the region of high velocity RMS characterizing the separation (B) and in front of the LE, (C).

Combined error

The combined error on the mean velocity for measurements at $z/c = 0.033$ is finally calculated by adding the maximum systematic error on the velocity $\varepsilon_{sys}(V)$, shown in Table 3.11, to the statistical value in Table 3.12, according to Eq. 3.62.

$$\varepsilon(\overline{V}) = \sqrt{\varepsilon_{st}^2\left(\overline{V}\right) + \varepsilon_{sys}{}^2(V)} \tag{3.62}$$

The maximum absolute error for the plane $z/c = 0.033$ is hence $\varepsilon(\overline{V}) = 0.6$ m/s and it is localized in the separation region. Additionally the relative combined error reaches the maximum in this region because of the low value of $\overline{V}$, which leads to $e(\overline{V}) = 12\%$.

3.10 Stereo Particle Image Velocimetry (SPIV)

SPIV measurements were performed in order to characterize the corner separation in spanwise direction within the inter-blade passage. The experimental set up, the calibration and the sources of error associated to this measurement technique are here discussed.

3.10.1 Experimental set up

SPIV measurements were performed utilizing LaVision® acquisition system. The light source was a dual cavity Nd:YAG laser, the maximum illumination energy is 50 mJ/pulse at 15 Hz repetition rate and the light sheet head was equipped of 17 mm focal length cylindrical lens. A pair of 1280×1024 pixels and 12 bit CCD cameras (PCO Sensicam) with lens-on-chip were equipped with 60 mm focal length lenses, the maximum frequency for frame was 8 Hz. The post-processing of acquired images was carried out utilizing DaVis® software. The multi-pass calculation utilized investigating windows of 32×32 pixels, improved by elliptical and circular Gaussian windows with an overlap of 50%.

The SPIV configuration was chosen installing the two cameras and the light sheet probe on the same mounting base on a robot capable of four-degrees of freedom. A picture of the experimental set up is shown in Fig. 3.20a. In order to characterize the flow in the inter-blade channel, six planes of measurements normal to the surface of the blade were investigated. The rotation of the base permitted the simultaneous positioning of cameras and light sheet. The two cameras were mounted symmetrically on each side of the light sheet, ESC (Each Side Configuration) with a half enclosed angle of 30°. The ESC was selected instead of SSC (Same Side Configuration) in order to better describe the propagation of corner separation in the stream-wise direction (Liu et al., 2006). The black cage in front of the laser head was placed in contact with the mirror made of plexiglass, at the investigation section. The installation of this device was necessary in order to avoid the mirror reflection of particles outside the test rig into the field of view of the cameras placed inside the test rig.

The laser light sheet thickness was set to 2 mm and the number of obtained vector fields was 1×10^5 in order to assure the convergence of averaged quantities presented in this work.

3.10.2 Calibration

The calibration of the Stereo-PIV was performed with a three-dimensional calibration plate. The surface of the calibration plate has steps of few millimeters which correspond to an upper surface and to a lower surface. The calibration plate was placed in the field of view of both cameras, flushing the laser sheet at the upper surface. The optical objective of both cameras was adjusted on the reference marks carved on both plate surfaces. Images of the plate were then acquired and processed by an iterative implemented algorithm of the commercial software. This process, called pinhole calibration (Wieneke, 2005), permitted to fix the settings of cameras and the cross-correlation algorithm in order to calculate the third component of the velocity, which was perpendicular to the calibration plane. The iterative calibration was run till admissible threshold of less than 3 pixel of averaged deviation was reached. This threshold is fixed by the software provider.

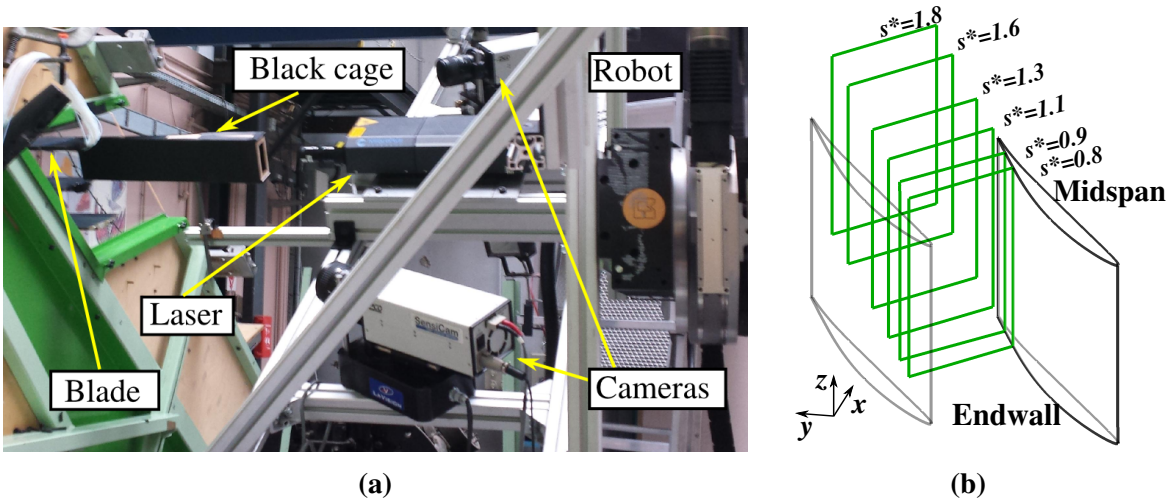

Fig. 3.20 Stereo PIV experimental set up on the cascade test rig (a). Planes of measurement in the reference inter-blade passage (b).

3.10.3 Uncertainty

Systematic error

The peak-locking coefficient for the SPIV measurements of the present work ranges between 0.1 and 0.2, which is larger than the limiting advised value 0.1. Consequently, it can be said that these measurements are affected by bias due to the peak-locking effect. Although avoiding peak-locking is the major requirement when performing PIV measurements, sometimes it is impossible to suppress this error. If the sub-pixel displacement estimator is imposed, as in case of Davis software, the peak-locking can be diminished solely by adjusting the focus of camera's objective or the PIV time delay Δt chosen in the measurement. Consequently, limitations on the resolution of the particles are imposed by the target field of view depending on the test rig and optical access, whereas limitations of Δt are imposed by the associated degradation of the quality of the measured displacement fluctuations.

However, if the level of peak-locking is not extreme, the measurements can still be exploited in order to calculate time averaged quantities. Indeed, the study of Christensen (2004) shows that the averaged velocity profiles are insensitive to peak-locking and, although RMS of velocity and Reynolds stress are quite sensitive to it, errors can be minimized by ensuring that displacements associated with the turbulent fluctuations are larger than 1 pixel in magnitude.

Concerning present measurements, in which the time delay of the PIV $\Delta t = 20\mu$sec is relatively long, the limit of 1 pixel implies that measurements can be considered meaningful if the velocity of the particle is higher than 7.6 m/s. The velocity calculated from these measurements showed that in the separation the averaged fluctuation of velocity is 6.9 m/s. This value is very close to the limit, implying that the level of Reynolds stresses is still affected by the error derived from the peak locking but can be considered meaningful.

Table 3.13 Statistical error of SPIV measurements in the inter-blade passage, configuration $i = 4°$, selected plane $s^* = 1.1$.

	Midspan	Separation	Blade wake
$\varepsilon_{st}(\overline{u}_s)$ [m/s]	0.01	0.17	0.12
$e_{st}(\overline{u}_s)$	0.03%	6%	0.7%
$\varepsilon_{st}(\overline{u_s{}'v_n{}'})[\mathrm{m}^2/\mathrm{s}^2]$	0.0034	1.18	0.40
$e_{st}(\overline{u_s{}'v_n{}'})$	0.34%	3%	4%

The percentage of rejected vectors in the post processing is between 3% and 11%. Near the endwall, high reflections and scatters of the light of the laser sheet introduced spurious vectors. In order to be conservative on this point, the region near the endwall was crop and discarded from final results.

Taking into account the maximum error associated to the cross correlation, i.e. 0.1 pixels, and the scale factor of the camera $sc = 0.1520$ mm/pixels, the maximum velocity deviation is calculated as in Eq. 3.54. Since the calibration for the SPIV is performed by the iterative pinhole reconstruction, the exact error of the calibration fit σ_{cal} is unknown. As investigated by Wieneke (2005) through experimental results with synthetic images, the three-components reconstruction error is well below 0.02 for most cases, hence the value $\sigma_{cal} = 0.02$ pixels is assumed in the present estimation. For the plane $s^* = 1.1$ it results $\varepsilon_{sys}(u_s; v_n; w) = 0.775$m/s.

In the region of corner separation the error of spatial positioning of the laser beam is not negligible because of high velocity gradient. The uncertainty $\sigma_p = 0.1$mm on the position of the robot induces an error in the positioning of the measurement plane and consequently an error on the final velocity u_s. Additionally, the residual disparity σ_{Disp} from the pinhole calibration ranges between 0.2 and 1.3 pixel, contributing to the velocity error associated to positioning. The total positioning error for SPIV is finally estimated as in Eq. 3.63.

$$\varepsilon_p(\overline{u}_s) = \frac{\partial u_s}{\partial s}\left(\sigma_p + sc\ \sigma_{Disp}\right) \tag{3.63}$$

The term $\frac{\partial u_s}{\partial s}$ is the stream-wise velocity gradient between planes. These systematic errors, the peak-locking value and the percentage of rejected vectors are summarized in Table 3.14 along with the final combined error.

Statistical error

The statistical error on the averaged quantities is calculated from the standard deviation of the quantity divided by the square root of the total acquisition samples. Three position are chosen in order to estimate absolute and relative error for the velocity in streamwise direction u_s normal to the plane of measurement and Reynolds stresses $\overline{u_s{}'v_n{}'}$. The values are summarized in Table 3.13.

Table 3.14 Quality parameters and errors for SPIV measurement, configuration $i = 4°$, selected plane $s^* = 1.1$.

Peak-locking		0.16	
Max rejected vectors		11%	
Scale sc [mm/pixel]		0.152	
Calibration Disparity σ_{Disp} [pixel]		1.298	
Reconstruction error σ_{cal} [pixel] (Wieneke, 2005)		0.02	
Max velocity error ε_{sys} [m/s]		0.775	
	Midspan	Separation	Blade wake
Positioning error $\varepsilon_p(\overline{u}_s)$ [m/s]	0.020	0.079	0.059
Statistical error $\varepsilon_{st}(\overline{u}_s)$ [m/s]	0.010	0.170	0.120
Combined error $\varepsilon(\overline{u}_s)$ [m/s]	0.775	0.797	0.787
Relative combined error $e(\overline{u}_s)$	2.3%	19.9%	8.7%

Combined error

The combined absolute error of cross correlations, positioning error and statistical error is calculated in the highest zone of velocity gradient, i.e. between plane $s^* = 1.1$ and $s^* = 1.3$ as in Eq. 3.64.

$$\varepsilon(u_s) = \sqrt{\varepsilon_{st}{}^2(\overline{u}_s) + \varepsilon_p{}^2(\overline{u}_s) + \varepsilon_{sys}{}^2(\overline{u}_s)} \tag{3.64}$$

The combined and relative errors are summarized in Table 3.14 for arbitrarly positions at midspan, in the separation and in the blade wake. The highest relative error in the separation generates from the low magnitude of the velocity in the detached region, i.e. $\overline{u}_s = 4$ m/s.

3.11 Signal treatments and analysis methods

This section presents the methods utilized during the analysis of signals acquired by measurements. Besides classical tools as the Fourier transform correlations and statistical moments, more complex methods such as coherence, wavelet transform and modal decomposition exist. If exploited adequately, these instruments can reveal the physical mechanisms hidden in data.

3.11.1 Average

The arithmetic average is used for temporal averages and spatial averages as well. For a discrete set of samples x obtained by measurements the average is defined as in the Eq. 3.65.

$$\overline{x} = \frac{1}{N}\sum_{i=1}^{N} x_i \tag{3.65}$$

3.11.2 Standard deviation and fluctuation Root Mean Square

In fluid dynamics one of the most useful quantity to describe the unsteadiness of a signal is the standard deviation, defined as in the Eq. 3.66.

$$\sigma_x = \sqrt{\frac{1}{N-1}\sum_{i=1}^{N}(x_i - \overline{x})^2} \tag{3.66}$$

This quantity estimates the magnitude of the dispersion of measurements around the average as defined in Eq. 3.66. It is necessary to stress that the fluctuation of the quantity is generated both by random events, such as the turbulence of the flow and the uncertainty, but additionally can include deterministic dynamics of the flow.

For this reason it is necessary to verify that no peaks are present in the spectral content in order to ensure the random nature of a phenomenon.

The standard deviation correspond to the root mean square of the fluctuating part of the signal. This quantity is of great importance in pressure and velocity measurements because it is the integral over the power spectrum and it quantifies the intensity of a process (Schewe, 1983).

Pressure RMS

The unsteady pressure coefficient $C_p(t)$ can be written as the sum of the unsteady perturbation of the pressure coefficient $C_{p'}(t)$ and the average value $\overline{C}_p$ (Bölcs and Körbächer, 1993) as shown in the Eq. 3.67.

$$\begin{aligned} C_p(t) &= \frac{p_s(t) - p_{s_\infty}}{p_{t_\infty} - p_{s_\infty}} \\ &= \frac{(p'_s(t) + \overline{p}_s) - p_{s_\infty}}{p_{t_\infty} - p_{s_\infty}} \\ &= C_{p'}(t) + \overline{C}_p \end{aligned} \tag{3.67}$$

The RMS value of the unsteady pressure coefficient can be written following Schulz et al. (1990b) in the Eq. 3.68.

$$C_{p_{RMS}} = \sqrt{\frac{1}{N}\sum_{i=1}^{N}(C_{p'i})^2} = \frac{p'_{RMS}}{p_{t_\infty} - p_{s_\infty}} = \frac{\sigma_p}{p_{t_\infty} - p_{s_\infty}} \tag{3.68}$$

In literature this is also called ratio of root-mean square of the static pressure fluctuation to free stream dynamic pressure. Data sets obtained from microphone measurements are already the values of fluctuations, i.e. p'_{s_i}. This is the reason why, in the Eq. 3.68, N is used instead of $N-1$.

Velocity fluctuation RMS

The RMS value of velocity fluctuations $V_{RMS\ xy}$ is used to analyze HS-PIV measurements and it is defined as in Eq. 3.69.

$$V_{RMS\ xy} = \sqrt{\frac{1}{N-1}\sum_{i=1}^{N}\left[V'_{xy}(t)^2\right]} = \sqrt{\frac{1}{N-1}\sum_{i=1}^{N}u'(t)^2 + \frac{1}{N-1}\sum_{i=1}^{N}v'(t)^2} \tag{3.69}$$

This quantity is similar to the Reynolds stress term $-\overline{u'v'}$ but more suited to highlight the region of maximum unsteadiness. The quantity $V_{RMS\ xy}$ describes indeed the absolute magnitude of the velocity fluctuations, avoiding the positive-to-negative changing in sign that the Reynolds stress term allows.

3.11.3 Skewness

The skewness of a PDF distribution is defined as the $3rd$-order moment m_3 of a signal and for discrete series the biased sample coefficient of skewness is defined as in Eq. 3.70.

$$Sk_3 = \frac{m_3}{\sqrt{m_2}^3} = \frac{\sum_{i=1}^{N}(X_i - \overline{X})^3/N}{\left(\sigma\sqrt{\frac{N-1}{N}}\right)^3} \tag{3.70}$$

where σ stands for the standard deviation of the population, X_i for the individual acquired sample, $\overline{X}$ for the mean of the set of samples, N for the total number of samples. The skewness describes the asymmetric deviation of the amplitude distribution of the PDF. For a Gaussian distribution it results $Sk_3 = 0$. Negative skewness indicates that the left side of the statistical distribution has a longer tail, so the pressure signal presents extreme low pressure fluctuations and no symmetric high fluctuations. Conversely, positive skewness values mean that the right side tail is longer and the time signal is characterized predominantly by peaks of very high positive amplitude.

3.11.4 Kurtosis

Kurtosis, also called flatness, can be formally defined as the standardized $4rd$-moment m_4 about the mean; for discrete series it is calculated as:

$$K_4 = \frac{m_4}{\sqrt{m_2}^4} = \frac{\sum_{i=1}^{N}(X_i - \overline{X})^4/N}{\left(\sigma\sqrt{\frac{N-1}{N}}\right)^4} \tag{3.71}$$

where σ, X_i, $\overline{X}$, N have already been defined for Eq. (3.70). The normal distribution has a kurtosis of 3, and the coefficient $Ku = K_4 - 3$ is often used to obtain a reference normal

distribution described by kurtosis values equal to zero. In the present work, the kurtosis is always considered as $Ku = K_4 - 3$.

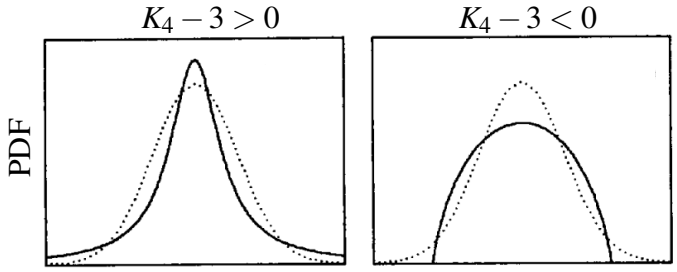

Fig. 3.21 Explaining illustration of kurtosis. Dotted lines show normal distributions, whereas the solid lines shows distributions with both positive kurtosis (left panel) and negative kurtosis (right panel), reproduced from DeCarlo (1997).

The left and right sketch of Fig. 3.21 illustrate distributions with positive kurtosis (leptokurtic), $Ku > 0$, and negative kurtosis (platykurtic), $Ku < 0$. The left panel shows that a distribution with positive kurtosis has heavier tails and larger peak than the Gaussian distribution, whereas the right panel shows that a distribution with negative kurtosis has lighter tails and it is flatter.

Tailedness and peakedness are both components of kurtosis because this statistical moment represents a movement of mass that does not affect the variance. In case of positive kurtosis heavier tails are related to a higher central peak.

3.11.5 Correlations

The determination of correlations between variables is one of the most effective means to establish casual relationships. Correlations are formed as averaging the product of sample pairs in time or in space. The magnitude of the correlation function tells how much energy has been lost or is no longer common to the two signals as the measured disturbance propagates or is transmitted between two points. This loss of energy can be related to heat dissipation, turbulence, or it may have been uncoupled, diverted or scattered into other direction. When a quantity is sensed at two distinct points with two sensors, the signal $v_1(t)$ and $v_2(t)$ will be correlated with each other if the signal from the upstream sensors is relatively delayed to the downstream sensors by a time τ, which compensates for the travel time between these sensors. The time delay at which the two signals have maximum correlation gives the averaged group speed of the traveling wave. The cross-correlation $R_{12}(\tau)$ between signals $v_1(t)$ and $v_2(t)$ is formed from the ensemble average of the product of the signals, as defined in Eq. 3.72.

$$R_{12}(\tau) = \frac{1}{T} \langle v_1(t+\tau) v_2(t) \rangle \tag{3.72}$$

In this definition angle brackets $< >$ denote the ensemble average and T the total time.

The correlation function is usually normalized as in Eq. 3.73 by the root square of both the auto-correlation of the signal v_1 and v_2, in order to obtain a coefficient between -1 and 1.

$$r_{12}(\tau) = \frac{R_{12}(\tau)}{\sqrt{R_{11}(0)R_{22}(0)}} \tag{3.73}$$

Peak values of the cross-correlation function exceeding thresholds as $r_{12} = \pm 0.2$ can be considered meaningful. Anyway, the maximum value of the cross-correlation should be considered meaningful only if it is higher than side oscillations of the entire cross-correlation function. According to the rule used in this work for the calculation of cross-correlations $R_{12}(\tau)$, $\tau > 0$ describes the traveling of correlated events from v_2 to v_1, whereas $\tau < 0$ describes the traveling of correlated events from v_1 to v_2.

3.11.6 The Fourier transform

The Fourier transform expresses a mathematical function of time as a function of frequency, known as its frequency spectrum. In case of digitized data as signals acquired by experimental measurements, the function is no more continuous but it is a set of discrete samples. Considering a periodic signal $s(t)$ of period T with N samples regularly spaced of Δt, its frequency spectrum $\hat{s}(k)$ is obtained with the Discrete Fourier Transform (DFT) defined as in Eq. 3.74

$$\hat{s}(k) = \sum_{n=0}^{N-1} s(n) e^{\left(-i\frac{2\pi kn}{N}\right)} \qquad 0 \leqslant k < N;\ T = N \cdot \Delta t \tag{3.74}$$

The spectrum $\hat{s}(k)$ is a complex quantity that can be decomposed in amplitude and phase. The spectrum amplitude returns the magnitude of each harmonic in the signal and it is calculated as the absolute value of the complex number, Eq. 3.75.

$$|\hat{s}(k)| = \sqrt{Re\left(\hat{s}(k)\right)^2 + Im\left(\hat{s}(k)\right)^2} \tag{3.75}$$

The phase spectrum indicates the phase shift of each harmonic, Eq. 3.76.

$$\phi\left(\hat{s}(k)\right) = \tan^{-1}\left[\frac{Im\left(\hat{s}(k)\right)}{Re\left(\hat{s}(k)\right)}\right] \tag{3.76}$$

3.11.7 The power spectral density

When measurements are carried out on several acquisition seconds and so the time period is large enough, it is possible to evaluate the power spectral density of the signal. This quantity refers to the energy distribution per unit of time, so it gives the information about the spectral energy distribution that would be obtained if the measured signal tended to infinity.

At first the total acquired signal t_s is divided in N segments, then the calculation of the PSD is obtained by averaging the square of the Fourier transform performed on these signal segments.

$$PSD(k) = \frac{1}{N}\sum_{i=1}^{N} |\hat{s}(k)_i|^2 \qquad 0 \leqslant i < N;\ t_s = N \cdot T \tag{3.77}$$

3.11.8 Coherence function

The cross-spectral density is the Fourier transform of the cross-correlation function of a signal. The continuous formulation of this quantity, without considering the discrete estimation related to the Fourier transform calculation, is written as in Eq. 3.78

$$\Phi_{12}(\omega) = \frac{1}{2\pi}\int_{-\infty}^{+\infty} R_{12}(\tau)e^{i\omega\tau}d\tau \tag{3.78}$$

The auto spectral density Φ_{11} is a special form of the cross-spectrum of the signal with itself, hence it is the Fourier transform of the auto-correlation function. In its discrete calculation, Φ_{11} is equivalent to $PSD(k)$. The normalized magnitude of the cross-spectral density is usually employed to quantify the variation of a signals over the distance. This function is the coherence and it is defined as in Eq. 3.79.

$$\gamma^2(\omega) = \frac{|\Phi_{12}(\omega)|^2}{\Phi_{11}(\omega)\Phi_{22}(\omega)} \tag{3.79}$$

The coherence shows the energy shared between two signals as a function of their frequency band.

3.11.9 Wavelet transform

The wavelet is a time-frequency transformation which permits to decompose the time series in frequency modes and to trace the variation of these modes in time. This approach is different from the short-time Fourier transformation because of the better resolution of high frequencies due to the scale of the wavelet functions.

Here, the starting time series q_n with equal time spacing δt and $n = 0 \ldots N-1$ is considered. The wavelet function $\psi_0(\eta)$, where η is a non dimensional time parameter, is admissible if it has zero mean and is localized both in time and space (Farge, 1992).

In the present work the Morlet function is taken as mother wavelet, which is given in Eq. 3.80.

$$\psi_0(\eta) = \pi^{-1/4}e^{i\omega_0\eta}e^{-\eta^2/2} \tag{3.80}$$

It consists of a plane wave modulated by a Gaussian as shown in Fig. 3.22. The value ω_0 is the non-dimensional frequency that permits to set the resolution of the energies in frequency and time: higher its value, higher the frequency resolution but lower the time resolution of the final power spectrum. In the present work the final value was chosen as $\omega_0 = 6$.

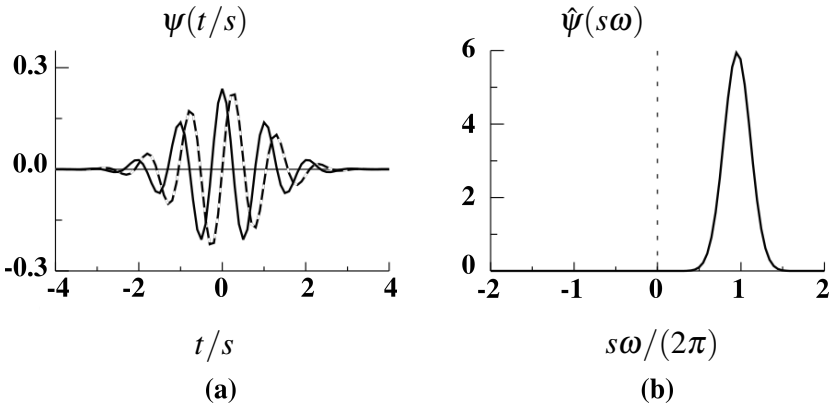

Fig. 3.22 The Morlet wavelet: figure (a) shows the plot of the real part (solid) and imaginary part (dashed) for the wavelets in the time domain. Figure (b) gives the corresponding wavelet in the frequency domain.

The continuous wavelet transform of discrete quantity q_n is defined as the convolution of q_n with a scaled and translated version of $\psi_0(\eta)$. The continuous wavelet transform used in this work can be written as in Eq. 3.81 by following the explication of Torrence and Compo (1998), where the wavelet function Ψ^* is the complex conjugate of Ψ.

$$CWT_n(s_j) = \sum_{i=0}^{N-1} q_i \psi^* \left[\frac{(i-n)\delta t}{s_j} \right] \tag{3.81}$$

The variation of the the wavelet scale s is used to expand and compress the wavelet function which is translated along the discrete time n to give a convolution with the starting signal. Such a convolution has to be calculated N times for each s and it is usually performed in the Fourier space to increase the calculation speed. Furthermore, the wavelet function ψ is the normalized version of ψ_0 at each scale s to ensure that resulting transforms are directly comparable to each others. More details about the normalization process are given in the work of Torrence and Compo (1998).

As result, the wavelet transform gives a real and an imaginary part corresponding to amplitude and phase respectively. In the present study only the wavelet power spectrum is exploited and it can be calculated as $|W_n(s)|^2$. Additionally, the power is normalized by the variance in order to give a measure of the power relative to the white noise as explained by Torrence and Compo (1998).

If the first step is the choice of the wavelet function, the second fundamental step is the choice of the set of scales s to use in the the wavelet transform of Eq. 3.81. According to Torrence and Compo (1998) the smallest resolvable scale is s_0, given in Eq. 3.82, which is used to determine the scales as fractional power of two, see Eq. 3.83, where J determines the largest scale as given in Eq. 3.84.

$$s_0 = \frac{1}{f_{max}} \left[4 \frac{\pi}{\omega_0 + \sqrt{2 + \omega_0}} \right] \tag{3.82}$$

$$s_j = s_0 2^{j\delta j}, \quad j = 0, 1, \ldots, J \tag{3.83}$$

$$J = \frac{1}{\delta_j} \log_2 \left(\frac{N\delta t}{s_0} \right) \tag{3.84}$$

In previous equations, the term $4\pi / \left(\omega_0 + \sqrt{2 + \omega_0^2} \right)$ represents the Fourier wavelength of the mother Morlet function, which is a constant propriety once the ω_0 is chosen.

In turbomachinery, one of the first remarkable examples of wavelet analysis was the work of Inoue et al. (2000), already presented in Section 1.6.2. The great flexibility of this technique when investigating intermittent unsteady flows in turbomachinery has been further remarked by Lewalle and Ashpis (2004), work dealing with the estimation of time-scales in a two-stage low pressure turbine test rig, and Schaefer et al. (2011) in a study about trailing edge vortical structures in a linear turbine cascade.

3.12 Test rig adjustment

This section presents the adjustments and parametric studies carried out on the test rig to find the correct set up. The pressure distribution on the blade surface reported by Ma (2012) for the case $i = 4°$ has been taken as reference for the set up of the test rig so the measurements were performed by using the firs Blade-I. During the setting campaign, high sensitivity to the position of top and bottom flap was highlighted. Furthermore the symmetry and uniformity of the incoming endwall boundary layer between left and right endwall of the test rig was regulated by adjustment of the inlet boundary layer on the left endwall.

3.12.1 Parameters of sensitivity of the cascade

Several measurements were achieved in order to set the blade and the cascade at the correct angle to match the reference configuration adopted by Ma (2012). In particular the blade pressure distribution, and hence the related size of the corner separation, have shown high sensitivity to the following parameters.

- **The angle of the blades**. Careful adjustment of the angle of the blades must be assured to reproduce the same results in each campaign of measurements. Even if the position of the blades is fixed in the cascade by screws, clearance exists in order to arrange the blades permitting rotations up to $\pm 2°$. Furthermore, blade 5, 6 and 7 are fixed on removable endwalls in order to disassemble the test rig between measurements campaign for operations of instrumentation. The verification of the angle must be assured also for these endwalls because clearance is present in the fixation mechanisms. Once the test rig was completely assembled, the stagger angle of the blades were

verified by a goniometer at midspan as well as close to the endwalls. Differences between the blades were within $\pm 0.2°$.

- **The pitchwise distance between the trailing edges of the blades**. The nominal value of the pitchwise distance is $s_p = 134$mm. In the real cascade it is not trivial to find a configuration were such theoretical value is respected for each blade on the whole span. The causes are ascribed to the slight bend of the entire cascade due to its own weight, slight lean of the blades and the existence of clearances between the fixed walls of the cascade and removable endwalls. The maximum difference in pitchwise distance to the nominal value was verified to be within ± 2 mm, i.e. a maximum relative error of $\pm 1.5\%$.

- **Upper and bottom flaps**. The adjustment of the flaps at the ends of the cascade was reported to be one of the major factors in the variation of the incidence on the blades, even if the geometry of the blades was already adjusted and verified. By tilting upward the bottom flap, the incidence on the blade decreases in the same manner as directly decreasing the angle of the entire cascade γ_c. For extremes configurations of the test-rig as $i = 0°$ and $i = 7°$, the adjustment of the upper flap is also necessary. The effect was investigated by varying the position of the bottom flap as shown in Fig. 3.23. Such a behavior of the incidence due to the flap position is to ascribe to the potential effect of the bottom flap, which increases/decreases the deviation of the flow upward as the as the flap is tilted up/down. In order to obtain the correct set up of the test rig, the incidence at the inlet was checked against the position of flaps before each measurement campaign by a five hole pressure probe positioned at the inlet hot-wire station, i.e. $4.13c_a$ upstream of the blade 5.

Such parameters were verified before each measurement, in order to ensure the correct inlet incidence angle and the reproducibility of the setting condition for different measurements campaign.

3.12.2 Symmetry and periodicity

Symmetry of the inlet boundary layer

The asymmetry of the inlet boundary layer on both left and right endwalls was investigated. Since the test rig design does not permit to have complete access to the inlet section, five hole pressure probe measurements were achieved downstream of the cascade removing five blades, in order to maintain the inlet flow unperturbed till the five hole probe station.

This campaign permitted to highlight that the left boundary layer was slightly thinner than the right one, as can be seen in Fig. 3.25a. This difference is better quantified by the velocity difference between left and right boundary layers shown in Fig. 3.25b. The cause of such asymmetry is unknown, it is probably to ascribe to the flow turning in the ducts that connect the test rig to the blower, situated in the basement of the building (not showed in this thesis).

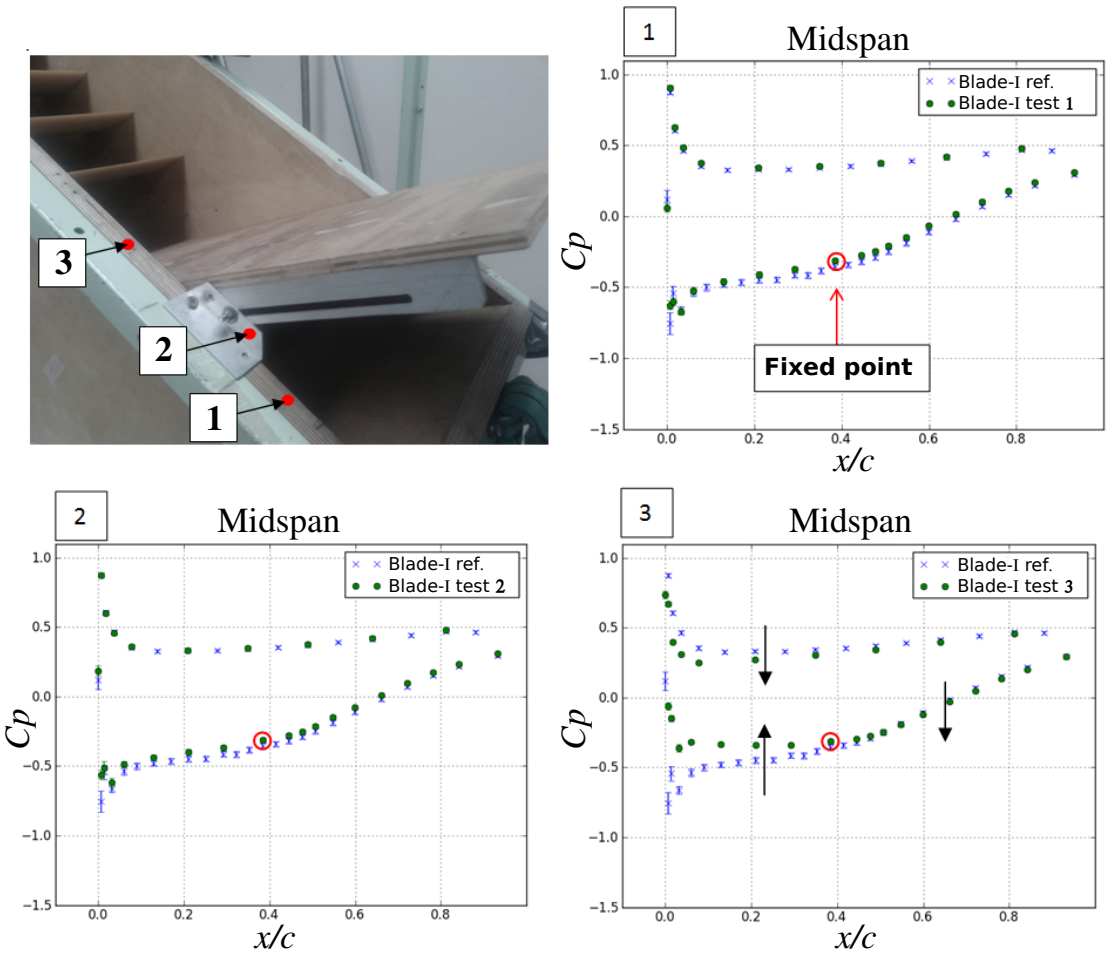

Fig. 3.23 Flap influence on the C_p of blade 5 at midspan: comparison between reference configuration and position 1, 2 and 3 of the bottom flap.

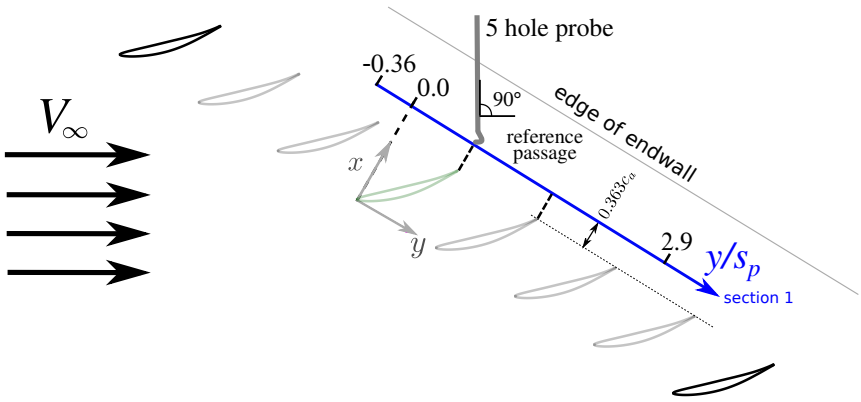

Fig. 3.24 Experimental set-up for the boundary layer symmetry investigation. Removed blades are sketched in light gray color.

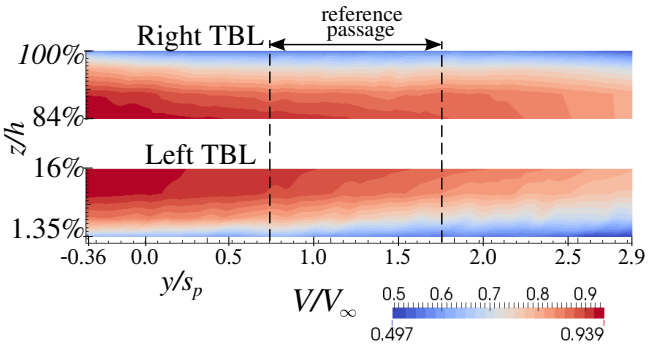

(a) Left and right endwall boundary layers measured by five hole pressure probe at section 1 downstream, blades removed.

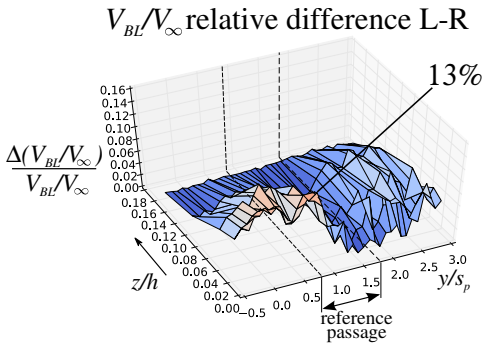

(b) Difference between left and right boundary layer.

Fig. 3.25 Original asymmetry between left and right endwall boundary layers.

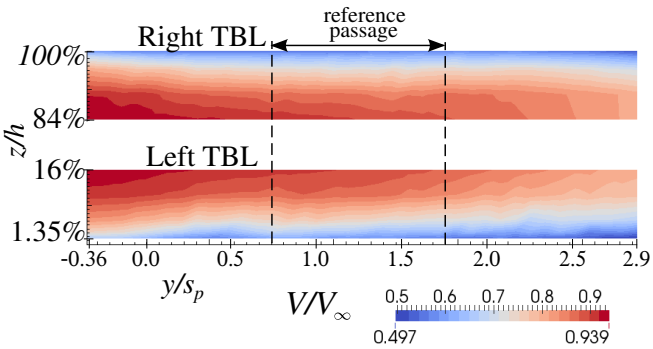

(a) Left and right endwall boundary layers measured by five hole pressure probe at section 1 downstream, blades removed.

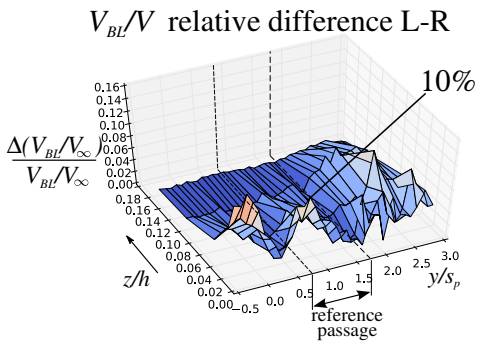

(b) Difference between left and right boundary layer.

Fig. 3.26 Final symmetry obtained between left and right endwall boundary layers.

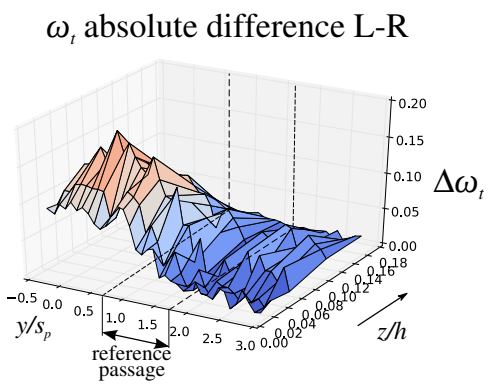

(a) Original asymmetry.

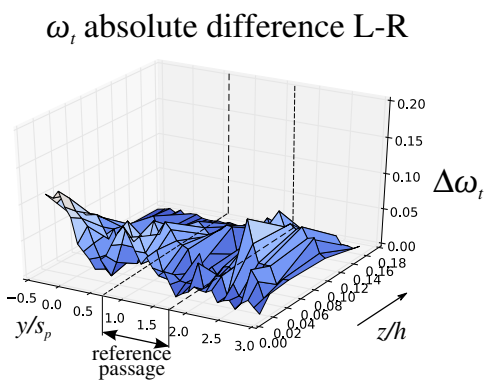

(b) Final symmetrical configuration.

Fig. 3.27 Total pressure losses comparison between original asymmetrical case (a) and final adjusted incoming boundary layers (b).

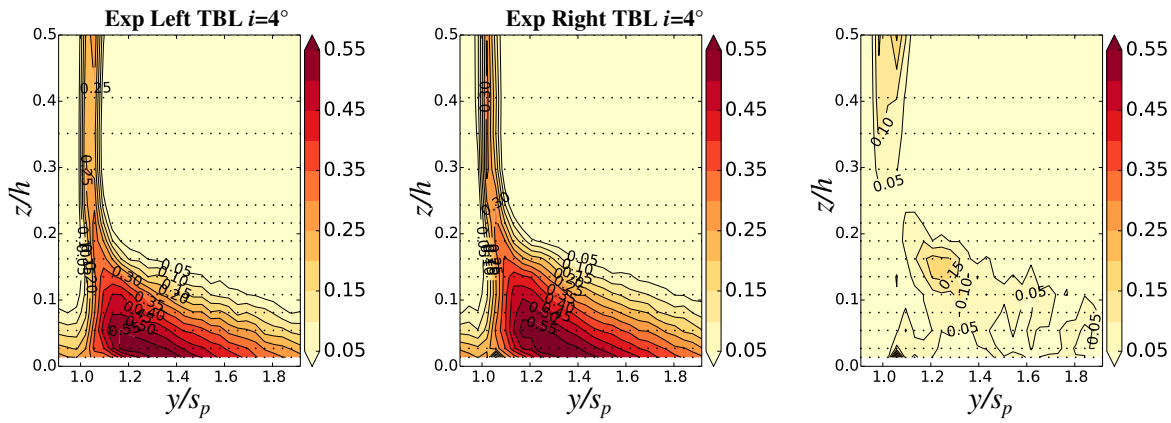

(a) Left CS **(b)** Right CS **(c)** L-R CS losses absolute difference

Fig. 3.28 Downstream total pressure losses ω_t showing the final symmetry obtained between left and right corner separations in the reference passage between Blade 5 and Blade 6.

In order to avoid the asymmetry, the left wall was equipped with two wood steps at $10c$ upstream of the blade to thicker the boundary layer only in the left upper part of the test rig. This operation permitted to obtain a symmetric boundary layer and consequently a more symmetric corner separation on the left and right walls of the reference blade passage, once the blades were re-installed in the test rig. The Fig. 3.26 shows the result achieved, with a sensible reduction of the difference between left and right velocity profiles, in particular between $z/h = 4\%$ ($z/c = 0.1$) and $z/h = 14\%$ ($z/c = 0.33$). A maximum 10% of discrepancy remained very near the endwall. A better description of the amelioration of the symmetry of the test rig is given by evaluating the difference in total pressure losses between the two sides, as shown in Fig. 3.27b: the bump in the region $-0.5 < y/s_p < 1$ is almost completely removed.

The results of total pressure losses downstream of the cascade are shown in Fig. 3.28, where left and right refer to the sides of the cascade, within the inter-blade passage between blade 5 and blade 6. The level of symmetry reached was the maximum achievable considering the intrinsic difference of inlet boundary layers of the test rig.

Periodicity of the flow through the cascade

Five hole pressure probe measurements additionally permitted to adjust the periodicity of the cascade. This process was not a trivial operation because of the interaction between the pitchwise irregularity of the inlet boundary layer and the slight differences between the pitchwise distance and angle of the blades. For this reason, the periodicity had to be considered with symmetry at the same time.

Fig. 3.29 shows the result of the obtained separations on the left side of the cascade downstream of four blades. The size of the corner separation in the reference passage is larger than the separation of the previous blade (first corner separation on the left) and smaller

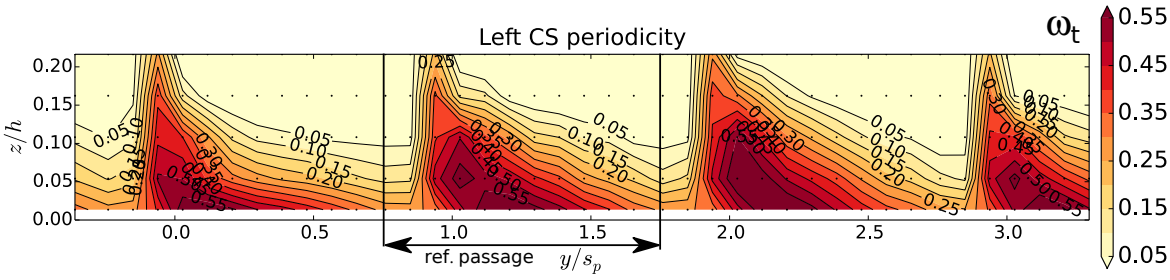

Fig. 3.29 Final obtained periodicity of total pressure losses on left side of the test rig.

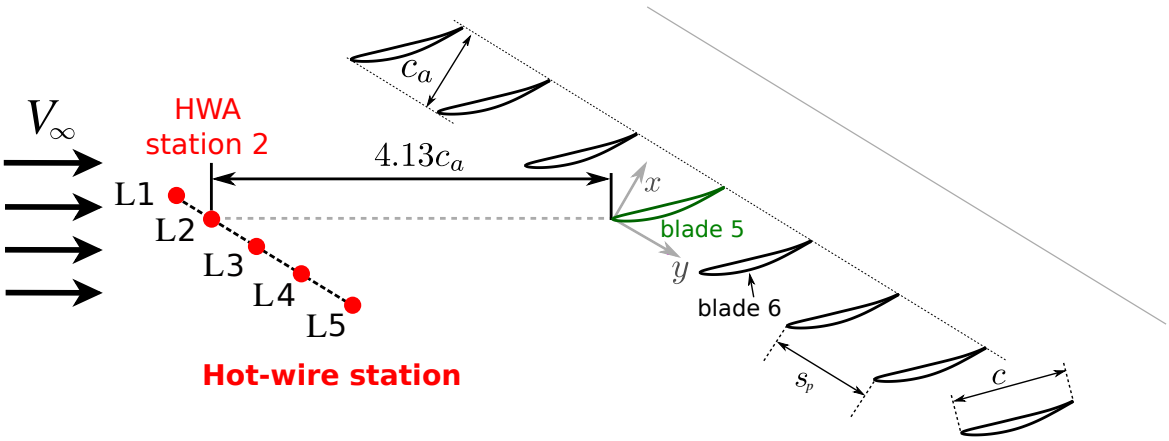

Fig. 3.30 Sketch of inlet hot wire station of measurement.

than the following separation (on the right). Such effect is caused by the enlargement of the inlet boundary layer profile in pitchwise direction because of the longer distance that the inlet flow has to travel to reach the successive blades.

3.13 Inlet boundary layer verification

The inlet boundary layer has a major role in the contribution to total size of the corner separation as shown in the numerical study of Gao (2014). The increase of the incoming boundary layer thickness enhances total pressure losses downstream of the blade row, in particular near the endwall.

Hot-wire measurements were carried-out at $4.13c_a$ upstream of the reference blade number 5, as shown in Fig. 3.30. The hot-wire technique, the experimental set up and the uncertainty adopted for these measurements are the same adopted in the work of Ma (2012).

Characteristic integral parameters of the inflow boundary layer at the cascade inlet are listed in Table 3.15. Present measurements are compared to past measurements of Ma (2012), taken at several pitchwise stations, and the experimental value which was the reference for the LES of Gao (2014).

The thickness of the boundary layer is denoted as δ_{99} because it is taken at the position of the inlet profile where the 99% of the free stream velocity magnitude is reached. Furthermore,

Table 3.15 Parameters of the inflow boundary layer.

	δ_{99}(mm)	δ_1(mm)	δ_2(mm)	$H_{12} = \delta_1/\delta_2$	u_τ(m/s)	$Re_{\delta_2} = V_\infty \delta_2/\nu$
L1-P0	30.1	3.7	2.9	1.29	1.46	7359
L2-P0	29.1	3.8	2.9	1.28	1.46	7374
L3-P0	30.1	4.0	3.1	1.29	1.46	7961
L3-P2	30.1	4.0	3.1	1.29	1.44	7930
L4-P0	32.1	4.5	3.5	1.28	1.46	9033
L4-P1	31.1	4.8	3.7	1.30	1.43	9502
L5-P1	30.1	4.1	3.2	1.28	1.45	8283
Uniform TBL	36.0	4.8	3.8	1.27	1.45	10082
Ref Exp	30.0	3.7	2.8	1.32	1.45	7200
LES	27.3	3.7	2.8	1.31	1.34	7400

the displacement thickness δ_1, the momentum thickness δ_2 and shape factor H_{12} are calculated according to Eq.s 3.85, 3.86 and 3.87, respectively. In this equations V_e is the mean velocity at the limit of the boundary layer.

$$\delta_1 = \int_0^\delta \left(1 - \frac{V}{V_e}\right) dz \tag{3.85}$$

$$\delta_2 = \int_0^\delta \frac{V}{V_e}\left(1 - \frac{V}{V_e}\right) dz \tag{3.86}$$

$$H_{12} = \frac{\delta_1}{\delta_2} \tag{3.87}$$

The friction velocity u_τ was not measured directly but evaluated indirectly from least-square fitting of the van Driest profile between $z^+ = 10 \sim 50$, as described in Ma (2012). The final integral parameters of the inlet boundary differs of 20% from past investigations.

However, this difference can be explained by analyzing the comparison shown in Fig. 3.31 between the adjusted uniform boundary layer and previous measurements presented in the work of Ma (2012). When analyzing the mean velocity $< u >^+$ in inner coordinates, in Fig. 3.31a, every measurement fits the Van Driest profile even if slight differences are visible in the defect law between the uniform TBL and previous campaign. Moreover, in the outer region, the level of the mean velocity of the uniform TBL is enclosed by the values measured by Ma.

This characteristic of the uniform TBL, i.e. to fall in the range of values of past measurements, is highlighted again when looking at the velocity RMS in inner coordinates, as shown in Fig. 3.31b. The distribution of blue points in the buffer and log region is enclosed within the distributions obtained for the measurements of the original boundary layer, matching the purple distribution L3-P0. The variation of the ${u'_{rms}}^+$ measured in the past is explained by

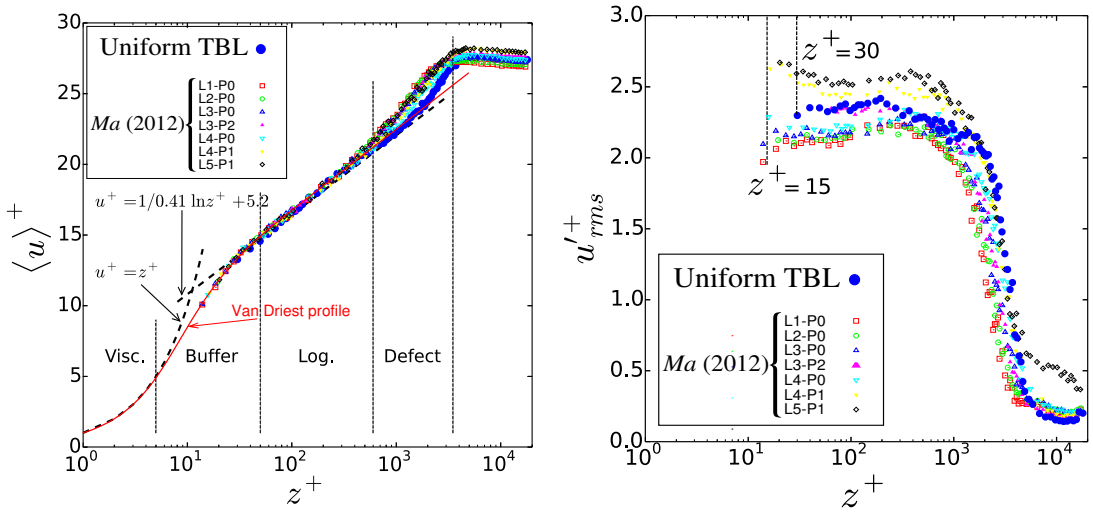

(a) (b)

Fig. 3.31 Comparison between experimental results of the inlet boundary layer at the reference section $4.13c_a$ upstream of the blade obtained after setting the uniformity and previous measurements shown in Ma (2012).

the fact that different locations in pitchwise direction were investigated in the work of Ma. The original incoming boundary layer on the left endwall was too thin in the upper part of the test, whereas increasing too fast in pitchwise direction, as proved by Fig. 3.25a, previously presented in Section 3.12.2.

As conclusion, this comparison confirms that the new inlet boundary layer is characterized by an improved uniformity of its evolution in pitchwise direction, matching the symmetry with the right boundary layer, and for this reason the inner turbulent quantities measured at L2 match the results which were previously obtained in the middle position L3.

The hot-wire investigation permits to check the time tracers of the time-resolved velocity as well as spectra at the inlet section. As can be seen in Fig. 3.32, the power spectral densities do not present any particular peak at frequencies lower than 5 KHz , evidence that the incoming flow is not affected by any vortex shedding nor periodical coherent structure in this range of frequencies. In general for spanwise distances corresponding to the thickness of the inlet boundary layer $\delta_{99}/h = 36/370 = 0.097$ ($\delta_{99}/c = 36/150 = 0.24$), i.e. from $z/h = 0.014$ ($z/c = 0.033$) to $z/h = 0.108$ ($z/c = 0.266$), no meaningful peaks are present. This proves that the wood steps installed for the symmetry adjustment were sufficiently far upstream ($\approx 10c$) of the blade row to avoid unsteady perturbations and to assure the dissipation of coherent structures locally generated by the step.

In the free stream, i.e at sections $z/h = 0.22$ ($z/c = 0.533$) and midspan $z/h = 0.5$ ($z/c = 1.233$), the turbulence level decreases in comparison to the wall boundary layer. The mean level of the energy associated to the streamwise fluctuation of velocity u^2 in the Fourier spectra decreases accordingly. Furthermore the energy decay appears earlier in the

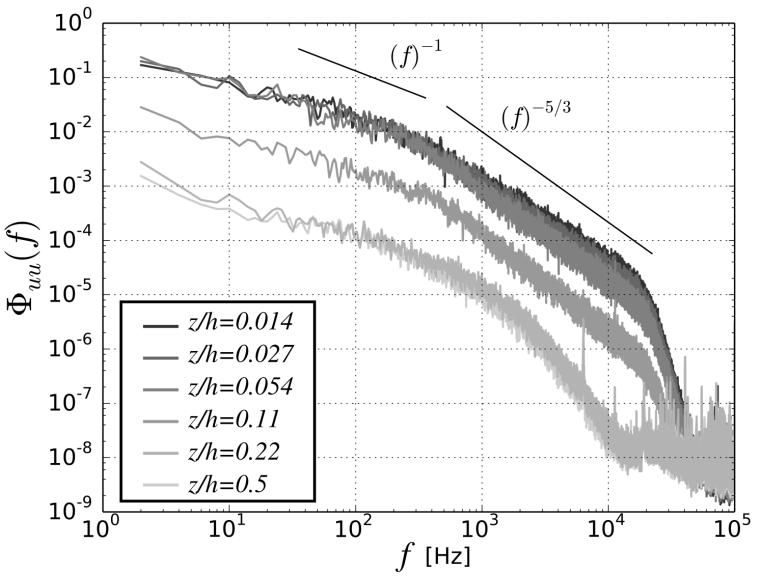

Fig. 3.32 Spectra of velocity for different points of the inlet boundary velocity profile measured at the reference section $4.13c_a$ upstream of the blade.

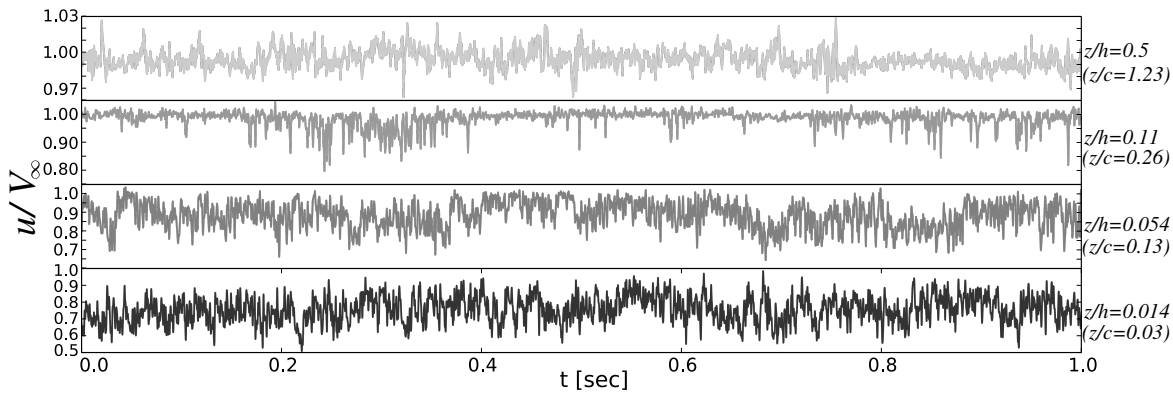

Fig. 3.33 Time tracers of velocity in different locations of the inlet velocity profile acquired at the reference section L2 $4.13c_a$ upstream of the blade. Extraction of 1 sec from the signal, low-pass filter applied at $f = 1$ KHz, adapted y-scale.

free stream than near the wall, as confirmed by the increasing of the slope of the spectrum between at 1 KHz and 10 KHz.

Even if spectra show that no periodic phenomena are present in the signal, time tracers must be verified. Unlike the universal equilibrium range indeed, the energy-containing range located at lowest frequencies depends on the particular flow and one-dimensional spectra provides in this case little direct information (Pope, 2001). Four position, two within the boundary layer $z/h = 0.014$ and $z/h = 0.054$ and two outside, i.e. $z/h = 0.11$ and midspan, are chosen and presented in Fig. 3.33. The y-scale of this plot is adapted, because the oscillations of the velocity at midspan are solely 10% of the oscillations near the endwall

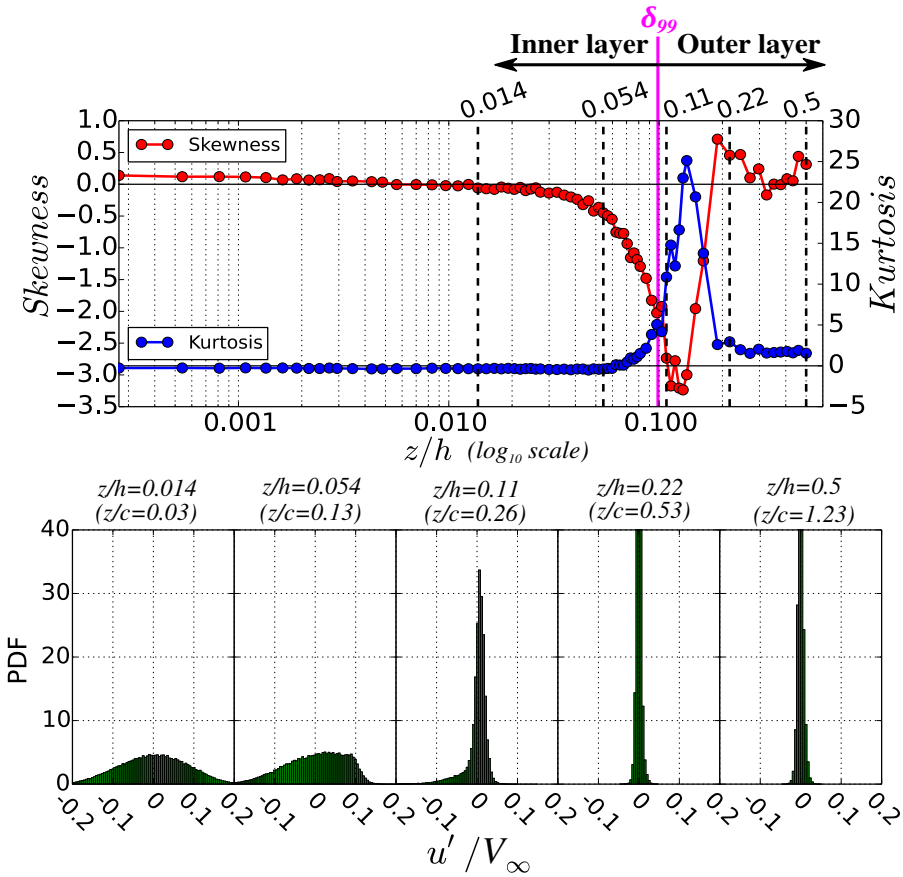

Fig. 3.34 Top figure: skewness and kurtsosis of the measured velocity profile at $4.13c_a$ upstream of the reference blade. Bottom figure: Probability distributions of velocity fluctuations in the streamwise direction u' normalized by the inlet velocity at five chosen positions z/c, represented also on the top figure.

in the boundary layer. At midspan no low frequencies oscillations of the signal are present but at $z/h = 0.11$, slight outside the boundary layer, drops of velocity are visible due to the unsteadiness of the largest structures in the boundary layer. In the inner region, both at section $z/h = 0.054$ ($z = 20$ mm) and $z/h = 0.014$ ($z = 5$ mm), a low frequency modulation of the signal can be recognized. Such oscillations are in agreement with small bumps in the power spectra at frequency comprised between 9 Hz and 15 Hz, recognizable in Fig. 3.32. These oscillations are not periodic but random in amplitude and frequency. For such reason it can be inferred that large scale random events are inherent characteristics of the development of the turbulent boundary layer in the present test rig.

Additionally, it is necessary to verify whether the existence of an hypothetical perturbation of the incoming free stream changes statistical distributions of the velocity. Probability distributions have been calculated in order to assure that the bimodal phenomenon reported at the boundary of the corner separation is not a consequence of a bimodal state of the incoming flow. The top figure of Fig. 3.34 represents the skewness and kurtosis of the velocity fluctuations in the streamwise direction sensed by the hot-wire probe at the position

L2. These measurements refers to the inlet boundary layer adjusted to be uniform on the left wall and symmetrical to the boundary layer of the right wall. The measured thickness of the BL at this position is $\delta_{99}/h = 0.097$. In the log-layer, i.e. below 6 mm considering the section at $z/h = 0.014$, the skewness is positive and the kurtosis Ku has zero value, which corresponds to the Gaussian distribution. The skewness then starts to assume negative values at the beginning of the defect region, reaching a maximum at the limit of the inner layer. This region, which crosses the boundary between inner and outer-layer, is characterized by high intermittency of fluctuations, verified by the peak of kurtosis and the jump of the skewness distribution between negative values and positive values.

For the selected positions, localized by dashed lines on the skewness/kurtosis graph, the probability density functions are calculated and shown in the bottom plot of Fig. 3.34. The distribution at $z/h = 0.014$ ($z = 5$ mm), which is positioned at the limit between the log region and the defect region, is Gaussian and the maximum velocity fluctuations exceed 20% of the inlet velocity. Only the negative part of these large fluctuations is conserved in the second point at $z/h = 0.054$. This because the mean value of the velocity rises whereas the eddies of the boundary layer still decelerate the flow producing large negative velocity fluctuations. The distribution is hardly skewed but not bimodal. At the boundary between inner and outer layer, this process is enhanced and the fluctuations diminished, whereas the distribution becomes sharper. In the outer layer, the level of largest fluctuation is within $\pm 4\%$ of the inlet velocity and the distribution is Gaussian with slight levels of positive skew. Such values are consistent with the turbulent level of the test rig measured by Ma (2012), $Tu = 0.8\%$.

3.14 Conclusions

Different techniques of measurement are used in this work and discussed in this chapter. The crucial points highlighted by the above discussion can be resumed as follows.

- Time-resolved unsteady pressure measurements on the surface of the blade are completely reliable from 10 Hz up to 10 KHz. Differently, higher uncertainty surrounds lower frequencies, from 3 Hz to 10 Hz, so the results showing energy in this range must be evaluated by comparison with other techniques, such as time-resolved PIV.

- Unsteady total pressure measurements carried out by time-resolved sensors placed at bimodal points in different blade passages show very low uncertainty and can be considered completely reliable in the whole frequency range. Additionally, the position of the sensor at points which experience the bimodal flow was assessed and corrected during the measurements.

- Stereo PIV measurements are affected by peak-locking. As a consequence, solely averaged velocities can be considered reliable, whereas turbulence quantities such as Reynolds stresses are probably under estimated in the region of higher unsteadiness.

- The 2D2C time-resolved PIV measurements show very low levels of peak-locking and total uncertainty, which leads to the conclusion that such measurements can be considered of high quality and completely reliable.

The second part of the chapter present the test rig adjustment, which resulted to be crucial for comparison and reliability of the present measurement. The major achievements on this topic are resumed as follows.

- The periodicity and symmetry of the flow through the blade row is affected by different parameters such as slight difference in the angle of the blades and their pitchwise distance. Furthermore, attention should be put in the set up of the bottom and top flaps of the test rig, which have an influence on the incidence angle upstream of the cascade because of the potential effect on the upstream flow.

- The original inlet boundary layer was verified to be non symmetric between the left and the right endwall of the cascade. In order to correct the symmetry and improve the uniformity of the boundary layer on the reference side of the cascade (left side), a wood step was installed on this wall ten chords upstream of the blades. Five hole pressure measurements were carried out in order to verify the achievement of the symmetry.

- The periodicity was adjusted but corner separations enlarge from the upper passages of the blade cascade to the bottom passages on both sides of the test rig. This is due to the longer distance traveled by the incoming flow to reach the bottom blades and the consequent enlargement of the endwall boundary layer in pitchwise direction.

- The incoming boundary layer upstream of the reference blade on the left side was verified by time-resolved hot wire measurements. The wood step used to increase the thick and the symmetry of the boundary layer does not influence the unsteadiness of the signals, since no well defined peaks appear in the power spectral densities of the velocity within the boundary layer. Furthermore, the statistical distributions of the velocity in the incoming boundary layer have been verified to be coherent with classical TBL and do not present the bimodality.

In conclusion, the study of the unsteadiness of the corner separation in compressors requires time-resolved measurements of high reliability and accuracy. If general conclusions on the behaviour of the separation want to be drawn, crucial efforts must be addressed to verify and characterize all sources of unsteadiness in the test rig in order to be capable of avoiding installation effects.

Chapter 4

Characterization of corner separation: Time-averaged VS Unsteady behavior

Contents

4.1 Introduction 121

4.2 Time averaged characterization 122

4.2.1 Inter-blade investigation 122

4.2.2 Downstream investigation 124

4.2.3 Comparison with previous work 130

4.3 The signature of the separation unsteadiness in pressure statistics . . 133

4.3.1 Main regions of unsteadiness in the suction surface pressure distribution 133

4.3.2 The separation detachment highlighted by skewness 133

4.3.3 Intermittency regions on the suction surface 136

4.4 The bimodal unsteadiness 137

4.4.1 Punctual time-resolved characterization 137

4.4.2 Decomposition of the unsteadiness 140

4.5 Summary and conclusions 142

4.1 Introduction

The common way to evaluate a separation is by measuring total losses downstream of the separation. Then, if time-resolved measurements are available, the fluctuations and statistics of the measured quantities are computed, but only by going further to higher order statistics, the hidden footprints of the unsteady character of the separation can be reveled. At first, this chapter presents to the reader the time-average characterization of the separation by the

average topology and Reynolds stresses in the blade passage, followed by the downstream characterization of the separation. Furthermore, the study is extended to the static pressure on the surface of the blade and the associated fluctuations as well as higher order statistical moments to uncover the signs of the unsteadiness of the separation. Finally, three points are chosen in the region of highest unsteadiness of the flow field, i.e. at the boundary of the time-averaged separation, to show the bimodal behaviour by describing statistical distributions and related time-tracers of the velocity.

4.2 Time averaged characterization

The present section describes time average quantities measured within the inter-blade passage and downstream of the cascade. The influence of the increase of inlet incidence between $i = 4°$ and $i = 7°$ is described through losses, static pressure coefficient, velocity, secondary flow and angles comparisons.

4.2.1 Inter-blade investigation

Average topology

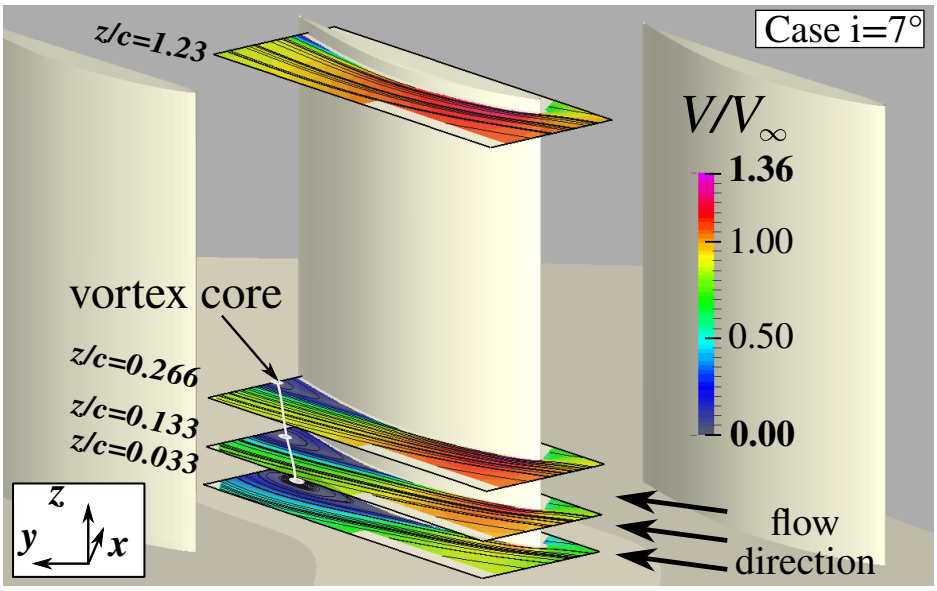

Fig. 4.1 Three dimensional visualization of 2D sections characterized by normalized absolute velocity and streamlines (black lines). Sections at $z/c = 0.033$, $z/c = 0.13$, $z/c = 0.266$ and $z/c = 1.23$ from the end-wall.

Generally, the topology of the corner separation is not unique but depends on the geometry of the blade and the endwalls. Anyway, the presence of a focus on the endwall in the aft part of the blade is expected for linear cascades with NACA profiles, simple zero lean blades and smooth endwalls. The magnitude of the 2D velocity for different sections along the

span acquired by HS-PIV is shown in Fig. 4.1. The configuration $i = 7°$ has been chosen for this description because the larger size of the separation permits a better visualization of the topology. The picture confirms that the time-averaged topology of the separation in the present cascade is characterized by a large vortex impinging on the end-wall near the trailing edge of the blade. Such a time-averaged structure follows the surface of blade in spanwise direction till it disappears in these measurements as the distance from the end-wall increases and the separation decreases. At this position, the leg of the time-averaged vortex turns and it aligns with the streamwise direction while is convected downstream. The case at lower incidences $i = 4°$ is not shown here but presents an identical topology characterized by a vortex core closer to the surface of the blade and less extended in spanwise direction.

Reynolds stresses

Stereo PIV measurements show the magnitude of Reynolds stress term, i.e. $\overline{u_s{}'v_n{}'}$, in Fig. 4.2 normalized by the quadratic magnitude of the inlet velocity.

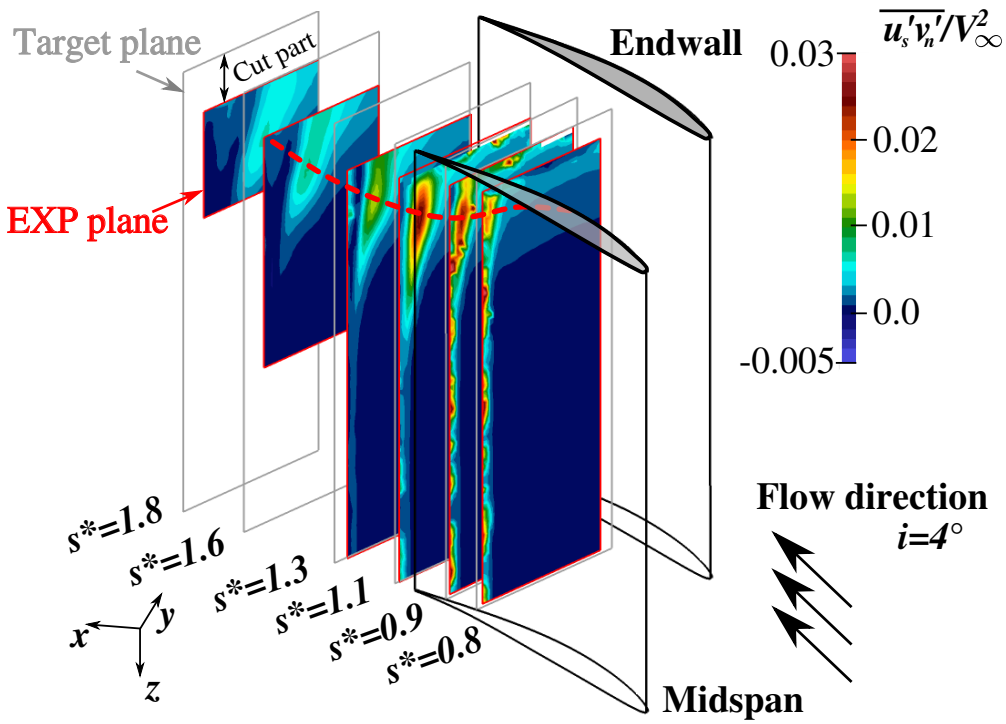

Fig. 4.2 Normalized Reynolds stresses achieved by SPIV measurements for the cascade configuration $i = 4°$. Target plane: reference plane of measurement. EXP plane: final region of the target plane retained after field cut process applied because of reflections and limitations of the field of view.

The final experimental planes are cuts of target planes due to light reflections in proximity of the endwall and field of view limitations due to the test rig. Even if the region closest to the endwall was not measured, the locus of larger Re stresses was captured by the SPIV. As highlighted by the red dashed line in Fig. 4.2, the locus of larger Re stresses describes a three

dimensional path that starts near the endwall in the corresponding position of the detachment of the front of the separation. This line then follows the separation boundary on the surface of the blade, shifting in spanwise direction away from the endwall but additionally lifting off from the surface of the blade. The result agrees with theory and demonstrates that when considering a corner separation, the region where the largest amount of energy dissipation takes place does not correspond to the inner part of the separated flow, but instead to the boundary between the separation and the free stream.

4.2.2 Downstream investigation

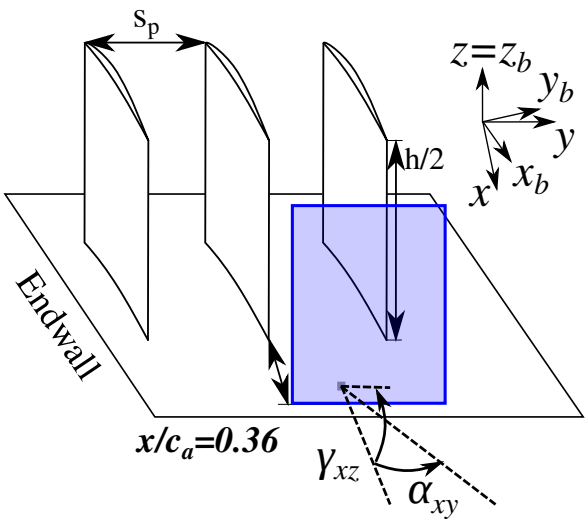

Fig. 4.3 Sketch of the plane of measurement at $x_c/c_a = 36.3\%$ downstream of the TE and angles: pitchwise angle α_{xy} and span-wise angle γ_{xz}.

Total pressure losses

Since one of the most common technique to evaluate the size and the deleterious effects of the corner separation is by calculation of total pressure losses, the five hole pressure measurements are discussed at first. The time-averaged total pressure p_{t5T} is achieved downstream of the blade by the five hole pressure probe at the section $x_c/c_a = 36.3\%$ from the TE of the blade. The total pressure losses, defined as in Eq. 4.1, are shown in Fig.s 4.4a and 4.5a for the case $i = 4°$ and $i = 7°$, respectively.

$$\omega_t = \frac{p_{t_\infty} - p_{t5T}}{p_{t_\infty} - p_{s_\infty}} \tag{4.1}$$

The wake increases and the separation size grows predominantly in the span-wise direction between $z/c = 0.2$ and $z/c = 0.5$. These results confirm that the overall total pressure losses increase as the inflow incidence angle i is increased. The magnitude of the maximum peak of losses near the endwall remains the same, i.e $\omega_{tCS} = 0.55$. By taking $\omega_{twake} = 0.275$ as

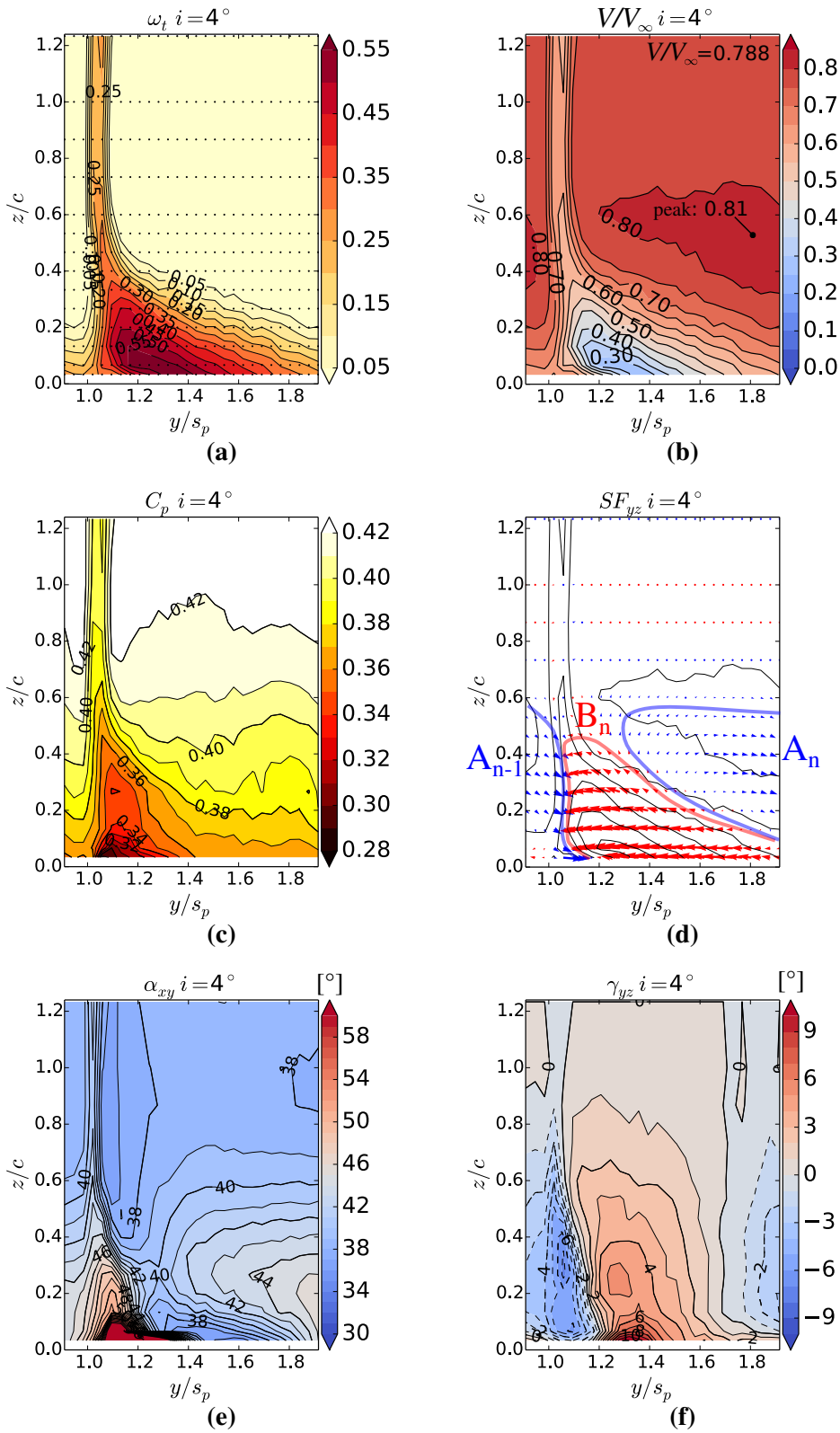

Fig. 4.4 Time average characterization of the corner separation at the section $x_c/c_a = 36.3\%$ downstream of the TE for the configuration $i = 4°$. Total pressure losses (a), absolute velocity $\overline{V}/V_\infty$ (b), static pressure coefficient (c), secondary flow vectors (d), pitchwise angle (e) and spanwise angle of the flow (f). In secondary flow figure (d) the blue vectors give $SF_y > 0$ whereas red vectors are $SF_y < 0$.

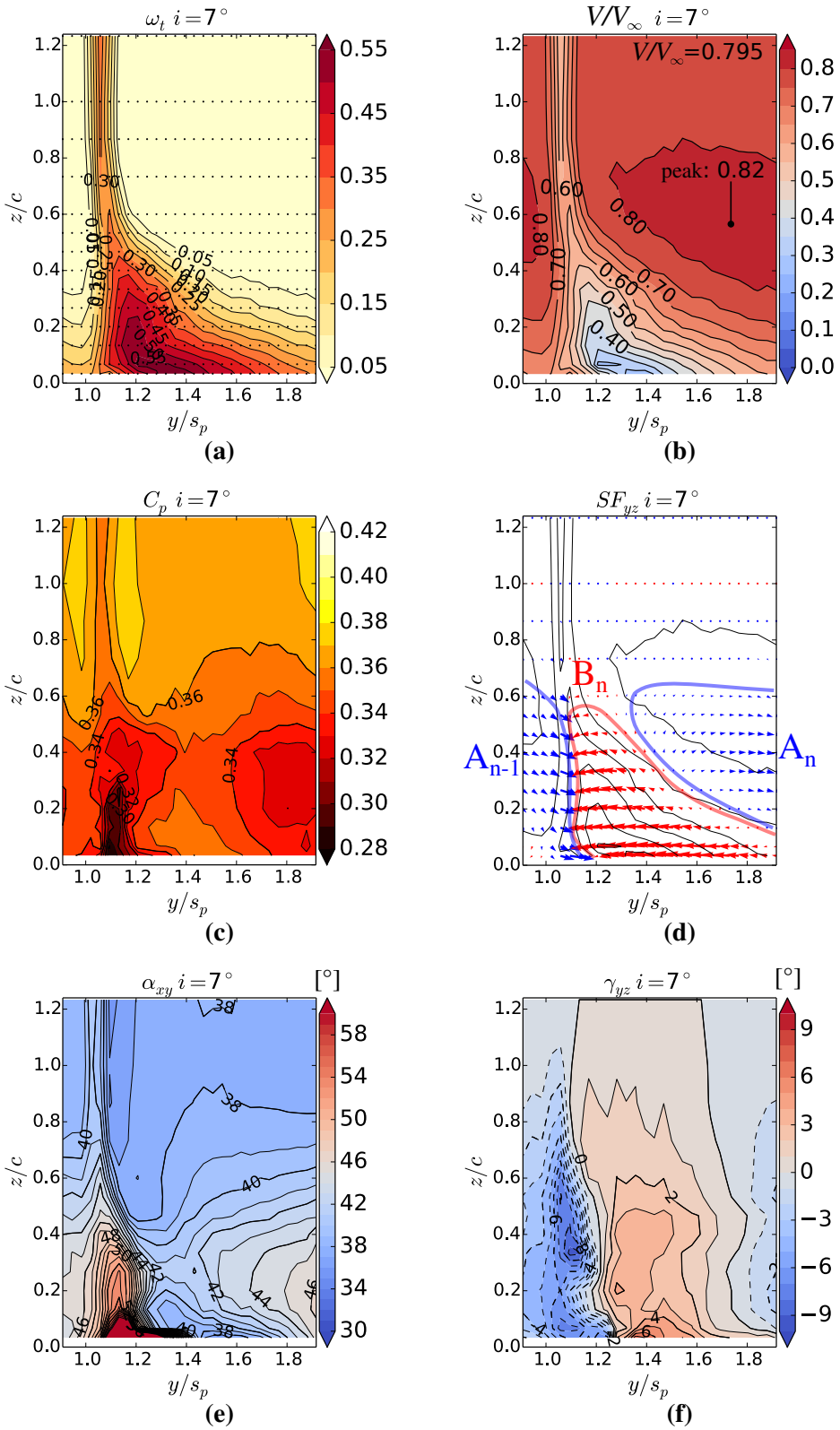

Fig. 4.5 Time average characterization of the corner separation at the section $x_c/c_a = 36.3\%$ downstream of the TE for the configuration $i = 7°$. Total pressure losses (a), absolute velocity $\overline{V}/V_\infty$ (b), static pressure coefficient (c), secondary flow vectors (d), pitchwise angle (e) and spanwise angle of the flow (f). In figure (d) the blue secondary flow vectors give $SF_y > 0$ whereas red vectors are $SF_y < 0$.

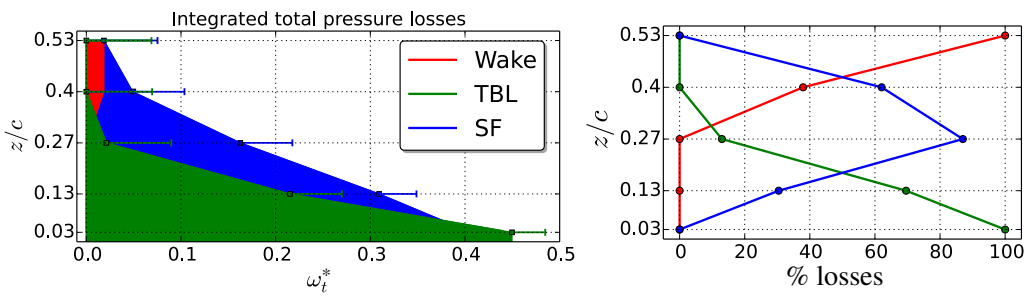

(a) **(b)**

Fig. 4.6 Figure (a) shows the pitchwise-mass-averaged total pressure loss coefficient from $z/c = 0.03$ (z= 5 mm) and $z/c = 0.53$ (z = 80 mm). Green: endwall boundary layer TBL. Red: wake. Blue: secondary flows losses SF. Bars represent the uncertainty associated to the measurements. Figure (b) resume the relative contribution of each term .

mean value for the losses in the blade wake, which is illustrated in Fig. 4.4a and Fig. 4.5a, it results $\omega_{tCS}/\omega_{twake} = 200\%$ for both the investigated incidences, as described by Denton (1993) and reviewed in Section 1.4.1. Finally, the shape of the total pressure deficit region is sharp and the iso-losses contours are well defined: such features are consistent with the outlet losses map for the fully turbulent flow induced by upstream rotors reproduced from Schulz et al. (1990b) in Fig. 1.16b of Section 1.5.

Losses decomposition

Exploiting the measurements of the incoming boundary layer carried out by removing five blades, described in Section 3.12.2, the losses production in the separation region can be decomposed. Fig. 4.6 illustrates that three main different sources of losses can be distinguished: the inlet boundary layer, the wake losses associated to the blade profile and finally the losses due to the secondary flow which form the corner separation.

The separation measured for this characterization is situated in the reference passage for the configuration at $i = 4°$. The compared quantity is the pitchwise-mass-averaged total pressure loss coefficient described by the Eq. 4.2. Since the investigated flow is incompressible, the density $\rho(y,z)$ is considered to be constant.

$$\omega_t{}^* = \frac{\int_0^{s_p} \omega_t \rho u \, \mathrm{dy}}{\int_0^{s_p} \rho u \, \mathrm{dy}} \tag{4.2}$$

The profile wake losses are estimated as the losses measured outside the corner separation region, i.e. at the section $z/c = 0.53$. These losses, which are basically due to the boundary layer developing on the surface of blade, are considered to give a contribution only outside the region of influence of the inlet boundary layer. This assumption is based on the idea that the existence of a blade profile boundary layer is not meaningful within the endwall boundary layer, since turbulent flow structures and mixing losses are already generated upstream of the blade. Conversely, the presence of the blade in such regions generates losses related to

the secondary flows. Subtracting the inlet boundary layer losses from the separation global losses it is possible to obtain the SF contribution.

Fig. 4.6 shows that near the endwall at $z/c = 0.03$, the entire contribution is given by the endwall boundary layer losses. These losses decrease in spanwise direction as the secondary flow contribution starts to rise, and fall down to 13% reaching the limit of the boundary layer at $z/c = 0.27$. In this section conversely the secondary flows produce the maximum losses, the complementary 87%, as described in Fig. 4.6b. The blade profile losses start to rise from section $z/c = 0.27$ moving farther from the endwall, whereas the losses due to the boundary layer reach the zero value at $z/c = 0.4$. The main influence at this spanwise position is given again by the secondary flows, but the overall losses are drastically reduced of a factor nine, since $\omega_t{}^*$ is decreased from the maximum value $\omega_t{}^* = 0.45$ at $z/c = 0.03$ to $\omega_t{}^* = 0.05$ at $z/c = 0.4$. Finally, the section $z/c = 0.53$ is not affected by the corner separation anymore, and the losses are reduced to the profile losses of the blade, which are then conserved from this section till midspan, as shown in Fig. 4.4a.

In conclusion, in the span height considered for this decomposition, i.e. from the endwall to the limit of influence of the corner separation, the overall amount of losses is distributed into such partials contributions: 57% related to the inlet boundary layer, 39% due to the secondary flows and 4% due to the profile losses.

Velocity and secondary flows

At the same downstream position, contours of the normalized time-averaged velocity $\overline{V}/V_\infty$ sensed by the five hole probe are shown in Fig.s 4.4b and 4.5b for both configurations of the test rig. The magnitude of the velocity at midspan outside the wake is 0.788 for $i = 4°$ and 0.795 for $i = 7°$, whereas in the core of the separation it reduces to 0.3. A region of velocity magnitude larger than 0.8 can be seen just outside the boundary of the separation for both configurations. The size of this region differs between the configuration investigated as well as the peak of the quantity $\overline{V}/V_\infty$, which rises from 0.81 to 0.82 as the incidence is increased.

Secondary flows associated to the presence of the separation are presented in Fig.s 4.4d and 4.5d for both configurations of the test rig. The secondary flow vectors can be calculated as described in Eq. 4.3

$$SF_{yz} = \begin{cases} v(y,z) - v(y,z)_{z/c=1.23} \\ w(y,z) - w(y,z)_{z/c=1.23} \end{cases} \tag{4.3}$$

Two distinct regions of the flow are highlighted for both configurations in Fig. 4.4d and Fig. 4.5d. The blue region, recognized as A_n for the reference passage and A_{n-1} for the preceding passage, corresponds to the secondary vorticity induced by the turning of the cascade, as expected by the mechanism discussed reviewing secondary flows in Section 1.3.2. The region associated to the corner separation, which is highlighted in red and identified as B_n, exists between the blue regions. This region is characterized by a strong secondary flow movement near the endwall from the pressure side of the following blade to the suction side of the reference blade, but also a spanwise movement at $y/s_p = 1.1$ from $z/c = 0.6$ towards the endwall. Here, the secondary flows of regions A_{n-1} and B_n collide, generating a strong

three-dimensional component normal to the plane of measurement and directed backwards to the TE of the blade.

In order to understand this interaction, three-dimensional secondary flow vectors SF_{xyz} are presented in Fig. 4.7. The direction of the vectors in the region corresponding to the core of losses is reversed, in agreement with the presence of a recirculating flow within the corner separation.

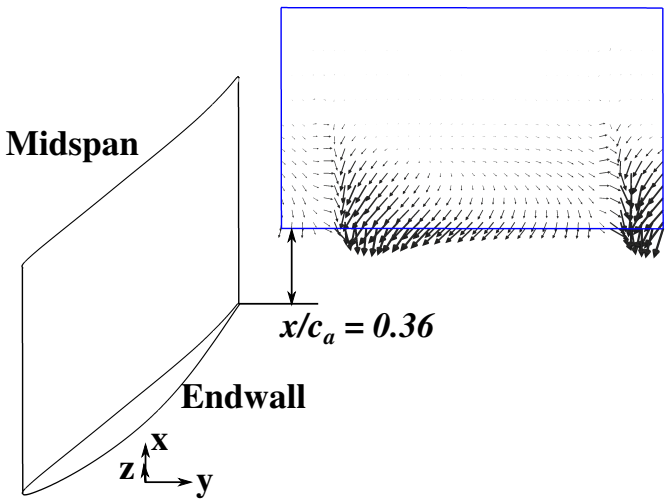

Fig. 4.7 Three-dimensional secondary vectors at $x_c/c_a = 36.3\%$ downstream of the TE for $i = 7°$.

Flow angles

The pitchwise flow angle α_{xy} is shown in Fig. 4.4e for $i = 4°$ and Fig. 4.5e for $i = 7°$. It can be seen that the corner separation causes under-turning of the flow near the endwall between $y/s_p = 1.0$ and $y/s_p = 1.4$, for both configurations. A region affected by angles larger than 45° extends in spanwise direction to $z/c = 0.25$ for the configuration $i = 4°$ and increases to $z/c = 0.4$ for $i = 7°$. The region of magnitude $50° < \alpha_{xy} < 55°$ is the one that most differs between the two configurations, spreading farther from the endwall in spanwise direction as the incidence is increased. This fact highlights the increasing of the vortical system associated to the corner separation more in spanwise direction than in pitchwise direction. This particularity can be explained by remembering that the main mechanism of losses near the endwall remains the development of endwall boundary layer and its interaction with the corner separation. Consequently, the under-turning and the total pressure losses peak do not increase since the incoming boundary layer upstream of the cascade remains unchanged between the two configurations.

The alteration of the three-dimensional topology of the flow leads to an increase of the spanwise flow and the associated angle γ_{xz}, as it can be recognized by comparing Fig. 4.4f for the case $i = 4°$ and Fig. 4.5f for the case $i = 7°$.

The incidence increment is associated to two main effects on the spanwise angle γ_{xz}: the increase of the negative magnitude of the angle in the blue region, located between $y/s_p = 1.0$ and $y/s_p = 1.2$ from $z/c = 0.35$ and $z/c = 0.9$, and the decrease of positive magnitude of γ_{xz} on the suction side of the wake, i.e. between $y/s_p = 1.2$ and $y/s_p = 1.6$ from $z/c = 0.0$ and $z/c = 0.5$.

The occurring of such opposite effects shows that the flow on the pressure side of the wake tends to recirculate toward the endwall contrasting the reverse recirculation on the suction side of the wake, which is highlighted by positive values of γ_{xz}. This effect is consistent with secondary flows contrasting directions at the boundary between regions A_{n-1} and B_n shown in Fig.'s 4.4d and 4.5d.

Static pressure recovery

The static pressure coefficient in the plane of measurement of the five hole probe is defined as in Eq. 4.4 and it is presented in Fig. 4.4c for the case $i = 4°$ and Fig. 4.5c for the case $i = 7°$.

$$C_{p_s} = \frac{p_{s_{5T}} - p_{s_\infty}}{p_{t_\infty} - p_{s_\infty}} \tag{4.4}$$

Two main effects can be recognized as the incidence increases. At first, the static pressure recovery decreases as the incidence is increased in the wake of the corner separation near the endwall. This effect is associated to the separation on the blade surface that produces the well-known plateau on the surface pressure distribution of the blade and opposes the correct diffusion within the inter-blade section.

The second effect concerns the diminishing of C_{p_s} in the free-stream region outside both the wake of the blade and the wake of the separation. This is the consequence of the blockage due to the separation, which deviates the flow in spanwise direction as confirmed by the region of positive values of flow angle γ_{xz}. In this process the flow additionally accelerates, as previously presented in Fig. 4.5b, leading to the consequent decrease of the static pressure, in close analogy with what occurs in a convergent duct.

Furthermore, for the case $i = 7°$, it can be noted that a region of $C_{p_s} < 0.34$ exists also between $y_s = 1.6$ and $y_s = 1.9$. The existence of this deficit of pressure recovery is probably caused by the interaction between the deviated flow with and the separation occurring in the following passage. The same decrease of static pressure exists indeed on the pressure side of the reference blade very near to the limit of the investigated domain, i.e. at $y/s_p < 1.0$ between $z/c = 0.0$ and $z/c = 0.6$. This is evidence that the increment of the incidence at off design conditions, and so the separation size, promotes the interaction between separations of neighbor passages enhancing detrimental effects on the overall pressure recovery.

4.2.3 Comparison with previous work

Reference pressure distribution

The pressure distribution on both pressure and suction side of the blade is shown in the three-dimensional plot of Fig. 4.8. The configuration at $i = 4°$ was chosen to verify the correct

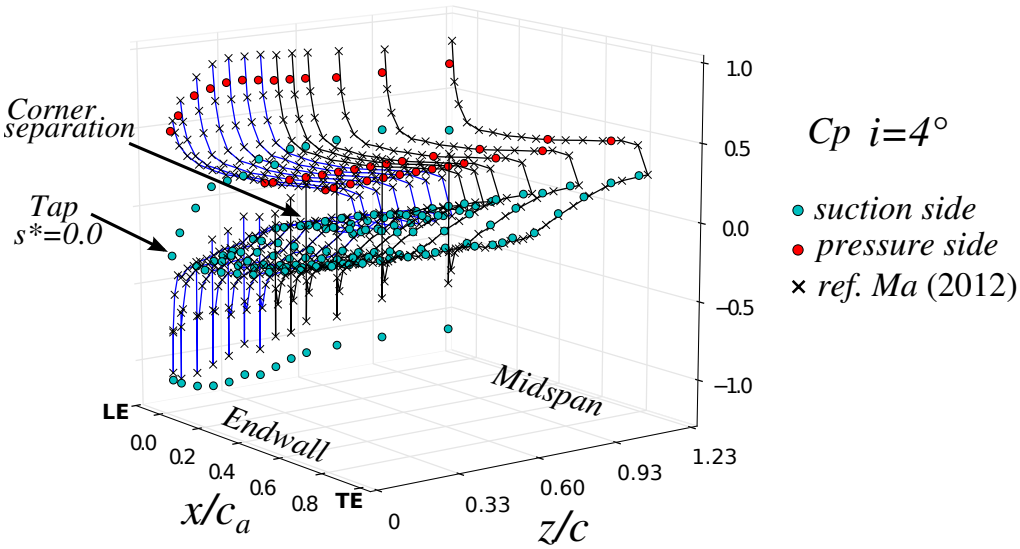

Fig. 4.8 Three dimensional visualization of static pressure coefficient C_p on the blade surface. Black cross indicated the reference data acquired in the previous work of Ma (2012).

cascade adjustment and the usage of Blade-II in comparison with the reference experimental campaign carried out by Ma (2012) with Blade-I.

The region of corner separation is highlighted by blue lines, which are affected by the plateau in the pressure distributions near the endwall on the aft part of the suction surface near the TE. This region is easily recognizable in the contour map of the pressure on the suction surface of the blade, see Fig. 4.11a in the following Section 4.3. In such a region the agreement between the reference and current measurements is excellent. Differences in proximity of the LE of the blade are probably due to small manufacturing differences in the position and the size of pressure taps at the LE. Even very small geometrical differences can lead to large pressure differences because of the large pressure gradient near the stagnation point. Anyway, the same trend in spanwise direction can be recognized for the tap at the stagnation point (tap $s^* = 0.0$) and also the first tap on the pressure surface. In conclusion, the overall good agreement between distributions confirms the correct configuration of the cascade.

Discrepancies in the size of the separation

The pressure distribution at the configuration $i = 4°$ was taken as reference but high discrepancies were subsequently found with the downstream investigation carried out in the previous work Ma (2012).

Fig. 4.9 and Fig. 4.10 resume the losses, pressure recovery and pitchwise angle associated to the configuration $i = 4°$ and $i = 6°$, respectively. For both configurations the separation is huge and worsens all the characteristics presented in the previous comparison between $i = 4°$ and $i = 7°$ of the measurements campaign carried out in the present work.

By comparing also with the LES results obtained by Gao (2014), introduced in the discussion about the simulation limits in Section 2.3.5 and presented in Fig. 2.8, it was

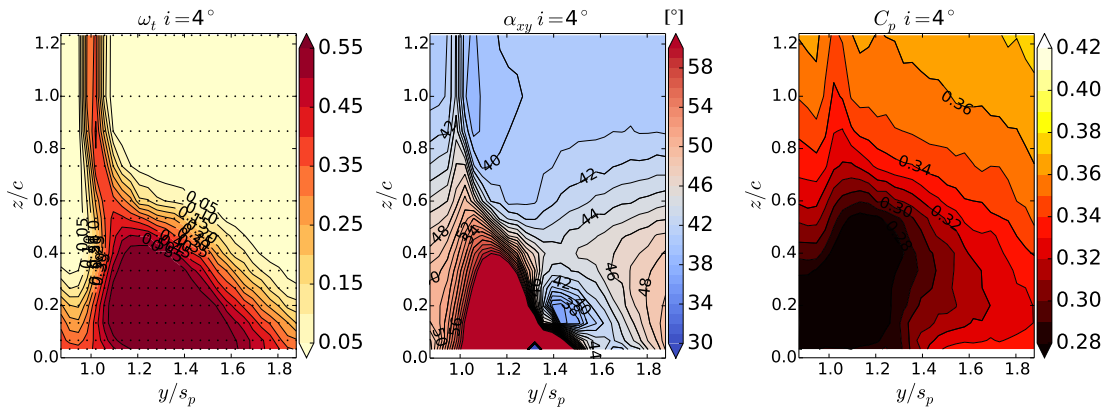

(a) **(b)** **(c)**

Fig. 4.9 Results of the previous campaign carried out by Ma (2012) at $i = 4°$.

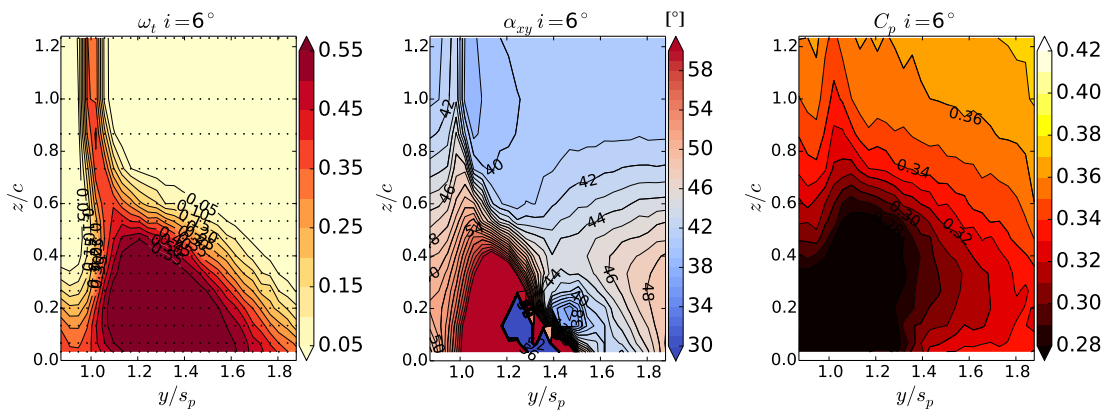

(a) **(b)** **(c)**

Fig. 4.10 Results of the previous campaign carried out by Ma (2012) at $i = 6°$.

evident how the measurements of Ma overestimated the corner separation existing at the reference configuration.

The explication of such a discrepancy has not been completely clarified, but the main variables that could have affected those results in such a detrimental way could be the incorrect adjustment of flaps of the test rig or the presence of a leakage in the endwall junctions.

Several tests were carried out during the present PhD work in order to find a configuration showing the same losses, but with the correct experimental set up such extreme losses were never found. Conversely, similar results were found only by admitting leakages in the endwall. Another proof of the presence of an error committed during Ma's measurements is assessed by the existence of preliminary results during the phase of first characterization of the test rig carried out by Ma that showed the same smaller separation obtained in the present work.

4.3 The signature of the separation unsteadiness in pressure statistics

In this section the statistical analysis is applied to pressure fluctuations achieved on the suction surface of the blade. The RMS of pressure fluctuations and high order statistical moments permit to uncover signatures of the intermittent behavior of the separation.

4.3.1 Main regions of unsteadiness in the suction surface pressure distribution

The Fig. 4.11b shows the contour map of the $C_{p_{RMS}}$ on the suction surface of the blade from the endwall to the midspan. Two regions of large fluctuations are clearly emphasized in this figure. The first one is the most prominent and it is situated at LE on the entire span of the blade. Large oscillations of the pressure sensed by the probes at the LE reflect indeed large oscillations of the stagnation point, which are caused by large variations of the local angle of attack. However the largest value of fluctuations $C_{p_{RMS}} = 0.239$ is located in the junction between the LE of the blade and the endwall, meaning that the interaction between the incoming turbulent boundary layer and the blade is the highest source of pressure fluctuation of the whole inter-blade channel. This region extends from $z/c = 0.033$ to $z/c = 0.267$, which is consistent with the thickness found for incoming endwall boundary layer $\delta_{99}/c = 0.24$.

Moving downstream over the suction surface of the blade, the value of RMS reaches a local minimum between $s^* = 0.2$ and $s^* = 0.3$ and subsequently it increases again near the endwall. Here, the second region of high fluctuations starts and it clearly covers the separated zone almost up to $z/c = 0.6$. A peak is visible from $z/c = 0.033$ to $z/c = 0.133$ at $s^* = 0.5$ and a ridge starting from this point decreases in spanwise direction curving downstream. This bump of positive $C_{p_{RMS}}$ uncovers the frontal edge of the separation detachment. Furthermore, a second bump is visible in the separated region on the aft of the blade, i.e. from $s^* = 0.8$ to the TE and from $z/c = 0.20$ to $z/c = 0.40$. This is induced by the large vortical structure which lays near the TE at the boundary between the separation and the attached flow, as it is expected by conventional time-averaged topologies.

4.3.2 The separation detachment highlighted by skewness

The Fig. 4.11c shows the contour map of skewness values, as defined in Section 3.11.3 on the suction surface of the instrumented blade from $z/c = 0.033$ to midspan $z/c = 1.233$. More details are provided about the separation boundary in this map. A first bump of positive values rises at $s^* = 0.35$ from $z/c = 0.033$ to $z/c = 0.4$ in spanwise direction. A second ridge of positive values covers an arched zone situated downstream at $s^* = 0.5$, which sweeps to $s^* = 0.6$ moving spanwise direction. In the first bump, the largest values are located at $z/c = 0.133$, whereas in the second arch two regions of higher values are recognizable in spanwise direction: the first one close to $z/c = 0.133$ and the second one from $z/c = 0.267$ to $z/c = 0.467$.

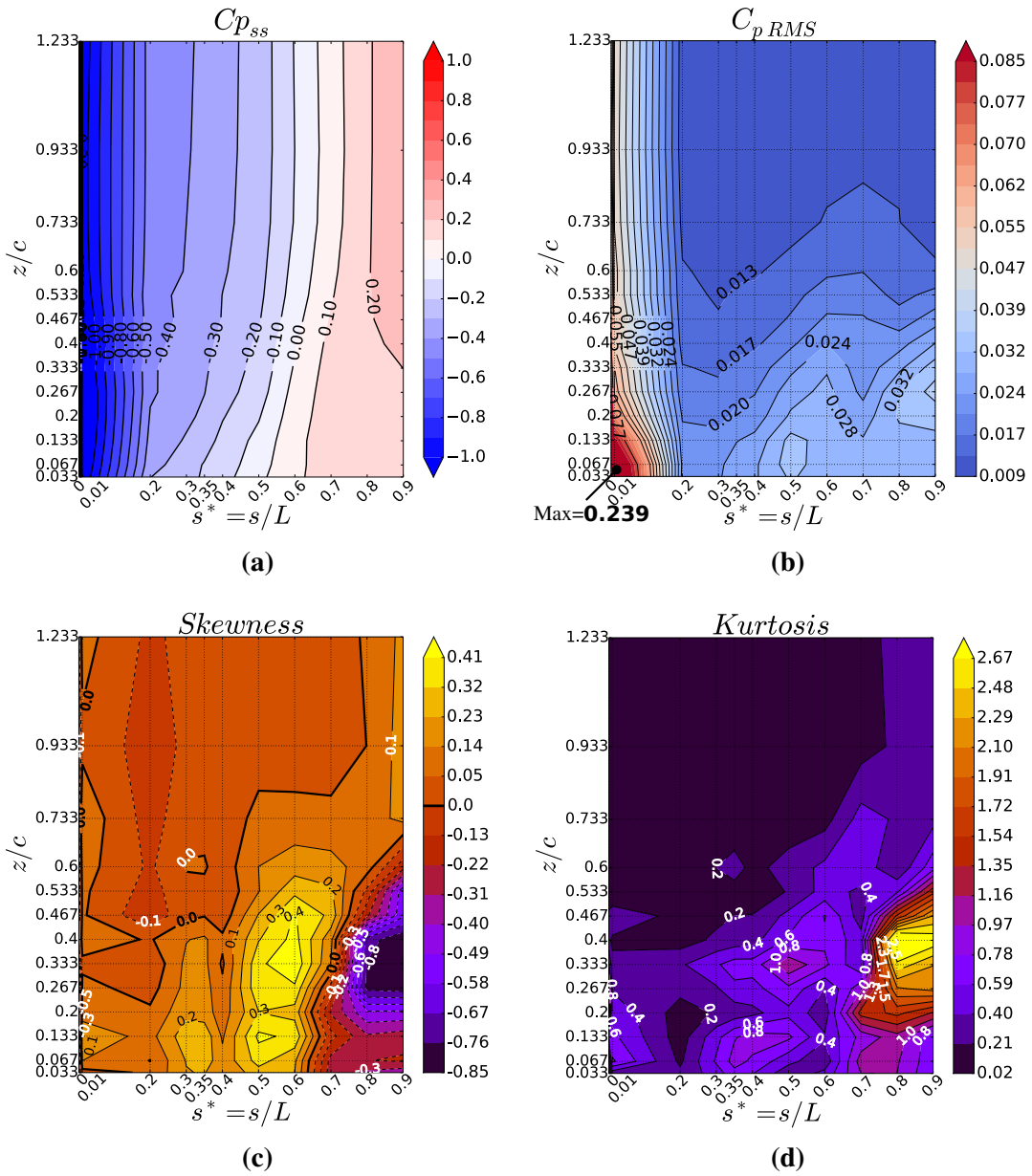

Fig. 4.11 Contour plot of $C_{p_{ss}}$ (a), $C_{p_{RMS}}$ (b), skewness (c) and kurtosis (d) on the suction surface of the blade, from end-wall ($z/c = 0.033$) to midspan ($z/c = 1.23$).

The question arises as to whether positive and negative values of skewness for wall-pressure distributions are associated to particular flow mechanisms when studying separations in fluid dynamics. The answer can be found in the literature: positive values of skewness in wall-pressure distributions localize regions where the flow on the body surface starts to separate. Comparing the skewness contour map with the contour map of $C_{p_{RMS}}$ in Fig. 4.11b, it is noticeable that these regions of large positive values of skewness are located in the region where the detachment of the corner separation takes place.

As evidence, Lee and Sung (2001) stated that local positive peaks of wall pressure in a wall-bounded turbulent flow are related to shear layers close to the wall, and vice-verse. Furthermore, Tsuji et al. (2007) pointed out that shear effects predominantly appear for positive pressure fluctuations and cause the positive tail to deviate from the Gaussian distribution leading to positive skewness. Bokde et al. (1999) underlined that this bidirectional relationship confirms that local positive pressure peaks are connected to the burst-sweep cycle, mechanism which plays a fundamental role in the generation of turbulence.

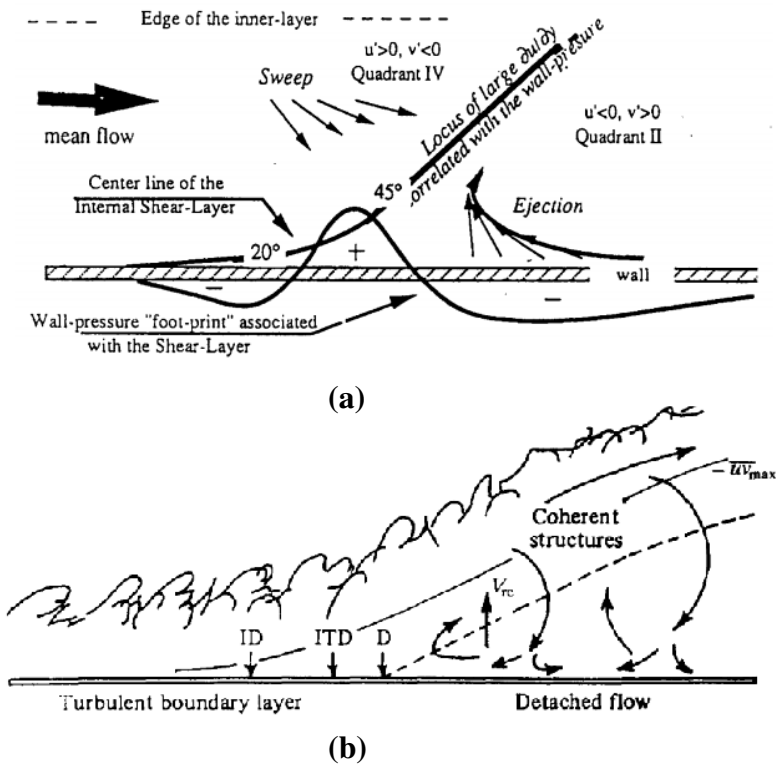

Fig. 4.12 Schematic of near wall turbulent motion and associated wall pressure (a), reproduced from Astolfi and Forestier (1993). Separation process sketch for turbulent boundary layers (b) as proposed by Simpson et al. (1981): solid line denotes maximum shear locations; dashed line denotes $V = 0$ locations with V_{re}= mean re-entrainment velocity along $V = 0$.

In case of 2D turbulent boundary layer separations described by Kammeyer (1995) and sketched in Fig. 4.12a, a high turbulent shear locus (solid line) precedes the detachment. This high shear locus is correlated with a particular “foot-print" of the wall-pressure, which shows a dominant peak of positive pressure fluctuations.

Fig. 4.12b, reproduced from Simpson et al. (1981), sketches the model proposed by Ashjaee and Johnston (1980) that individuates three main phases describing the consequent separation. As already presented in Section 2.4 for the intermittency of flow regimes in diffusers, in the separation process can be recognized a first point called point of incipient detachment (ID), which is characterized by 1% of reverse flow, secondly a point called point of intermittent transitory detachment (ITD), where the reverse flow grows to 20%, and finally

the point locating the transitory detachment phase (TD). In this third highly unsteady region, the reverse flow reaches the 50% and it is possible to localize the complete detachment point (D), which is characterized by $V = 0$ and $\tau_w = 0$. Concerning the skewness map of Fig. 4.11c, the presence of the second higher value ridge just upstream of the completely separated region, which conversely is located downstream of the black line of $Sk_3 = 0$ starting at $s^* = 0.6$, is in agreement with the model here described.

The two ridges of positive skewness enclose the zone of intermittent unsteady detachment because they show an oscillation of the separation line around a time averaged expected position. This is the first clue that the frontal boundary of the separation moves on the suction surface of the blade from a position more retreat downstream to a position farther upstream. The flow visualizations of Chapter 5 will prove that this movement is additionally associated with the sudden increase of the size of the separation.

Conversely, the frequent occurrence of negative pressure peaks is statistically highlighted by negative values of skewness, which are generally related to the existence of vortical structures, as explained by Laadhari et al. (1994). Present pressure results show a region of large negative values of skewness within the separation close to the TE, revealing the position of the time averaged tornado-like vortex previously described in Section 4.2.1. Another region of negative skewness can be recognized at the LE near the end-wall, from $z/c = 0.067$ to $z/c = 0.267$. This highlights the presence of vortical structures at the LE of the blade due to the interaction between the end-wall turbulent boundary layer and the boundary layer on the LE.

4.3.3 Intermittency regions on the suction surface

Additional information about the intermittency of a separated boundary layer can be gained by investigating the fourth statistical moment of the pressure fluctuations, described by the formulation given in Section 3.11.4. Accordingly to Lilley and Hodgson (1960), large positive values of kurtosis indicate a highly intermittent behavior of wall pressure fluctuations which are characterized by spikes of large amplitude, as pointed out also by Kim et al. (1987) and Kammeyer (1995).

In the contour map of the kurtosis calculated for wall static pressure data shown in Fig. 4.11d, only positive values were found, especially in the region affected by the corner separation. Starting the analysis of the kurtosis results from the LE, a region of large values can be seen on the first and second Channel ($s^* = 0.0$ and $s^* = 0.1$) between $z/c = 0.033$ and $z/c = 0.33$ with a bump reaching $Ku = 0.7$ at $z/c = 0.267$. Since this region is affected also by negative values of skewness, as previously explained in Section 4.3.2, its presence empathizes the existence of unsteady coherent structures at the edge of the end-wall boundary layer.

Moving downstream toward the separation boundary, two spots of higher kurtosis are present at ($s^* = 0.4$, $z/c = 0.033$) and ($s^* = 0.5$, $z/c = 0.33$). Comparing these locations with the ridge of positive skewness of Fig. 4.11c, it is possible to identify spots of high values of kurtosis appearing immediately before the maximum bump of skewness, i.e. $Sk_3 = 0.48$.

The interpretation of this phenomenon can be found in the relation between the existence of positive pressure fluctuations (positive skewness) and the burst-sweep cycle due to the passage of an inclined shear layer (Thomas and Bull, 1983), as shown in Fig. 4.12a. The presence of abrupt positive and negative pressure peaks coexisting with zero pressure fluctuations, i.e.large values of $Ku > 0$ in statistical distributions, immediately upstream of positive ridges of skewness is associated to highly intermittentcy and to the unstable behavior of the origin of the inclined shear layer. As predicted by a conceptual model for vortical dynamics in the wall region of a boundary layer proposed by Acarlar and Smith and reviewed by Alfonsi (2006), the bursting of a low-speed streak is the consequence of vortex roll-up process occurring exactly in the unstable shear layer on the top and at sides of the streak.

At this point, such an interesting relationship between the instability of the shear layer and the pressure fluctuation can be extended to the bursting process. The bursting process is not yet well understood but has been associated with an important role in the processes of production and transfer of turbulent energy between the inner and outer regions of the boundary layer. This energy transfer seems to be related to the inverse energy cascade of the turbulence, also called *backscatter*. The hybrid RANS-LES numerical investigation carried out by Wang and Yuan (2013) on corner separation reports values of helicity higher than 0.6 in the separated flow demonstrating that the high non-homogeneous shear in such regions increases the turbulence anisotropy, non-equilibrium and energy backscatter. Finally, the maximum value of kurtosis on the blade $Ku = 0.3$ appears in the region dominated by the tornado-like-vortex laying in the aft part of the blade. In this position again, the peak is immediately before the negative nadir of skewness. In this case the high intermittency is related to the unsteadiness of the vortex core which oscillates on the suction surface of the blade.

4.4 The bimodal unsteadiness

As emerged in the analysis of statistical moments of wall pressure fluctuations, unsteadiness and intermittency characterize the detachment point of the shear layer from the blade suction surface. In order to deeply investigate this mechanism, results of time-resolved PIV measurements at the closest section to the endwall, i.e. $z/c = 0.033$, have been chosen for the discussion of the flow unsteadiness.

4.4.1 Punctual time-resolved characterization

Two-dimensional streamlines and RMS of velocity fluctuations are presented in Fig.'s 4.13a and 4.13b at $z/c = 0.033$ for both the configuration $i = 4°$ and $7°$, respectively .

The time-averaged line of the separation is represented in figures by the dashed line, which encloses the recirculation region by following streamlines that detach from the surface of the blade. It is evident the double effect of the increment of the inlet incidence: the averaged recirculation region doubles and the frontal boundary of the separation moves upstream. This movement is associated also to the increment of the velocity fluctuations $V_{RMS\ xy}$ in front of the separation, over the time-averaged separation line. The increase of the

incidence enlarges both the magnitude of fluctuations and the extension of the associated region.

The characterization of RMS of the flow confirms the unsteadiness of the shear layer at the front of the separation, already uncovered by skewness and kurtosis analysis in Sections 4.3.2 and 4.3.3. The question arises as to what is hidden behind this high-fluctuation region when three points are taken as subject of study.

Fig. 4.14 presents the statistical distributions, or PDF, and the raw signals of three points p_1, p_2 and p_3, selected as shown in Fig. 4.13b around the time-averaged separation line. Probability density functions are the histograms of the raw signal. Histograms incorporate all the statistical moments, i.e. the mean (first moments), standard deviation (second moment), skewness (third moment), flatness (fourth moment) and so on towards higher orders. The quantity analyzed is the velocity u_s corresponding to the velocity component which is tangential to the suction surface of the blade, normalized by the inlet velocity V_∞. The point $p3$ is outside the time-average separation line, so the distribution presents as expected an unique peak centered around the value $u_s/V_\infty = 0.6$.

Conversely, the point $p1$ is underneath the time-average separation line, immediately above the surface of the blade, at position $n/c = 1.7\%$. This region is affected by the separation and the recirculation flow, which drives the back-flow on the surface of the blade.

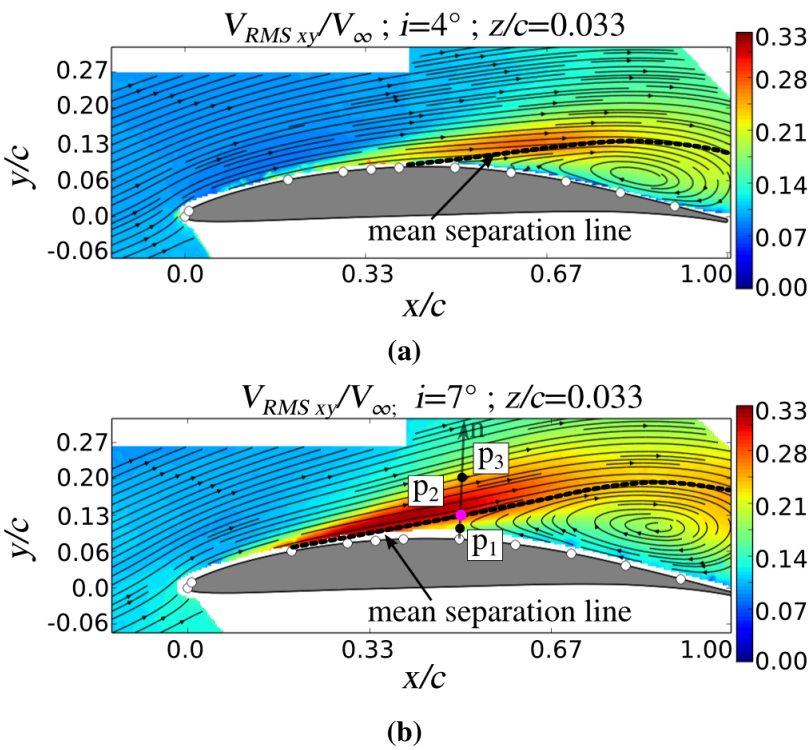

Fig. 4.13 Velocity RMS at section $z/c = 0.033$ for the configuration $i = 4°$ in Figure (a) and the configuration $i = 7°$ in Figure (b). Localization of positions $p1$, $p2$ and $p3$ utilized for the bimodal analysis in Section 4.4.

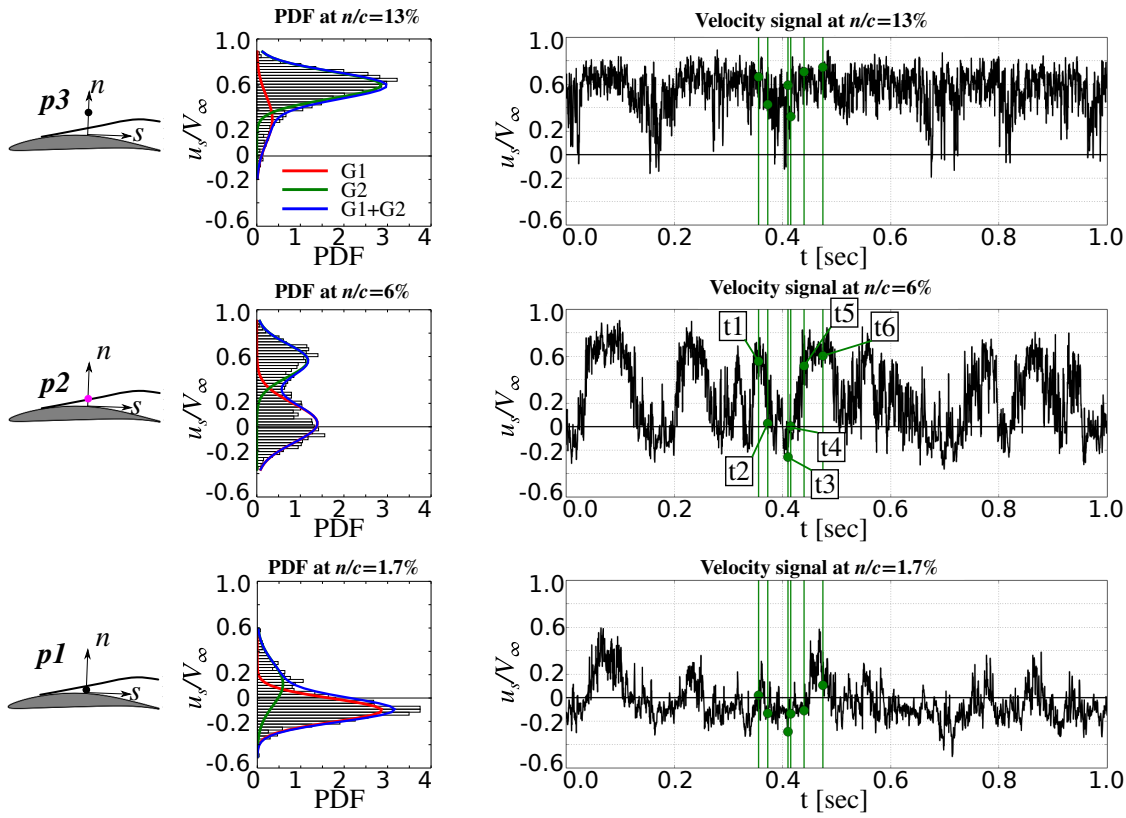

Fig. 4.14 The bimodal behavior presented for the measurement case $i = 7°$, $z/c = 0.033$ at half of the blade profile $s^* = 0.5$. Comparison of velocity distributions and time tracers (middle plots, $n/c = 6\%$ from the surface of the blade) and not-bimodal points ($n/c = 1.7\%$ and $n/c = 13\%$). Green lines: instants from t1 to t6 selected for flow visualizations in Fig. 5.1.

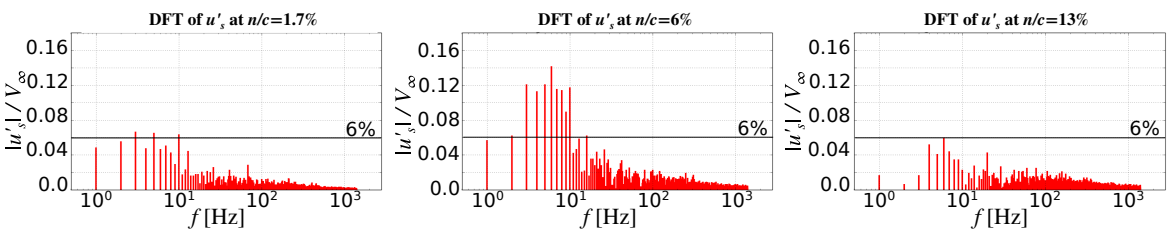

Fig. 4.15 Fourier transforms of velocity time tracers shown in Fig. 4.14 for the measurement case $i = 7°$, $z/c = 0.033$ at half of the blade profile $s^* = 0.5$.

Such a back-flow is described by the Gaussian peak centered on the negative value of the tangential velocity $u_s/V_\infty = -0.2$ in the PDF distribution of the point $p1$.

Finally, the existence of the bimodal distribution is confirmed by the double peaks statistical distribution in the vicinity of the boundary of the separation, i.e. position $p2$ at $n/c = 6\%$. Two preferred states, or modes, of the flow are described by bimodal PDFs. The first mode is associated to the peak corresponding to the free stream flow, i.e. $u_s/V_\infty = 0.6$,

and it describes a streamwise flow in the same direction of the main flow. The separation boundary at these instants is underneath the bimodal point, since the coordinates of the point $p2$ are fixed in space. This state of the flow represents the closed separation. Contrarily, the second mode corresponding to the bump of the PDF at $u_s/V_\infty = -0.1$ underlines that the point $p2$ experiences a back-flow in opposite direction to the main flow. The back-flow is characteristic of the flow within the separation in the recirculation region, therefore this state of the flow demonstrates that the separation is larger and its boundary is situated over the position $p2$, which describes an open separation. These two states have an equal statistical occurrence, implying that the separation oscillates between closed and open state not randomly, but reaching a stable position into each state once the switch occurs. When calculating the time-average of the raw signal, which corresponds to the mean of the PDF, the value $u_s/V_\infty = 0.18$ is obtained (see Fig 4.16b). This velocity value corresponds to the local minimum between the two bumps in the bimodal distribution, so it is not meaningful in the description of the flow since it represents a flow state that occurs in minority.

Additionally Fig 4.15 presents the Fourier transforms related to the selected raw signals. The comparison between the energy contain of the bimodal point $p2$ and the not-bimodal points $p1$ and $p3$ highlights the increment of energy at low-frequency scales approaching the bimodal region. Sudden switches between positive and negative values of velocity produce an aperiodic signal: the Fourier transform of the bimodal point $p2$ assesses the presence of velocity fluctuations larger than 6% V_∞ at frequencies below 10 Hz but without any preferred well-defined peak value.

4.4.2 Decomposition of the unsteadiness

A further investigation of PDFs consists in the decomposition of the contributions of the recognized states of the flow. For this reason, the mode associated to the back-flow is called Mode 1 and the mode associated to the co-flow higher velocity is called Mode 2. Both modes can be fit by a Gaussian distribution, in particular green fits are used for the Mode 2 and red fits are used for the Mode 1, as shown for the PDFs in Fig. 4.14. The combination of such Gaussian fits gives the final blue fit, which represents correctly the distribution obtained by measurements.

The same process can be applied to all the spatial points forming the field of measurement. Since the bimodal behavior affects only the component of velocity tangential to the surface of the blade u_s without affecting the normal component u_n, as explained in the review of the bimodal phenomenon in Section 2.2.2, PDF of u_s can be extracted on a line that is perpendicular to the surface of the blade crossing the mean separation line, i.e. in direction n. The PDF of u_s accounts for the entire bimodal contribution if the bimodal flow affects the investigated position.

Fig. 4.16a and Fig. 4.16b show the evolution of the value of the mean and the standard deviation of the Gaussian fits applied to the PDF of u_s on the extracted line in n-direction. This line is chosen at the position $s^* = 0.7$ for the configuration $i = 4°$ and at $s^* = 0.5$ for $i = 7°$ in order to cross the separation at the same distance from the blade. For the lower incidence case it can be seen that the mean of the Mode 1 $\overline{u}_{1s}(n)$ represents a detached velocity profile,

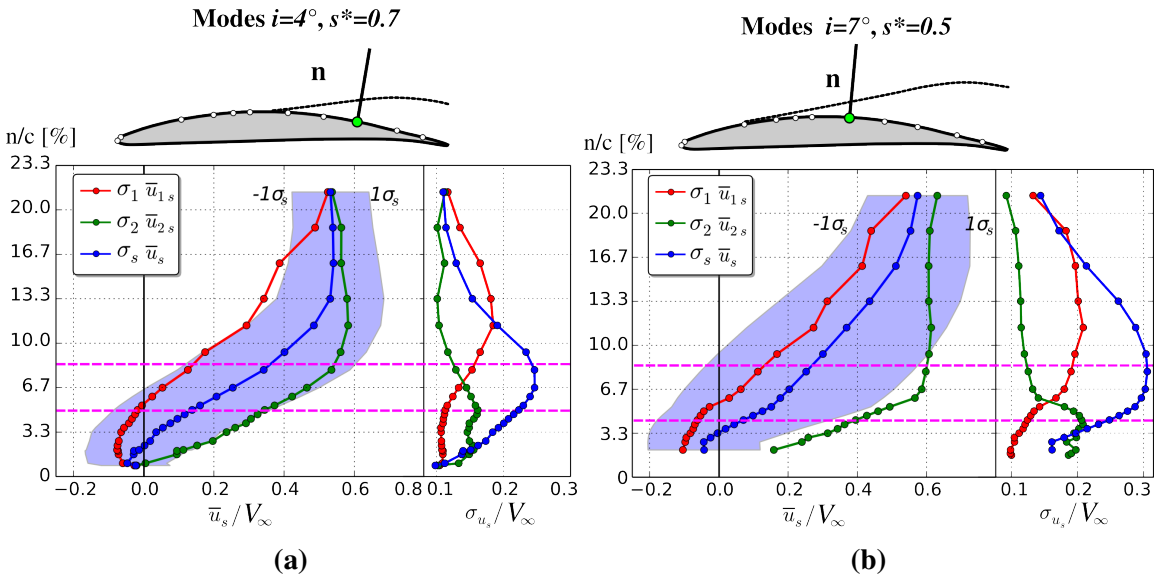

Fig. 4.16 Mean velocity profiles and standard deviation of Mode 1 and Mode 2 composing the PDFs at section $z/c = 0.033$. The time-averaged velocity profile of the original distribution are represented by $\overline{u}_s$ and σ_s. Figure (a): configuration $i = 4°$, extraction line n at $s^* = 0.7$. Figure (b): configuration $i = 7°$, extraction line n at $s^* = 0.5$.

since close to the endwall negative values of the velocity are present. Additionally, the slope $\partial u_s/\partial n$ of the profile becomes negative below $n/c = 2\%$, demonstrating the typical feature of a separated flow. Conversely, the Mode 2 can be reduced to an attached flow, since the velocity profile does not reach negative values and the slope remains positive close to the endwall. The blue line represents the mean velocity $\overline{u}_s$ of the original distribution, fitted by the blue double-bump fit. The standard deviation of the velocity at each extracted point is represented on the right side both in Fig. 4.16a and in Fig. 4.16b. The standard deviation σ_s of the original distribution is also represented by blue regions between $\pm 1\sigma$, which encloses the mean velocity profile $meanu_s$.

The velocity profiles of Mode 1 and 2 are situated at the boundary of the standard deviation region, in some points also beyond such limits. This is the case for $\overline{u}_{1s}(n)$ in the range $12\% < n/c < 16.7\%$ for $i = 4°$ and for $\overline{u}_{2s}(n)$ in the range $2\% < n/c < 10\%$ for $i = 7°$. Such a difference between the means values of the two distinct Gaussian fits and the global mean of the original PDFs underlines that the prediction of a bimodal flow field through time-averaged techniques leads to high misprediction of the real states of the flow. The purple dashed lines delimit the region affected by bimodal PDFs. It can be seen that this interval corresponds to the region of maximum σ_s, where the oscillations of the flow are maximum. The distance between $\overline{u}_{1s}$ and $\overline{u}_{2s}$ is also maximum in the bimodal region and it increases by increasing the incidence angle.

From such a tendency it can be deduced that the gap between the two competing modes of the flow increases as the inlet incidence increases, which is associated to the increasing of the blade loading. The separated profile is almost the same between the two configurations and the time-average mean profile $\overline{u}_s$ moves toward the separated profile. Conversely, the

attached profile shows increased velocities, especially in the bimodal region at $n/c = 6.7\%$, where $+10\% V_\infty$ is attained by rising the incidence.

In conclusion, the calculation of time-averages in case of bimodal phenomena, without any awareness of their existence, leads to a serious misprediction of the true flow field topology. Attention should be put when considering this misprediction in a multistage environment because such opposite states of the flow, which are associated to the bimodal unsteadiness, are the most favorable conditions for the multistage mismatching, discussed in Section 1.4.4.

Statistics of the temporal variation of the tangential velocity in proximity of the time-averaged separation surface should be checked in experimental investigations to asses the presence of the bimodal unsteadiness.

Since the local investigation of bimodal points provides only a limited insight into the causes of the above-discussed instability, a global two-dimensional analysis of the recorded whole-field information appears to be more appropriate as it will be elaborated in the Chapter 5.

4.5 Summary and conclusions

Results of the common technique to describe the corner separation are shown in this chapter for both investigated configurations $i = 4^\circ$ and $i = 7^\circ$ at first. The time averaged characterization shows that the separation is located in the corner between the suction surface and the endwall of the reference blade passage. In particular, its existence is assessed by high total pressure losses downstream of the cascade, flow under-turning, spanwise deviation and the presence of the characteristic plateau in the static pressure distribution on the blade surface. Additionally, the time-averaged topology confirms the existence of a tornado-like vortex within the separation. This vortex rises from a focus on the endwall and plunges on the aft part of the blade. Large values of velocity fluctuations localize the boundary of the separation and its growth as the inlet incidence is increased.

Time-averaged results can be adequate to give an overall description in order to evaluate the performance of the cascade but they hide major dynamics related to the unsteadiness of the separation. Conversely, the statistical analysis of unsteady signals shows that high-order statistical moments of unsteady wall pressure fluctuations are capable to capture first proofs of the separation unsteadiness. Bumps of positive and negative skewness, identifying flow detachment and coherent vortical structures respectively, localize the frontal boundary of the separation and the tornado-like vortex, in agreement with the time averaged description. Additionally, such loci uncover the coexistence of two preferred positions for the separation front. This particularity suggests a chord-wise movement of the frontal boundary of the separation.

Furthermore, the intermittent nature of the unstable shear layer at this critical position is highlighted by kurtosis of pressure distributions, which confirms the existence of local regions of transitory detachment. According to literature, the vortex roll-up induces the bursting of low-speed streaks within the unstable shear layer. This bursting process is therefore related

to the inverse energy cascade of the turbulence between the inner and outer regions of the boundary layer, also called *backscatter*.

Such evidences are finally ascertained by the time-resolved investigation of the velocity in proximity of the time-averaged separation line ensuring the existence of the bimodal unsteadiness of the separation. The comparison between bimodal and not bimodal time-tracers of the velocity uncovers sudden switches between positive and negative values. These oscillations are not periodic since no sharp peaks are present in the associated Fourier spectra, whereas the increment of energy is spread on a wide low-frequency range. These results additionally confirm the main findings of the precedent experimental works carried out by Ma (2012), which reported the bimodal unsteadiness and its aperiodicity even with a dubious set up of the test rig, which induced massive corner separations.

In conclusion, the time-resolved characterization demonstrates that the time-averaged description of corner separation is useful to understand the basic features of the flow but mispredicts the real unsteady flow of the separation and the associated blockage. The real unsteady behaviour of the separation is represented by two preferred extreme states of the flow: a state where the separation is open, associated to high losses and blockage, and an opposite configuration where the separation is closed. Such effects should be carefully considered in the design of multistage compressors because affecting in the worst way the mismatching between stages.

Chapter 5

Investigation of unsteady dynamics of corner separation

Contents

5.1 Introduction 145

5.2 Dynamics of the bimodal unsteadiness 146

5.2.1 Unsteady topology 146

5.2.2 Investigation of synchronized static pressures on the suction surface of the blade 149

5.3 The role of random incoming perturbations 156

5.3.1 Temporal evolution of flow angle of attack 156

5.3.2 Correlation between unsteady pressures on the blade 158

5.3.3 Effect of extreme incoming perturbations on the separation 159

5.4 The upstream effect of the separation blockage 163

5.4.1 Conditional ensemble average of pressure signals 163

5.4.2 Modal analysis 166

5.5 Comparison with diffuser regimes 174

5.6 Interactions between adjacent corner separations 176

5.6.1 Meaningful interactions 176

5.6.2 The pitchwise disturbance propagation 177

5.7 Summary and conclusions 183

5.1 Introduction

The time-averaged representation hides different dynamics related to the unsteadiness of the corner separation, as introduced in Chapter 4. The following investigation is focused on the

unsteady behavior of the corner separation. Starting from flow visualizations obtained with time-resolved PIV measurements in the inter-blade reference passage, the main dynamics involved in the separation switch are here uncovered. These mechanisms are additionally related to time-resolved static pressures simultaneously acquired on the suction surface of the blade. Two main dynamics are recognized to play a major role in the bimodal unsteadiness of the separation: small-scale high-frequency perturbations triggering the switch of the separation and large-scale low-frequency oscillations of the flow due to the overall separation movement leading to the back switch. Section 2 addresses to the small-scale streamwise mechanism by further relating the pressure and velocity fields by correlations and wavelet analysis. Differently, Section 3 describes the feedback effect that the variation of the flow blockage has on the flow upstream the blade. To accomplish the task, POD decomposition of the flow field and conditional ensemble averages of pressure time tracers are presented and discussed. Finally, Section 4 tries to answer the question concerning the interaction between unsteadiness of adjacent corner separations by exploiting time-resolved total pressure measurements carried out simultaneously in multiple inter-blade passages.

5.2 Dynamics of the bimodal unsteadiness

5.2.1 Unsteady topology

In order to understand the overall flow in sections of the separated region in the corner, time-resolved 2D2C PIV measurements are presented in Fig. 5.1, for the configuration $i = 7^\circ$ at the spanwise section $z/c = 0.033$ ($z/\delta_{99} = 13.8\%$). As shown in Section 4.4, this configuration constitutes the most suitable configuration to understand the flow since it represents the worst case scenario of separation, when the highest unsteadiness can be investigated.

The unsteady topology of the flow is visualized by means of path lines, where virtual particles are located in the PIV flow measurements plane and tracked according to the velocity vectors obtained from the PIV measurements. Two distinct seed lines are used for this visualization: virtual particles are "released" along a vertical red line located at the inlet of the PIV measurement plane and a white line located close to the blade suction surface. The time tracking of both white and red particles permits to evaluate the unsteady development of the separation region. Representative time instants of the flow, from $t1$ to $t6$ are consequently chosen to explain the flow dynamics, as shown in Fig. 5.1 (a-f).

Along with the particle tracking, the contour map of the instantaneous angle in the front part of the blade is also presented in these figures. This angle is calculated as in Eq. 5.1 in the frame of reference of the blade. The zero value of the angle is attained when the flow vector is aligned with the chord of the blade. In this frame of reference the incidence $i = 7^\circ$ corresponds to $\alpha_b = 18.8^\circ$, which is also defined as $\alpha_b(i = 7^\circ)$.

$$\alpha_b = \tan^{-1}\left(\frac{v_b}{u_b}\right) \tag{5.1}$$

Additionally, the points chosen for the visualization of the time tracers of the velocity in Fig. 4.14 in the bimodal analysis of the previous chapter are localized in these particle tracing

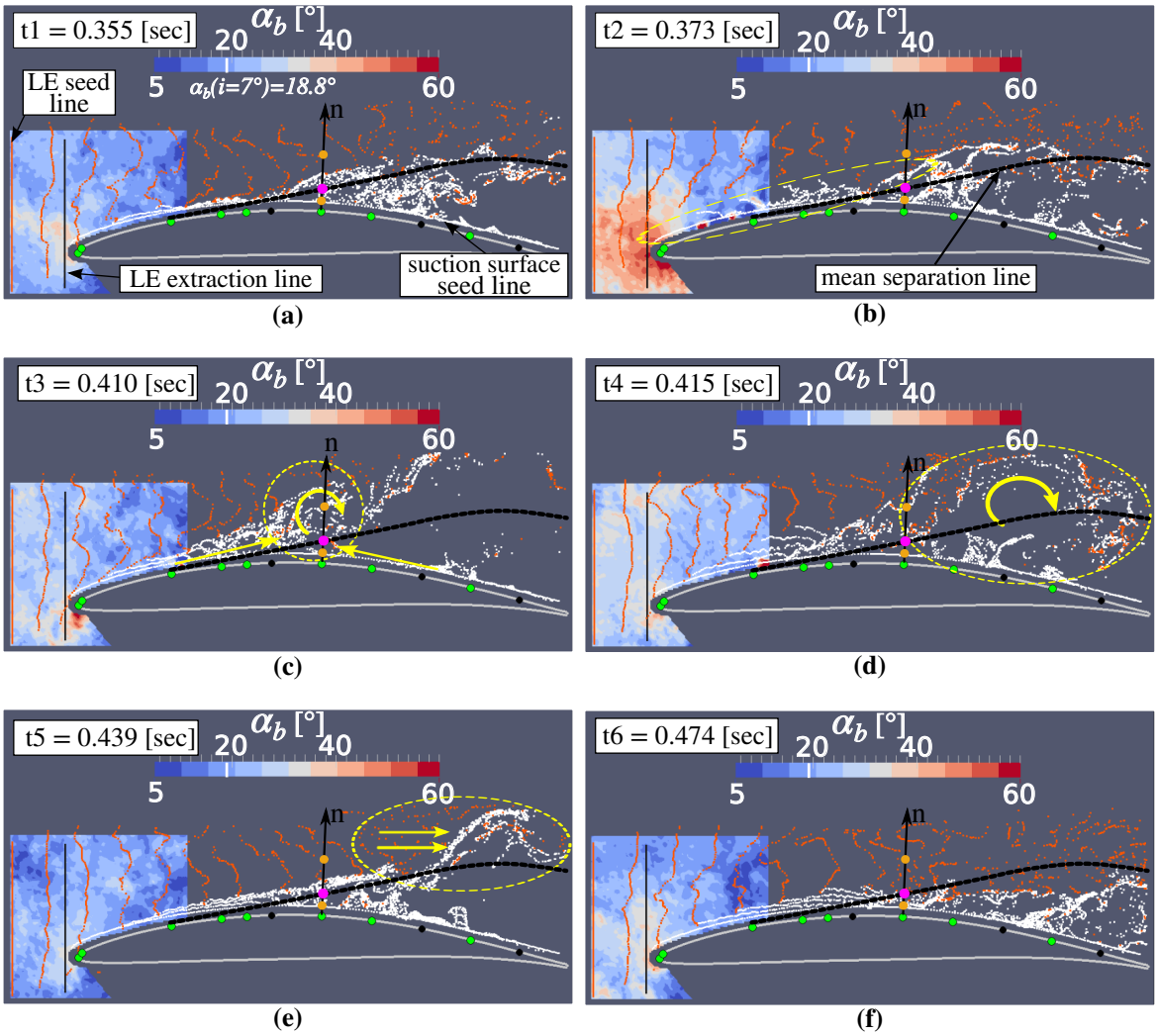

Fig. 5.1 Visualization of main dynamics of the development of the separation, case $i = 7°$, $z/c = 0.033$. Closed separation at $t1$, propagation of perturbations from LE to separation at $t2$, separation-backflow collision at $t3$, large recirculation at $t4$, vortex sweep at $t5$ and reestablishing of closed separation at $t6$.

images. The purple point localizes the bimodal point p_2, whereas orange points localize p_1 and p_3, within and outside the time-averaged separation, respectively. The time-averaged separation boundary is indeed represented by the black dotted line. The position of these three points and the separation boundary are fixed and replicated on each figure from (a) to (f) in order to help the reader to visualize the variations of the real size of the separation. This in turn is highlighted by the extent of the region drawn by white particles.

At the beginning of the sequence of instants, $t1$ in Fig. 5.1a, the separation size is contained and the region in front of LE does not present regions of excessive flow angle values. However, the successive selected instant $t2$ shown in Fig. 5.1b captures the appearance at the LE of an extended region of $\alpha_b > 40°$, i.e. beyond two times the configuration incidence

of $\alpha_b(i = 7°)$. Such a region is the signature of large vortical structures that impact the LE of the blade. The co-occurring perturbations, highlighted within the dotted yellow ellipse in Fig. 5.1b, adversely influence the boundary of the separation; thus its development. The visualisation of the animated video of such measurements confirms that such higher vorticity structures disturb the boundary of the separation by blending with the already existing recirculation region in the middle of the suction surface of the blade. This process triggers the increasing of the separation size and strength. Furthermore, the characteristic streamwise convection velocity of these structures, which is calculated on the distance from the LE to the half-cord, yields to the value of $U_c/V_\infty = 0.33$.

The second major element playing a role in the sudden growth of the separation is the backflow close to the aft part of the suction side of the blade. As shown in Fig. 5.1c, this backflow is always present in the recirculation region, but is strengthened by the opening of the separation. As a result, this backflow collides with the boundary layer of the blade that arrives from the LE in the middle part of the suction surface. The collision ejects large eddies that are characterized by a diameter of one tenth of the blade chord, as proved in Fig. 5.1c, further increasing the size of the separation as well. The chord-wise movement of the separation onset follows its growth in size, started at $t2$, which establishes a time interval (from $t2$ to $t4$) characterizing the separation movement toward the LE against the flow direction.

In this elapsed time, the value of $u_s(t)$ at the bimodal position, i.e. purple point, reaches negative values, as presented in the velocity signal of position $p2$ at $n/c = 6\%$, $s^* = 0.5$, $z/c = 0.033$ in Fig. 4.14. In the end of such a time interval at $t4$, the separation reaches its maximal size with a massive recirculation of diameter about one half of the chord, see Fig. 5.1d. The open separation continues to exist till $t5$, increasing also the blockage.

Since the present measurements are only 2D the correct value of the 3D blockage occurring in the whole inter-blade passage can not be correctly quantified. However, accordingly to the complete study of Gand (2011) on corner separation in junction flows, it is fair to infer that when the 2D size of the separation increases, its 3D volume and the associated blockage increase accordingly. This massive increment of blockage deviates and slows down the incoming flow till the large recirculation region can not be maintained any longer by the inter-blade passage. The particles at the bimodal position experience acceleration with a sudden increase of the velocity through positive values, from $t4$ to $t5$ in Fig. 4.14. Larger eddies break down and are swept downstream by the flow, as highlighted in yellow in Fig. 5.1e. This in turn leads to a (at least partly) re-attachment of the separation, see Fig. 5.1f, with accordingly higher positive velocities in the bimodal positions. The cycle described is aperiodic and variable in intensity and time extent, as can be evinced by Fig. 4.14, but for the present case the time scale of the phenomenon can be identified as $\Delta t_{CS} = t6 - t1 = 0.119$ sec. This value gives $\Delta t_{CS}/t^* = 31.7$, in terms of characteristic time of the flow t^*, equivalent to the reduced frequency $f_{rCS} = 0.03$.

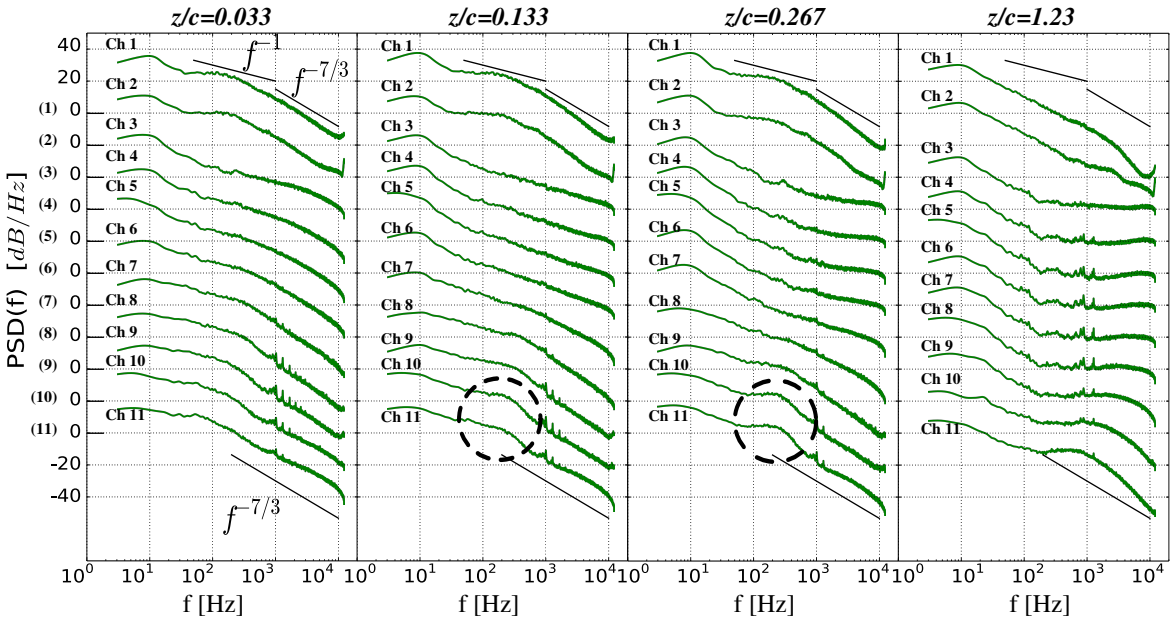

Fig. 5.2 Pressure spectra at different sections from Channel 1 to 11 on the suction surface of the blade, case $i = 7°$. Steps between each zero level are characterized by $20dB$ variations. Dashed circles highlight the bump due to the tornado-like vortex in the aft part of the blade.

5.2.2 Investigation of synchronized static pressures on the suction surface of the blade

The synchronized static pressures acquired with microphones during the PIV measurement are analyzed below. Power spectral densities and coherence shown here have been calculated accordingly to Eq. 3.77 and Eq. 3.79 respectively, on the long acquisitions data set described in Section 3.6.3. Additionally, the pressure time tracers at section $z/c = 0.033$ synchronized to the PIV flow visualization are discussed. These signals are investigated individually by applying different filters, and collectively, by the calculation of the unsteady blade loading.

Power spectral density

It is generally accepted that in pressure spectra significant contributions to high frequencies and high wave numbers are attributed to small scale turbulent structures in the near wall region of the turbulent boundary layer. On the other hand contributions to low frequencies and low wave numbers are associated with the presence of larger structures in the outer layer (Camussi et al., 2008).

Fig. 5.2 shows the variation of the power spectral density of channels from LE to TE for different spanwise sections beside theoretical slopes -1 and $-7/3$. PSD of channels located near the LE of the blade, i.e. Channel 1 and Channel 2, at the section $z/c = 0.033$ are in agreement with the theoretical slopes but the low frequency band, i.e. between 3 Hz and 40 Hz, is characterized by a bump of energy. Spectra of channels situated on the frontal part of the detached zone (from Channel 3 at $s^* = 0.2$ to Channel 5 at $s^* = 0.35$) show a fast

decrease of the PSD intensity in the frequency range $20-200$ Hz, which follows the bump at low frequencies. Conversely, spectra within the separated flow from the Channel 7 till the TE show an increase of energy related to small structures in the frequency range within 50 Hz and 1 KHz.

The second main evolution is the drain of energy content between 100 Hz and 1 KHz in spanwise direction toward midspan, i.e. $z/c = 1.26$, whereas the bump at lower frequencies is conserved. Channels 1 and 2 show this variation only at midspan, whereas all the channels from 3 to 11 present a progressive energy decrease from the endwall towards midspan. Such an evolution is in agreement with the existence of the separation, which slopes farther away from the endwall. This suggests that large energy pressure oscillations at low frequency are handled by large scale dynamics associated to the separation, while pressure fluctuations at high frequency reflect the signature of smaller eddies existing within the completely separated zone.

This concept additionally permits to explain the bump in the range between 100 Hz and 700 Hz, as highlighted by dashed circles in Fig. 5.2 for the Channel 10 ($s^* = 0.8$) and 11 ($s^* = 0.9$) at section $z/c = 0.13$ and $z/c = 0.26$, respectively. This bump is due to the presence of the main tornado-like structure laying on the aft part of the suction surface. It demonstrates that such a structure meanders as an ensemble of eddies of different sizes spreading energy over a wide frequency range, rather than in a concentrated peak.

Finally, peaks appear in spectra of channels from 7 to 11 between 800 Hz and 1 KHz at each section investigated. These peaks are well defined, visible both at sections near the end-wall and at midspan and present multiple harmonics at higher frequencies. Such evidences lead to the conclusion that they are a consequence of the noise of the facility. Furthermore the associated energy is comprised between $-10dB$ and $-20dB$ and the reduced frequency $f_r = f/f^*$ is higher than $f_r = 3$, so their influence on the blade pressure distribution is negligible. However, in order to avoid spurious results in correlations between the pressure signals, the pressure time tracers discussed hereinafter are low-pass filtered at 1 KHz.

Pressure coherence at different range of frequency

The existence of two dynamics in the pressure distributions can be highlighted by studying the coherence between the pressure tracers, defined as in Eq. 3.79 in Section 3.11.8.

The signal acquired at the LE for the Channel 1 is taken as reference for the calculation of the cross coherence with downstream Channels 2-11 on the suction surface of the blade. Fig. 5.3 shows this shared energy, as a function of the distance from the reference channel on x-axis and the frequency on the y-axis. Four spanwise sections are investigated and compared between the configuration $i = 4°$ and $i = 7°$. Since $\delta_{99}/c = 0.24$ is the thickness of the incoming boundary layer, it is interesting to compare sections which are within the inlet boundary layer, i.e. $z/c = 0.033$ and $z/c = 0.13$, with the section closest to δ_{99}, i.e. $z/c = 0.26$, and the section at midspan $z/c = 1.23$. The presence of two different loci $LC1$ and $LC2$ of high coherence is highlighted in Fig. 5.3.

A first region of large coherence $LC1$ is present at higher frequencies, from 50 Hz to 1 KHz. This locus is characterized by the negative frequency-distance slope.

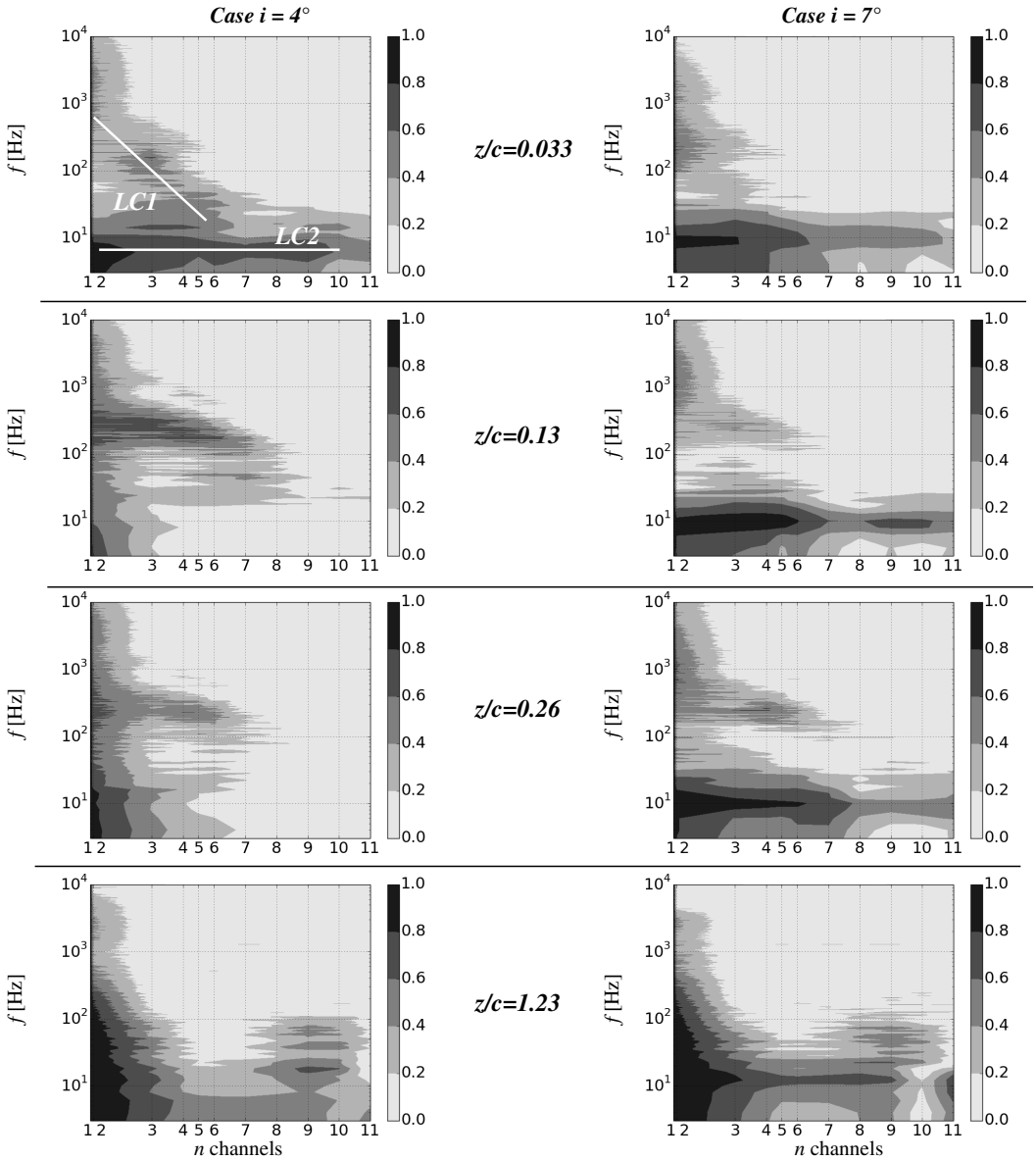

Fig. 5.3 Coherence at different spanwise sections between the Channel 1 and consecutive Channels (2-11) in streamwise direction.

This particularity is related to the convection mechanism of turbulent coherent structures. According to Lowson (1965), high frequency small-scale eddies lose coherence after a convection distance around four wave lengths, whereas low frequency large scale eddies lose coherence in a way which is not a function of wave length. Furthermore, high frequency components are convected at a slow speed, around 0.6 V_∞, and the convection velocity of the low frequency components attains 0.8 V_∞ at large transducer intervals. Intermediate scales progressively lose coherence and velocity accordingly to increase of frequency, giving the negative slope in coherence maps. This type of coherence highlights a streamwise convection

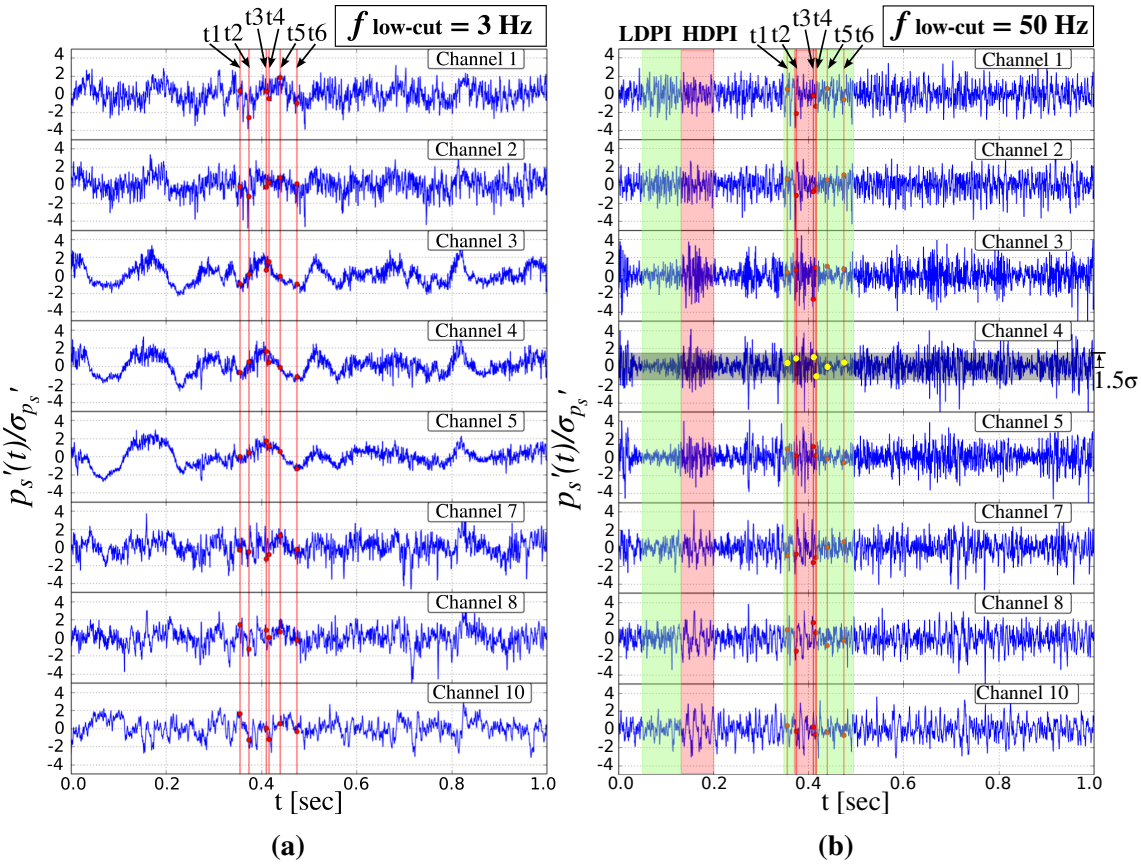

Fig. 5.4 Time pressure signals for the selected Channels, green points in Fig. 5.1: (a) 3 Hz low-cut signals, (b) 50 Hz low-cut signals with indication of LDPI and HDPI region. Red vertical lines represent the time instants selected in Fig. 5.6 and 5.1.

dynamic which is associated to the structures existing within the incoming endwall boundary, since it is absent at midspan.

A second locus, defined as $LC2$, is recognizable by the horizontal region at very low frequencies, around 10 Hz, which is visible at $z/c = 0.033$ for both the configuration $i = 4°$ and configuration $i = 7°$.

Even if low frequency oscillations of the pressure distribution on the blade suction surface are characterized by high uncertainty, as described in the Chapter 3, their existence is confirmed by the unsteadiness of the velocity field acquired by PIV measurements. This enhances the physical significance of the low frequency locus of coherence.

$LC2$ is characterized by a horizontal slope, which means that the Channel 1 at the LE and the channels downstream within the separation region share equivalent oscillations of the static pressure at 10 Hz. However the undergoing mechanism is different than the mechanism described by the existence of the higher frequency locus $LC1$. The coherence locus $LC2$ can not give any further insight on the direction of the propagation, but it can highlight the extend of the appearance of such a low frequency.

Fig. 5.3 shows that the extend of $LC2$ changes as the incidence increases. Whereas the configuration $i = 4^\circ$ shows the locus only very near the endwall at $z/c = 0.033$, the configuration $i = 7^\circ$ maintains $LC2$ also at $z/c = 0.13$, $z/c = 0.26$ and midspan. Such particularity can be explained by the increasing of the size and unsteadiness of the separation as the incidence is incremented.

The configuration $i = 7^\circ$ is indeed affected by a larger separated flow, which lifts from the surface of the blade more upstream than the case $i = 4^\circ$, as shown in Fig. 4.13 of Section 4.4.1. Additionally, it has been proved in Section 4.4.2 that the velocity oscillations of the flow during the bimodal switch of the separation increase. It is believed that this enlarged size and higher unsteadiness of the separation front boundary enhance the global perturbation of the static pressure field leading to a broader extent of the appearance of such low frequency pressure oscillations upstream of the blade and in the entire inter-blade passage.

In conclusion, it is clear that the study of cause-effect relationships between static pressures time tracers of corner separated flow is not trivial and further investigations are necessary in order to understand such dynamics.

In order to target this task, comparison of filtered signals, correlations between pressures time tracers, wavelet analysis and conditional ensemble averages have been conducted and will be shown in the following sections.

Filtered time tracers

The simultaneous pressure acquisition divided by the standard deviation of selected channels at $z/c = 0.033$ is shown in Fig. 5.4. Displayed channels corresponds to the green points on the suction surface of the blade presented in Fig. 5.1. Two different high-pass filters are used at low frequency, i.e. 3 Hz and 50 Hz, whereas the highest frequency allowed is limited to 1 KHz in order to discard peaks generated by the noise of the test rig. Fig. 5.4a therefore shows time tracers of pressure signals characterized by frequencies comprised between 3 Hz and 1 KHz. Low frequencies characterize large pressure fluctuations from Channel 1 to Channel 8. The value can be estimated between 6 Hz and 8 Hz, which corresponds to the reduced frequency $f_r \approx 0.03$. Such low frequencies progressively diminish until the TE, as it is visible for Channel 10. As inference, unsteady static pressure fluctuations on the blade surface are driven by a global low-frequency dynamic of the flow. The analysis conducted in Section 5.2.1 has shown that the flow mode described by such low frequencies is the movement of the separation on the suction surface. Higher-frequency fluctuations in Channel 10 can be attributed to the effects of smaller structures of the recirculation, overwhelming the main dynamic of the flow field.

By high-pass-filtering the signals with a low cut frequency of 50 Hz, time tracers as in Fig. 5.4b are obtained. This frequency corresponds to the reduced frequency $f_r = 0.1875$. Taking the Channel 4 as reference, since its critical position at the onset of the mean separation line, high deviation pressure intervals, called hereinafter HDPI, can be distinguished as time-intervals where the pressure fluctuations p_s' exceed the arbitrary threshold of $\pm 1.5\sigma_{p_s}{}'$. Conversely, low deviation pressure intervals, called hereinafter LDPI, denote pressure intervals where pressure fluctuations are below such a limit. Switches between low-fluctuations and high-fluctuations intervals are consequently found for Channels 3, 4 and 5.

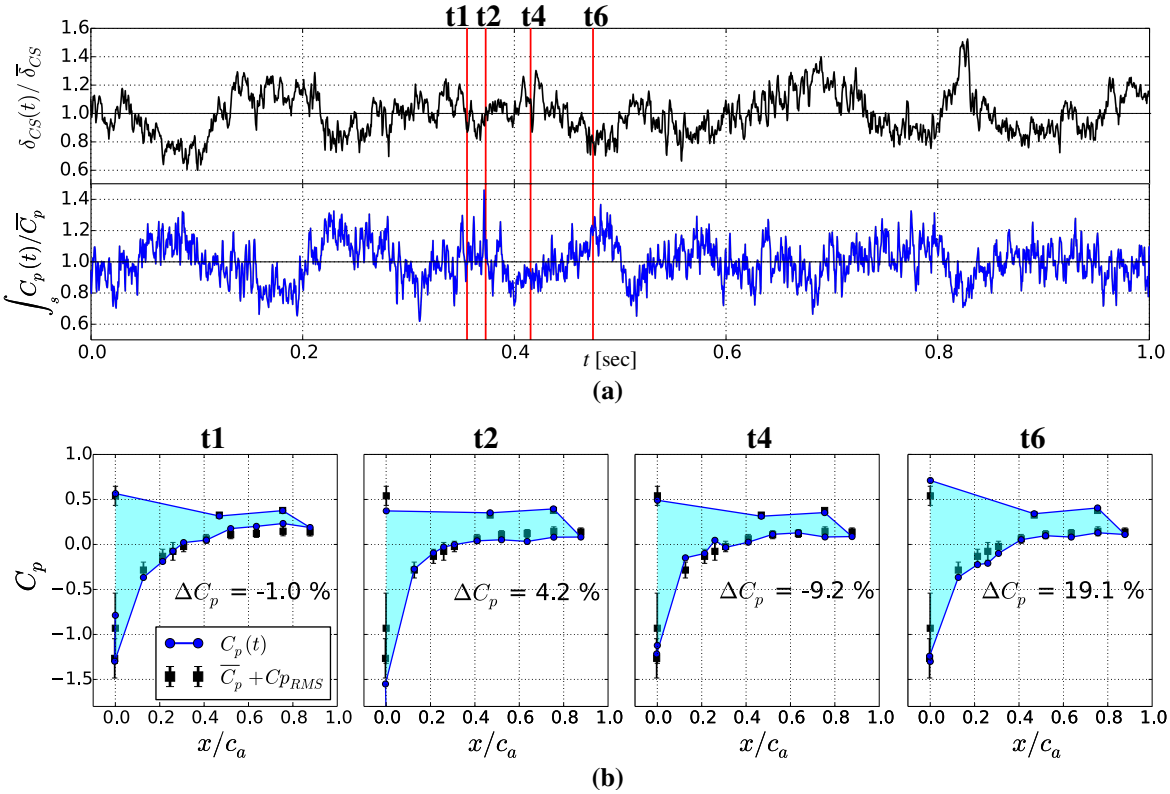

Fig. 5.5 Figure (a): displacement thickness calculated in the separation compared with integrated pressure distributions on the surface of the blade. Figure (b): unsteady pressure distributions captured for the selected instants $t1$, $t2$, $t4$ and $t6$ in relation to the flow visualization described in Section 5.2.1.

Comparing the selected instants from $t1$ to $t6$ of the flow visualization presented in Fig. 5.1 with their corresponding position on pressure signals filtered at 50 Hz (yellow points on vertical red lines in Fig. 5.4b), there is evidence to infer that the closed-to-open separation switch, i.e. from $t2$ to $t3$, occurs during HDPI inception. Vice-versa, the open-to-closed separation switch, from $t4$ to $t5$ as shown in the flow topology visualization of Fig. 5.1, occurs during LDPI inception in the pressure fluctuation time tracer of Channel 4. LDPI is hence maintained as long as the separation remains closed, till the occurrence of a following HDPI denoting that the separation size increases again. HDPIs are consequently important because their appearance is a signature in pressure fluctuations of the open separation inception. Such intervals are barely recognizable in the original signals high-pass filtered at 3 Hz.

The Section 5.3.2 will show cross-correlations calculated between these signals, both for pressures high-pass filtered at 3 Hz and 50 Hz. This will permit to clarify which dynamic underpins the existence of HDPI and LDPI.

Variation of the pressure distribution

In order to conduct the analysis, two integral quantities are defined as follows for pressure and velocity, respectively.

- The integral of the pressure distribution on the blade $\int_s C_p(t)$, which is proportional to the blade loading and equivalent to the Zweifel coefficient.
- The displacement thickness calculated across the separation at the fixed position $x/c = 0.93$ defined as in Eq 5.2.

$$\delta_{CS} = \int_{y_{CS}} \left(1 - \frac{u_b}{V_\infty}\right) \mathrm{d}y \tag{5.2}$$

The variation of the global pressure distribution is shown in Fig. 5.5a in comparison with δ_{CS}. It can be seen that the integrated C_p oscillates between $\pm 20\%$ of the mean value, with extreme peaks that can reach $\pm 40\%$. Such low frequencies pressure oscillations are in agreement with the low frequency oscillation of δ_{CS}, which confirms the physical meaning of the pressure measurements obtained by microphones.

Furthermore, the main correlation between the separation size and the integrated C_p is produced by the low frequency oscillation even if higher frequency oscillations characterize the signals during the whole measurement time. The maximum correlation peak has a negative value of -0.47, which confirms the counter-phase evolution of such time tracers directly visible in Fig. 5.5a: when the separation increases on the suction surface of the blade, the integrated pressure distribution decreases accordingly.

It is commonly known that the integrated pressure distribution is proportional to the blade loading, which in turn is associated both to the angle of attack of the flow and the flow diffusion within the stator passage, i.e. the extension of the separation. In present results, the increasing of the angle of attack is associated to the incoming vortical structures within the boundary layer as discussed in Section 5.2.1, which rise the magnitude of positive values of the C_p. This contribution is revealed by the variation of the C_p distribution between the instant $t1$ and $t2$ in Fig. 5.5b, where the pressure at the LE of the blade decreases for the closest probes to the LE, Channel 1 and 2 on the suction side and Channel 1 on the pressure side. The second contribution is confirmed in Fig. 5.5b for the instant $t4$, where the large separation highlighted by large positive values of δ_{CS} creates large pressure oscillations between $x/c_a = 0.1$ and $x/c_a = 0.4$ and it diminishes the blade loading in the aft part of the blade.

Since the pressure fluctuations on the pressure side of the blade are lower than at the suction side of the blade, the decrease of the blade loading during the separation growth phase, i.e. between $t2$ and $t4$, can be mainly associated to the decrease of the pressure gradient in the reference passage, i.e. above the suction surface of the blade. This process starts in the aft part of the blade but it propagates to the LE of the blade, leading to the lowest level of pressure distribution at the instant $t = 0.4$ sec. After such a reduction of diffusion in the passage, the closed separation is reestablished and the performance of the blade increase again, as for the instant $t6$ in Fig. 5.5b.

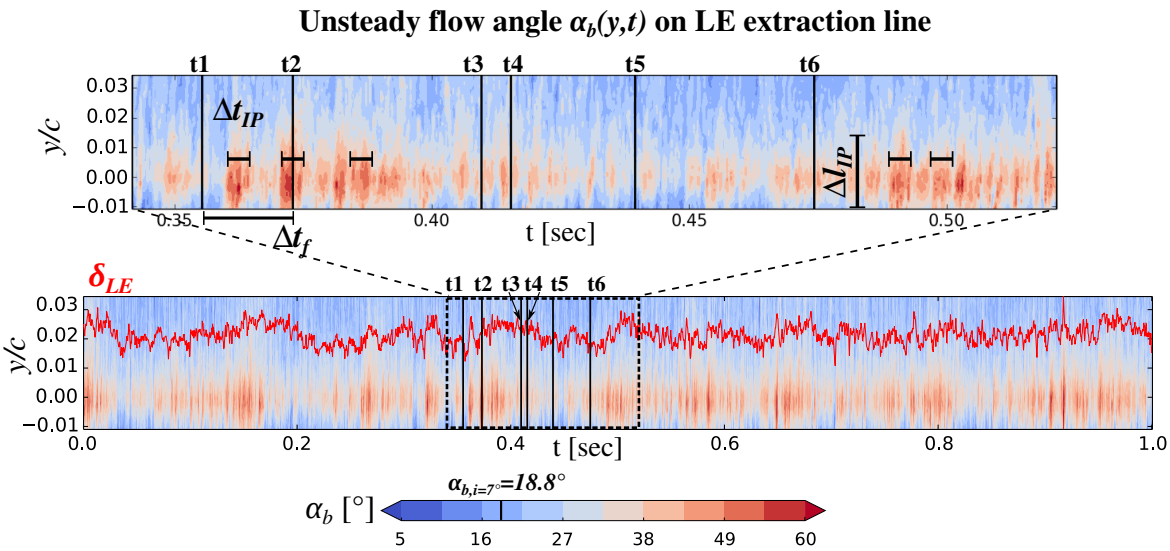

Fig. 5.6 Unsteady flow angle map α_b of the extracted line in front of the LE, black line in Fig. 5.1.

In conclusion, this Section shows that the pressure oscillations at frequencies lower than 10 Hz are consistent with the separation size variation observed by flow visualizations. As inference, the pressure measurements carried out by microphones can be considered meaningful also within this frequency range. Furthermore, two different dynamics of the flow are reflected in the pressure time tracers: a global low-frequency dynamic of the flow of $f_r \approx 0.04$ and a local higher-frequency dynamic of the flow of $0.2 < f_r < 3$.

5.3 The role of random incoming perturbations

Flow visualizations have shown the existence of incoming random events which perturb the separation boundary. This section focuses on the characterization of such events highlighted by the variation of the angle of the flow and their impact on the separation behavior.

5.3.1 Temporal evolution of flow angle of attack

In order to better investigate the unsteadiness of incoming flow structures, the black vertical line located in front of the LE, see Fig. 5.1, is used to monitor the unsteady angle α_b of the incoming flow. The temporal evolution of α_b is shown in Fig. 5.6. Red regions of flow angle values larger than two times the value of $\alpha_{b,i=7°}$ represent the spatial massive structures of the incoming boundary layer, which impact the LE of the blade, as shown at the instant $t2$ in Fig 5.1. Such structures can be better recognized in the zoom of the time-resolved angle in the upper part of the Fig. 5.6.

The order of magnitude of the spatial and temporal extent of such extreme incoming perturbations is defined as Δt_{IP} and Δl_{IP}, which are shown by strokes in the figure. For perturbations of $\alpha_b > 40°$ it results $\Delta l_{IP} = 0.25c$ and $\Delta t_{IP} = 0.005$ sec, which corresponds to

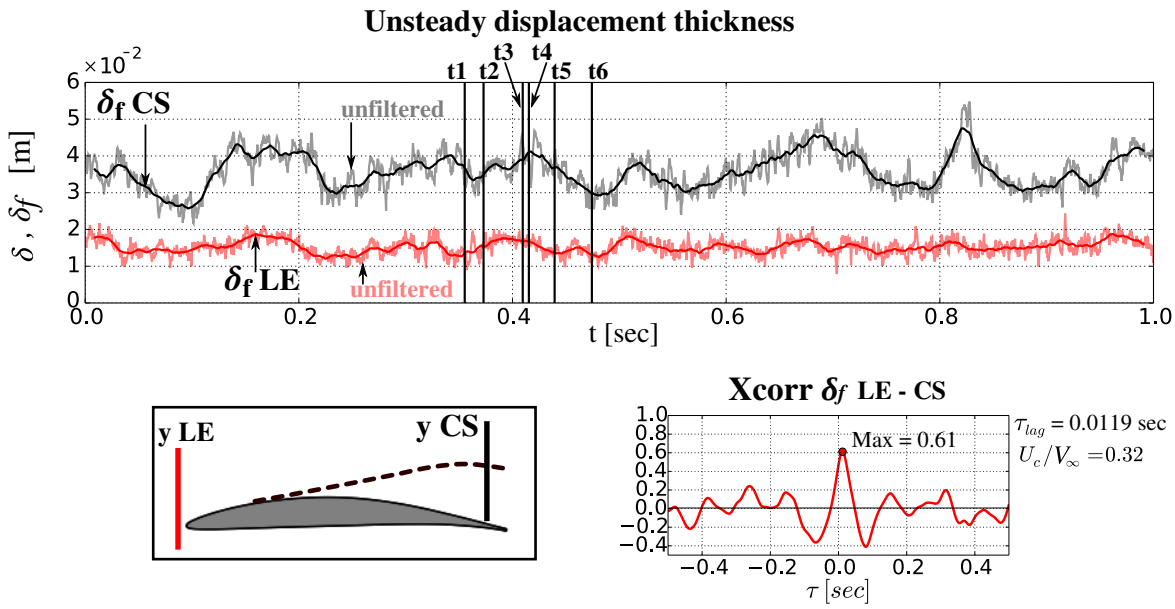

Fig. 5.7 Filtered displacement thicknesses calculated at LE and across the separation. The filtered lines are superposed to the unfiltered signals. Below: position of the extraction lines (on the left) and associated correlation (on the right).

$f_{IP} \approx 200$ Hz ($f_r \approx 0.76$). Such values quantify the high frequency associated to the extreme perturbations of the angle of attack, confirming the finding of the locus $LC1$ in the high frequency range of coherence maps between static pressures on the surface of the blade.

The analysis of the unsteady flow angle shows additionally that extreme flow perturbations are modulated by lower frequency oscillations, both in time and space, in agreement with the idea that larger eddies employ a longer time to pass through a fixed position. In other words, extreme incoming perturbations arrive in temporal sequences as groups of massive structures persisting for longer times than the single extreme event.

In the same fashion that δ_{CS} defined before in Eq. 5.2, the displacement thickness calculated on the extraction line in front of the blade LE at $x/c = -0.044$ is chosen as the integral estimator of upstream oscillations. The pertinence of this choice is verified by the matching between the fluctuations of δ_{LE} and the appearance of regions of large values of α_b, as shown in Fig 5.6.

With this integral parameter at hand, the unsteadiness of the upstream flow can be compared and correlated with the unsteadiness of the separation, as shown in Fig 5.7. Furthermore, it is useful to smooth both δ_{LE} and δ_{CS} in order to uniform the oscillation of the angle of attack and of the separation without filtering the contribution of the appearance of extreme events. In flow visualizations of Section 5.2.1 it was observed that groups of extreme perturbations persisting at least for time intervals longer than $\Delta t_f = t2 - t1 = 0.018$ sec are necessary to trigger the separation switch. For this reason, the characteristic time Δt_f can be arbitrarily assumed in order to average the displacement thickness on a window of 50 samples.

The comparison of the obtained smoothed results in Fig. 5.7 highlights the existence of the relationship between time-extended events at LE and variations of the size of the separation.

The correlation between $\delta_{f_{LE}}$ and $\delta_{f_{CS}}$ is verified by a positive value of 0.61 and gives positive time lag $\tau_{lag}/t^* = 3.17$. This result verifies that flow perturbations travel from the front of the LE to the separation and directly effects the separation size. By choosing the chord as characteristic length, which is equal to the distance between the extraction line at the inlet and across the separation in Fig. 5.7, the cross correlation time-delay quantifies the convection velocity as $U_{cLE-CS} = 12.8$ m/s, which is $U_{cLE-CS}/V_\infty = 0.32$. This convection velocity is consistent with the results of correlations between pressure signals high-pass filtered at 50 Hz further presented in Section 5.3.2.

In conclusion, unsteady incoming perturbations consist of massive incoming perturbations organized in groups, which arrive at low frequency rates and trigger the switch of the separation.

5.3.2 Correlation between unsteady pressures on the blade

The determination of the correlation between variables is one of the most effective means to establish casual relationships. When performing cross correlations at $z/c = 0.033$, $i = 7°$ between pressures on the suction surface of the blade shown in Fig. 5.4 of Section 5.2.2, it is useful to distinguish two cases, according to the reported frequency contain.

Correlations are computed separately for static pressure time tracers containing solely the low frequency, i.e. filtered to keep the frequencies between 3 Hz and 50 Hz, and signals with frequency content spanning between 50 Hz and 1000 Hz. The correlations can be further divided as shown in Table 5.1, and discussed as follows.

Table 5.1 Summary of correlations between static pressures on the blade suction surface.

Xcorr Ch i - Ch j		f range 3-50 Hz		f range 50-1000 Hz	
		Max corr	U_c	Max corr	U_c
Part I	$2-3$	0.8	-14.9 m/s	0.3	-130 m/s
	$2-4$	0.7	-17.4 m/s	0.2	-198.4 m/s
	$2-5$	0.6	-148.7 m/s	0.2	-382.2 m/s
Part II	$3-4$	0.9	13.2 m/s	0.3	16.1 m/s
	$4-5$	0.9	5.8 m/s	0.6	13.6 m/s
	$4-6$	0.9	5.2 m/s	0.4	14.1 m/s
	$4-7$	0.6	3.5 m/s	0.2	13.0 m/s

- The first part of table Table 5.1 shows the correlations of these two different filtered signals for correlations between the Channel 2 at the LE of the blade and channels downstream, i.e. at the boundary of the separation. It can be seen that in every

case the velocity given by the correlations between the selected channels is negative, since the time lag of the correlations is negative and the distance between the taps is considered positive in every case. Such correlations highlight the effect of the pressure perturbations which travel back, i.e. from probes located in the separated part of the suction surface to Channel 2 where the maximum acceleration of the flow takes place.

This can be explained only by the effect of the movement of the separation toward the leading edge during the closed-to-open process of the switch. In this case the dynamic is not local but global, because such correlations are the ensemble contribution of acoustic waves generated by eddies which form the boundary of the separation. It is known from literature (Fang and Atassi, 1993) that acoustic waves propagates upstream but also in every direction and they are reflected by the surfaces of neighboring blades and endwalls. Therefore microphones at the LE not only sense the main contribution of the blockage induced by the separation but also the sum of the reflected pressure waves traveling in the blade passage. For this reason values of velocity for the upstream propagation largely differ and these pressure correlations can solely lead to a qualitative description of the influence of the separation on the upstream flow.

- The second part of table Table 5.1 shows the correlations calculated between the channels in the region across the boundary of the separation, i.e. for probes between tap 3 and 7 at $z/c = 0.033$, $i = 7°$. Positive, i.e. co-flow, convection velocities result for both filtered signals, which highlight stream-wise perturbations traveling on the first half of the suction surface of the blade. Furthermore, it can be seen that the unique value of propagation velocity $U_c/V_\infty = 33\%$ is found when filtering the low frequency of the pressure fluctuations by keeping uniquely the contribution between 50 Hz and 1000 Hz of the signal. These signals are the pressure tracers shown in Fig. 5.4b, i.e. characterized by the sequence of HDPI and LDPI intervals, and U_c agrees with the convection velocity calculated for the co-stream coherent structures described in Section 5.2.1 and shown in Fig. 5.1b.

In conclusion, HDPI events can be considered the pressure signature of the coherent vortical structures presented at first in Section 5.2.1, which come from the incoming endwall boundary layer, strike the blade LE and travel on the suction surface of the blade. When reaching the detachment point such eddies destabilizes the separation and set with their vorticity the new frontal limit of the separation.

These facts enhance the hypothesis already presented in Section 5.2.1 that critical switches of separation are associated by lower-energy higher-frequency mechanisms, i.e. smaller structures characterized by HDPI signatures of static wall pressure, which are hidden by high-energy dynamics of the flow. This concept will be further investigated and demonstrated in Section 5.3.3, using wavelet transform to relate pressure and velocity, and in Section 5.4.2, using modal analysis to evaluate the energy of different dynamics.

5.3.3 Effect of extreme incoming perturbations on the separation

The incoming perturbations of the endwall boundary layer that destabilize the boundary of the separation are here investigated by applying the wavelet transform to the pressure

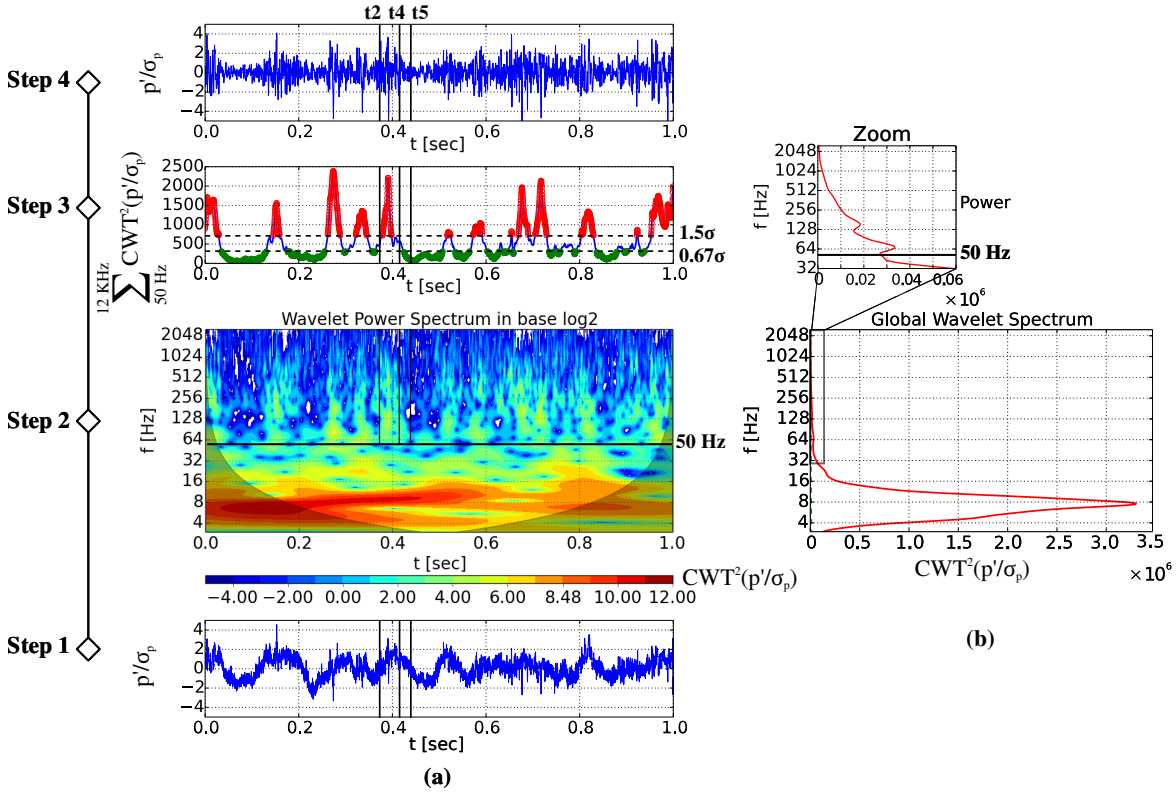

Fig. 5.8 Wavelet analysis of the pressure signal acquired by the Channel 4 synchronized with HS-PIV.

signals of the configuration $i = 7°$. The original signal of the Channel 4, which contains the low-frequency high-energy oscillations, is taken in the Step 1 and its wavelet power spectrum is shown in Fig. 5.8a at the Step 2.

In the wavelet power spectrum map, larger powers are localized in the low frequency range, below 16 Hz, but significant powers can be recognized also above 50 Hz. In order to highlight their contribution, the spectrum is integrated by preserving only frequencies higher than 50 Hz. The result, presented in Fig. 5.8a at the Step 3 of the analysis, shows the alternation of low and high levels, hereinafter referred to as wavelet peaks.

As argued before, the low frequency dynamic hides the higher frequency fluctuations but these are equally important since are related to the coherent vortical structures convected on the suction surface of the blade. The occurrence of peaks at high frequencies in the wavelet spectrum in Fig. 5.8a at the Step 3 is related to the separation switch, as demonstrated below.

Two distinct time-sets can be obtained by choosing the instants where the integrated wavelet spectrum of Step 3 crosses an arbitrary threshold of 1.5σ or is below the threshold 0.67σ. Since velocity and pressure measurements are synchronous, these time-sets are exploited to divide the entire time-resolved velocity data set in two distinct ensembles, to which the time-average is subsequently applied.

The streamlines traced for both these two cases in Fig 5.9 highlight the variation of the separation size. The ensemble average of the data set conditioned by the appearance of

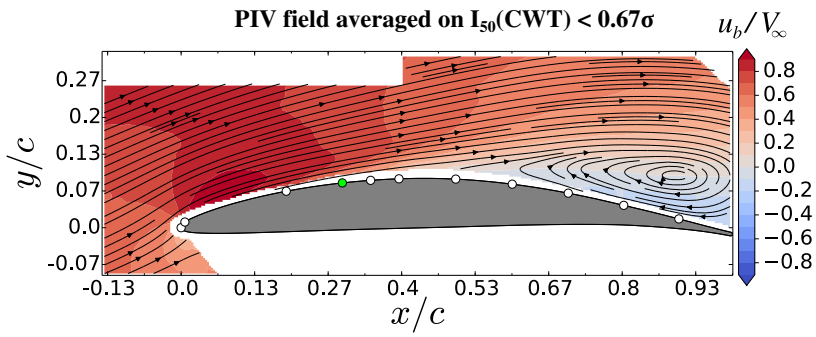

(a)

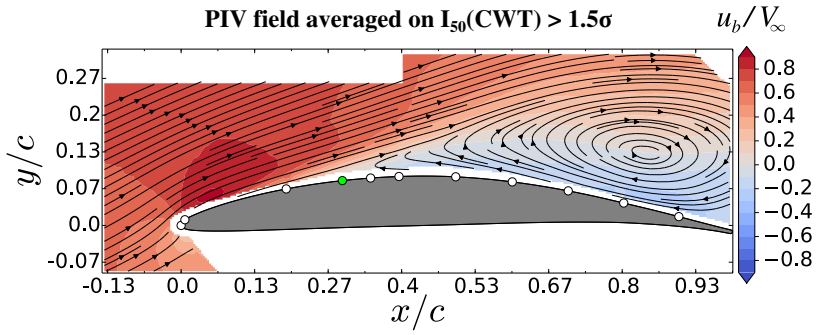

(b)

Fig. 5.9 Wavelet conditional ensemble averaged of velocity u_b at section $z/c = 0.033$, $i = 7°$. Closed separation (a) and open separation (b) corresponding to two different wavelet power spectral thresholds as illustrated in Step 3 of Fig. 5.8a. Green point: trigger probe number 4.

peaks, i.e. the red circles in Fig. 5.8a at Step 3, gives the time-averaged field representing the massive separation in Fig. 5.9b. Conversely, the time averaged data set triggered on low values of the integrated wavelet power, i.e. green circles in Step 3, results in a pattern characterized by the closed separation, see Fig. 5.9a.

The difference between the two flow fields is additionally recognized by contours of chord-wise velocity u_b normalized by the inlet velocity. The blue region, which highlights the back-flow, increases for the open separation. Conversely, the acceleration region on the first third of the suction surface of blade near the LE decreases, showing a direct effect of the growth of the blockage on the upstream flow.

The integrated wavelet power of Fig. 5.8a at Step 3 is additionally compared with the high-pass frequency signal of the pressure acquired by the Channel 4, previously presented in Fig. 5.4b and reproduced in Fig. 5.8a at the Step 4. It can be seen that wavelet peaks match the occurrence of HDPI signatures in the pressure time-tracer. Vertical black lines on the Fig. 5.8a correspond to the previous instants $t2$, $t4$,$t5$ associated respectively to closed separation, open separation and sweep of the recirculation region during the closing process.

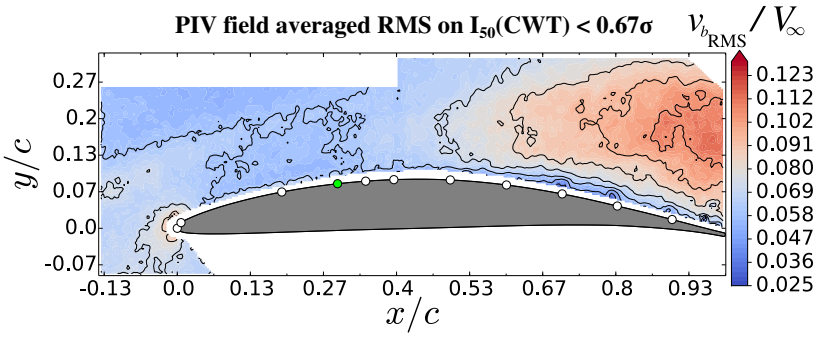

(a)

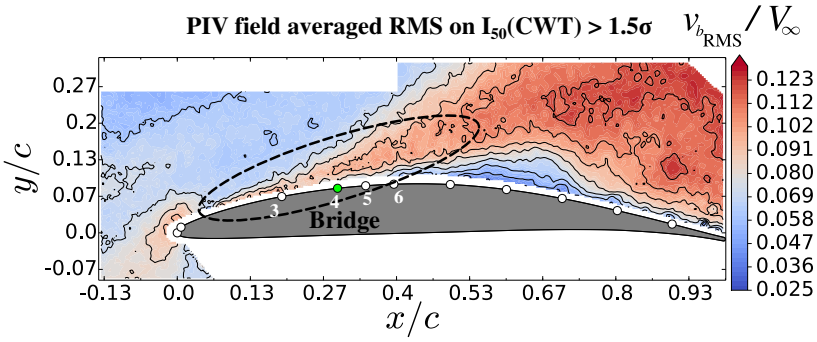

(b)

Fig. 5.10 Wavelet conditional ensemble RMS of v_b at section $z/c = 0.033$, $i = 7°$. Closed separation (a) and open separation (b), green point: trigger probe number 4. Dotted ellipse: “bridge" of high RMS associated to convected structures.

The wavelet peak is located just between the closed and open separation, i.e. instants $t2$ and $t4$, confirming that the HDPI occur at the inception of the opening process. Finally the existence of the LDPI is correlated to the reattachment of the flow and the disappearance of the separation, i.e. at the instant $t5$.

Further insight into the relation between the destabilizing vortical structures and the closed-to-open switch can be obtained by calculating the wavelet ensemble RMS value of the velocity v_b. The results shown in Fig. 5.10 are contour of normalized v_{bRMS}, which highlights the region associated to high fluctuations of the velocity normal to the blade chord, hence representing the ejection process of coherent structures related to the flow detachment process. Larger values are present in the aft part of the blade at the boundary between the time-averaged recirculation region and the free-stream, both in Fig. 5.10a and Fig. 5.10b. However, only the open separation, i.e. Fig. 5.10b, shows a connection between this region and the front part of the blade suction side, in particular with the position of Channels 3, 4 (green point), 5 and 6. Here, larger fluctuations of the flow uncover the presence of the destabilizing structures that are convected from the LE toward the separation. The absence

of this "bridge" in the closed configuration of Fig. 5.10a remarks the cause-effect relation between the occurrence of such perturbations and the switch inception.

The cause-effect mechanism supporting the close-to-open switch is therefore confirmed to be attributed to the influence of incoming perturbations on the separation and not the inverse. This because the correlations of the Part 2 of the Table 5.1 between the channels from 3 to 6 give a positive convection velocity in the stream-wise direction.

Finally, the same wavelet averaged process was tested on the low frequency range by integrating the low frequency variation in the wavelet power spectrum. In contrast with what previously obtained by focusing only on the higher-frequencies, the final conditional ensemble averages of this case (not presented here) do not shown two distinct states of the flow but the same mean separation. This is the counter proof that small scale perturbations convected downstream and merging with the already existent eddies of the separation, are responsible for the destabilization of the separation boundary and the consequent closed-to-open switch.

5.4 The upstream effect of the separation blockage

5.4.1 Conditional ensemble average of pressure signals

In order to investigate the relationship between the LE movement of the stagnation point and the footprint of the separation on the suction surface of the blade, conditional ensemble averages of pressure signals have been performed and are here analyzed.

The skewness analysis illustrated in Section 4.3.2 has remarked that positive pressure peaks on the suction surface of the blade are related to the onset of the separation. Fig. 5.12 and Fig. 5.13 show that those pressure peaks could be detected if the ensemble average is conditioned by the LE negative pressure events for the case $i = 4°$ and $i = 7°$, respectively.

Conditional ensemble averages of the original time signals can be computed by averaging windows of signal triggered on the largest values of pressure fluctuations (i.e pressure peaks). This permits to individuate the existence and the influence of a selected time-averaged pressure signature on another signal. The temporal average is performed over all the signal segments, which consist in windows of arbitrary width centered on selected time instants ${t_0}^i$, as formalized in Eq. 5.3.

$$\langle p_1(t_w)\rangle = \frac{1}{N_w}\sum_{i=1}^{N_w} p_1(t_w - {t_0}^i) \tag{5.3}$$

Here N_w is the number of windows utilized and $t_w \in [{t_0}^i - \tau; {t_0}^i + \tau]$ is the time variable in the window, which depends on the chosen size of τ. The same computation is applied to the second signal preserving the same trigger instant ${t_0}^i$. Finally, by superposing the two ensemble averages it is possible to characterize the correlation between the two signals induced by the selected events. The conditional ensemble average is well suited to individuate correlations depending on aperiodic phenomena and it is often utilized to analyze unsteady pressure measurements by microphones as done by Laadhari et al. (1994) and Camussi et al. (2008). In the present investigation, the pressure signals have been low-pass filtered at

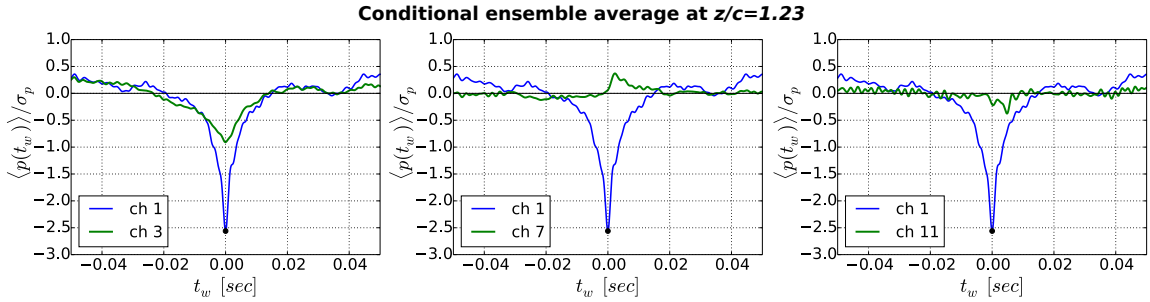

Fig. 5.11 Ensemble average comparisons for negative thresholds between channel 1 at $s^* = 0.0$ and channels downstream, section at midspan ($z/c = 1.23$).

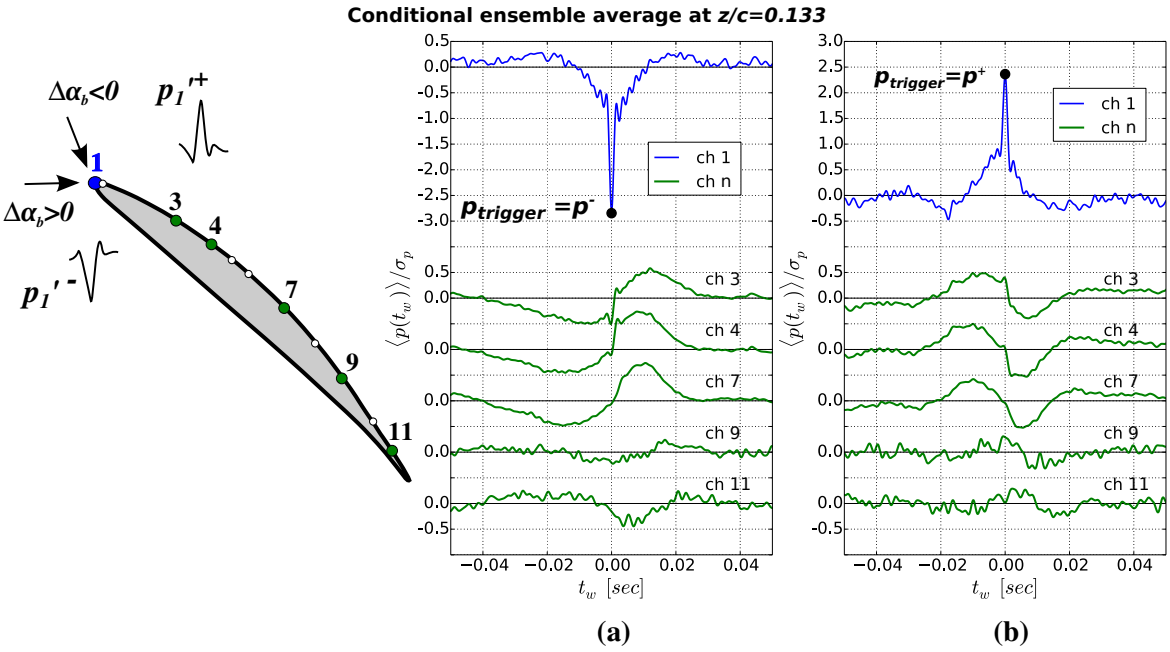

Fig. 5.12 Ensemble average comparisons between channel 1 at $s^* = 0.0$ and channels downstream for positive and negative triggers in the separated region ($z/c = 0.133$).

500 Hz and their ensemble averages have been triggered on instants at which the pressure fluctuations exceed the threshold value of 2σ.

At midspan, see Fig. 5.11, the flow does not present the separation so the peaks of the ensemble averages of Channel 1 and 3 have the same sign. Anyway, it is possible to remark the presence of a positive peak for the conditional ensemble average of Channel 7, underlying slight oscillations of the blade shear layer near mid-chord.

Fig. 5.12a shows ensemble averages of channels from 3 to 11 triggered on negative pressure peaks of Channel 1 at LE at the section $z/c = 0.133$ from the endwall, while Fig. 5.12b presents the ensemble averages triggered on positive pressure peaks of Channel 1 at LE.

The meaning of the aforementioned negative and positive pressure peaks detected in Channel 1 can be understood through the aid of the sketch on the left part of Fig. 5.12. The

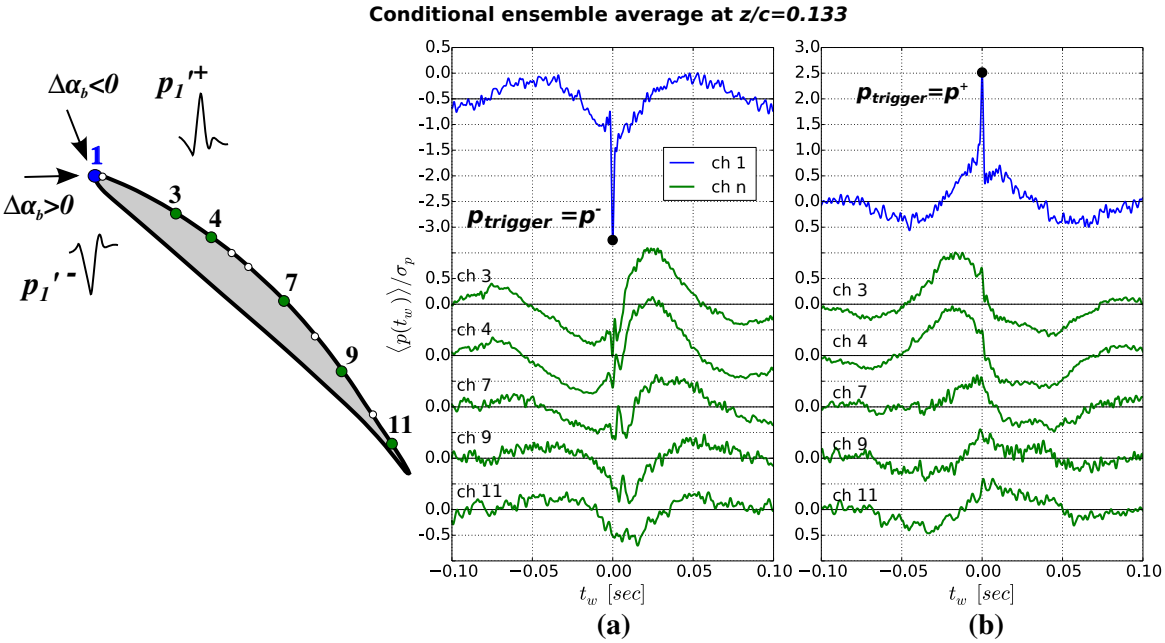

Fig. 5.13 Ensemble average comparisons for configuration $i = 7°$ between Channel 1 at $s^* = 0.0$ and channels downstream for negative (a) and positive (b) triggers in the separated region ($z/c = 0.133$).

fact that the Channel 1, the nearest one to the stagnation point, experiences low pressure levels is explained by the movement of the stagnation point toward the pressure side of the LE. This is caused by an instantaneous increment of the angle of attack, i.e. over-incidence. Reversely, positive pressure fluctuations sensed by Channel 1 are related to the movement of the stagnation point toward the Channel 1, which is the result of a local decrease of the angle of attack of the blade, i.e. under-incidence.

In Fig. 5.12a, conditional ensemble averages of Channels 3, 4 and 7 triggered on negative peaks of Channel 1 show positive bumps, i.e. positive pressure fluctuations, which reveal the detachment of the flow accordingly to the discussion elaborated in Section 4.3.2. The new result highlighted by Fig. 5.12a is the existence of such bumps after the trigger time zero, i.e. for $\tau_w > 0$, which describes a streamwise relationship between the pressure fluctuations at the LE and at the separation front.

In particular, the ensemble average of Channel 7 ($s^* = 0.5$) gives the highest correlation bump in agreement with the skewness map of Fig. 4.11c, which has revealed that the position $s^* = 0.5$ is the statistically preferred for the location of the frontal separation boundary in the configuration $i = 4°$. Anyway referring to Fig. 5.12a, the conditional ensemble averages of the Channel 3 and 4, respectively at $s^* = 0.2$ and $s^* = 0.3$, present a positive peak as high as in Channel 7. This is consistent with the unsteady movement of the separation front due to the separation switch described in Section 5.2.1 for the configuration $i = 7°$, but existing also for the configuration $i = 4°$.

The events of the Channel 1 are no more correlated with channels beyond the detachment point, see channels 9 and 11, because of the 3D dynamics of the flow within the recirculation

region. When looking at conditional ensemble averages shown in Fig. 5.12b, which are triggered by positive pressure peaks of Channel 1, the same curves are found, but in this second case positive bumps appear before the trigger time 0, i.e. in the interval $\tau_w < 0$. A different mechanism underpins this case in comparison with the first, but a relation exist between them and can be explained as follow.

1. Sudden increases of the local angle of attack associated to large negative pressure fluctuations of Channel 1 induce positive pressure fluctuation in Channels 3, 4 and 7, which highlight the detachment mechanism accordingly to the theory reviewed in Fig. 4.12. This relation is streamwise since the time-lag is positive.

2. Positive pressure fluctuation in Channels 3, 4 and 7 appear before the positive pressure fluctuations sensed by the Channel 1. Channel 1 shows such positive fluctuations when the stagnation point moves closer to the tap as result of the decrease of the local angle of attack.

3. The turnover of negative and positive pressure fluctuations in the pressure time-tracer of Channel 1 is explained by the fact that random increments of the angle of attack are correlated to the flow detachment associated to the front of the separation. This in turn increases the size and the blockage of the separation, which leads to the feedback effect of blocking the incoming flow and decreasing the local angle of attack of the flow at the leading edge of the blade. This mechanism causes the appearance of opposite large positive pressure fluctuations in Channel 1. It is fair to theorize that in the case of LE under-incidence the separation is then almost suppressed restoring the initial state.

It is necessary to stress that this process is not periodic but aleatory.

Equivalent characteristics are found for the conditional ensemble averages of pressure signals acquired for the configuration $i = 7°$, as shown in Fig. 5.13a and Fig. 5.13b. In such cases the positive pressure bumps of green ensemble averages related to downstream channels on the suction surface appear early upstream, are wider in time and larger in amplitude. Such details are in agreement with the movement of the separation farther upstream when the inlet incidence of the cascade is increased. Furthermore, such larger amplitudes of the pressure bumps in the separation at $i = 7°$ remark that increasing the incidence the the separation unsteadiness and the related pressure oscillations intensify.

5.4.2 Modal analysis

To combine the information on statistics and whole-field, the proper orthogonal decomposition (POD) is applied to the recorded velocity data in the configuration $i = 7°$ at $z/c = 0.033$. To guide the reader, first a brief introduction of the POD is provided, which is largely summarized from Kriegseis et al. (2010) and Fernando et al. (2014).

The modal decomposition of the global measurement field is then compared with the decomposition of two local regions of the flow: the separation and the LE region. Finally, the eigenvalues associated to the modes of these two domains are cross-correlated and discussed.

Proper orthogonal decomposition (POD)

The POD is utilized to decompose the PIV flow field $V(x,t)$ into independent modes $\Phi_j(x)$ and associated time coefficients $\mathrm{a}_j(t)$ forming a new base on which the original flow can be reconstructed. The instantaneous flow field $V(x,t)$ is at first decomposed into the mean flow component $\bar{v}(x)$ and the fluctuating part $v'(x,t)$ such as

$$V(x,t) = \bar{v}(x) + v'(x,t) \tag{5.4}$$

The deviations $v'(x,t)$ from the mean lead to an eigenvalue problem whose eigenvectors $\Phi_j(x)$ are the POD modes with the corresponding eigenvalues λ_j, separating the correlated non homogeneous flow structures from uncorrelated random fluctuations. The spatial velocity distribution for time step t_i to describe a flow field of D data points, i.e x_k $(k = 1 : D)$, can be written as

$$\mathbf{v}_i = \begin{bmatrix} v'(x_1,t_i) \\ v'(x_2,t_i) \\ \vdots \\ v'(x_D,t_i) \end{bmatrix} \tag{5.5}$$

The velocity vectors $\boldsymbol{v}_i (i = 1 : N)$ over N time steps are collected to form the velocity matrix

$$\mathbf{V} = [\boldsymbol{v}_1 \ \boldsymbol{v}_2 \ \cdots \ \boldsymbol{v}_N] \tag{5.6}$$

Hence the covariance matrix can be built

$$\mathbf{R} = \mathbf{V}\mathbf{V}^T \tag{5.7}$$

permitting to solve the eigenvalue problem

$$\mathbf{R}\boldsymbol{\Psi} = \boldsymbol{\lambda}\boldsymbol{\Psi} \tag{5.8}$$

with $\boldsymbol{\lambda}$ and $\boldsymbol{\Psi}$ the eigenvalue diagonal matrix and the matrix of the eigenvectors Φ_j $(j = 1 : N)$, respectively

$$\boldsymbol{\Psi} = [\Phi_1 \ \Phi_2 \ \cdots \ \Phi_N]^T \tag{5.9}$$

The contribution of each mode to the overall signal power is given by the relative energy contribution

$$P_j = \frac{\lambda}{\|\boldsymbol{\lambda}\|} \tag{5.10}$$

Since the eigenvalues of $\boldsymbol{\lambda}$ are arranged in a decreasing order $(\lambda_{j+1} < \lambda_j)$, the powers P_j decrease with the increasing of the index j. Finally, reconstruction of the velocity fields $\boldsymbol{v}_i$ with $\boldsymbol{\Psi}$ leads to the time arrays $\mathbf{a}_i$ of a_j coefficients.

$$\mathbf{a}_i = \boldsymbol{\Psi}\boldsymbol{v}_i \tag{5.11}$$

The modes $\Phi_j(x)$ and the associated time tracers $\mathrm{a}_j(t)$ are the objects of the following analyses.

Global POD modes investigation

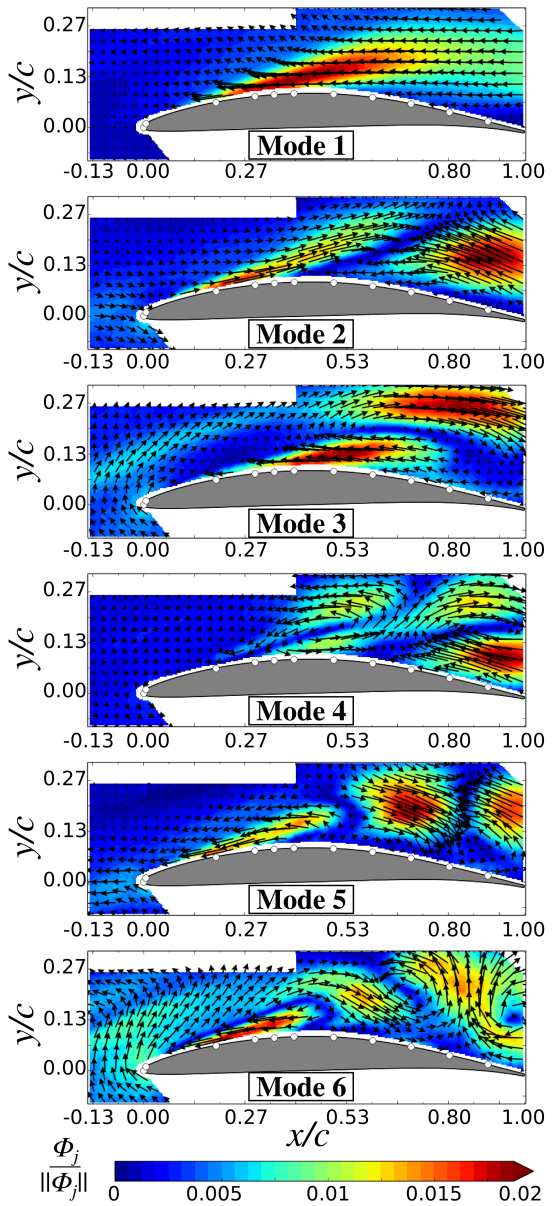

(a) First 6 modes of the POD

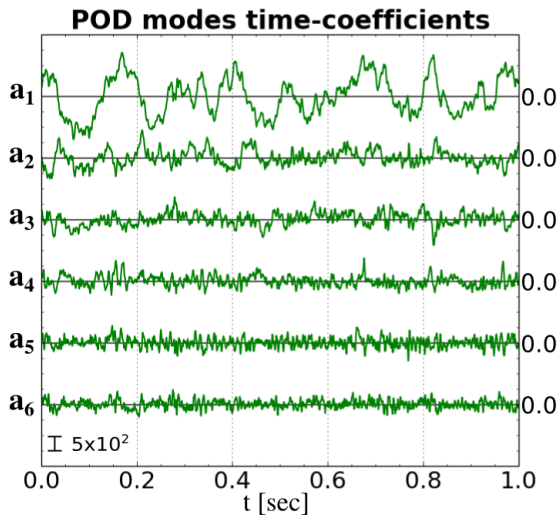

(b) POD time coefficients a_j $(j = 1:6)$ corresponding to the first six modes obtained by global POD field calculation for 1 sec of acquisition, $N_1 = 2781$.

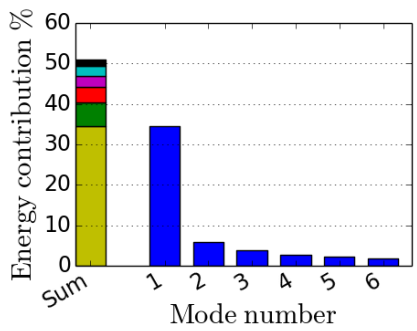

(c) Energy of the first 6 modes of POD, cumulated energies of the six modes are sketched in the first left column.

Fig. 5.14 Results of POD performed on the global field of data-set $i7°$ at $z/c = 0.033$, time data-set 1 sec ($N_1 = 2781$ samples).

The first six modes of the global POD and the associated energy are presented in Figs. 5.14a and 5.14c, respectively. The Mode 1 is predominant, containing more than 30% of the relative energy contribution to the entire energy of the investigated flow field. The flow pattern of Mode 1 is mainly composed of a translatory velocity pattern which is largely aligned with the blade, as shown in Fig. 5.14a by black vectors and better depicted in

Fig. 5.15. Since this pattern largely covers the separated region of the averaged flow field, as evinced by comparison with results presented in Section 5.2.1, this mode directly affects the size of the recirculation zone.

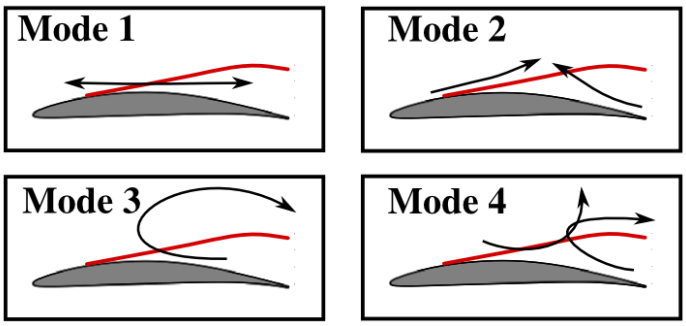

Fig. 5.15 Interpretation of Fig. 5.14a: sketch of the direction of the most extended vectors for the first four modes of POD applied to 2D velocity field, configuration $i = 7^\circ$ at $z/c = 0.033$, 1 sec data-set measurement.

The shear layer translates from a position more upstream to a position more downstream and contains the lower frequencies associated to the high-energy large scales. Looking at the time coefficients of the modes as represented in Fig. 5.14b, it can be pointed out that this pattern is the Mode 1, which drives also the low-frequency fluctuations of the pressure signals presented above. After the first mode, the relative energy contain decreases to values ranging between 6% (Mode 2) and 2% (Mode 6) of the entire energy of the flow field, see Fig. 5.14c. Referring to Fig. 5.14a and its interpretation in Fig. 5.15, Mode 2 represents the dynamic described by the flow visualization analysis as the competition between the strong backflow coming from the TE and the boundary layer coming from the LE of the blade, which results in the ejection of structures towards the free stream. Mode 2 is therefore a pattern describing the separation lift from the surface of the blade. Mode 3 again is associated with the big recirculation region that forms in the aft part of the blade. The vortical structure of this pattern corresponds to a circulation-variation of the forming vortex. Mode 4 describes a second pattern associated to the deformation of the separation boundary and can be considered, as Mode 2, a pattern of the separation lift. Finally, Mode 5 and 6 partly account for the contribution of perturbations convected from the highly turbulent region in front of the LE through the separation.

Local POD modes investigation

In order to study the desired cause-effect relations more accurately, the global flow field is now further divided into distinct yet interrelating smaller flow domains at which the POD is then applied separately. Such an approach becomes particularly important if single large-scale events predominate the modal decomposition of the flow. For the problem at hand this is obviously the case, as a fair third of the fluctuating energy (contribution of global Mode 1) is contained in the separation region. However, it is remarked that this pattern,

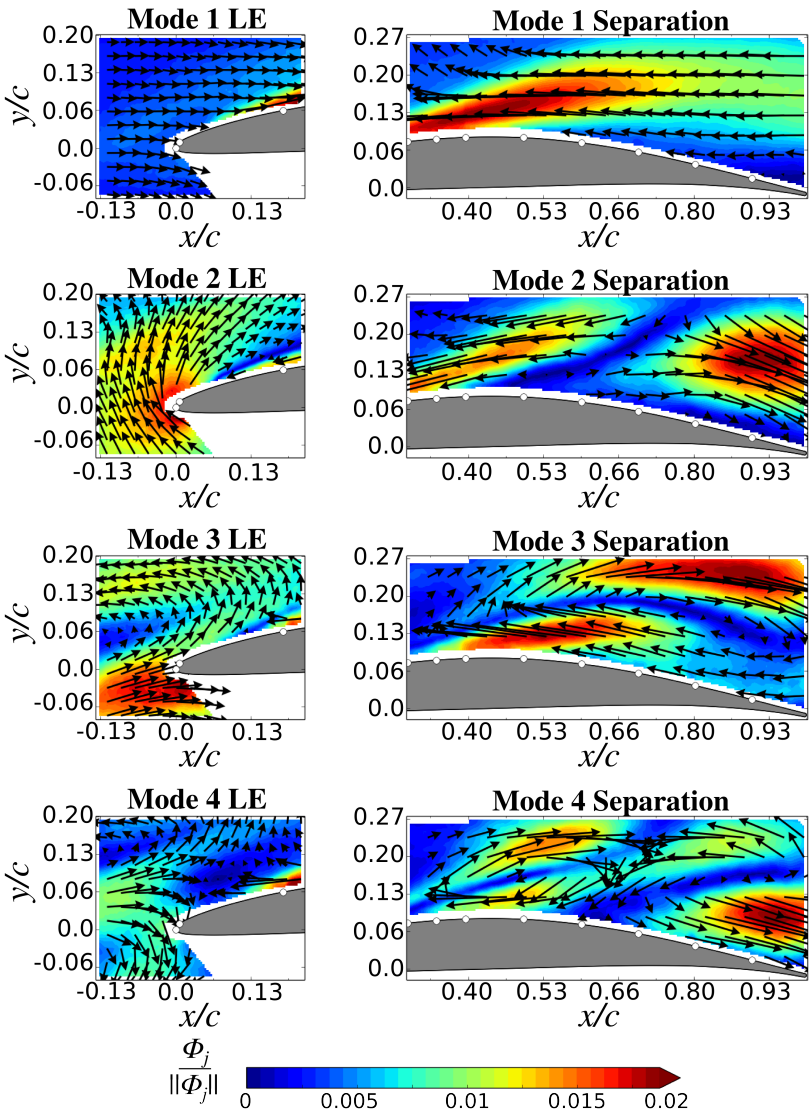

Fig. 5.16 First 4 modes of POD on cut sections of the original field: Leading edge (LE) and Separation

i.e the separation movement, is triggered by small-scale extreme events, as presented in Section 5.2.1 and Section 5.3.3.

This idea supports the present procedure consisting in the division of the field in two selected regions at which the POD is then applied separately. The first cut focuses on the LE of the blade, domain which will be referred to as the leading edge region (LER). The second region comprises the predominating separated recirculation zone, which should remain largely unchanged when POD is processed with the cropped domain. Accordingly, this part of the flow will be referred to as the separated region (SR).

The first four modes of both cropped flow fields (LER/SR) and corresponding relative powers are presented in Figs. 5.16 and 5.17, respectively. It can be noticed that the POD of the SR reveals a similar modal content to the full POD at comparable eigenvalues. This

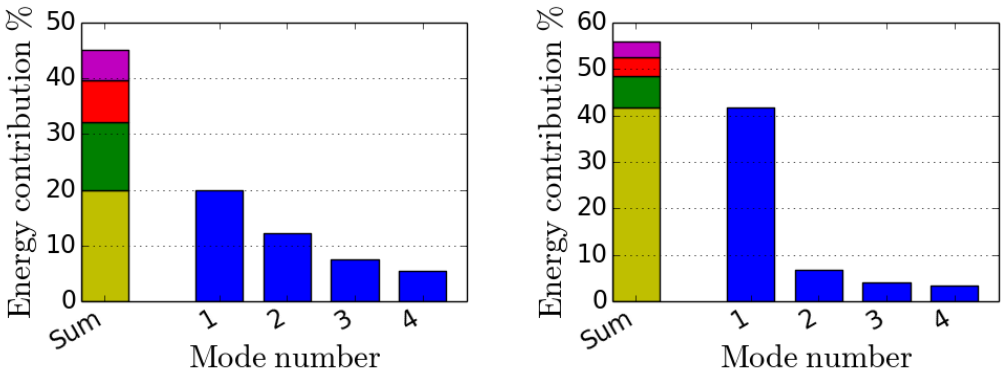

(a) LER **(b)** SR

Fig. 5.17 Energy of the first 4 modes of local POD applied to cut sections of the original field: (a) Leading edge (LER), and (b) Separation (SR). Cumulated energy is sketched in the first left column of each diagram.

observation directly supports the second above-stated hypothesis. In contrast, the POD of the LER presents a different distribution with a gradual decreasing of the energy associated to higher order modes. The modes of the LER are patterns of fluctuations of the velocity vectors in magnitude and direction and basically describe flow angle perturbations in front of the LE of the blade. Mode 1 of the LER shows the starting point of the boundary of the separation on the suction surface, revealed by larger vector magnitudes in the region at $x/c = 0.13$. In this region, Mode 1 enclose the 20% of the energy contribution for the LE local field, see Fig 5.17a. Modes 2, 3 and 4 present again the region at $x/c = 0.13$ on the suction surface, but they are additionally characterized by regions of relevant vector magnitudes between $x/c = -0.13$ and $x/c = 0$. These vectors describe the coherent motion of structures in front of the leading edge of the blade and, cumulated together, they account for the 25% of energy contribution in the LER.

Local modes correlation

In order to investigate the relationship between the separation and the LE region, the histories of the reconstructed time coefficients of modes have been cross-correlated and couples showing meaningful correlations are presented in Fig. 5.18 and the discussion resumed in Table 5.2. The cross-correlation $R_{mn}(\tau)$ between signals $\mathrm{a}_{mSR}(t)$ and $\mathrm{a}_{nLER}(t)$ is formed from the ensemble average:

$$R_{mn}(\tau) = \frac{1}{T} \langle \mathrm{a}_{mSR}(t+\tau)\mathrm{a}_{nLER}(t) \rangle \tag{5.12}$$

where the angle brackets denote the ensemble average, $\mathrm{a}_{mSR}(t)$ is the m-mode of the separation region and $\mathrm{a}_{nLER}(t)$ is the n-mode of the LE region. The resulting function is divided by the auto-correlation peak of the time tracer associated with the respective mode of the

Table 5.2 Summary of POD correlations between LE region and separation region.

LER	SR	|peak|	Mechanism	Direction
1	1	0.7	Separation translation	Forward ($\tau > 0$)
2	1	0.4	Flow angle perturbation - Separation translation	
1	2	0.4	Separation translation - Separation lift	
2	2	0.35	Flow angle perturbation - Separation lift	
4	1	0.3	Flow blockage - Separation translation	Backward ($\tau < 0$)
2	3	0.3	Flow angle perturbation - Separation recirculation	

separation region, in order to obtain a coefficient between -1 and 1, as in Eq. 5.13.

$$r_{mn}(\tau) = \frac{R_{mn}(\tau)}{\sqrt{R_{mm}(0)R_{nn}(0)}} \tag{5.13}$$

The value of $r_{mn} = \pm 0.2$ is arbitrarily chosen as threshold in order to consider meaningful cross-correlation. Therefore the peak of the correlation coefficient is used to evaluate the time-lag τ solely if $r_{mn} > 0.2$. The way these correlations are performed permits to infer that $\tau > 0$ highlights correlated events traveling from LE to separation in the co-flow direction, and $\tau < 0$ highlights vice-versa correlated events traveling from the separation to the LE region of the flow in the counter-flow direction.

Mode 1 of the leading edge domain (M1LER) and Mode 1 of separation (M1SR) are well correlated as demonstrated in Fig. 5.18a. The correlation peak is negative because the two modes have inverted vectors. By comparing their vector fields in Fig. 5.16, it can be seen that these modes represent the same flow: the chord-wise oscillation of the separation which is Mode 1 for the global POD. The associated positive lag means that the fluctuating information travels from the leading edge to the separation, i.e. over a distance of $x/c = 0.5$, in a delta time of $\tau = 3.9 \times 10^{-3}$, which results in a value of convection velocity $U_c = 19.2 m/s$ in agreement with the convection velocity theory (Lowson, 1965).

The correlation between the mode M2LER and M1SR shown in Fig. 5.18b is also positive in magnitude. The interpretation is that fluctuations of velocity which increase the local flow angle at the LE induce an upstream movement of the separation onset. The associated time-lag is positive but it leads to the convection velocity $U_c = 0.5c/(31.6 \times 10^{-3}) = 2.4 m/s$, a propagation velocity slower than the value found in the previous cross-correlation between M1LER and M1SR.

The modes M1LER and M2SR show a negative correlation peak $r(\tau) < -0.45$ in Fig. 5.18c with a positive time-lag, which leads to a convection velocity of $U_c = 34 m/s$ between the LE and the middle of the suction surface. Therefore, a chord-wise acceleration at the LE, beside the effect already described for M1LER-M1SR, increases also the co-flow with a consequent increase of the collision strength described by the Mode 2 of the separation region. The mode M2SR is also influenced by the fluctuation of the flow angle at the

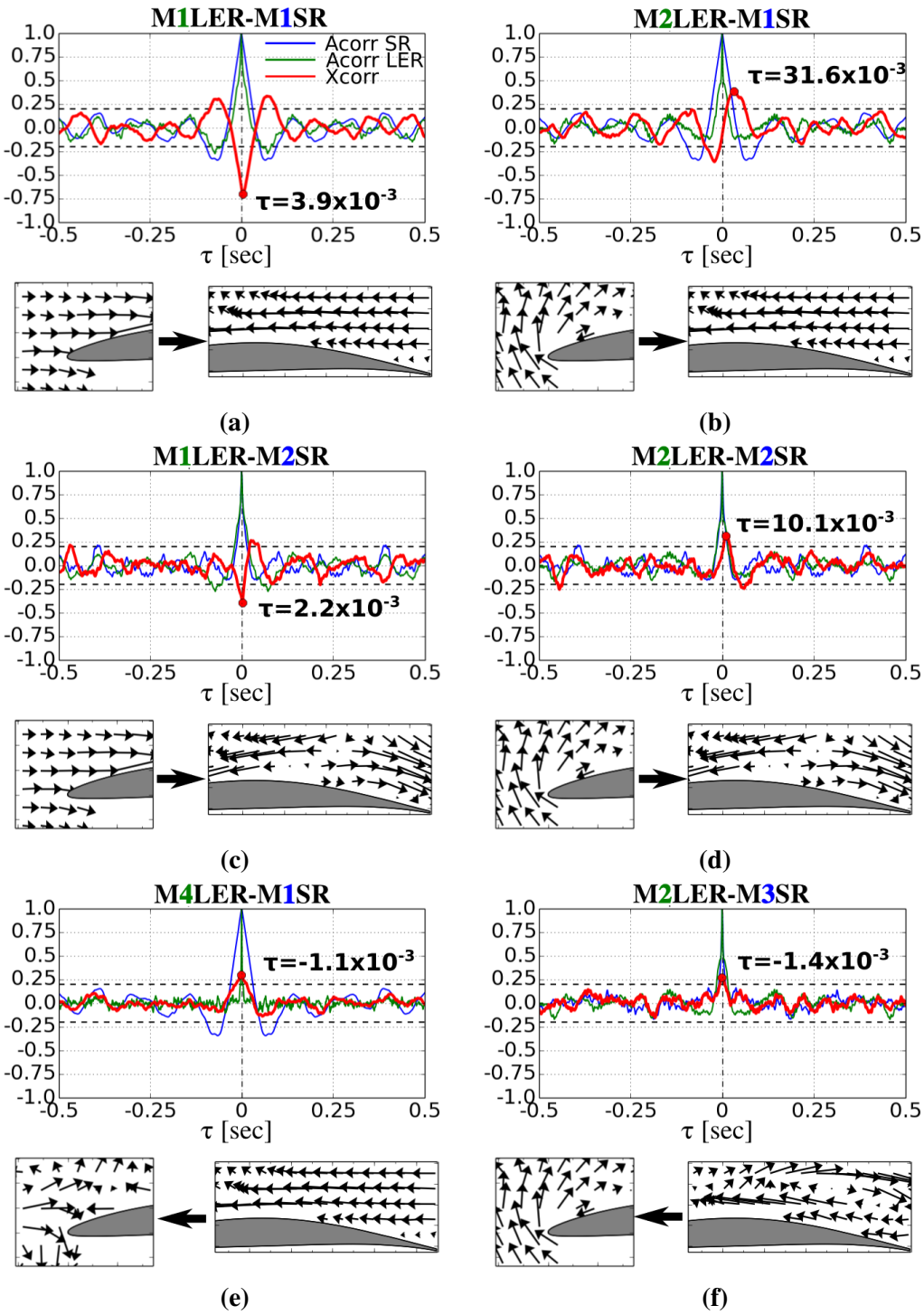

Fig. 5.18 Red lines: highest correlations between different modes of the two selected regions, LE and Separation. Blue lines: auto-correlation of separation region modes; green lines: auto-correlation of LE region modes. Corresponding selected modes for correlations are sketched below each correlation graph.

LE represented by mode M2LER, but their correlation, shown in in Fig. 5.18d, leads to a convection velocity $U_c = 7.4m/s$ which is slower than the previous correlation with M1LER.

The correlations presented above describe signals convected in the streamwise direction, but it is of major interest to individuate which modes contribute to the feedback effect caused by the blockage on the upstream flow. The first back-ward correlation is shown in Fig. 5.18e and it is calculated between the mode M1SR and the mode M4LER. The correlation presents a negative time-lag $\tau = -1.1 \times 10^{-3}$, which is also the shorter lag found. Therefore, the information is predominantly transferred from the separation to the LE region with a negative speed two times higher than the inlet velocity. This negative velocity is associated with the potential effect of blockage, which almost instantaneously influence the upstream flow in front of the blade. Accordingly to such a phenomenon, the black vectors of Mode M4LER appear to diverge at the LE of the blade as obliged to face an enlarged obstacle.

The second backward correlation is sketched in Fig. 5.18f showing that Mode 3 in the separation (M3SR) influences the incidence variation at the LE, i.e. M2LER. The negative lag $\tau = -1.4 \times 10^{-3}$ demonstrates that Mode 3, which is the coherent large rotating structure in the center of the separation, has an instantaneous impact on the fluctuations of the local flow angle at the LE. The peak is positive since if the rotating structure is clockwise, the size of the separation grows and the flow is again obliged to increase its deviation with a consequent increase of the local incidence.

5.5 Comparison with diffuser regimes

The previous investigation has shown that the flow within the inter-blade passage is characterized by intermittent switches between closed and open state of the separation. Furthermore, low frequency large oscillations of the pressure have been detected on the blade surface. These unsteady dynamics have major characteristics in common with the well reported large transitory stall regime in diffusers, reviewed in Section 2.4. Consequently, it is interesting to verify if empiric maps built in order to describe simple two-dimensional diffusers can provide predictions of the state of the flow in the blade passage of the present study, which is also a diffuser. The parameters of the geometry of the inter-blade passage, see Section 3.2, are combined with the incidence angle to reduce the system to an equivalent curved diffuser. Finally Fig. 5.19b shows the configuration $i = 4°$ and $i = 7°$ in comparison with empiric maps adapted for diffusers with circular arc center line and linear area distribution presented in the work of Fox and Kline (1962). In their correlations it can be seen that the turning angle has no significant effect on line $a - a$ for turning angles of thirty degrees or less, hence the curbed diffuser channel can be reduced to a straight-walled diffuser.

Following the approach provided by Fox and Kline (1962), the effective divergence angle $2\theta_{eff}$ can be calculated as in Eq. 5.14.

$$AS = \frac{W_2}{W_1} = 1 + \frac{2N}{W_1} \tan \theta_{eff} \tag{5.14}$$

All the variables are calculated only as functions of the geometry of the diffuser, hence Eq.s 5.15 and 5.16 are used. This choice was made in order to adapt the approach to

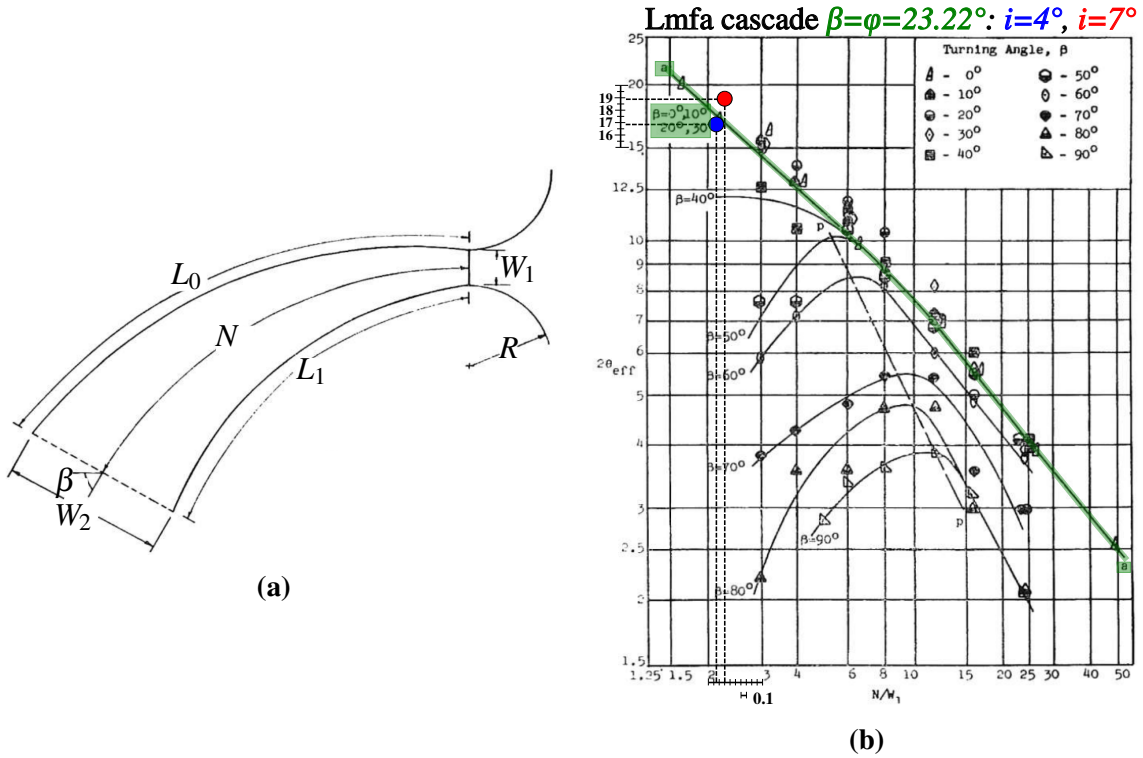

Fig. 5.19 Curved diffuser geometry (a) and location of first appreciable stall as a function of turning angle (b), reproduced from Fox and Kline (1962). The blue circle localizes the LMFA cascade operational point for $i = 4°$, the red circle for $i = 7°$.

the inter-blade section facing an incoming flow with specific incidence. The variation of the incidence is accounted in the calculation of the inlet section W_1. Conversely, the flow deviation angle δ^0 due to the separation is neglected and the adopted exit section W_2 is the result of the geometry of the blade row only. This assumption is made because the flow deviation is a consequence of the flow regime in the curved diffuser, therefore it can not be assumed *a priori* to evaluate the operational point of the blade passage.

$$W_1 = S_p \cos(\gamma + \varphi/2 + i) \qquad W_2 = S_p \cos(\gamma - \varphi/2) = 0.115\text{m} \tag{5.15}$$

$$N = 2\pi r \frac{\varphi}{360} = 0.151\text{m} \qquad r = \frac{c/2}{\sin(\varphi/2)} = 0.373\text{m} \tag{5.16}$$

For the case $i = 7°$, the inlet section results $W_1 = 0.065$ m and the Eq. 5.14 leads to the results summarized in the Eq. 5.17.

$$\frac{N}{W_1} = 2.32 \qquad \frac{W_2}{W_1} = 1.768 \qquad \rightarrow 2\theta_{eff} = 18.77° \;\; (i = 7°) \tag{5.17}$$

For the case $i = 4°$, the exit section W_2 is kept constant, whereas the variation of incidence has a geometrical influence on the inlet section, i.e. $W_1 = 0.070$ m. The results are resumed in Eq. 5.18.

$$\frac{N}{W_1} = 2.16 \qquad \frac{W_2}{W_1} = 1.64 \qquad \rightarrow 2\theta_{eff} = 16.87° \;\; (i = 4°) \tag{5.18}$$

Fig. 5.19b shows that the resulting points are close to the transition line $a-a$ (green line) given by the empirical correlations of Fox and Kline (1962) for curved diffuser with turning angle comprised between $\beta = 0°$ and $\beta = 30°$. In particular, the case $i = 4°$ is slightly under the line, even if still in the region starting to experience the appreciable stall. Conversely, the case $i = 7°$ is above the $a-a$ line meaning that the regime in the inter-blade passage matches the high unsteadiness region where transitory stall occurs.

5.6 Interactions between adjacent corner separations

The question arose from the previous sections is whether the corner separation unsteadiness of a single blade passage can influence the flow in adjacent passages and propagate as a perturbation in pitchwise direction.

In order to answer this question, unsteady total pressure measurements were carried out with in-house manufactured probes equipped with Kulite XCE-093-1PSID and Kulite MIC-093 sensors, as discussed in Section 3.8.

One probe for each corner separation was build and placed in the test rig to measure the unsteady signal in chosen bimodal points. With a total of six probes, the corner separation of three blade passages on each side (left and right endwall) was investigated in the first configuration, sketched in Fig. 5.20a. Additionally, a second configuration was set up to monitor five passages on the left endwall and only one corner separation on the opposite side in the reference passage, see Fig. 5.20b.

The position of the probes was slightly adjusted before performing the final measurements, by tracking the points where the flow shows the higher bimodality around the nominal position, without changing the spanwise position of the probe. This because the position of bimodal points depends on the exact size of the separation, which slightly differs between the blade passages, as discussed in Chapter 3.

5.6.1 Meaningful interactions

The necessity to perform measurements on both sides of the test rig is derived from the necessity to verify the existence of an interaction between corner separations on the left and right endwall in the same inter-blade passage. Table. 5.3 resumes the results obtained by cross correlating each probe with the others.

Such results show that very low negative correlations exist between sensors placed in the same passage at opposite sides. Conversely, higher correlations are found between sensors on the same side of the test rig.

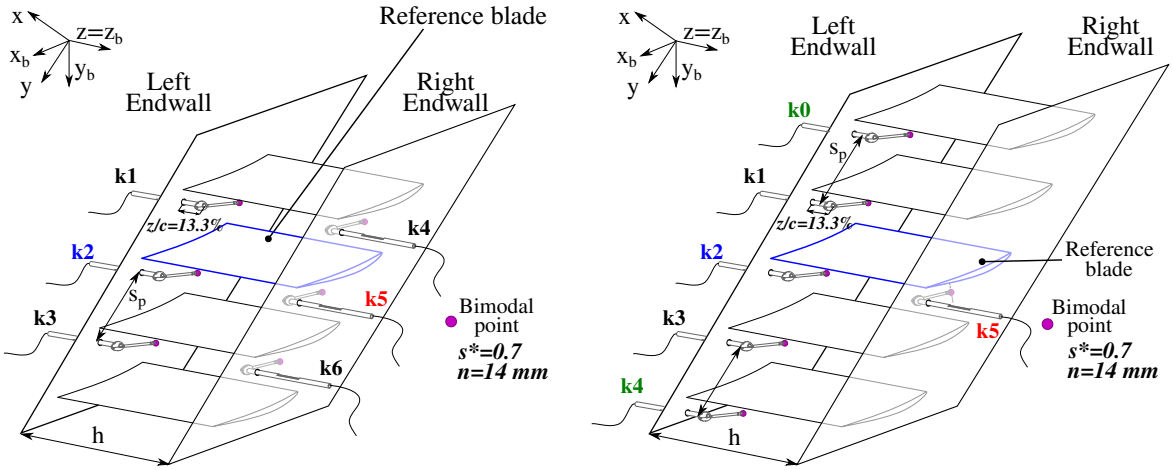

(a) Configuration A (3+3) **(b)** Configuration B (5+1)

Fig. 5.20 Different configurations for the experimental investigation carried out with time-resolved total pressure probes.

Fig. 5.21 shows that the correlation between sensors on the same side of the test rig is coherent and describes the propagation of the disturbance in pitchwise direction. The lag is negative when correlating the middle sensors k1 and k4 with the upper blade, whereas the lag becomes positive when correlating with the following passage. Moreover, the signal acquired by the sensor k4 shows the same time lag and the same propagation velocity than the sensor k1.

These results are of particular importance for two reasons. At first, they demonstrate that both sides of the test rig present the same propagation of a disturbance in the pitchwise direction, since same lags and same velocities have been found. Secondly, a question was open as whether such a disturbance could have been generated by the wood step used to increase the thick of the left boundary layer or other imperfections of the internal wall of the duct. The present result shows conversely that on both sides the bimodal points are correlated in pitchwise direction, so considering that the boundary layer on the right side is unperturbed, the disturbance propagation can be ascribe solely to the perturbation due to the unsteadiness of the corner separations in neighbors passages on the same side wall.

5.6.2 The pitchwise disturbance propagation

More information is necessary on the same side of the test rig to better describe meaningful correlations which exist solely in pitchwise direction. The configuration B was adopted for this reason, so in order to characterize the generation and evolution of the pitchwise correlation. An overall view of the resulting measurement is given in Fig. 5.22. The distributions of total pressure losses ω_t of each signals are shown on the left, along with the corresponding extraction of 1 sec of the time tracer in the middle and the Fourier transform of the entire signal on the right. The upper bump of ω_t (between values of 0.6 and 1.2) corresponds to the open corner separation, whereas the bottom bump corresponds to the

Table 5.3 Summary of correlations between multi-passage pressure signals in configuration A.

kX \ kY	k0	k1	k2	k3	k4	k5
k0	1	0.23	0.12	-0.09	-0.07	0.06
k1		1	0.11	-0.09	-0.07	-0.07
k2			1	-0.07	-0.08	-0.07
k3				1	0.22	0.11
k4					1	0.11
k5						1

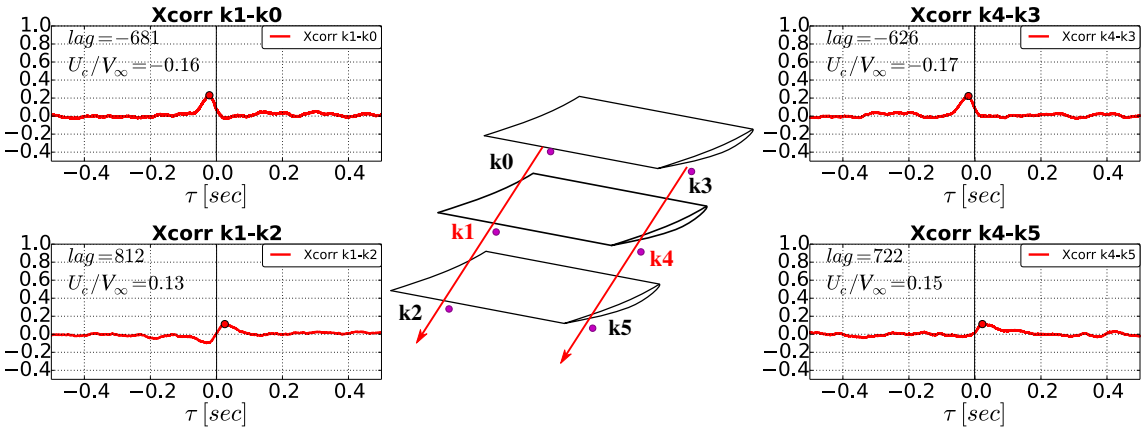

Fig. 5.21 Correlation between total pressure measurements carried out within three passages on both sides of the cascade (Configuration A).

closed state. The similarity of these measurements with the extracted points of HS-PIV measurements, confirm that the bimodal state is detectable both by dynamic pressure and velocity measurements.

As can be seen, the ω_t bimodal distribution is not the same in each passage, and can be located at higher or lower mean levels. Anyway, the existence of the bistable state of the separation does not depend on such a mean value of total pressure losses. The distributions differ also in what concerns the distance of the two bumps, which is explained by the associated Fourier transform on the right of the figures: a higher separation of the PDF bumps corresponds to a higher energy contain in the lower frequency range between 1 Hz and 10 Hz.

Correlations between the reference signal k2 with neighboring passages in pitchwise direction are confirmed in Fig 5.23. The convection velocity is calculated from the resulting time-lag between the peak of the cross correlation and the value $\tau = 0$.

A correlation exists between the signals, and the related convection velocity has a finite value that is positive when considering a traveling signal from k0 to k4, i.e. disturbances

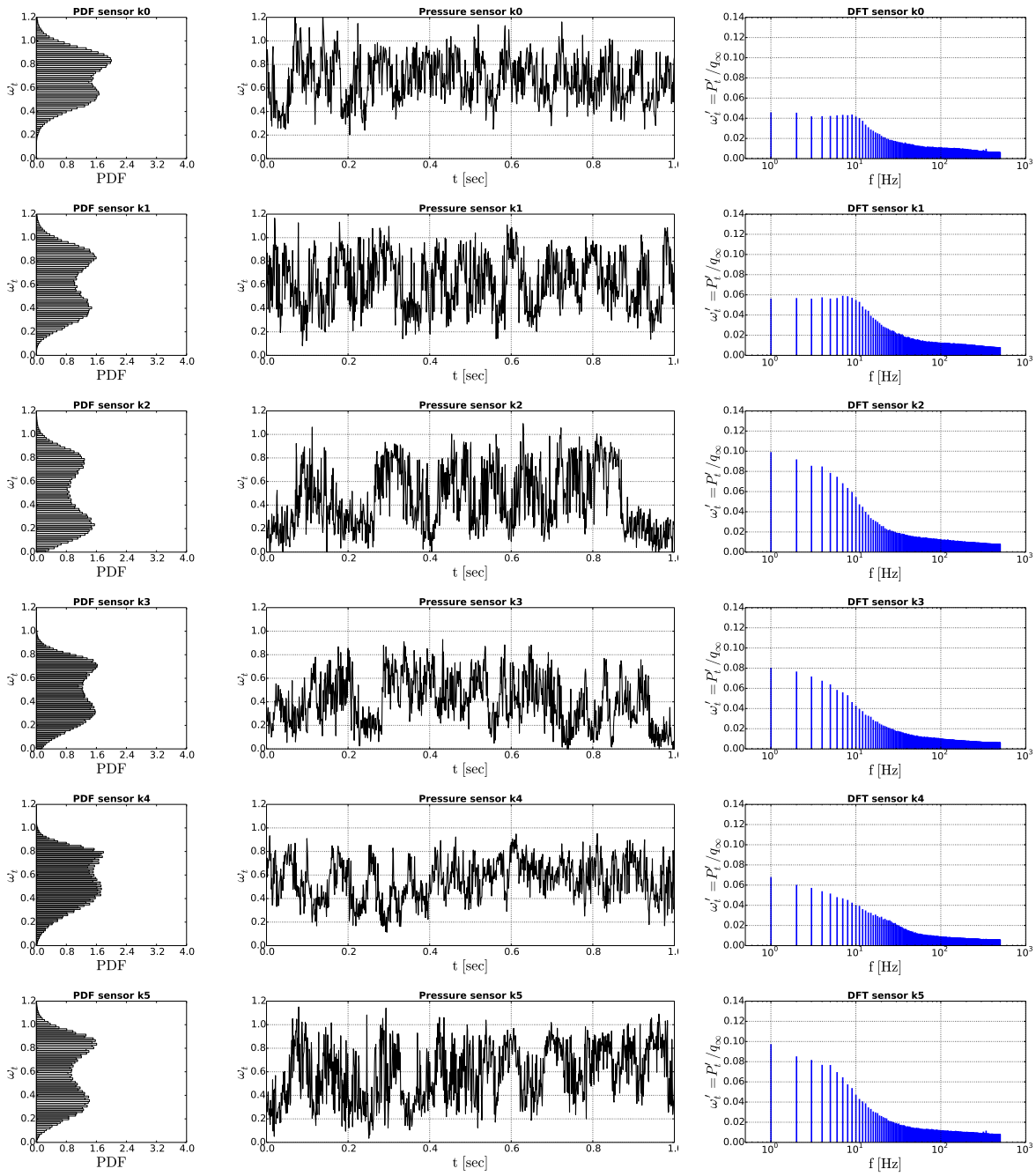

Fig. 5.22 Configuration B: time-resolved total pressure losses distributions (left column), associated time tracer for 1 second of acquisition (central column), and related Fourier spectra (right column).

that travel from the suction surface of a blade n to the pressure surface of the blade $n+1$. This is in agreement with the models of stall propagation presented in Chapter 1, i.e. in circumferential direction considered as positive when oriented in the same sense of the stagger of the blades.

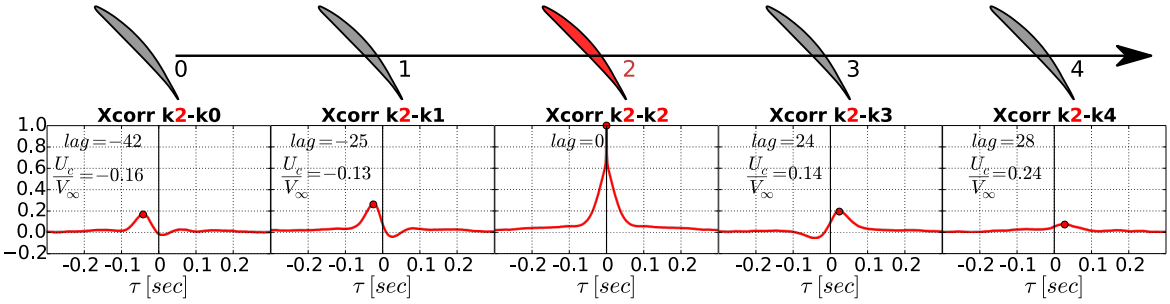

Fig. 5.23 Correlation between the reference passage, probe k2, and the four adjacent passages on the left side of the cascade (Configuration B).

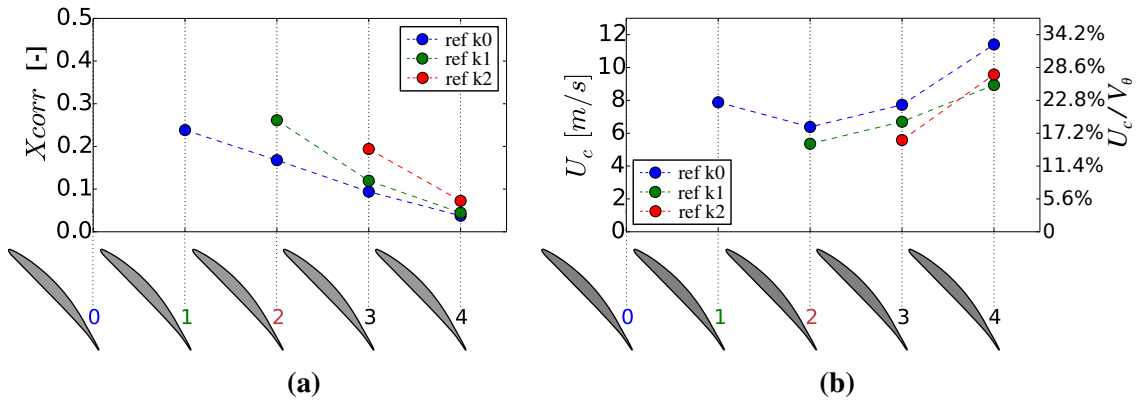

Fig. 5.24 Correlations between adjacent passages in configuration B. Figure (a): correlation peaks. Figure (b): related convection velocities.

Fig. 5.24 resumes the results of the correlations performed for Probe k0, k1 and k2 with the following probes in pitchwise direction. The value of the correlation peak decreases as the distance from the first probe increases. As can be seen in Fig. 5.24a, the value diminishes from 0.2 to 0.07 for every probe. This effect is probably due to the fact that the test rig is a linear cascade and does not permit to propagate the disturbance. The associated value of the convection velocity for each cross correlation is shown in Fig. 5.24b. The convection velocity can be compared to the velocity component of the flow in pitchwise direction at midspan $V_\theta = V_\infty \tan(\alpha_1)$. It can be seen that the velocity of disturbances ranges between $U_c/V_\theta = 17\%$ for closest correlations, as between probes k1-k2 and k2-k3, and up to $U_c/V_\theta = 30\%$ for correlations with the probe k4. The latter are however characterized by lower correlation magnitudes, so the resulted apparent acceleration could be explained by the time-deformation of the pressure oscillations of the signal k4, which through the correlation algorithm would result in shorter time lags and so higher velocities. The mean value of these results is $U_c/V_\theta = 22\%$, which is in agreement with propagation velocities of rotating instabilities reported in experimental investigations of high loaded annular compressor cascades in presence of radial clearance at the hub. The work of Beselt and Peitsch (2012) shows indeed that rotating instabilities at the hub always propagate at approximately 24% of the circumferential component of flow, for values of inlet Mach number ranging between

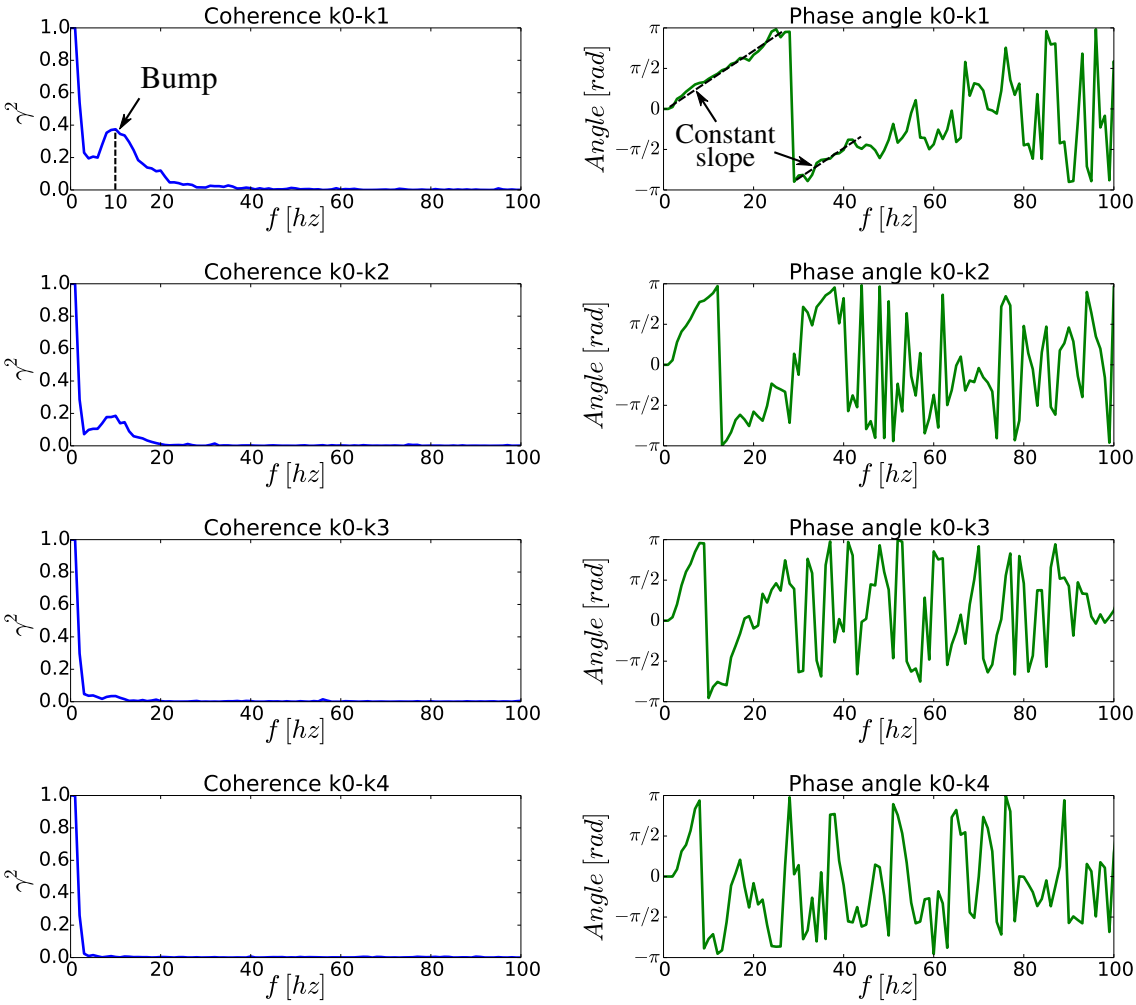

Fig. 5.25 Coherence analysis of the pitchwise disturbance between the first passage (probe k0) and following passages (k2-k4) in configuration B. Figure (a): coherence amplitudes. Figure (b): phase-lag angles.

$M = 0.2$ and $M = 0.7$. In conclusion, adjacent passages interact because of the pulsation of neighboring separations, but the synchronicity between oscillations is damped since the bottom boundary of the linear cascade obstruct the free rotation of the disturbance.

In order to gain deeper insights into such phenomena it is necessary to calculate the coherence function in term of power and phase shift, both as function of the frequency. The same post-processing performed by Beselt et al. (2013a) for rotating instabilities studies, reviewed in Section 1.6.2, is adopted and shown in Fig. 5.25.

Fig. 5.25a shows the existence of a bump in coherence amplitudes at very low frequencies in the range between 6 and 20 Hz. The peak of the bump is located at $f \approx 10$ Hz, which corresponds to the Strouhal number $St = cf/V_{ax} = 0.1$, where V_{ax} is the mean axial velocity

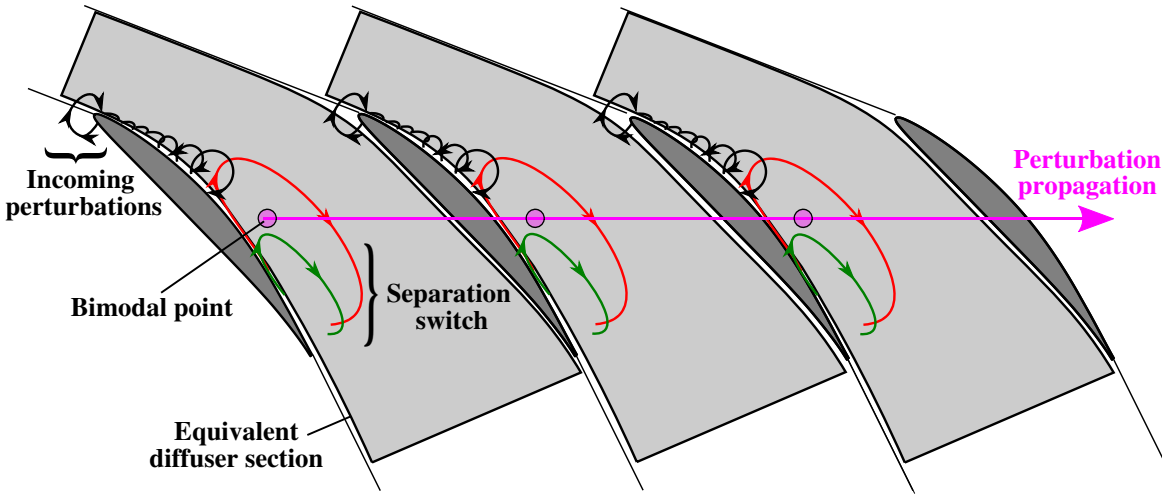

Fig. 5.26 Sketch of the equivalent parallel diffuser system setting the propagation of disturbances in pitchwise direction.

in the middle section. This values is lower than the results of $St = 0.19$ reported by Beselt and Peitsch (2012), but sharing the same order of magnitude. Such results enhance the hypothesis that bimodal switches of the corner separation could be a trigger mechanism for rotating instability in annular blade rows. The bump slowly decreases moving on to following passages, passing from a value of $\gamma^2 = 0.4$ between the probes k0 and k1 to the $\gamma^2 = 0$ in the last coherence plot between the probe k0 and the probe k4.

The associated shift angle between signals is calculated in Fig. 5.25. The linear trend of the function in the low frequency range, between 0 Hz and 30 Hz, is the final effective proof that a disturbance exists and it travels across the inter-blade passages. These results present the same phenomenon described by Beselt et al. (2013a) and reviewed in Section 1.6.2. The presence of bumps in the amplitude of the coherence function and the linearity of the shift lag in the corresponding frequency range mean that a specific flow dynamic, characterized by time scales associated to frequencies between 5 Hz and 20 Hz, develops in pitchwise direction.The linearity of the shift angle against frequency usually exists when the rotating instabilities are detected, because the slope of the $angle(f)$ line is the defined convection velocity characterizing the propagation of the disturb. During the measurements, it was remarked that the maximum frequency for which the linear trend of the phase-lag is visible depends on the total time of the experimental acquisition. The correlation of longer signals permits to refine the detection of the disturbance propagation for higher frequencies. These measurements were hence performed with an acquisition frequency $f_s = 1$ KHz for a total time $t = 600$ sec.

Even if it is not pertinent to consider this perturbation a rotating disturbance in case of a linear cascade, the present results show a clear foot-print of the pitchwise propagation. The question as whether the corner separation unsteady variations in stator rows could generate the propagation of rotating disturbances in circunferential direction is consequently answered positively. Even for a simply configuration, as the case of study of the present work on an isolated blade row without tip gap and uniform inlet flow, blade passages show correlations

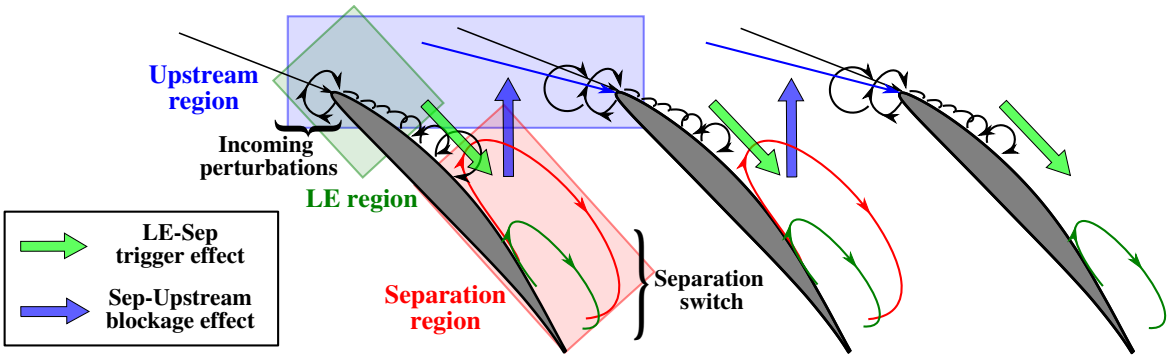

Fig. 5.27 Proposed mechanism of mutual interaction between upstream perturbations and separation switch generating the pitchwise propagation. LE and separation regions derive from POD analysis.

with a defined convection velocity. The existing models predict this propagation if a complete stall of the blade (Emmons et al., 1955), a leading edge separation (Pullan et al., 2015) or tip gap exist, but such theories do not take into account the propagation of the disturbance caused uniquely by the switch of the corner separation near the endwalls with zero tip clearance and without leading edge separation.

As shown before, the effect of the diffuser instability on the unsteady dynamic of the blade row have to be taken into account. Each stator inter-blade passage is indeed a diffuser working a the stability limit between unstalled flow and transitory stall, as shown in Fig. 5.26. Consequently, the cascade acts as a row of equivalent parallel diffusers with their own inherent instability, which is excited by the random large structures of the incoming endwall boundary layer. As resumed in Fig. 5.27, these two dynamics coexist and generate the bimodal behaviour of the separation, with large oscillations between the two preferred states of reduced and massive separation. Then, these low frequency perturbations propagate in pitchwise direction across the cascade on both left and right endwalls.

5.7 Summary and conclusions

The unsteadiness of the corner separation behind the bimodal behavior results to be described by the same dynamics underpinning the transitory stall regime in planar diffusers.

In the investigated compressor cascade, the mechanism of the separation switch can be summarized by four main phases, resumed as follows in case the closed separation state is assumed at the beginning.

1. Random structures existing in the incoming endwall boundary layer strike the blade LE, then are convected downstream and finally merge with the boundary of the separation. This mechanism perturbs the boundary of the separation starting the inception of the switch closed-to-open.
2. The recirculating region grows, and the collision between the enforced back-flow above the aft part of the suction side and the incoming perturbations produces the intermittent

ejection of structures toward the free-stream. This pushes the front of the separation even farther upstream toward the LE and represents the stall-growth phase.

3. The final open separation configuration is hence established and it is characterized by a massive recirculation region associated to highly unsteady shedding of coherent structures at its boundary. The blockage in the passage reaches the maximum value in this phase.
4. After a time interval of apparent equilibrium, which is established by the existence of the open separation, the structures composing the recirculation region suddenly break down and are swept downstream. The open separation is not sustained anymore in the passage and the closed separation state is re-established. This phase can be recognized with the stall wash-out phase.

Two different principal dynamics intervene in the process presented before. The first accounts for the switch closed-to-open and it is represented by the arrival of large coherent structures within the incoming endwall boundary layer. Evidence of their presence is provided not only by flow visualizations, but also by high frequency pressure signatures on the first half of the suction surface of the blade. These perturbations are convected from the LE of the blade toward the separation, since convection velocities calculated for cross-correlations of both velocity and static surface pressures provide co-stream value of $U_c/V_\infty = 0.3$.

Finally, the proof of the primary role of these coherent structures in the inception of the separation growth is provided by the wavelet analysis. The occurrence of high deviation pressure signatures associated to these structures is detected by peaks in the wavelet spectrum and such peaks result to be the triggers for the switch between the closed and the open separation.

Beside this mechanism, the second fundamental dynamic does not compete to the high-frequency small-scale structures but instead to the low-frequency large-scale variations of the flow field in the whole inter-blade passage. These low-frequency oscillations characterize both pressure on the surface of the blade where the flow detaches and velocities in the bimodal points. Additionally, the size of the separation is described by large variations at low-frequency of the related displacement thickness, calculated on an extracted line near the TE of the blade.

Consequently, low-frequency variations account for the most energetic dynamics of the flow, among others the movement of the separation boundary farther upstream toward the LE and the consequent blockage increase. This movement is clearly highlighted by the Mode 1 of POD decomposition, which has been found to contain almost 30% of the total energy of the velocity field at the investigated section of blade span near the endwall.

Finally, this low-frequency dynamic negotiates the separation wash-out through the feedback effect of the blockage and the recirculation variation on the incoming flow. In order to prove this effect, POD has been conducted separately on the local region of the flow ahead the trailing edge and on the local region capturing the separation. Such a distinction has permitted to cross-correlate the separation dynamics with low-energy mechanisms, such as perturbations of the field ahead the blade LE, hidden by the high-energy chord-wise movement of the separation.

Among the expected co-flow correlations, two feedback relations have been found. These represent the perturbation of the local angle of attack at the LE induced by the blockage and the variation of the recirculation of the flow in the separated region, described by the Mode 1 and Mode 3.

The perturbation of the stagnation point position is also suggested by the conditional ensemble average of static pressures on the suction surface of the blade, showing a co-flow and a back-flow relationship between oscillations of static pressure sensed at the LE of the blade and pressure variations related to the detachment of the flow at the boundary of the separation.

With this comprehension at hand, the single stator blade passage results to act like a diffuser affected by corner separation in transitory stall regime. The question concerning the relation between the unsteadiness of a single corner separation and the behavior of corner separations of adjacent passages has been answered thanks to the simultaneous acquisition of time-resolved unsteady total pressure at bimodal positions in multiple adjacent passages. Coherence between such bimodal signals and linearity of the associated cross-phase angle prove that perturbations generated by a single passage instability are able to travel in pitchwise direction and propagate to adjacent passages. This perturbation is caused by the unsteadiness of the separation in the blade diffuser. The blockage due to massive enlargements of the separations affects the flow in front of the blade, probably affecting also the flow upstream of the following blade. This mechanism enhances the appearance of incoming massive structures that trigger the separation switch in the following interblade passage. The disturbance is then transferred to successive passages through the same mechanism. It is interesting to underline that in the present case the disturbance propagation is due solely to the unsteady switch of the corner separation, without the complete stall of the flow or LE separation vortex described by other studies on rotating instabilities in compressors. In conclusion, these results report for the first time a case of instability propagation appearing in a unstalled linear compressor cascade.

Chapter 6

Conclusions and perspectives

The aim of this thesis was to investigate and understand the dynamics of the flow underpinning the bimodal behavior of the corner separation.

The problem has been divided in two major investigations: the study of the unsteadiness of a single corner separation and the study of the interaction between adjacent passages. Major results concerning the first investigation were obtained by time-resolved velocity measurements, which were carried out synchronously with static pressure measurements on the surfaces of the blade. Conversely, the interaction between adjacent passages was investigated by equipping each corner separation on both sides of the test rig with time-resolved unsteady pressure sensors placed at positions where the flow shows the bimodal behavior.

When investigating the physic of unsteady mechanisms, measured data sets must be analyzed through adapted post-processing tools. For this reason correlations, cross-coherence, POD and wavelet transform have been widely exploited in order to target the understanding of the cause-effect relationships.

The major findings of Chapter 4 and 5 are summarized at first, then perspectives for future works are presented in the end.

6.1 Conclusions

Time-resolved flow visualizations show that the real nature of the separation at off-design conditions is highly unsteady, topologically complex and inherently unstable. The time-averaged description of corner separation is useful to understand basic features of the flow but mispredicts the real unsteady topologies of the separation and the associated blockage. In contrast, the real unsteady behavior of the separation is represented by intermittent switches between two preferred extreme states of the flow, which can be identified as open and closed separation. This effect should be carefully considered in the design of multistage compressors because affecting in the worst way the mismatching between stages. Furthermore, massively open states of the separation represent extreme events, which promotes the inception of instabilities.

The inherent unsteadiness of the blade passage

The switch process accounts for the 30% of the entire energy of the flow field and it is characterized by low frequencies with large oscillations, which produces a bump around 10 Hz. The existence of such oscillations is ensured by both velocity and pressure measurements.

The switch process is generated by different co-existing mechanisms related to different frequency ranges and scales, which interact to produce the overall unsteadiness of the flow. Among others, random massive structures are detected by extreme perturbations of flow angle in the incoming end-wall boundary layer. Such perturbations strike the blade leading edge inducing the generation of perturbations of smaller size and higher vorticity. It is possible to follow the path of such structures, which are convected on the suction surface, merge with the detached shear layer and destabilize the separation. The closed-to-open switch is therefore triggered. Furthermore, the elevated adverse pressure gradient existing in the passage when the separation is closed promotes the upstream shift of the separation boundary. The recirculation region and the reverse flow are consequently increased, as well as the ejection of eddies from the blade suction side toward the main flow. As the separation continues to grow and moves upstream towards the leading edge of the blade, the blockage faced by the incoming flow increases whereas the diffusion within the inter-blade passage decreases. These two mechanisms are proved to influence the upstream flow in front of the blade by POD analysis, pressure conditional ensemble average and pressure correlations. The extension of the incoming perturbations and the angle of attack then diminish. As a result, the path of shed eddies, which constitute the the boundary between the free stream and the recirculation flow, is tilted down towards the suction surface of the blade. This process leads to the overall decrease of the separation size, which stabilizes on a closed state and in extreme cases it is almost suppressed.

Such a behavior presents global unsteady dynamics equivalent to the intermittent regime occurring in planar diffusers at high divergence angles, called *transitory stall*. Furthermore, this operational regime is obtained at the investigated off-design incidences when the inter-blade passage is reduced to an equivalent two dimensional diffuser and it is compared with available correlation maps for curved diffuser.

In conclusion, the intrinsic unsteadiness of the corner separation in a single inter-blade passage is explained by the unsteadiness of an incoming turbulent flow which is diffused in a high divergence passage. Even if the boundary layer of the blade at midspan is not completely separated, close to the endwall the corner separation presents the typical low frequency intermittent oscillations reported for transitory stall regime in planar diffusers.

The interaction of multiple passages

In a blade cascade, the unsteadiness of one passage does not exist alone as in an isolated diffuser, but it coexists along with the separation unsteadiness of the adjacent blade passages.

Correlations have been found between adjacent bimodal separations on both left and right endwalls in pitchwise direction, i.e. moving from the pressure side to the suction side of the blade. The coherence between unsteady time tracers of total pressure is also in this case localized at very low frequencies, represented by a bump in the coherence function around

10 Hz. (Strouhal number $St \approx 0.1$) The existence of a pitch-wise coherent propagation is additionally ensured by the linearity of the cross-phase as a function of the frequency, which is usually found in studies of rotating instabilities.

In the present cascade the disturbance is generated from each passage and it propagates through neighbors inter-blade passages with a starting velocity comprised between 17 % and 30 % of the tangential flow velocity. Such magnitudes of velocity are comparable with the results of investigations of rotating instabilities in annular compressor cascade reported in the literature. Furthermore, the strongest correlation between different corner separations exists in pitchwise direction as compared to spanwise direction.

The proposed explanation to this behavior can be summarized as follows. The switch of the size of the separation affects the upstream flow by influencing the diffusion and the blockage. Such an influence is global and it strengthens as the separation size reaches extreme open states, mainly near the endwall. In this region, even the flow upstream the following blade is perturbed and the disturbance is hence propagated in pitchwise direction from blade to blade.

The data obtained in the present work lead to the conclusion that the pitchwise perturbation, which relates adjacent passages, is not the consequence of the oscillation of an isolated separation, but instead it is a perturbation generated by each separation within each corner.

Final proposed mechanism

The final conclusion is that the intermittent switch of corner separations is due to the interaction between extreme high energy incoming perturbations and the diffusing nature of the inter-blade passage. The separation unsteadiness and the magnitude of the associated low frequency oscillations of both pressure and velocity are increased as the operational incidence is increased. Additionally, such low frequencies oscillations affect the upstream flow as well as the entire inter-blade passage through global variations of the blockage and the diffusion within the inter-blade passage. When the separation reaches it maximum size, i.e. before the open-to-closed switch, such feedback effect enhances the magnitude and size of the upstream vortical structures in the vicinity of the adjacent blade. In this way the open separation influences the unsteady behavior of the following inter-blade passage. Since this process is valid also for the separation itself, which perceives the perturbation of previous passages, a periodic mechanism could be expected. Contrarily each separation, even if perturbed, still maintains its own dynamic of growth related to the single diffuser instability, which can be synchronous or asynchronous with the incoming large vortical structures. This competing interaction could explain the damping of the perturbation magnitude in pitchwise direction. A damped global perturbation sustained by multiple instabilities traveling a different velocities, i.e. the eddies constituting adjacent corner separations, would explain why the bimodal unsteadiness and the pitchwise propagation are described by a bump in the frequency spectrum instead of a well defined peak.

6.2 Perspectives

In order to assess and quantify the influence of a single separation on the following passages, PIV measurements covering at least one pitch distance should be performed. Synchronized unsteady pressure measurements within the inter-blade passage would be also useful to correlate and understand the unsteady variation of the diffusion within the blade passage.

On the numerical side, LES simulation of multiple passages should be carried out at the inlet incidence $i = 7^\circ$, in order to capture the interaction between multiple passages and the pitchwise propagation.

To elucidate the propagation phenomenon experimentally, the same dynamic should be studied in an annular cascade. In this case it would be possible to clarify if the perturbation continues to travel and enlarges or it is damped by the asynchronous behavior of adjacent blade passages. More generally, simultaneous unsteady velocity fields near the endwalls in different circumferential positions should be targeted when performing detailed experimental studies on stall in turbomachinery.

Finally, the effect of the upstream rotor should be investigated since it imposes the additional periodic perturbation related to the blade passing frequency, increasing the complexity of the unsteady dynamics.

References

Abbott, I. H., Von Doenhoff, A. E., and Stivers Jr, L. (1945). NACA Report No 824: Summary of airfoil data. Technical report.

Adenubi, S. O. (1976). Performance and flow regime of annular diffusers with axial turbomachine discharge inlet conditions. *Journal of Fluids Engineering*, 98(2):236–242.

Alfonsi, G. (2006). Coherent structures of turbulence: methods of eduction and results. *Applied Mechanics Reviews*, 59:307.

Ashjaee, J. and Johnston, J. (1980). Straight-walled, two-dimensional diffusers-transitory stall and peak pressure recovery. *Journal of Fluids Engineering*, 102(3):275–282.

Astolfi, J. and Forestier, B. (1993). Flow noise associated with near-wall turbulence structure. *ASME-publication-fed*, 168.

Barankiewicz, W. S. and Hathaway, M. D. (1998). Impact of variable-geometry stator hub leakage in a low speed axial compressor. In *ASME 1998 International Gas Turbine and Aeroengine Congress and Exhibition*. American Society of Mechanical Engineers.

Bendat, J. (1978). Statistical errors in measurement of coherence functions and input/output quantities. *Journal of Sound and Vibration*, 59(3):405–421.

Beselt, C., Pardowitz, B., van Rennings, R., Sorge, R., Peitsch, D., Enghardt, L., Thiele, F., Ehrenfried, K., and Thamsen, P. U. (2013a). Influence of the clearance size on rotating instability in an axial compressor stator. In *10th European Turbomachinery Conference, Lappeenranta, Finland, Apr*, pages 15–19.

Beselt, C. and Peitsch, D. (2012). Influence of mach number and aerodynamic loading on rotating instability in an annular compressor cascade. In *ASME Turbo Expo 2012: Turbine Technical Conference and Exposition*, pages 2711–2720. American Society of Mechanical Engineers.

Beselt, C., van Rennings, R., Peitsch, D., and Thiele, F. (2013b). Impact of hub clearance on endwall flow in a highly loaded axial compressor stator. *ASME Paper No. GT2013-95463*.

Bokde, A. L., Lueptow, R. M., and Abraham, B. (1999). Spanwise structure of wall pressure on a cylinder in axial flow. *Physics of Fluids*, 11:151.

Bölcs, A. and Körbächer, H. (1993). Periodicity and repetitivity of unsteady measurements of an annular turbine cascade at off design flow conditions. Technical report, ASME 93-GT-107.

Boudet, J., Caro, J., Shao, L., and Lévêque, E. (2007). Numerical studies towards practical large-eddy simulation. *Journal of Thermal Science*, 16(4):328–336.

Bradshaw, P. (1987). Turbulent secondary flows. *Annual review of fluid mechanics*, 19(1):53–74.

Cahuzac, A., Boudet, J., Jacob, M., and Kausche, P. (2011). Large-eddy simulation of a rotor tip-clearance flow. *AIAA Paper*, (2011-2947).

Camussi, R., Robert, G., Jacob, M. C., et al. (2008). Cross-wavelet analysis of wall pressure fluctuations beneath incompressible turbulent boundary layers. *Journal of Fluid Mechanics*, 617:11.

Choi, M., Baek, J. H., Oh, S. H., and Ki, D. J. (2008). Role of hub-corner-separation on rotating stall in an axial compressor. *Transactions of the Japan Society for Aeronautical and Space Sciences*, 51(172):93–100.

Christensen, K. (2004). The influence of peak-locking errors on turbulence statistics computed from PIV ensembles. *Experiments in Fluids*, 36(3):484–497.

Courtiade, N. (2012). *Experimental analysis of the unsteady flow and instabilities in a high-speed multistage compressor*. PhD thesis, Ecole Centrale de Lyon.

Cumpsty, N. (1990). Discussion:"Three-dimensional relief in turbomachinery blading"(Wadia, AR, and Beacher, BF, 1990, ASME J. Turbomach., 112, pp. 587–596). *Journal of Turbomachinery*, 112(4):596–598.

Cumpsty, N. (2010). Some lessons learned. *Journal of turbomachinery*, 132(4).

Cumpsty, N. A. (1989). *Compressor aerodynamics*. Longman Scientific & Technical.

Day, I. and Cumpsty, N. (1978). The measurement and interpretation of flow within rotating stall cells in axial compressors. *Journal of Mechanical Engineering Science*, 20(2):101–114.

Day, I. J. (2016). Stall, surge, and 75 years of research. *Journal of Turbomachinery*, 138(1):011001.

DeCarlo, L. T. (1997). On the meaning and use of kurtosis. *Psychological Methods*, 2(3):292.

Denton, J. D. (1993). Loss mechanisms in turbomachines. In *ASME 1993 International Gas Turbine and Aeroengine Congress and Exposition*. American Society of Mechanical Engineers.

Devenport, W. and Simpson, R. (1990). Time-dependent and time-averaged turbulence structure near the nose of a wing-body junction. *Journal of Fluid Mechanics*, 210(1):23–55.

Dickens, P., Smith, J., and Wolfe, J. (2007). Improved precision in measurements of acoustic impedance spectra using resonance-free calibration loads and controlled error distribution. *The Journal of the Acoustical Society of America*, 121:1471.

Dickens, T. and Day, I. (2011). The design of highly loaded axial compressors. *Journal of Turbomachinery*, 133(3).

Dixon, S. L. and Hall, C. (2013). *Fluid mechanics and thermodynamics of turbomachinery*. Butterworth-Heinemann.

Dodds, J. and Vahdati, M. (2015). Rotating stall observations in a high speed compressor-Part II: Numerical study. *Journal of Turbomachinery*, 137(5):051003.

Dong, Y., Gallimore, S. J., and Hodson, H. P. (1987). Three-dimensional flows and loss reduction in axial compressors. *Journal of Turbomachinery*, 109(3):354–361.

Dring, R., Joslyn, H., and Hardin, L. (1982). An investigation of axial compressor rotor aerodynamics. *Journal of Engineering for Power*, 104(1):84–96.

Délery, J. M. (2001). Robert Legendre and Henri Werlé: toward the elucidation of three-dimensional separation. *Annual review of fluid mechanics*, 33(1):129–154.

Emmons, H., Pearson, C., Grant, H., et al. (1955). Compressor surge and stall propagation. *Trans. ASME*, 77(4):455–469.

Evans, B. J. (1971). *Effects of free-stream turbulence on blade performance in a compressor cascade.* PhD thesis, University of Cambridge.

Fang, J. and Atassi, H. M. (1993). Compressible flows with vortical disturbances around a cascade of loaded airfoils. In *Unsteady Aerodynamics, Aeroacoustics, and Aeroelasticity of Turbomachines and Propellers*, pages 149–176. Springer.

Farge, M. (1992). Wavelet transforms and their applications to turbulence. *Annual review of fluid mechanics*, 24(1):395–458.

Fernando, J. N., Kriegseis, J., and Rival, D. E. (2014). Modal analysis of confined square and rectangular cavity flows. *International Journal of Heat and Fluid Flow*, 47:123–134.

Flegg, G. (1974). *From geometry to topology*. Courier Corporation.

Fox, R. W. and Kline, S. (1962). Flow regimes in curved subsonic diffusers. *Journal of Basic Engineering*, 84(3):303–312.

Gand, F. (2011). *Dynamique des écoulements de jonction en régime turbulent*. PhD thesis, Université Pierre et Marie Curie-Paris VI.

Gand, F., Deck, S., Brunet, V., and Sagaut, P. (2010). Flow dynamics past a simplified wing body junction. *Physics of Fluids (1994-present)*, 22(11).

Gao, F. (2014). *Advanced numerical simulation of corner separation in a linear compressor cascade*. PhD thesis, École Centrale de Lyon.

Gao, F., Ma, W., Zambonini, G., Boudet, J., Ottavy, X., Lu, L., and Shao, L. (2015a). Large-eddy simulation of 3D corner separation in a linear compressor cascade. *Physics of Fluids*, 27(8):085105.

Gao, F., Zambonini, G., Boudet, J., Ottavy, X., Lu, L., and Shao, L. (2015b). Unsteady behavior of corner separation in a compressor cascade: Large eddy simulation and experimental study. *Journal of Power and Energy*, 229(5):508–519.

Gbadebo, S. A., Cumpsty, N. A., and Hynes, T. P. (2005). Three-dimensional separations in axial compressors. *Journal of Turbomachinery*, 127(2):331–339.

Gbadebo, S. A., Cumpsty, N. A., and Hynes, T. P. (2008). Control of three-dimensional separations in axial compressors by tailored boundary layer suction. *Journal of Turbomachinery*, 130(1).

Gessner, F. (1973). The origin of secondary flow in turbulent flow along a corner. *Journal of Fluid Mechanics*, 58(01):1–25.

Godard, A. (2010). *Etude numérique et expérimentale d'un compresseur aspiré*. PhD thesis, École Centrale de Lyon.

Goodhand, M. N. and Miller, R. J. (2012). The impact of real geometries on three-dimensional separations in compressors. *Journal of turbomachinery*, 134(2):021007.

Hah, C. and Loellbach, J. (1999). Development of hub corner stall and its influence on the performance of axial compressor blade rows. *Journal of turbomachinery*, 121(1):67–77.

Horlock, J., Louis, J., Percival, P., and Lakshminarayana, B. (1966). Wall stall in compressor cascades. *Journal of Basic Engineering*, 88(3):637–648.

Horlock, J. H. (1973). *Axial flow compressors, fluid mechanics and thermodynamics*. RE Krieger Publishing Company.

Inoue, M., Kuroumaru, M., Tanino, T., and Furukawa, M. (2000). Propagation of multiple short-length-scale stall cells in an axial compressor rotor. *Journal of Turbomachinery*, 122(1):45–54.

Inoue, M., Kuroumaru, M., Tanino, T., Yoshida, S., and Furukawa, M. (2001). Comparative studies on short and long length-scale stall cell propagating in an axial compressor rotor. *Journal of Turbomachinery*, 123(1):24.

Inoue, M., Kuroumaru, M., Yoshida, S., Minami, T., Yamada, K., and Furukawa, M. (2004). Effect of tip clearance on stall evolution process in a low-speed axial compressor stage. In *ASME Turbo Expo 2004: Power for Land, Sea, and Air*, pages 385–394. American Society of Mechanical Engineers.

Kaiser, K. and McDonald, A. (1980). Effect of wake-type nonuniform inlet velocity profiles on first appreciable stall in plane-wall diffusers. *Journal of Fluids Engineering*, 102(3):283–289.

Kammeyer, M. (1995). An experimental investigation of organized turbulent motions and wall-pressure fluctuations in complex flows. Technical report, DTIC Document.

Kang, S. and Hirsch, C. (1991). Three dimensional flow in a linear compressor cascade at design conditions. In *ASME 1991 International Gas Turbine and Aeroengine Congress and Exposition*. American Society of Mechanical Engineers.

Khalid, S. A., Khalsa, A. S., Waitz, I. A., Cumpsty, N. A., Adamczyk, J. J., Marble, F. E., Tan, C. S., and Greitzer, E. M. (1999). Endwall blockage in axial compressors. *Journal of Turbomachinery*, 121(3):499–509.

Kim, J., Moin, P., and Moser, R. (1987). Turbulence statistics in fully developed channel flow at low Reynolds number. *Journal of Fluid Mechanics*, 177(1):133–166.

Kriegseis, J., Dehler, T., Gnirß, M., and Tropea, C. (2010). Common-base proper orthogonal decomposition as a means of quantitative data comparison. *Measurement Science and Technology*, 21(8):085403.

Kwong, A. and Dowling, A. (1994). Unsteady flow in diffusers. *Journal of Fluids Engineering*, 116(4):842–847.

Laadhari, F., Morel, R., and Alcaraz, E. (1994). Combined visualisation and measurements in transitional boundary layers. *European Journal of Mechanics*, 13:473–473.

Lakshminarayana, B. (1996). *Fluid dynamics and heat transfer of turbomachinery*. John Wiley & Sons.

Lakshminarayana, B. and Horlock, J. t. (1967). *Leakage and secondary flows in compressor cascades*. HM Stationery Office.

Lee, I. and Sung, H. (1999). Development of an array of pressure sensors with PVDF film. *Experiments in Fluids*, 26(1-2):27–35.

Lee, I. and Sung, H. (2001). Characteristics of wall pressure fluctuations in separated and reattaching flows over a backward-facing step: Time-mean statistics and cross-spectral analyses. *Experiments in Fluids*, 30(3):262–272.

Lei, V., Spakovszky, Z., and Greitzer, E. (2008). A criterion for axial compressor hub-corner stall. *Journal of Turbomachinery*, 130(3).

Lévêque, E., Toschi, F., Shao, L., and Bertoglio, J.-P. (2007). Shear-improved smagorinsky model for large-eddy simulation of wall-bounded turbulent flows. *Journal of Fluid Mechanics*, 570:491–502.

Lewalle, J. and Ashpis, D. E. (2004). Estimation of time scales in unsteady flows in a turbomachinery rig. *NASA/TM - 2004-209452*.

Lewin, E., Kozulovic, D., and Stark, U. (2010). Experimental and numerical analysis of hub-corner stall in compressor cascades. In *ASME Turbo Expo 2010: Power for Land, Sea, and Air*, pages 289–299. American Society of Mechanical Engineers.

Li, Y. S. and Cumpsty, N. A. (1991). Mixing in axial flow compressors: Part II- Measurements in a single-stage compressor and a duct. *Journal of Turbomachinery*, 113(2):166–172.

Lieblein, S. (1959). Loss and stall analysis of compressor cascades. *Journal of Basic Engineering*, 81(3):389–400.

Lieblein, S., Schwenk, F. C., and Broderick, R. L. (1953). Diffusion factor for estimating losses and limiting blade loadings in axial-flow-compressor blade elements. Technical report, DTIC Document.

Lilley, G. and Hodgson, T. (1960). *On surface pressure fluctuations in turbulent boundary layers*. Advisory Group for Aeronautical Research and Development Paris (France).

Liu, B., Yu, X., Liu, H., Jiang, H., Yuan, H., and Xu, Y. (2006). Application of SPIV in turbomachinery. *Exp Fluids*, 40(4):621–642.

Lowson, M. (1965). *Pressure fluctuations in turbulent boundary layers*. NASA Technical Note TN D-3156, NASA National Aeronautics and Space Administration.

Ma, W. (2012). *Experimental investigation of corner stall in a linear compressor cascade*. PhD thesis, École Centrale de Lyon.

Marsden, O., Bailly, C., Bogey, C., and Jondeau, E. (2012). Investigation of flow features and acoustic radiation of a round cavity. *Journal of Sound and Vibration*, 331(15):3521–3543.

Monier, J.-F., Gao, F., Boudet, J., Shao, L., and Lu, L. (2016). Budget analysis of turbulent kinetic energy in corner separation: RANS vs LES. In *ECCOMAS Congress 2016: VII European Congress on Computational Methods in Applied Sciences and Engineering*.

Moore Jr, C. A. and Kline, S. J. (1958). Some effects of vanes and of turbulence in two-dimensional wide-angle subsonic diffusers. *NACA Technical note 4080*.

Mueller, T. J. (2002). *Aeroacoustic measurements*. Springer.

März, J., Hah, C., and Neise, W. (2002). An experimental and numerical investigation into the mechanisms of rotating instability. *Journal of Turbomachinery*, 124(3):367.

Pardowitz, B., Moreau, A., Tapken, U., and Enghardt, L. (2015). Experimental identification of rotating instability of an axial fan with shrouded rotor. *Proceedings of the Institution of Mechanical Engineers, Part A: Journal of Power and Energy*, 229(5):520–528.

Pope, S. B. (2001). *Turbulent flows*. IOP Publishing.

Pullan, G., Young, A., Day, I., Greitzer, E., and Spakovszky, Z. (2015). Origins and structure of spike-type rotating stall. *Journal of Turbomachinery*, 137(5):051007.

Raffel, M., Willert, C. E., Wereley, S., and Kompenhans, J. (2013). *Particle image velocimetry: a practical guide*. Springer.

Reneau, L. R., Johnston, J., and Kline, S. J. (1967). Performance and design of straight, two-dimensional diffusers. *Journal of Basic Engineering*, 89(1):141–150.

Salze, É., Bailly, C., Marsden, O., Jondeau, E., and Juvé, D. (2014). An experimental characterization of wall pressure wavevector-frequency spectra in the presence of pressure gradients. In *20th AIAA/CEAS Aeroacoustics Conference, AIAA Paper*, volume 2909.

Schaefer, P., Cierpka, C., Rehder, H.-J., and Roehle, I. (2011). Wavelet analysis of vortical structures in turbomachinery applied to PIV data. In *ASME 2011 Turbo Expo: Turbine Technical Conference and Exposition*, pages 1529–1538.

Schewe, G. (1983). On the structure and resolution of wall-pressure fluctuations associated with turbulent boundary-layer flow. *Journal of Fluid Mechanics*, 134:311–328.

Schulz, H. and Gallus, H. (1988). Experimental investigation of the three-dimensional flow in an annular compressor cascade. *Journal of Turbomachinery*, 110(4):467–478.

Schulz, H., Gallus, H., and Lakshminarayana, B. (1990a). Three-dimensional separated flow field in the endwall region of an annular compressor cascade in the presence of rotor-stator interaction: Part 1- Quasi-steady flow field and comparison with steady-state data. *Journal of Turbomachinery*, 112(4):669–678.

Schulz, H., Gallus, H., and Lakshminarayana, B. (1990b). Three-dimensional separated flow field in the endwall region of an annular compressor cascade in the presence of rotor-stator interaction: Part 2- Unsteady flow and pressure field. *Journal of Turbomachinery*, 112(4):679–688.

Simpson, R. L. (2001). Junction flows. *Annual Review of Fluid Mechanics*, 33(1):415–443.

Simpson, R. L., Chew, Y., and Shivaprasad, B. (1981). The structure of a separating turbulent boundary layer. Part 1. Mean flow and Reynolds stresses. *Journal of Fluid Mechanics*, 113:23–51.

Smith, C. R. and Kline, S. J. (1974). An experimental investigation of the transitory stall regime in two-dimensional diffusers. *Journal of Fluids Engineering*, 96(1):11–15.

Smith, C. R. and Layne, J. L. (1979). An experimental investigation of flow unsteadiness generated by transitory stall in plane-wall diffusers. *Journal of Fluids Engineering*, 101(2):181.

Spalart, P. R. (2000). Strategies for turbulence modelling and simulations. *International Journal of Heat and Fluid Flow*, 21(3):252–263.

Stanislas, M., Okamoto, K., Kähler, C. J., Westerweel, J., and Scarano, F. (2008). Main results of the third international PIV challenge. *Experiments in Fluids*, 45(1):27–71.

Tabachnick, B. and Fidell, L. (1996). *Using Multivariate Statistics*. Harper Collins College Publishers, New York.

Taylor, J. V. and Miller, R. J. (2015). Competing 3D mechanisms in compressor flows. In *ASME Turbo Expo 2015*. American Society of Mechanical Engineers.

Thomas, A. and Bull, M. (1983). On the role of wall-pressure fluctuations in deterministic motions in the turbulent boundary layer. *J. Fluid Mech*, 128:283–322.

Torrence, C. and Compo, G. P. (1998). A practical guide to wavelet analysis. *Bulletin of the American Meteorological Society*, 79(1):61–78.

Tsuji, Y., Fransson, J. H., Alfredsson, P. H., and Johansson, A. V. (2007). Pressure statistics and their scaling in high-Reynolds-number turbulent boundary layers. *Journal of Fluid Mechanics*, 585:1–40.

Ventsel, H. (1973). *Théorie des probabilités*. Mir.

Wadia, A. and Beacher, B. (1990). Three-dimensional relief in turbomachinery blading. *Journal of Turbomachinery*, 112(4):587–596.

Wagner, J., Dring, R., and Joslyn, H. (1985). Inlet boundary layer effects in an axial compressor rotor: Part 1 blade-to-blade effects. *Journal of Engineering for Gas Turbines and Power*, 107(2):374–380.

Wang, Z.-N. and Yuan, X. (2013). Unsteady mechanisms of compressor corner separation over a range of incidences based on hybrid LES-RANS. In *Proceedings of ASME Turbo Expo 2013: Turbine Technical Conference and Exposition*.

Wieneke, B. (2005). Stereo-piv using self-calibration on particle images. *Experiments in fluids*, 39(2):267–280.

Wolf, S. and Johnston, J. (1969). Effects of nonuniform inlet velocity profiles on flow regimes and performance in two-dimensional diffusers. *Journal of Basic Engineering*, 91(3):462–474.

Yamada, K., Furukawa, M., Nakakido, S., Matsuoka, A., and Nakayama, K. (2015). Large-scale DES analysis of unsteady flow field in a multi-stage axial flow compressor at off-design condition using K computer. In *ASME Turbo Expo 2015: Turbine Technical Conference and Exposition*. American Society of Mechanical Engineers.

Young, A., Day, I., and Pullan, G. (2011). Stall warning by blade pressure signature analysis. In *ASME 2011 Turbo Expo: Turbine Technical Conference and Exposition*, pages 1589–1599. American Society of Mechanical Engineers.

Young Jr, W. H., James F, M., and Danny R, H. (1978). A laser velocimeter flow survey above a stalled wing. *NASA Langley Technical Paper 1266, TR 78-50*.

Yu, X., Zhang, Z., and Liu, B. (2013). The evolution of the flow topologies of 3d separations in the stator passage of an axial compressor stage. *Experimental Thermal and Fluid Science*, 44:301–311.

Zambonini, G. and Ottavy, X. (2015). Unsteady pressure investigations of corner separated flow in a linear compressor cascade. In *ASME Turbo Expo 2015*. American Society of Mechanical Engineers.

Zambonini, G., Ottavy, X., and Kriegseis, J. (2017). Corner separation dynamics in a linear compressor cascade. *Journal of Fluids Engineering*.

Zierke, W. and Deutsch, S. (1989). The measurement of boundary layers on a compressor blade in cascade Volume I-Experimental technique, analysis, and results. Technical report, NASA.

dernière page de la thèse

AUTORISATION DE SOUTENANCE

Vu les dispositions de l'arrêté du 7 août 2006,

Vu la demande du Directeur de Thèse

Monsieur X. OTTAVY

et les rapports de

M. R. MILLER
Professeur - University of Cambridge - Department of Engineering - Trumpington Street Cambridge CB2 1PZ - Royaume-Uni

et de

M. D-G. PASTRONE
Professeur - Politecnico di Torino - Dipartimento di Ingegneria Meccanica e Aerospaziale Corso Duca degli Abruzzi 24 - 10129 Torino - Italie

Monsieur ZAMBONINI Gherardo

est autorisé à soutenir une thèse pour l'obtention du grade de **DOCTEUR**

Ecole doctorale MECANIQUE, ENERGETIQUE, GENIE CIVIL ET ACOUSTIQUE

Fait à Ecully, le 29 novembre 2016

P/Le directeur de l'E.C.L.
La directrice des Etudes

ECOLE CENTRALE DE LYON
Service Scolarité
ECULLY

M-A. GALLAND